

# **Metal nanoparticle growth through *in situ* exsolution from barium cerate zirconate**

Mei Wang

A thesis submitted for the degree of PhD  
at the  
University of St Andrews



2021

Full metadata for this thesis is available in  
St Andrews Research Repository  
at:

<https://research-repository.st-andrews.ac.uk/>

Identifier to use to cite or link to this thesis:

DOI: <https://doi.org/10.17630/sta/773>

This item is protected by original copyright



## **Candidate's declaration**

I, Mei Wang, do hereby certify that this thesis, submitted for the degree of PhD, which is approximately 60,000 words in length, has been written by me, and that it is the record of work carried out by me, or principally by myself in collaboration with others as acknowledged, and that it has not been submitted in any previous application for any degree.

I was admitted as a research student at the University of St Andrews in August 2016.

I received funding from an organisation or institution and have acknowledged the funder(s) in the full text of my thesis.

Date 14/12/2020 Signature of candidate

## **Supervisor's declaration**

I hereby certify that the candidate has fulfilled the conditions of the Resolution and Regulations appropriate for the degree of PhD in the University of St Andrews and that the candidate is qualified to submit this thesis in application for that degree.

Date 14/12/2020 Signature of supervisor

## **Permission for publication**

In submitting this thesis to the University of St Andrews we understand that we are giving permission for it to be made available for use in accordance with the regulations of the University Library for the time being in force, subject to any copyright vested in the work not being affected thereby. We also understand, unless exempt by an award of an embargo as requested below, that the title and the abstract will be published, and that a copy of the work may be made and supplied to any bona fide library or research worker, that this thesis will be electronically accessible for personal or research use and that the library has the right to migrate this thesis into new electronic forms as required to ensure continued access to the thesis.

I, Mei Wang, confirm that my thesis does not contain any third-party material that requires copyright clearance.

The following is an agreed request by candidate and supervisor regarding the publication of this thesis:

**Printed copy**

Embargo on all of print copy for a period of 2 years on the following ground(s):

- Publication would preclude future publication

**Supporting statement for printed embargo request**

The work in this thesis has not been published.

**Electronic copy**

Embargo on all of electronic copy for a period of 2 years on the following ground(s):

- Publication would preclude future publication

**Supporting statement for electronic embargo request**

This work has not been published.

**Title and Abstract**

- I agree to the title and abstract being published.

Date 14/12/2020 Signature of candidate

Date 14/12/2020 Signature of supervisor



## **Underpinning Research Data or Digital Outputs**

### **Candidate's declaration**

I, Mei Wang, understand that by declaring that I have original research data or digital outputs, I should make every effort in meeting the University's and research funders' requirements on the deposit and sharing of research data or research digital outputs.

Date 14/12/2020 Signature of candidate

### **Permission for publication of underpinning research data or digital outputs**

We understand that for any original research data or digital outputs which are deposited, we are giving permission for them to be made available for use in accordance with the requirements of the University and research funders, for the time being in force.

We also understand that the title and the description will be published, and that the underpinning research data or digital outputs will be electronically accessible for use in accordance with the license specified at the point of deposit, unless exempt by award of an embargo as requested below.

The following is an agreed request by candidate and supervisor regarding the publication of underpinning research data or digital outputs:

Embargo on all of electronic files for a period of 2 years on the following ground(s):

- Publication would preclude future publication

### **Supporting statement for embargo request**

This work has not been published.

### **Title and Description**

- I require an embargo on the title and description

Date 14/12/2020 Signature of candidate

Date 14/12/2020 Signature of supervisor



## ACKNOWLEDGEMENTS

I would like to express my sincere gratitude to my supervisor, Professor John T. S. Irvine, for giving me this opportunity to study in his research group. I am especially grateful to him for helping me to explore solid state chemistry, always being kind and patient to provide key guidance, and encouraging me to be optimistic. His guidance has a great influence on my research study and life.

I am also grateful to Dr. Cristian Savaniu for generously sharing his time and knowledge, being patient to teach me the experimental process such as solid state synthesis, tape casting, and conductivity test, etc, teaching me with Rietveld refinement of the XRD data and fitting AC impedance data.

I would also like to thank the JTSI group, especially those who helped me with various matters throughout my PhD: Dr. Jianing Hui for answering my most random questions and sharing his research experience; Dr. Paul Connor for providing me very useful suggestions on some key points; Dr. David Miller for training me on scanning electron microscopy on Scios, carrying out TEM characterization and helping me with EBSD sample preparation; Dr. Aaron Naden for always being kind to characterize my TEM samples and to explain the results; Dr. Georgios Tsimekas for assisting me a lot with the cell setup; Mr. Kamil Nowicki for the tape casting in organic system; Mr. Ross Blackley for training me on JSM-5600 scanning electron microscope and JSM-6700F Field Emission Gun (FEG) microscope; Mrs. Maria Nowosielska for TGA and DTA measurements; Mr. Stefan Saxin for TGA and ICP measurements; Mr. Shitao Wu and Dr. Shuai He for helping me with analysing TEM data; Mrs. Julie Nairn for lab maintenance; Mrs. Candice Mitchell for paperwork; Dr. Jie Hou, Dr. Jingwei Li, Mr. Yunfeng Tian, Mr. Min Xu, Mr. Peng Ma and many other colleagues for sharing with their experiment experiences. I would also like to express my gratitude to Prof. Wuzong Zhou and Prof. Manfred Buck for the supervision on the annual assessment and to Prof. Nikos Bonanos for the valuable advise on my thesis.

I would like to express my great gratitude to my family who always supports me and gives me a lot of care.

I gratefully acknowledge the China Scholarship Council for funding and the Engineering and Physical Sciences Research Council (EPSRC) for providing the Scios instrument.

## Abstract

Protonic ceramic fuel cells (PCFCs) have great potential in applications compared with oxygen-ion-conducting-electrolyte based cells due to their relatively high ionic conductivity under intermediate and low temperature operating conditions. In addition, water is produced at the air electrode side of a proton-conducting fuel cell without diluting the fuel in the fuel electrode side, which provides higher operating voltage than an oxygen ion conducting SOFC. Among the proton-conducting materials, the most traditionally and widely used one is barium cerate-zirconate based perovskite oxide. It is simple to tailor its proton conductivity and stability by adjusting the doping concentration of  $\text{Ce}^{4+}$  and  $\text{Zr}^{4+}$ . In a highly performed cell, the fuel electrode plays a vital role. The conventional fuel electrode is fabricated by metal-electrolyte composites, where the metal particles provide the catalytic activity and electronic conductivity and the electrolyte material ensures the proton conductivity. The main drawbacks of this cermet electrode are metal sintering and carbon coking, which degrades the cell performance in a long run.

In past decades, exsolution has been proposed as an effective way for *in situ* nanoparticles growth from perovskite oxide by a controlled phase decomposition process. Exsolved nanoparticles are socketed strongly in parent perovskite and show better resistance towards coarsening and coking compared with conventional electrodes. The nanoparticles exsolution from perovskite can be simply accomplished by doping the catalytically active transition metal into the perovskite structure, followed by chemical or electrochemical reduction.

The exsolution phenomenon has been well investigated on perovskite titanate oxide. However, little study has been focused on the exsolution from protonic conducting oxides and their applications in PCFCs. This thesis explores the exsolution behavior from the doped barium cerate zirconate oxide. Generally, nicely distributed particles are obtained on the BCZY perovskite through the *in situ* exsolution approach.

Different from the previously observed process, where the B-site cations diffuse from bulk to surface for nucleation, here, the exsolution from BCZY perovskite competes with a phase segregation/decomposition process. In reduction, Ba-M-O phases (M is transition metal) are firstly formed on the perovskite surface, followed by the exsolution of transition metal ions from the Ba-M-O phases. This mechanism determines that for the B-site exsolutions from barium cerate zirconate oxide, A-site deficiency is unnecessary. Moreover, the cell parameters are found to have a significant effect on the electronic conductivity and stability of the materials with exsolution, which should draw the attention when optimizing the material properties in order to obtain a good performance.

By doping two transition metals on B-site, alloy particles are able to be achieved by exsolution. Compared with the single metal exsolution, the migration tendency of the metal ions to the surface is hindered by the other one. In this work, the co-exsolved Ni-Cu alloy particles show a much tidier nanoparticles distribution than the single particles, with a smaller particle size and higher population. Moreover, the doping of bimetal promotes their solubility in the perovskite structure. While the addition limit of sintering aids (Ni, Co, Cu etc.) is generally believed to be within 1 wt% (about 4 mol%) and sintering aids-rich impurities are constantly observed during the perovskite sintering, the nickel and copper bimetal doped BCZY perovskite shows a single pure phase, with a solubility of at least 5 mol% of the total doping concentration.

More importantly, the Cu particles exsolved from the doped BCZY oxide show a strong catalytic activity towards CO oxidation reaction. Furthermore, the morphology of Cu particles is reconstructed by oxygen plasma, exhibiting even higher catalytic activity. This gives a great view in plasma modifying catalyst morphology, hence enhancing performance. The recent work on the catalytic tests of BCZY supported Cu particles shows a very high activity and promising performance, which draws a lot of value on the exsolution from BCZY.

# Contents

1 Introduction.....	1
1.1 Energy consumption.....	1
1.2. Why CO <sub>2</sub> conversion? .....	1
1.3 Solid oxide electrolysis cells and solid oxide fuel cells .....	3
1.4 Oxygen ion conductor and proton conductor .....	6
1.4.1 Electrolyte.....	6
1.4.2 Oxygen ion conductors.....	6
1.4.3 Proton conductors.....	7
1.4.4 Review on BaCeO <sub>3</sub> .....	9
1.5 Proton conduction background.....	12
1.5.1 Perovskite background .....	12
1.5.2 Proton defect formation.....	15
1.5.3 Proton transportation mechanism .....	16
1.5.4 Electronegativity effect on hydration enthalpy .....	17
1.5.5 Protonic defects stability .....	18
1.5.6 Proton mobility and its activation enthalpy .....	19
1.6 Electrodes and exsolution.....	22
1.6.1 Electrodes .....	22
1.6.2 Exsolution mechanism.....	23
1.6.3 The extent of A-site deficiency in Perovskite .....	30
1.7 Phase diagram.....	32
1.7.1 Y <sub>2</sub> O <sub>3</sub> -BaO-CuO system .....	32
1.7.2 BaO-CuO system.....	34
1.7.3 NiO-BaO system .....	37
1.8 Aim of this thesis.....	38
1.9 Outline of this thesis.....	39
1.10 List of publications .....	40
References .....	40

2 Experimental .....	50
2.1 Sample preparation.....	50
2.1.1 Solid state synthesis.....	50
2.1.2 Exsolution.....	50
2.1.3 Tape casting.....	51
2.1.4 Preparation of solid oxide cell.....	55
2.2 Characterization methods and techniques .....	57
2.2.1 Powder X-ray diffraction.....	57
2.2.2 Scanning electron microscopy.....	58
2.2.3 Transmission electron microscopy .....	62
2.2.4 TEM sample preparation via focus ion beam.....	63
2.2.5 X-ray photoelectron spectroscopy .....	64
2.2.6 Dilatometry analysis .....	64
2.2.7 Thermogravimetry analysis .....	65
2.2.8 AC impedance spectroscopy .....	65
2.2.9 DC Conductivity.....	69
2.2.10 Inductively coupled plasma – Optical emission spectrometry .....	70
References .....	71
3 In situ growth Cu nanoparticles from doped BCZY perovskite .....	72
3.1 Introduction .....	72
3.2 Microstructure and phase identification of Cu-doped BCZY.....	73
3.2.1 Microstructure of the as-prepared Cu-doped BCZY .....	73
3.2.2 Phase identification of the as-prepared Cu-doped BCZY .....	75
3.2.3 Effect of Cu concentration on the unit cell parameter of BCZYC .....	79
3.2.4 Axial $c/a$ ratios of as-prepared Cu-doped BCZY oxides.....	81
3.3 Copper exsolution from BCZYC perovskite.....	86
3.3.1 Phase identification of BCZYC oxide after reduction.....	86
3.3.2 Unit cell parameter and axial $c/a$ ratios of the reduced BCZYC oxides.....	87
3.3.3 Microstructure of the reduced BCZYC pellets.....	90
3.3.4 Particle tracking for exsolution process study .....	96
3.3.5 Analysis with phase diagram of BaO-CuO system .....	101



3.3.6 VT-XRD characterization of polished BCZYC pellet.....	106
3.3.7 TGA test on the BCZYC oxide in reducing atmosphere.....	110
3.4 Plasma treatment on the reduced BCZYC pellet.....	112
3.5 DC Conductivity tests on BCZYC oxide .....	117
3.5.1 DC conductivity tests of BCZYC oxide prepared from two-steps.....	117
3.5.2 DC conductivity tests on BCZYC oxides prepared from one-step.....	119
3.5.3 TEM analysis of the BCZYC oxide after DC conductivity test .....	126
3.5.4 Surface etching of the BCZYC sample after DC conductivity test.....	129
3.6 CO oxidation test on BCZYC oxide with copper exsolution .....	132
3.7 Conclusions .....	134
References .....	134
<b>4 Influence of cation stoichiometry on Ni exsolution from <math>Ba_xCe_{0.5}Zr_{0.3}Y_{0.2-y}Ni_yO_{3-\delta}</math></b>	
.....	141
4.1 Introduction .....	141
4.2 XRD characterization of $Ba_xCe_{0.5}Zr_{0.3}Y_{0.2-y}Ni_yO_{3-\delta}$ .....	142
4.3 Microstructure of $Ba_xCe_{0.5}Zr_{0.3}Y_{0.2-y}Ni_yO_{3-\delta}$ .....	143
4.3.1 Microstructure of the as-prepared $Ba_xCe_{0.5}Zr_{0.3}Y_{0.2-y}Ni_yO_{3-\delta}$ .....	143
4.3.2 Characterization of the reduced $BaCe_{0.5}Zr_{0.3}Y_{0.16}Ni_{0.04}O_{3-\delta}$ pellet.....	147
4.3.3 Characterization of reduced $BaCe_{0.5}Zr_{0.3}Y_{0.14}Ni_{0.06}O_{3-\delta}$ pellet.....	150
4.3.4 Characterization of reduced $Ba_{0.95}Ce_{0.5}Zr_{0.3}Y_{0.14}Ni_{0.06}O_{3-\delta}$ pellet.....	156
4.4 DC conductivity test.....	157
4.5 Conclusion.....	160
References .....	161
<b>5 Exsolution of Ni-Cu alloy from the co-doped BCZY perovskite.....</b>	<b>166</b>
5.1 Introduction .....	166
5.2 Phase identification and microstructure of Ni, Cu co-doped BCZY .....	166
5.2.1 Phase identification of Ni, Cu co-doped BCZY .....	166
5.2.2 Microstructure of Ni, Cu co-doped BCZY.....	167
5.3 Exsolution from the Ni, Cu co-doped BCZY .....	168
5.3.1 Microstructure of exsolutions as a function of stoichiometry and temperature	
.....	168

5.3.2 The influence of Ni and Cu doping concentration on the Ni/Cu ratio of the exsolved alloy particles .....	182
5.3.3 EBSD investigation on exsolutions from Ni, Cu co-doped BCZY oxide ....	187
5.4 Thermogravimetric analysis .....	190
5.5 Electric conductivity and ionic transport number.....	191
5.5.1 DC conductivity test.....	191
5.5.2 AC conductivity test.....	192
5.5.3 Ionic proton transference number.....	199
5.6 Conclusions .....	200
References .....	202
6 Cell fabrication and optimization.....	206
6.1 Introduction .....	206
6.2 Influence of ZnO sintering aid on the sinterability of BCZY .....	207
6.2.1 Phase characterization of the prepared BCZY.....	207
6.2.2 Preparation of BCZY with the addition of ZnO .....	208
6.3 Optimisation of tape recipe and sintering procedure .....	213
6.3.1 BCZYZ tape using water as a solvent .....	213
6.3.2 Optimization of the sintering procedure .....	214
6.3.3 Preparation of BCZYZ tape use an organic solvent .....	219
6.3.4 Preparation of Ni, Cu-doped BCZY electrode tape.....	222
6.4 Slurry coating of the electrodes .....	225
6.4.1 Sintered powder for coating slurry preparation.....	225
6.4.2 Pre-calcined powder for coating slurry preparation .....	227
6.5 Electrochemical switching to drive exsolution.....	229
6.6 Electrode impregnation and impedance testing.....	230
6.6.1 Impregnation of LSCF and Ni electrode .....	230
6.6.2 AC impedance and I-V curve .....	232
6.7 Conclusions .....	235
References .....	236
Conclusions.....	239



# 1 Introduction

## 1.1 Energy consumption

Energy plays an important role in the development of society throughout history. The demand for energy is also rising gradually in some main fields like industry, transport and domestic. Among the various energy resources, fossil fuels dominate the global energy economy over the past thirty years, seen from Figure 1-1. But the conversion efficiency of power stations for fossil fuels is only about 40%-65%, which means only about half the energy in the primary fuel is converted into electrical energy. However, looking at the world energy consumption trend, renewable energy is expected to take more proportion in the next 20 years.

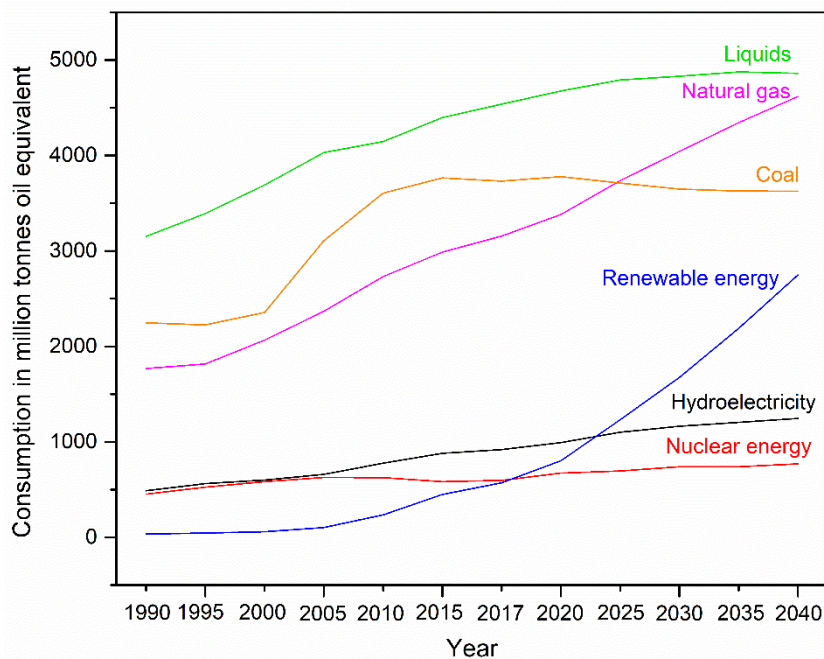


Figure 1-1. Projected global energy consumption<sup>1</sup>.

## 1.2. Why CO<sub>2</sub> conversion?

The biosphere currently converts carbon dioxide to useful products through photosynthesis. This is a low-efficiency process (typically only 1-2%) yet for many millennia it has successfully achieved equilibrium in the biosphere. Unfortunately, the

advent of our current fossil fuel civilization is driving the atmosphere away from this equilibrium with an ever-increasing concentration of CO<sub>2</sub> produced from the combustion of fossil carbons. This imbalance is widely accepted to be a major cause of global warming and climate change, and civilization ignores this threat at its peril. Furthermore, the increasing use of fossil fuels cannot be sustained and we face catastrophic energy and raw materials (i.e. chemical feedstocks) shortages in future decades. Figure 1-2 reveals the global annual atmospheric CO<sub>2</sub> concentration over the past 2000 years, indicating that it is fairly stable at 270-285 parts per million (ppm) before the 18<sup>th</sup> century<sup>2</sup>. After that, the Industrial Revolution led to the rapid rise of global CO<sub>2</sub> emission, especially in recent decades. It is reported that the global temperature has risen by 1 to 1.2 °C now because of global warming. It is therefore, imperative to reinforce the biological conversion of CO<sub>2</sub> with technological solutions offering higher efficiency and use of other energy sources in addition to direct solar, with an emphasis on high product selectivity.

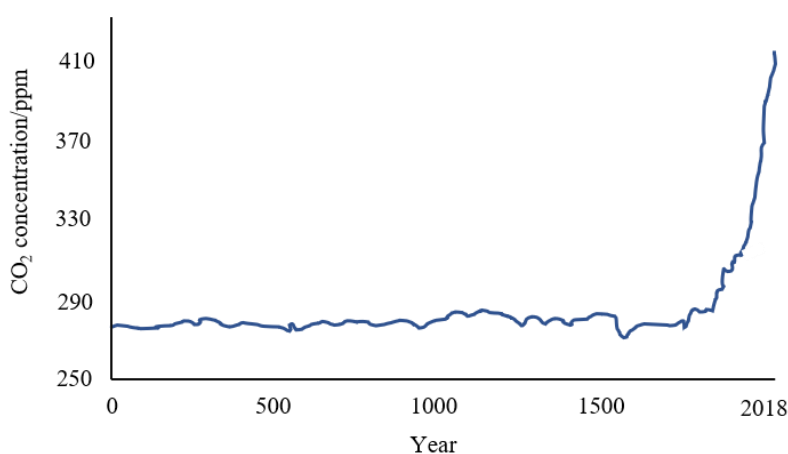


Figure 1-2. Atmospheric CO<sub>2</sub> concentration over the last 2000 years. Figure reproduced from Ref. 2.

One of the solutions is exploring environmentally friendly alternatives to fossil fuels, such as wind, wave, tidal, solar and nuclear to reduce CO<sub>2</sub> emissions<sup>3-4</sup>. But renewable energy technologies are still too immature to utilise the energy production to people's daily life. CO<sub>2</sub> sequestration is another solution, but it is likely to have an

energy cost. Conversion of CO<sub>2</sub> to useful fuels and chemical feedstocks, not only reduces CO<sub>2</sub> in the atmosphere, but also reduces dependency on fossil carbons, increasing energy security.

The concept of CO<sub>2</sub> conversion is to utilize produced CO<sub>2</sub>, i.e. from a chemical plant or cement manufacturer, as a vector to utilize clean electricity producing fuels and feedstocks. Cleaner and safer methods for conversion to hydrocarbon feedstocks via the coupled Water-Gas-Shift (WGS) and Fischer-Tropsch processes are therefore highly attractive.

The critical step is the reduction of carbon dioxide into a useful precursor (CO) using clean energy. The ability to reduce CO<sub>2</sub> efficiently could play a role in reducing greenhouse gas emissions and moving us towards, a more sustainable economy. CO produced by CO<sub>2</sub> reduction can be used in chemical production or reacted with H<sub>2</sub> to produce liquid fuel via the Fischer-Tropsch reaction. Indeed, synthetic hydrocarbons are proposed to be the promising alternative to the supposed energy carrier of hydrogen, given their convenience in energy storage and transportation<sup>5-7</sup>.

### **1.3 Solid oxide electrolysis cells and solid oxide fuel cells**

In the search for efficient processes to reduce CO<sub>2</sub>, Solid Oxide Electrolysis Cells (SOECs) appear to be promising candidates by realising CO<sub>2</sub> reduction and H<sub>2</sub> production at the same time. In order to understand the CO<sub>2</sub> electrolysis process under a solid oxide electrolyser, we need to have a brief introduction about SOEC first.

Solid Oxide Electrolysis Cells are essentially Solid oxide Fuel Cells (SOFCs) operated in reverse, meaning that current is applied to the cell instead of being drawn from the cell. The operating principle for SOFC and SOEC is shown in Figure 1-3.

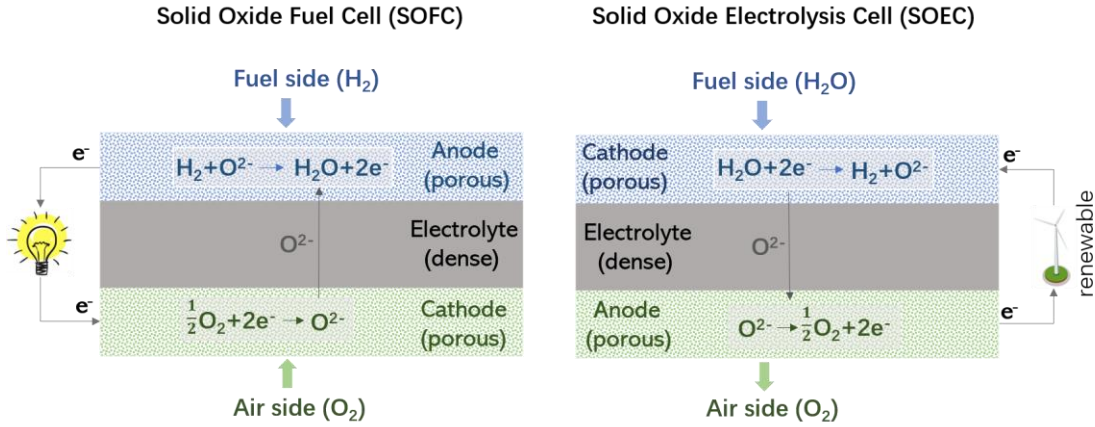
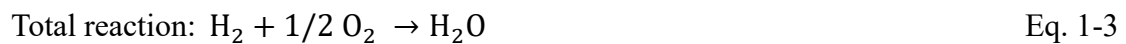


Figure 1-3. Operating principles of a solid oxide fuel cell (left) and solid oxide electrolysis cell (right).

A traditional SOFC consists of three parts: porous cathode (air electrode) and anode (fuel electrode), separated by a dense electrolyte (ceramic membrane, the most widely used is yttria-stabilized zirconia, YSZ). Oxygen is reduced to O<sup>2-</sup> by the electrons from the external circuit at the cathode (Eq. 1-1). Then the produced oxygen anion O<sup>2-</sup> diffuses through the dense electrolyte to the anode driven by oxygen partial pressure difference, reacting with the fuel (usually H<sub>2</sub>) at the anode and releasing the oxidation product (H<sub>2</sub>O) and electrons (Eq. 1-2). The electron transportation from the external circuit can then produce electricity. Thus, SOFCs play a role in converting chemical energy into electrical energy. Thermodynamically, this electrochemical process can keep going as long as the feed from both sides is continuously supplied.



Reversibly, SOEC is operated oppositely by generating fuels from electrical energy and heat, converting electrical energy into chemical energy. As shown in Figure 1-3, H<sub>2</sub>O is split into hydrogen and oxygen anion under the externally supplied voltage. Then, the produced O<sup>2-</sup> travels across the electrolyte to the anode to be oxidized into oxygen and consequently release electrons. The whole reaction is listed as Eq. 1-4.



Typically, the operating temperature for a solid oxide electrolysis cell is between 700-1000 °C. Although the high operating temperature can provide faster electrode kinetics<sup>8</sup>, the thermodynamic relation explained in Figure 1-4 indicates that the higher operating temperature would lead to more heat release. Therefore, the chemical-to-electrical energy-conversion efficiency will be lowered with higher operation temperature, which is not favourable for fuel cells. The relation in Figure 1-4 shows that the electric energy required for the reaction ( $\Delta G$ ) decreases with increasing temperature (provide more thermal energy,  $T\Delta S$ ) while the total energy demand ( $\Delta H$ ) only rises slightly. Thus, in the high temperature steam electrolysis (HTSE), the higher operating temperature will lower the electrical energy demand, which makes the electrical-to-chemical energy-conversion efficiency to be above 100% (in an ideal electrolysis cell). The heat can be supplied by the joule produced during the reaction in the cell<sup>9</sup>, making HTSE much more energy efficient.

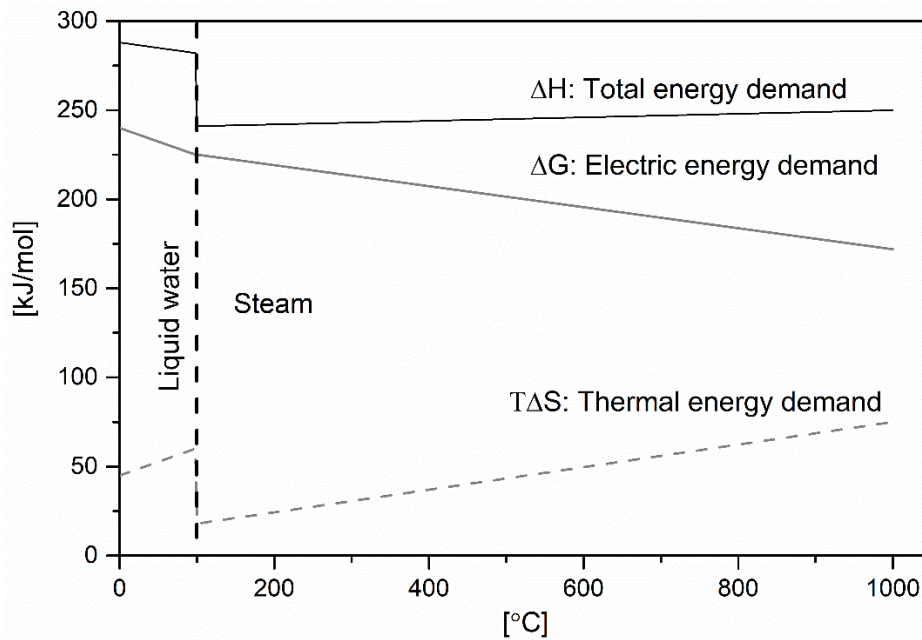


Figure 1-4. Electrical, heat and total energy requirements for water electrolysis as a function of temperature. Figure reproduced from Ref.10, Elsevier.<sup>10</sup>



Solid oxide electrolysis cells (SOECs) can electrolyze not only H<sub>2</sub>O but also the mixture of CO<sub>2</sub> and H<sub>2</sub>O to produce syngas (a mixture of CO and H<sub>2</sub>) by Reverse Water-Gas-Shift (RWGS) reaction. Syngas can be then converted into many types of hydrocarbon fuels<sup>11</sup>, such as methane and methanol, through the Fischer-Tropsch process. This CO<sub>2</sub> and H<sub>2</sub>O co-electrolysis provide a carbon-neutral process by decreasing and utilizing CO<sub>2</sub> into fuel at the same time. In this way, energy can be stored in the form of synthetic hydrocarbon fuels.

## **1.4 Oxygen ion conductor and proton conductor**

### **1.4.1 Electrolyte**

As an important component of SOEC, the property of electrolyte influences not only the cell output performance and operating temperature, but also the choice of the electrode materials to be compatible with it. In order to perform efficiently in the cell, the electrolyte needs to meet the following requirements: (a) it should be dense enough to prevent the direct reaction between fuel and oxygen gas from the two electrodes. (b) possess negligible electronic conductivity in order to force the produced electrons to travel through the external circuit. Meanwhile, electrolyte needs to possess ionic conductivity that allows ions (oxygen anion or protons) to transfer between electrodes. (c) should have sufficient chemical stability not to react with electrode materials during processing and operation and to withstand the considerable oxygen partial pressure gradient between electrodes, and in other words, electrolyte needs to be stable both in highly reducing and oxidizing conditions. (d) compatible thermal expansion coefficient with other cell components connected with it, for mechanical integrity of the cell. (e) Last but not least, electrolyte should have good mechanical strength and must be cost-effective<sup>12-13</sup>.

### **1.4.2 Oxygen ion conductors**

Up to now, the most widely studied and used electrolyte is yttrium stabilized zirconia (YSZ). Known as an excellent oxygen-ion conductor, YSZ has sufficient

conductivity to operate in an SOFC at a temperature higher than 800 °C due to the high activation enthalpy for oxygen ion conduction. Although current SOFC technology based on oxygen ion conductors is well established, the high operating temperature still causes challenges including materials incompatibility, expensive sealing technology, cell interconnect issues, and material mechanical problems, etc<sup>14</sup>. Moreover, the electrical efficiency is still significantly lower than theoretical value<sup>15</sup>. Another limitation that needs to be mentioned is that the water would be produced or supplied at the same electrode side with fuel in an oxygen conducting cell, which will dilute the fuel, reducing the Nernst potential.

In comparison, an intermediate-temperature (600-800 °C) SOFCs design could remove most of the disadvantages existing in high-temperature one while keeping most of the advantages. Although the utilization of a thin film of electrolyte could reduce the cell operation temperature, it still needs to work at a temperature as low as 800 °C in YSZ based SOFC. Therefore, exploiting electrolyte with high ion conductivity at moderate temperature is the key to solve this problem.

### **1.4.3 Proton conductors**

Protons were firstly shown to exist in some oxides in 1960s<sup>16</sup>. After that, systematic investigations were carried out by Iwahara<sup>17</sup> group on the doped oxides such as LaYO<sub>3</sub>, LaAlO<sub>3</sub> and SrZrO<sub>3</sub>, which was well known as oxygen ion conductor before, presented proton conductivity in steam containing atmosphere at elevated temperature. However, their conductivities were very low. Later, Iwahara et al. discovered other perovskite materials with higher proton conductivity, SrCeO<sub>3</sub><sup>18-21</sup> and BaCeO<sub>3</sub><sup>22-23</sup> based compounds, performing complete fuel cell and steam electrolysis tests in a laboratory scale. Other researchers<sup>24-26</sup> illustrated that Gd-doped BaCeO<sub>3</sub> ceramics were fully dominated by protonic conduction at 600°C while showed an oxide ion conduction at 1000 °C. In the temperature range of 600-1000 °C, mixed conduction was observed. Although the power density is not very high, only 0.2 W cm<sup>-2</sup> at 800 °C, if the cells could be optimized, e.g., decreasing the electrolyte thickness and using an

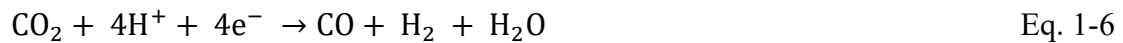
electrode with better performance, it would be very promising for the proton conducting electrolyte to work at lower temperature with higher performance.

When CO<sub>2</sub> and H<sub>2</sub>O co-electrolysis happens on a proton conducting SOEC, as illustrated in Figure 1-5, steam is electrochemically split to H<sup>+</sup> and releases O<sub>2</sub> by external electrical potential (Eq. 1-5). The protons transport across the proton conducting electrolyte to the cathode and *in situ* reduce CO<sub>2</sub> at the three-phase boundary (Eq. 1-6). It is also possible that H<sub>2</sub> is produced at this side according to Eq 1-7. In this case, the proton can be utilized directly to produce syngas if selective catalysts are adopted at the cathode. Various hydrocarbons can then be obtained by Fischer-Tropsch synthesis using the precursor synthetic gas.

Anode:



Cathode:



The overall reaction of the steam and CO<sub>2</sub> co-electrolysis is obtained by adding Eqs. (1-5) – (1-6), leading to:

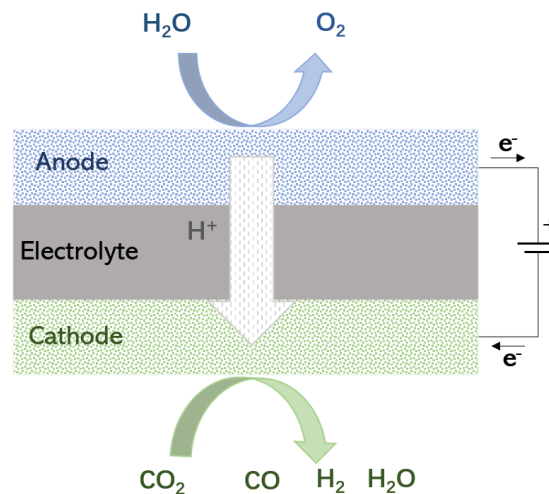
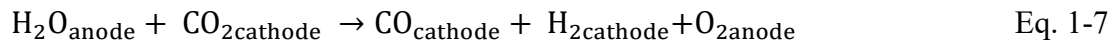


Figure 1-5. Electrolysis cell configuration on a proton conducting solid oxide electrolyte.

### 1.4.4 Review on BaCeO<sub>3</sub>

After more than twenty years of research, the perovskite-type (ABX<sub>3</sub>) cerates and zirconates system have been well established in the proton conductor area, and BaCeO<sub>3</sub>-based materials in particular exhibit remarkable high proton conductivity in oxides<sup>27-29</sup>. Other typed of oxides were also been investigated, such as fluorite-related structured binary rare earth oxides and pyrochlore structured ternary oxides<sup>30-31</sup>. These range of materials' conductivities were either obtained from experiments or calculated from available data, and their proton conductivities as a function of temperature was compared by K.D. Kreuer<sup>32</sup>, as shown in Figure 1-6. It demonstrates that the higher proton conductivity is observed among perovskite-type structure with BaCeO<sub>3</sub>-based compounds. However, stability turns out to be a severe problem for barium cerates, especially in CO<sub>2</sub> containing atmosphere even with a low concentration and water vapour participating environment. The oxides can decompose in these situation and form barium carbonates (Eq. 1-8) or barium hydroxides (Eq. 1-9)<sup>33</sup>.

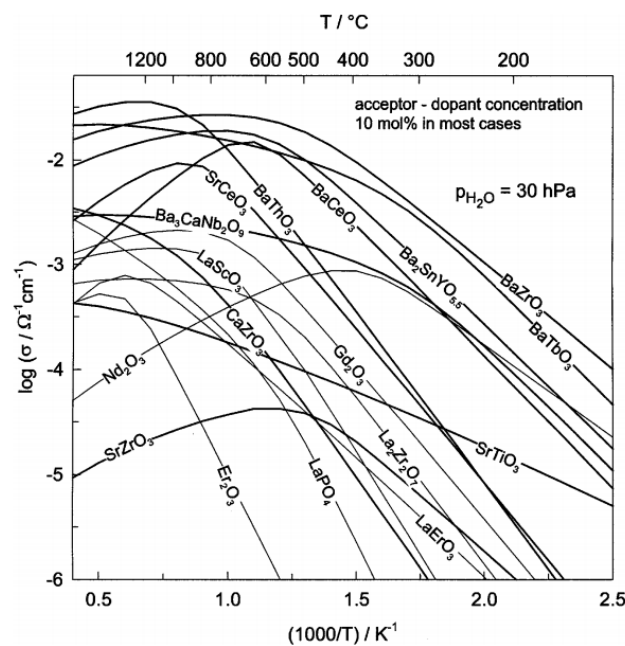


Figure 1-6. Proton conductivities of various oxides.<sup>32</sup>

Various doping ( $\text{Ti}^{4+}$ ,  $\text{Gd}^{3+}$ ,  $\text{In}^{3+}$ ,  $\text{Zr}^{4+}$ ,  $\text{Ta}^{5+}$ , etc) approaches were adopted to enhance  $\text{BaCeO}_3$  stability<sup>34-36</sup>, and out of these systems cerates and zirconates were found to be mutually soluble, and many investigations were done based on the cerate-zirconate solid solution to develop the adequate electrolyte with good stability and relatively high proton conductivity. However, it seems that high proton conductivity and material stability are antagonistic<sup>37</sup>.  $\text{BaZrO}_3$  was proved to be stable in  $\text{CO}_2$  and  $\text{H}_2\text{O}$  containing atmosphere because the higher electronegativity of Zr reduced the basicity of material, which decreased the interaction of oxide with acid gases. However, the lower basicity is not favourable to the formation of protonic defects, which was demonstrated by researchers that while stability increased when enhancing doping amount of Zr, protonic conductivity of barium cerate would decrease, proving that the increased stability is at the cost of reducing proton conductivity<sup>29</sup>. Furthermore, Zr doping strategy can also lead to a poor sinterability of materials, which will require a very high sintering temperature (up to 1800 °C) to obtain dense ceramics. It will not only cause more heat consumption but also result in metal evaporation problem. The high sintering temperature also makes it less flexible to choose an electrode material with enough porosity after co-firing in some specific cell preparation method. Therefore, other doping methods need to be considered.

One of the most effective way to lower the sintering temperature is by decreasing particle size of the oxide powder in either chemical means (alkoxide route<sup>38</sup>, sol-gel method<sup>39</sup>, combustion method<sup>40</sup>) or mechanical process<sup>41</sup> (grinding powder in a planetary mill). Another possible way is through the addition of sintering additives (for example some 3d-elements oxides,  $\text{Ni}^{2+}$ ,  $\text{Cu}^{2+}$ ,  $\text{Zn}^{2+}$ ) in the process of conventional solid-state synthesis. It was found that only a small amount of sintering aids was able to decrease the sintering temperature and improve stability without impairing material conductivity. In the literature, this technology is referred to as a solid-state reactive sintering method<sup>42</sup>. The basic mechanism of action for the sintering aids in lowering the sintering temperature is the low melting point of Ba-M-O or Y-Ba-M-O phase that helps the growth of grain boundary. It was reported that the addition of  $\text{CuO}$  allowed

the BaCeO<sub>3</sub> sintering temperature to be as low as 1000°C to get dense<sup>43</sup>. Gorbova and co-authors<sup>44</sup> investigated the effect of CuO on the densification behaviour and conductivity of Gd-doped BaCeO<sub>3</sub> (BCG) ceramics, revealing that only 1 mol% of CuO could reduce both the calcination and sintering temperature by 250 and 150 °C respectively. When sintered at 1450 °C for 3h, BaCe<sub>0.9</sub>Gd<sub>0.1</sub>O<sub>3-δ</sub> only has ~86% density while samples with Cu doping achieved almost ~95% of relative density. Conductivity tests showed that BCG doped with Cu had higher conductivity than undoped samples, which was only 68 mS cm<sup>-1</sup> for BaCe<sub>0.8</sub>Gd<sub>0.2</sub>O<sub>3-δ</sub> but 92 mS cm<sup>-1</sup> was achieved for BaCe<sub>0.84</sub>Gd<sub>0.15</sub>Cu<sub>0.01</sub> at 900°C in wet air. Copper oxide favoured the sintering ability of Ba-containing ceramics in that the low-temperature melting point of Cu<sub>2</sub>O (~1030°C), BaCuO<sub>2</sub> (1000°C) and Ba<sub>2</sub>CuO<sub>3</sub> (800°C)<sup>45</sup> provided a liquid phase during firing for enhancing densification and grain growth, reported by Yang et al<sup>46</sup>. In addition, a eutectic can be formed between BaCuO<sub>2</sub> and CuO at a temperature above 900 °C. Similar sintering behaviour was also found in cobalt or nickel oxide doped ceramic material, published by Ricote et al.<sup>47</sup> The sintering temperature of BaZr<sub>0.9-x</sub>Ce<sub>x</sub>Y<sub>0.1</sub>O<sub>3-δ</sub> decreased by about 250 °C with the addition of 1 or 2 mol% of cobalt or Ni, achieving a high relative density of 94%. However, the ionic conductivity was decreased with Co or Ni doping in BaZr<sub>0.9</sub>Y<sub>0.1</sub>O<sub>3-δ</sub> while it did not change much for BaZr<sub>0.7</sub>Ce<sub>0.2</sub>Y<sub>0.1</sub>O<sub>3-δ</sub> with or without sintering aids. A similar phenomenon was also observed by Babilo and Haile<sup>48</sup>, who found that the introduction of 4mol% nickel, copper and zinc oxides could considerably enhance the sinterability of BaZr<sub>0.85</sub>Y<sub>0.15</sub>O<sub>3-δ</sub>, especially with Zn doping that over 93% of theoretical density was obtained for BaZr<sub>0.85</sub>Y<sub>0.15</sub>O<sub>3-δ</sub> at 1300 °C. The conductivity in H<sub>2</sub>O saturated N<sub>2</sub> was only slightly lower than that of unmodified sample, analysed with A.C. impedance spectroscopy results. It demonstrated that zinc oxide was a very promising candidate for reducing sintering temperature without impacting much on the material conductivity.

By optimizing the doping ratio of B-site cations, Tao et al.<sup>49</sup> synthesised a new protonic conductor, BaCe<sub>0.5</sub>Zr<sub>0.3</sub>Y<sub>0.16</sub>Zn<sub>0.04</sub>O<sub>3-δ</sub>, and its total conductivity reached 3.14 mS cm<sup>-1</sup> at 400 °C in wet 5% H<sub>2</sub> and over 10 mS cm<sup>-1</sup> above 600 °C. Moreover, thermal

gravimetric analysis (TGA) test under pure CO<sub>2</sub> proved satisfactory chemical stability of this new oxide compared to the other doped BaCeO<sub>3</sub> materials. Other doping elements were also exploited for BaCeO<sub>3</sub> to improve the sinterability, chemical stability and remain the same electrical performance. Bi et al.<sup>50</sup> offer a new approach to solve the antagonistic between the stability and conductivity by doping BaCeO<sub>3</sub> with the trivalent element indium (10%-30%) that possesses high electronegativity. The resulted In-doped BaCeO<sub>3</sub> reached dense at relatively low temperature and stayed stable in CO<sub>2</sub> containing atmosphere, showing the great possibility to be used in proton conducting SOFC or SOEC application.

## **1.5 Proton conduction background**

### **1.5.1 Perovskite background**

“Perovskite” was first discovered by Gustav Rose in 1839 for samples existing in the Ural Mountains. It was named after a Russian mineralogist, Count Lev Aleksevich Von Perovski. Although perovskite was originally used to describe the compound of calcium titanium oxide (CaTiO<sub>3</sub>), currently it is generally employed to name a group of oxides with a formula of ABO<sub>3</sub> and similar structures. Typically, the A-site cation is usually larger than the B-site and has a similar size with oxygen anion. Figure 1-7 (a) depicts an ideal cubic perovskite structure, with B-site cations occupying the corners of the cube, in six-fold coordinated, while A-site cations are located in the cube centre, in twelve-fold coordinated, and oxide ions are placed half way of the edges. Figure 1-7 (b) illustrates another way to view the structure with A-site ions sitting on the cube corners, and B site ions in the middle of the cube and the hole of the oxide ions octahedron. Oxide ions are now occupying the face centre of the cube. Figure 1-7 (c) shows that the BO<sub>6</sub> octahedra are not isolated in the system but share oxide ion in the three dimensions, resulting in the corner-sharing octahedra network.

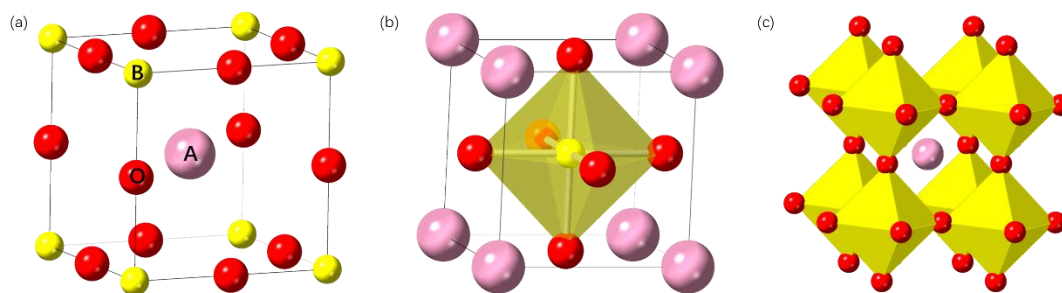


Figure 1-7 (a, b) Visualising the ideal cubic perovskite structure in two different way, (c) corner-sharing network of  $\text{BO}_6$  octahedra.

One of the distinct properties of perovskite is that it can accommodate distortions from the ideal cubic structure, providing flexibility for incorporating cations of different sizes. For example, the stoichiometric valence combination can be  $\text{A}^{1+}\text{B}^{5+}\text{O}_3$ ,  $\text{A}^{2+}\text{B}^{4+}\text{O}_3$ ,  $\text{A}^{3+}\text{B}^{3+}\text{O}_3$ , where the A-site can be occupied by either  $\text{M}^+$  ( $\text{Na}^+$ ,  $\text{K}^+$ ),  $\text{M}^{2+}$  ( $\text{Ca}^{2+}$ ,  $\text{Ba}^{2+}$ ,  $\text{Sr}^{2+}$ ), or  $\text{M}^{3+}$  ( $\text{La}^{3+}$ ,  $\text{Fe}^{3+}$ ) and the B-site can be  $\text{M}^{5+}$  ( $\text{Nb}^{5+}$ ,  $\text{W}^{5+}$ ),  $\text{M}^{4+}$  ( $\text{Ce}^{4+}$ ,  $\text{Ti}^{4+}$ ) or  $\text{M}^{3+}$  ( $\text{Mn}^{3+}$ ,  $\text{Fe}^{3+}$ ). In addition, vacancy and atomic-scale intergrowths with other structural motifs can be accepted within the perovskite structure, determining the possibility of a variety of valence at the A and B-sites cations. This doping strategy of varied valence would provide an effective way to tailor material property and create various defects in the structure under either oxidizing or reducing environment. For example, when the overall valence of A-site and B-site cations is less than 6, the missing charge will be compensated by introducing oxygen vacancies. A-site can also accommodate vacancies in some cases to design the material with a specific property. The allowed existence of defects in the perovskite structure provides its flexibility in redox cycling, making materials to be redox stable and work well in the SOFC or SOEC application.

In an ideal cubic perovskite structure, the relationship between radiuses of A site and B site cations can be calculated from the unit cell parameter (Eq. 1-10).

$$a = r_B + r_O = \frac{r_A + r_O}{\sqrt{2}} \quad \text{Eq. 1-10}$$

Where  $a$  is the cubic unit cell parameter, and  $r_A$ ,  $r_B$  and  $r_O$  is the ionic radii of A, B



and oxide ion, respectively. However, only a few oxides form an ideal cubic structure, like SrTiO<sub>3</sub>, most perovskites have a mismatch between A and B site. Tilting or distortion will happen in this case, resulting in tetragonal or orthorhombic structure or that with lower symmetry. In order to evaluate the degree of distortion from the ideal cubic structure and predict the stability in the structure system, the Goldschmidt tolerance factor ( $\tau$ ) was given, defined as the size mismatch between A-O and B-O bond lengths which are calculated from the sum of empirical ionic radii ( $r_A$ ,  $r_B$ ,  $r_O$ ) (Eq. 1-11).

$$\tau = \frac{r_{AO}}{\sqrt{2}r_{BO}} = \frac{r_A + r_O}{\sqrt{2}(r_B + r_O)} \quad \text{Eq. 1-11}$$

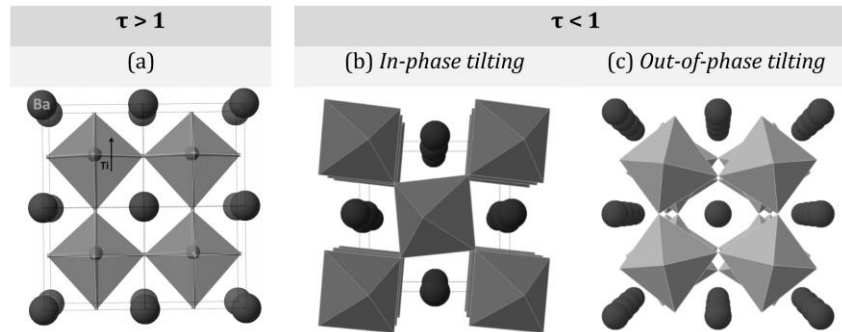


Figure 1-8. Distortion of the perovskite structure. (a) For  $\tau > 1$ , the BO<sub>6</sub> octahedra are slightly stretched, For  $\tau < 1$ , octahedra undergo a cooperative tilting, when the adjacent layer tilt in the same direction, giving rise to in-phase tilting (b), when in the opposite direction, resulting in out-of-phase tilting (c).

For the ideal cubic structure (e.g., SrTiO<sub>3</sub> and BaZrO<sub>3</sub>),  $\tau$  is almost unity. For  $\tau > 1$ , the A-site cation is too large for the cuboctahedra cavity formed between BO<sub>6</sub> octahedra, therefore, BO<sub>6</sub> octahedra need to stretch a bit to accommodate the large A-site cation, and the resulted structure is presented in Figure 1-8 (a). In this case, B-site cation is not at the octahedral symmetry centre any more. In the situation when  $\tau < 1$ , it may come from the smaller cation substitution on the A-site or larger cation on B-site. Therefore, A-site cations are too small in the cuboctahedral cavity to contact with all the twelve oxide ions. The structure mismatch is then adjusted by cooperative rotations of the octahedra but remaining the whole corner-sharing connectivity, the A-site cation

can contact all the 12 oxide ions in this way. This process is called octahedral tilting and can be divided into in-phase tilting ( tilt in the same direction, Figure 1-8 b) and out-of-phase titling<sup>51</sup> (tilt in the opposite direction, Figure 1-8 c).

Octahedra tilting may give rise to some consequences on material property. It is known that the electronic conductivity for some materials come from the electron hopping between the B-site cation in the structure. When tilting happens, the angle between B-O-B bond drops from  $180^\circ$  to  $(180^\circ - \Phi)$ , and the more tilting, the larger  $\Phi$ . This will influence directly the interaction between B-site and oxide ion (orbital overlap, inter-atomic distance etc) and result in the change on the properties like band gap, the width of conduction band<sup>52-53</sup>. Moreover, titling sometime cannot always make the smaller A-site cation bonding with 12 oxide ions, which makes the A-site cation coordinate with only 8-10 ions. The asymmetric environment may, in turn, have an effect on oxide ions diffusion pathway<sup>54</sup>. Generally, cations size mismatch generating tolerance factor in the range of  $0.78 < \tau < 1$  can be accommodated by titling in the perovskite structure.

It is found that the extent of distortion can decrease with increasing temperature<sup>55-57</sup>, and in some structures, it can even transfer into cubic symmetry at high temperature. This is probably because the A-O bond expands more than the B-O bond during heating, thus the tolerance factor will be approaching 1.

### 1.5.2 Proton defect formation

For perovskite structure, the protonic defects are introduced with the dissociative absorption of water, which requires the existence of oxide ion vacancies,  $V_O^{\bullet\bullet}$ . The vacancies can be formed either by intrinsically varying the ratio of the constituents in the compounds (e.g.,  $A_{1\pm x}BO_{3-\delta}$ ) or by extrinsically doping a lower-valent cation (e.g.  $AB_{1-y}M_yO_{3-\delta}$ ) on the B-site to compensate for the electroneutrality. In the case of doping strategy, the lower-valent cation can substitute up to 25% of the B-site cation. The modification of stoichiometric perovskite oxides provides materials with the optimized property. In high-temperature perovskite-type proton conductors,  $ABO_3$  (A = Ca, Sr, Ba;

B = Ce, Zr) are most frequently modified to enhance its proton conductivity. For example, for the most conventional developed  $A^{2+}B^{4+}O_3$  configuration of  $BaCeO_3$ , the replacement of  $Ce^{4+}$  by a trivalent cation  $M^{3+}$  enables the appearance of extra oxygen vacancies  $V_O^{\bullet\bullet}$  in the crystal structure, and this process occurs according to the following Eq. 1-12 given in Kröger-Vink notation:



When exposing to water vapour or  $H_2$  containing atmosphere at elevated temperature, proton defects appear in the form of hydroxyl ions by incorporating water molecules, represented by Eq. 1-13:



where the water molecule dissociates into a hydroxide ion and a proton. While the hydroxide ion occupied an oxygen vacancy, the proton is covalently bonded with lattice oxygen, producing two positively charged proton carriers ( $OH_O^{\bullet}$ ) that are free to hop between oxide sites. Because the formation of proton defects is accompanied by a significant weight gain in Eq. 1-14, the protonic conduction property and proton concentration can be evaluated by thermal gravimetric analysis (TGA).

### 1.5.3 Proton transportation mechanism

The most widely accepted explanation for proton transfer is the Grotthuss mechanism<sup>58-59</sup>. In the Grotthuss mechanism, proton conduction occurs in an infinite network of hydrogen bonds. Two steps (Figure 1-9) are responsible for the proton transfer in this process, rotational diffusion of the protonic defect and proton migrate by hopping from one oxide ion toward another nearest-neighbouring one in the lattice with oxygen remaining on their crystallographic positions, as symbolized by:  $OH^{\bullet\bullet}O \rightarrow O^{\bullet\bullet}HO$ . Quantum molecular dynamics (MD) simulations<sup>60-62</sup> illustrated that rotational diffusion process was fast with low-activation barriers, indicating the rate-limiting step is the proton transfer reaction associated with bond breaking. However, Kreuer<sup>60</sup> suggested that proton transfer was mainly through the Grotthuss-type mechanism (hopping and rotating) at moderate-temperature range, while at high

temperature, the vehicle mechanism was also involved. That is, the proton movement takes place with the help of a carrier (vehicle), e.g.,  $\text{H}_3\text{O}^+$ .

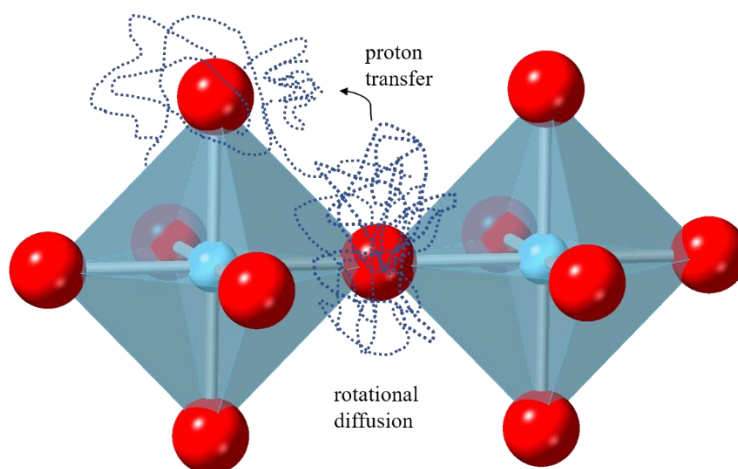


Figure 1-9 The trace of a proton in a perovskite showing that two principle features of proton transport: rotational diffusion and proton transfer<sup>63</sup> (data have been obtained by a quantum-MD simulation of a proton in cubic  $\text{BaCeO}_3$ ). Figure reproduced from Ref. 63, Annual Reviews.

#### 1.5.4 Electronegativity effect on hydration enthalpy

In the formation of proton defects, the process of water molecule dissociating into a hydroxide ion and a proton can be regarded as an amphoteric reaction, where the oxide acts as an acid to absorb the hydroxide ion by oxide ion vacancy and a base accomplishing the protonation of lattice oxide ion. Atomistic simulation results reveal a negative hydration enthalpy for  $\text{CaZrO}_3$ ,  $\text{SrZrO}_3$  and  $\text{BaCeO}_3$ , indicating the dominated proton conductivity at low-temperature range in these materials. However, there is some controversy about how the structure and chemical parameter will influence the enthalpy of the hydration reaction<sup>64-65</sup>. But an increasing number of investigations show that the reaction enthalpy becomes more exothermic with decreasing electronegativity of the cations (decreasing Bronsted basicity of the oxide), especially the B-site cation with larger electronegativity variation range in the

perovskite. For example, with a decrease order of electronegativity in titanate, niobite, stannate, zirconate and cerate, the equilibrium constant of the hydration reaction is in an increasing order<sup>66</sup>. This electronegativity effect seems to be in conflict with the amphoteric reaction process we mentioned above. Consider now that the hydration reaction is divided into two steps, the first is the occupancy of oxide ion into the oxygen vacancy and the second the protonation of the lattice oxide ion including both the new formed one and the already existed one in the structure<sup>64</sup>. Typically, it is the second step that determines the difference in the thermodynamics property of hydration reaction while the first step seems to prevail in perovskite oxides<sup>65</sup>. But the reason is not clear now.

When correlating with the electronegativity difference  $\Delta X_{B-A}$  between the B-site cations and the A-site cations of the perovskite, a better correlation is observed between the electronegativity and hydration enthalpy.<sup>67</sup> Specifically, perovskites with smaller B-A electronegativity differences have the more negative values of hydration enthalpies. However, the relationship is not perfectly linear with much scatter, either resulting from limited equilibrium measurements or actual points, further research is essential to find out other underlying and finer correlations.

### **1.5.5 Protonic defects stability**

Apart from the variation of the hydration enthalpy, hydration entropy can also be evaluated together with the dehydration temperature of oxides. The dehydration temperature can reflect the stability of the protonic defects. Different from the chemical stability of perovskite oxide against the acid atmosphere, where it increases with higher electronegativity, the stability of protonic defects varies in opposite order. For example, with an increasing order in chemical stability in cerate, zirconate and titanate, their protonic defects stability is in a decreasing trend. It is also found that crystallographic symmetry does not have the same much influence on the perovskite thermodynamic stability as on its protonic defect stability<sup>32</sup>. For example, BaCeO<sub>3</sub> and SrCeO<sub>3</sub> have almost identical stability towards CO<sub>2</sub> but SrCeO<sub>3</sub> shows worse stability with protonic

defects because of its stronger orthorhombic distortion. Acceptor dopants are then supposed to affect the protonic defect stability of the host perovskite due to the reduction of local symmetry, as evidenced in Figure 1-10 by the decreased stability of Y-doped BaCeO<sub>3</sub> and Sc-doped SrTiO<sub>3</sub> compared with the undoped samples. But this does not work well with Y-doped BaZrO<sub>3</sub>, which is considered as a perfect acceptor dopant for BaZrO<sub>3</sub>.

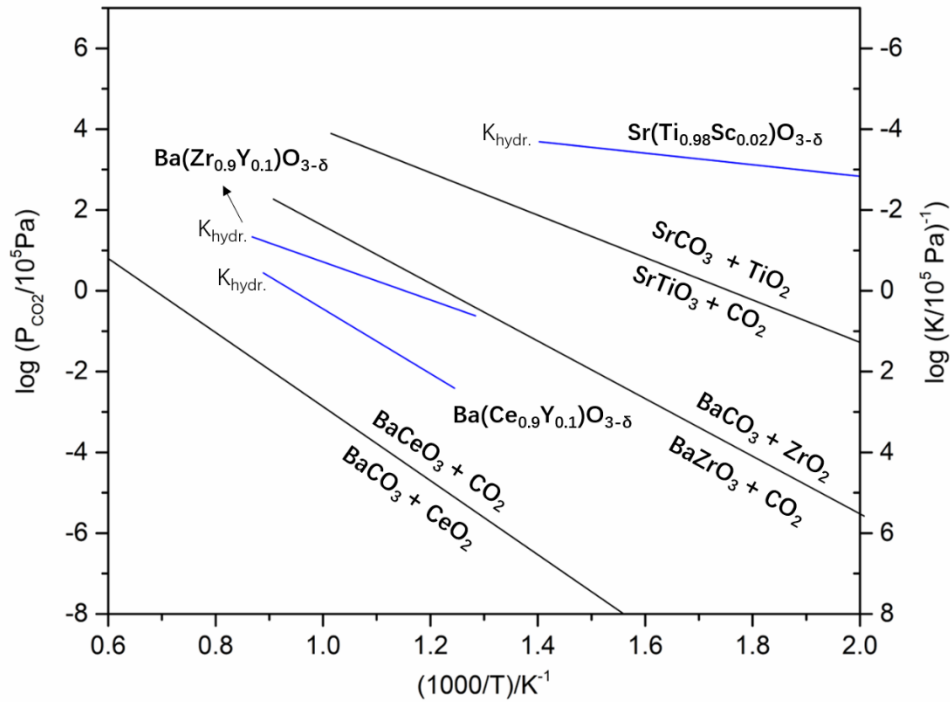


Figure 1-10 Equilibrium constant of hydration reaction for Y-doped BaCeO<sub>3</sub>, BaZrO<sub>3</sub>, and Sc-doped SrTiO<sub>3</sub> compared with the reaction equilibrium of the host BaCeO<sub>3</sub>, BaZrO<sub>3</sub> and SrTiO<sub>3</sub> compounds with CO<sub>2</sub><sup>66</sup>. Figure reproduced from Ref. 66, Elsevier

### 1.5.6 Proton mobility and its activation enthalpy

Quantum-MD simulations found that in the transfer process, proton moves from outside the BO<sub>6</sub> octahedron but not along the edge of two octahedron oxygen, forming a strongly bent hydrogen bond<sup>68</sup>. It is supposed that the repulsive interaction between the proton and the highly positive charged B-site cation (H/B-repulsion) renders the formation of a linear hydrogen bond. Figure 1-11 (a) illustrates the proton diffusion

path in BaCeO<sub>3</sub> simulated by Kreuer<sup>60</sup>. In the beginning, hydroxyl ion was formed at oxygen atom A with a proton at position 1. By rotational motion around oxygen A, the proton can move from position 1 to position 2. The rotational motion of the proton around the oxygen atom was found to be in the plane perpendicular to Ce-O-Ce axis, shown as a ring-like object in Figure 1-11 (b). Because of the Ce-O bending, the proton then moves to position 3 and forms a hydrogen bond with oxygen atom B. Transfer from position 3 to position 4, there exists an energy barrier. If the bond length between A and B can be shortened to reduce the energy barrier, proton then may transfer to position 4. At this position, the Ce-O bending motion would eventually break the hydrogen bond with oxygen A and the proton move to position 5, which is equivalent to position 1, accomplishing a proton transfer from one oxygen site to the neighbouring one.

The contribution of bond energy change (H/B repulsion elongates B-O bond) to the activation enthalpy can be estimated by H/B-repulsion. This is further supported by the fact that cubic perovskite structure with pentavalent B-site cation has a significantly higher activation enthalpy of proton mobility than that with tetravalent B-site cation<sup>69</sup>.

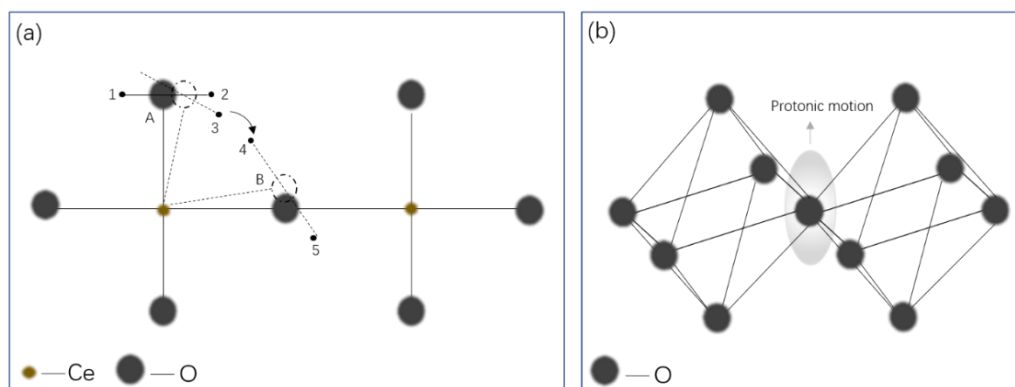


Figure 1-11. (a) Suggested proton diffusion path between two oxygen atoms. Proton diffuses from position 1, passing through position 2, 3, and 4 until arriving at position 5. (b) The ring-like object around an oxide ion generated by protonic motion (T=900 K)<sup>60</sup>. Figure reproduced from Ref.60, Elsevier

In addition, deviation from an ideal cubic structure can also lead to an increase in

the activation energy for proton mobility. Münch et al.<sup>70</sup> compared Y-doped BaCeO<sub>3</sub> and SrCeO<sub>3</sub> and found that Y-SrCeO<sub>3</sub> showed higher activation enthalpy for proton diffusion and lower conductivity owing to its large orthorhombic distortion structure. It comes to think about the effect of acceptor dopant on the activation enthalpy. Aliovalent dopants with matching ionic radii are supposed to have a little negative impact on the activation energy of host perovskite owing to its less influence on the structure symmetry change. This is adapted for oxide ion conductivity, however, not suitable for proton conductivity. For example, large cation of Y<sup>3+</sup> doped BaZrO<sub>3</sub> showed high proton mobility than size-matched cation Sc<sup>3+</sup> and In<sup>3+</sup> doped oxides. Although the large Y<sup>3+</sup> doping lead to local lattice expansion and even tetragonal distortion at higher doping level, the acid/base property of the coordinating oxygen kept almost unchanged<sup>71</sup>, leading to the chemical match contribute more on the proton mobility than size match. Proton mobility and activation enthalpy are independent of Y<sup>3+</sup> concentration (up to 20%). But in the case of BaCeO<sub>3</sub>, Y<sup>3+</sup> doping increases its activation enthalpy and decreases the proton mobility.

It is then not surprising to find in Figure 1-6 that BaZrO<sub>3</sub> is among the best proton conductor with the highest proton conductivity. BaZrO<sub>3</sub> has a perfect cubic structure with the highest lattice constant, which enables high solubility limit of proton defects and provides high proton mobility. The activation enthalpy for proton defects diffusion is also decreased by the strong Zr/O covalency bond which reduces the repulsion interaction between Zr and proton.

In addition to the factor of the chemical match with the oxygen ions suggested by Krewer et al.,<sup>72</sup> defect association was proposed to result in a higher conduction activation energy with increasing dopant concentration. Karmonic et al.<sup>73</sup> carried out neutron vibrational spectroscopic measurements and found that a considerable amount of protons were associated with the dopant in the doped SrCeO<sub>3</sub>. Meanwhile, Hempelmann et al.<sup>74</sup> proved the existence of trapping centres that is adjacent to the dopant ion. By analysing the pre-exponential factor of the conductivity of Yb-doped SrCeO<sub>3</sub>, Scherban and Nowick<sup>75</sup> proposed that not all the dissolved protons are mobile



carriers. Moreover, the OH-dopant binding energies were calculated by Davies et al.,<sup>76</sup> which illustrated the negative values for  $\text{Sc}^{3+}$  and  $\text{Y}^{3+}$  -doped  $\text{SrZrO}_3$ , suggesting that all OH-dopant pairs were bound. Among the three dopants,  $\text{Sc}^{3+}$  showed the highest binding energy and  $\text{Y}^{3+}$  had the smallest. The defect association may give rise to larger activation energy which would limit the proton mobility.

## 1.6 Electrodes and exsolution

### 1.6.1 Electrodes

Apart from the electrolyte, electrodes process (anode and cathode) plays a crucial role in cell performance. For a given electrode material, it should fulfil several requirements, including high electrocatalytic activity towards desirable reactions on that electrode side, ion transport property, electronic conductivity, porosity allowing gas diffusion, stability under working conditions (reduction or oxidation condition), thermal compatibility with other cell components (electrolyte or interconnect), tolerance with poisonous gases. For its electrocatalytic property, various approaches were applied to prepare the nano-catalysts on the electrodes, such as mechanical mixing of electrode material with catalysts, impregnation of catalysts solution on the electrode scaffold, etc. Sometimes the ionic (IC) and electronic conduction (EC) can be provided by a single material, regarded as mixed ionic and electronic conductor (MIEC). For composites electrode with IC and EC two phases, the active sites are those interfaces where IC, EC and gas-phase meets together (referred to as triple phase boundary, 3PB), as shown in Figure 1-12 (a). In the case of electrodes made from the MIEC, the electrochemical reaction takes place at the whole electrode surface exposed to the gas phase, which is the entire solid/gas two-phase boundaries, referred to as 2PB (Figure 1-12 b). Considerable work focuses on maximizing the reactive boundary by optimising the microstructure of the electrode or by applying different preparation methods.

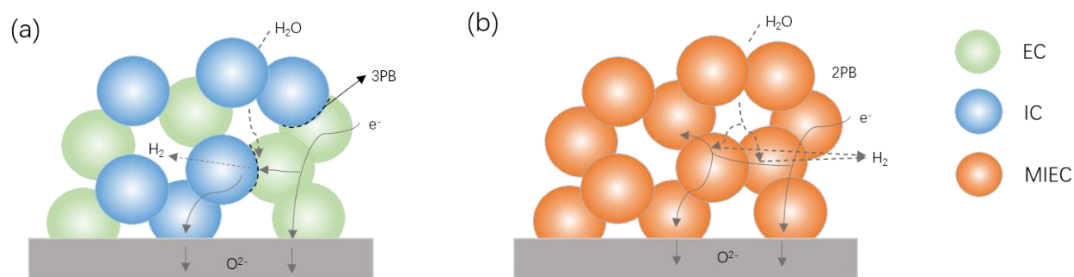


Figure 1-12. (a) 3PB fuel-electrode in IC-EC composite structure (SOEC mode), (B) 2PB fuel electrode in single-phase MIEC structure (SOEC) mode.

### 1.6.2 Exsolution mechanism

In-situ exsolution from perovskite oxides has been found to be a very promising method to obtain metal nanoparticles with catalytic activity while the parent perovskite is used directly as the electrode materials. This process is quite easy to achieve by simply doping the catalytic cation on the B-site of the perovskite lattice under high-temperature sintering in oxidized condition, followed by exposing the oxide material to reducing atmosphere (for example, 5% H<sub>2</sub>/Ar) at about 500-1000 °C or by electrochemical switching for only minutes, applying a certain voltage to the electrode. Then the B-site dopant cation can partially exsolve to the material surface in the form of nanoparticles, as illustrated in Figure 1-13.

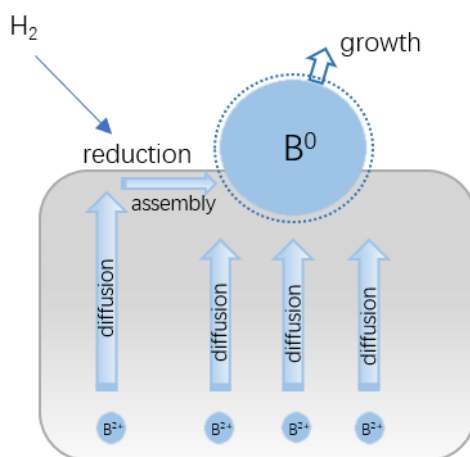
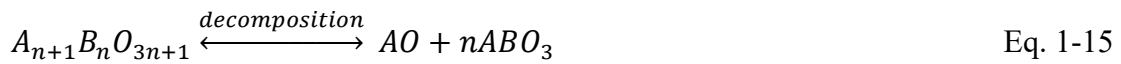
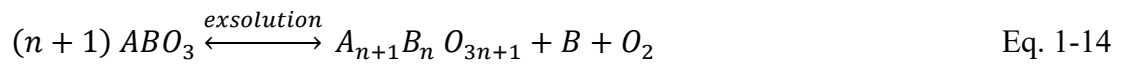
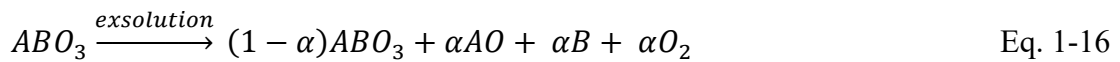


Figure 1-13. Illustration of metal exsolution from perovskite.

Before the systematic investigations of exsolution from perovskite carried out by Neagu et al.<sup>77</sup> in recent years, the observation of nanocatalysts grown from the perovskite lattice under reducing atmosphere can be traced back to almost twenty years ago, when Nishihata et al.<sup>78</sup> found that palladium (Pd) reversibly moved out of and into the  $\text{LaFe}_{0.57}\text{Co}_{0.38}\text{Pd}_{0.05}\text{O}_3$  perovskite lattice when cycled between reductive and oxidative atmosphere. In comparison with the Pd-impregnated  $\gamma\text{-Al}_2\text{O}_3$  catalysts, the ‘intelligent’ Pd-perovskite catalysts showed higher resistive to ageing during the conversion of CO and  $\text{NO}_x$  measurements. Afterwards, this technique was used in decorating perovskite surfaces with catalytically active Pd, Ni, Ru, Rh and Pt nanoparticles in the application of SOFC<sup>79-82</sup> and automotive emission control<sup>78, 83-84</sup>. However, in many cases, except the preferred metal nanoparticles, the large A-site cation, such as  $\text{La}^{3+}$ , also precipitated on the perovskite surface in the form of  $\text{La}_2\text{O}_3$  or  $\text{La}(\text{OH})_3$  after reduction treatment,<sup>78, 85</sup> which is usually detrimental to the catalytic performance and electric conduction of materials. This is because with the ongoing exsolution of B-site cation, the left parent oxide possesses more amount of A-site cation than the nominal stoichiometry, that is A-site excess, perhaps arranging as Ruddlesden-Popper phases (Eq. 1-14). While perovskite can only tolerant a limited A-site excess, the A-site cation would be expelled out of the lattice to keep the perovskite structure in a stable state (Eq. 1-15).

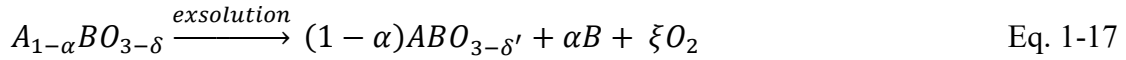


Or the total reaction can be expressed as Eq. 1-16:



The concept of exsolution applied in the above perovskite is all based on the stoichiometric compositions, with  $\text{A/B}=1$ , and only for limited kinds of easily reducible cations. By control of non-stoichiometry ( $\text{A/B}<1$ ,  $\text{A}_{1-\alpha}\text{BO}_{3-\delta}$ ), Neagu et al.<sup>77</sup> found that by tailoring the non-stoichiometry, harder-to-reduce cations that have higher Gibbs free energy in the reduction reaction can also be exsolved and the undesirable precipitation

of A-site cation-containing phases can be inhibited, as exemplified by Eq. 1-17.



This is because, on one hand, the A-site deficient  $A_{1-\alpha}BO_{3-\delta}$  can be regarded as B-site excess, which may drive the B-site cation exsolved from the perovskite lattice naturally to maintain a stable stoichiometric structure. On the other hand, under the pre-existence of A-site deficiency, the B-site exsolution would drive the perovskite composition towards a stable  $ABO_3$  stoichiometry but not A-site excess, which alleviates the formation tendency of AO precipitations. The beneficial effect of non-stoichiometry on the B-site exsolution can be observed in Ni exsolution from the tailored perovskite stoichiometry and is explained as follows.  $ABO_{3+\gamma}$ ,  $A_{1-\alpha}BO_3$  and  $A_{1-\alpha}BO_{3-\delta}$  -type perovskite oxides were designed by adjusting the doping content of trivalent  $La^{3+}$  on the A-site, represented by  $(La_{0.3}Sr_{0.7})(Ni_{0.06}Ti_{0.94})O_{3.09}$ ,  $(La_{0.52}Sr_{0.28})(Ni_{0.06}Ti_{0.94})O_3$ ,  $(La_{0.4}Sr_{0.4})(Ni_{0.06}Ti_{0.94})O_{3-\delta}$ , respectively.<sup>86</sup> However, XPS investigation revealed an A and O-site enriched surface that was even developed on the A-site deficient oxide, which could act to locally suppress B-site exsolution. This A, O-site enrichment on the surface was generally observed in perovskite and inherently formed during high-temperature annealing in oxidizing atmosphere.<sup>87</sup> Therefore, a “cleaved” surface, which belonged to the ‘bulk surfaces’, was also used to investigate exsolution due to its nominal designed stoichiometry. After reduction, no particle was observed on the native surface of the  $ABO_{3+\gamma}$  -type oxide, and only limited number of nanoparticles were occasionally observed on its cleaved surface (Figure 1-14 a), further illustrating the detrimental effect of A-site excess on particle nucleation. On the cleavage of  $A_{1-\alpha}BO_3$  (Figure 1-14 b), numerous particles were distributed uniformly and can also be seen on the regular surface.  $A_{1-\alpha}BO_{3-\delta}$  -type oxide in Figure 1-14 (c) showed a terraced-like surface morphology and a lot of particles were located on the terrace edge. The easy to exsolve on the surface of the deficient host perovskite proved the controllable nanoparticle exsolution with non-stoichiometry.

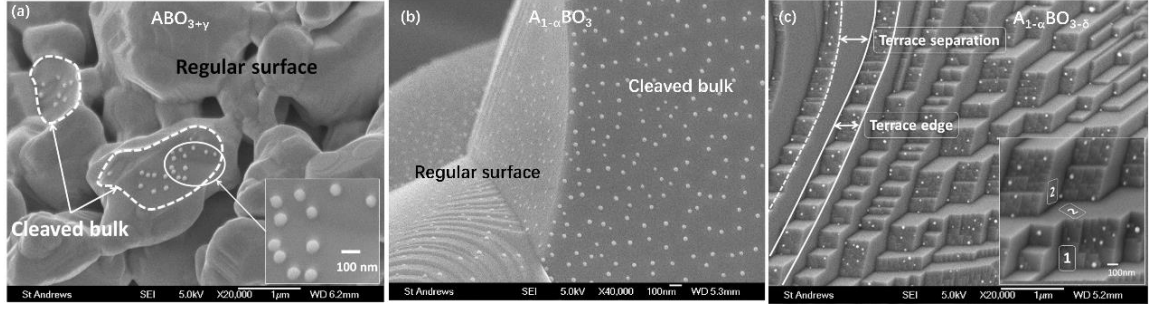


Figure 1-14. The key role of non-stoichiometry and perovskite surface structuring in the B-site exsolution, exemplified by SEM images presenting Ni exsolutions from (a)  $(\text{La}_{0.3}\text{Sr}_{0.7})(\text{Ni}_{0.06}\text{Ti}_{0.94})\text{O}_{3.09}$ ,  $(\text{ABO}_{3+\gamma})$ , (b)  $(\text{La}_{0.52}\text{Sr}_{0.28})(\text{Ni}_{0.06}\text{Ti}_{0.94})\text{O}_3$ ,  $(\text{A}_{1-\alpha}\text{BO}_3)$  and (c)  $(\text{La}_{0.4}\text{Sr}_{0.4})(\text{Ni}_{0.06}\text{Ti}_{0.94})\text{O}_{3-\delta}$ ,  $(\text{A}_{1-\alpha}\text{BO}_{3-\delta})$ . The samples were reduced at 900 °C for 15h in 5%  $\text{H}_2/\text{Ar}$ . Figure adapted from Ref. 86.

In order to explain the promoting effect of A-site deficiency on exsolution at an atomic scale, we need to describe the general exsolution process in detail first. Initially, when an  $\text{A}_{1-\alpha}\text{BO}_3$  perovskite is exposed in reducing atmosphere (e.g., 5%  $\text{H}_2/\text{Ar}$ ) at elevated temperature, oxygen ions are stripped from the perovskite lattice due to the low  $p\text{O}_2$  in the atmosphere, resulting in formation of oxygen vacancies and electrons as follows:



The perovskite becomes A-site deficient and oxygen deficient  $\text{A}_{1-\alpha}\text{BO}_{3-\delta}$ :



With further reduction, the number of oxygen vacancies reaches the limit value that can be accommodated in the perovskite structure,  $\delta_{\text{lim}}$ :



After that, the continuing reduction would lead to the destabilization of the perovskite lattice that cannot be tolerated simply by octahedra tilting. In this case, reducible B-site cations are exposed and favourable in nucleation:



Note here the nucleation is not necessary in the form of metal. For the B-site

occupancy consisting of only cations with positive Gibbs free energy  $\Delta G$  of the reduction reaction, it would exsolve in the form of metal oxide, such as  $\text{TiO}_{2-\delta}$  from  $\text{La}_{0.4}\text{Sr}_{0.4}\text{TiO}_3$ . Nucleation is preferred to occur primarily on the surface of the host lattice where the nucleation barrier is supposed to be lowered by crystal defects.<sup>88</sup> Moreover, since lattice oxygen is firstly stripped from the very surface of the perovskite oxide, numerous oxygen vacancies are created on the surface of the grain, but only a few or ‘none’ exist in the layers beneath. Thus, an oxygen concentration gradient is produced which drives the bulk oxygen ions naturally migrating towards the surface to balance out the gradient. Meanwhile, the nucleation of the B-site cation on the surface also drains exsolvable B-site cations diffusing from the bulk to the surface to balance the compositional gradient. This compensation process fuels the growth of the metal clusters and cations diffusion is reported from about 100 nm depth of the surface.<sup>89</sup> Here, we see that the metal nucleation occurs in fact in the form of Schottky-type defect reaction expressed by Kröger-Vink notation as follows:



Coupled with oxygen vacancies induced through reduction, the presence of A-site vacancies may facilitate the destabilization process of the lattice due to the high deficiency on two of its three primitive sites, as shown in Figure 1-15. The removal of oxygen ions can be thus visualized as locally secluding the B-site cations from the main perovskite framework into incipient exsolution. Unit cells occupied with A sites remain unaltered, while the ones with A-site deficiency is expelled due to the initial ‘B-site excess’ state.<sup>77</sup>

The defects, such as A-site and oxygen vacancies, assist not only with the nucleation but also ions migration by minimizing lattice collisions and supplying hopping sites, which in turn drive the exsolution of active B-site cations.<sup>90</sup>

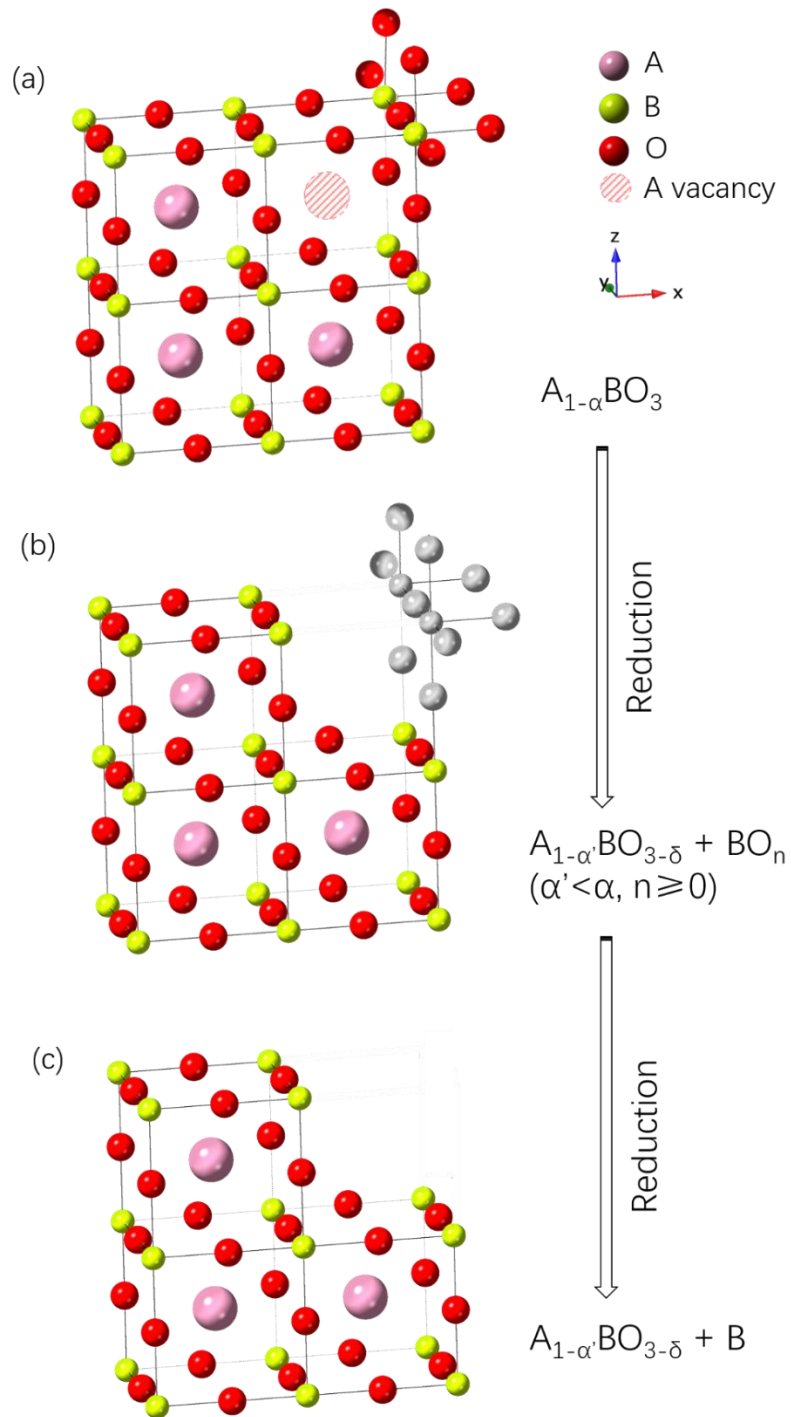


Figure 1-15. Schematic of the B-site cation exsolving from A-site-deficient perovskite. The larger silver spheres, small grey spheres highlighted in yellow, large dark spheres represent O-sites, B-sites and A-sites, respectively. A-site vacancy is depicted in a large hashed red sphere<sup>77</sup>. Figure reproduced from Ref. 77, Nature Publishing Group.

Apart from the beneficial effect of non-stoichiometry on promoting the reduction of ions and alleviating the segregation of AO island on the surface, A-site deficiency can play a role in trigger the formation of exsolutions that beyond thermodynamically favourable matter. As in the previous exsolutions on stoichiometric oxides, most exsolvable cations ( $\text{Ru}^{4+}$ ,  $\text{Rh}^{3+}$ ,  $\text{Pd}^{2+}$ ,  $\text{Pt}^{2+}$ ) that are reported are easier to reduce and have a very negative reduction free enthalpy values,  $\Delta G < -200$  kJ/mol, meaning that the exsolution of these cations is spontaneous. However, with the existence of A-site deficiency, the thermodynamically unfavourable reduction of  $\text{TiO}_2$  to  $\text{Ti}_2\text{O}_3$  ( $\Delta G_{\text{TiO}_2 \rightarrow \text{Ti}_2\text{O}_3} = +38$  KJ/mol,  $T=1100$  °C) can be triggered in the perovskite. This suggests that A-site deficient can act as a general driving force for exsolution, more general than the reducibility of the cations.

As we mentioned at the beginning, the unique property of exsolution method is that nanoparticles grown from the perovskite lattice exhibit enhanced thermal stability and significant resistance towards coking during the catalytic or SOFC test. In comparison with the deposited particles, the exsolved Ni particles are reported to present distinct lower tendency to agglomerate and coke when exposing in reductive atmosphere at high temperature for tens of hours. Only less extent of coalescence occurs in the exsolved particles when particles are initially close to each other.<sup>89</sup> Generally, exsolved particles are pinned to their original location and showing high stability in the metal-oxide interfaces. Aside from the thermal stability, when exposed in a hydrocarbon environment, conventionally deposited Ni particles are uplifted by the formation of carbon fibres at the metal-oxide interface owing to the catalytic activity of Ni (Figure 1-16 a), which would result in irreversible catalysts damage. Whereas, Ni particles prepared by exsolution exhibited exceptionally low extent of coking with limited short carbon fibres laying on the oxide support (Figure 1-16 b), suggesting a remarkable resistance to coking.<sup>89</sup> The high thermal stability and coking resistance is proposed to result from the socketing nature of the exsolved particles in the host material that about one-third of the volume is immersed in the host lattice (Figure 1-16 c).<sup>89</sup> Additionally, lattice strain is found to exist between the particles and the host



perovskite due to the crystallographic coherence (Figure 1-16 d), further contributing to the different physical and chemical properties of the exsolved particles.<sup>89</sup>

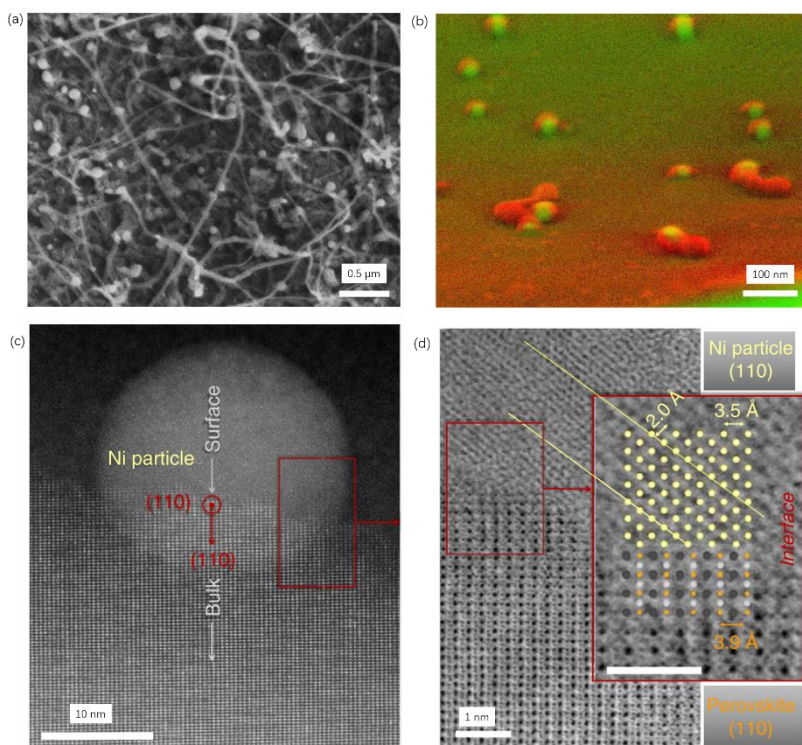


Figure 1-16. (a) Ni particles prepared by vapour deposition after coking test, (b) False colour micrograph of Ni particles obtained by exsolution after coking test, (c) Dark field TEM micrograph of a Ni particle exsolved on (110) surface after ageing (~3% H<sub>2</sub>O/5% H<sub>2</sub>/Ar, 930 °C, 60h), (d) detailed TEM micrograph of the metal-perovskite interface. Figure adapted from Ref. 89, Nature Publishing Group.

### 1.6.3 The extent of A-site deficiency in Perovskite

It is found that the extent of A-site deficiency in a specific material highly depends on the doping cations, and materials with A-site deficiency exceed the maximum tolerated vacancy would comprise a cation stoichiometric perovskite phase and a secondary phase.<sup>91</sup> Transition metal perovskites are found to accommodate low range of A-site deficiency, especially for oxides with a high fraction of nickel cations resided on the B-sublattice, as investigated experimentally by in situ neutron diffraction analysis, transmission electron microscopy and thermogravimetric analysis. This is

proposed by Konyshva and co-worker<sup>91</sup> to be relevant to the Me-O bonds energy. When “one-vacancy” on the A-site exists in the perovskite structure, at the local level the coordination number (CN) of the connected twelve O<sup>2-</sup> ions would change from 6 to 5. Since O<sup>2-</sup> ions cannot support a 5 fold coordinated state<sup>92</sup>, the distorted oxygen sublattice need to be compensated within the perovskite structure. In Na<sub>x</sub>WO<sub>3</sub> and La<sub>1/3</sub>Nb(Ta)O<sub>3</sub>, transition metal cations are in the high valence of 6+ or 5+, leading to a high degree of covalence in the Me-O bonds (W-O, Nb-O, and Ta-O) and Me-O network thus tends to be stable. As a result, the oxygen sublattice can be stabilized, and a high proportion of cations vacancies at the twelve coordinated A-sites can be tolerated. In contrast, nickel cations in perovskite can flexibly change their oxidation state between 2+ and 3+ valence, giving rise to a less stable [NiO<sub>6</sub>] octahedra and thus an unstable perovskite structure. Konyshva and co-workers<sup>91</sup> summarized the correlation between the maximum A-site deficiency in perovskites and the average B-O (<B-O>) bond energy or the average metal (A, B)- O bond energy <ABE>, illustrated in Figure 1-17. The <ABE> values can help to assess the effect of the chemical origin of A-site cations on the maximum A-site deficiency (Figure 1-17 b). The negative values indicate the thermodynamic favourable character of the formation of the bond. The average <B-O> bond energy shows an almost linear dependence upon the maximum A-site deficiency. With the most stable <B-O> bonds, La<sub>1/3</sub>Nb(Ta)O<sub>3</sub> exhibits the highest tolerance to A-site deficiency, achieving a fraction of 2/3. Compounds containing a high concentration of Ti show relatively less capacity toward A-site deficiency due to the lowered <B-O> bond energy. Extrapolate to the zero value of the maximum A-site deficiency in Figure 1-17 (a), the corresponded <B-O> value means that perovskite lattice with <B-O> bond energy varying between -175 – -190 kJ mol<sup>-1</sup> can accommodate negligible A-site deficiency. This approach provides a convenient prediction for designing perovskite materials with a single phase.

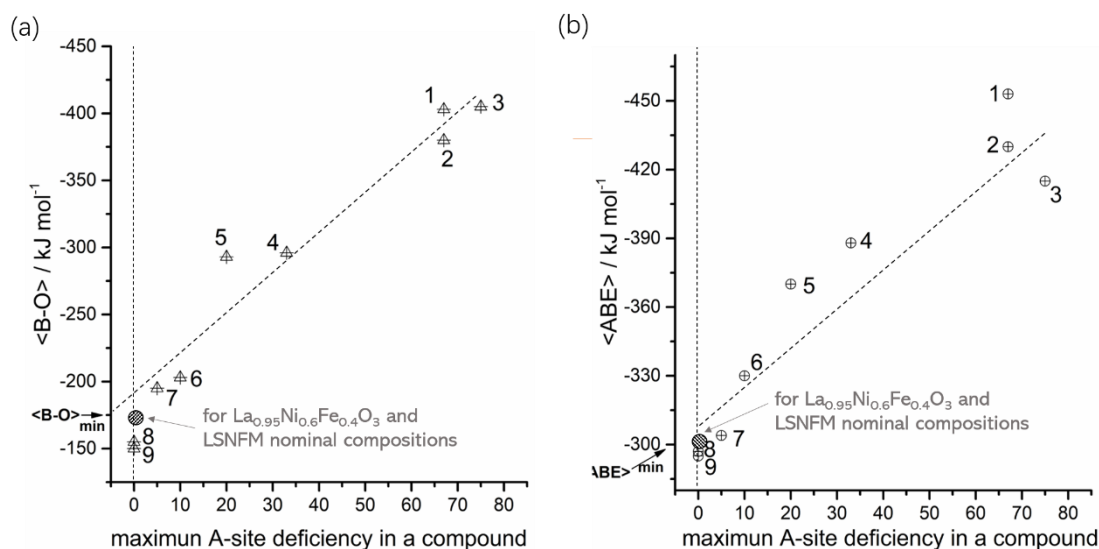


Figure 1-17. Correlation between the maximum value of A-site deficiency in the perovskite with (a) average <B-O> bond energy and (b) average <ABE> bond energy estimated from the thermodynamic data for 1. La<sub>1/3</sub>TaO<sub>3</sub>; 2. La<sub>1/3</sub>NbO<sub>3</sub>; 3. Na<sub>0.25</sub>WO<sub>3</sub>; 4. La<sub>2/3</sub>(Ti<sup>4+</sup><sub>0.5</sub>Ti<sup>3+</sup><sub>0.5</sub>)O<sub>3-δ</sub>; 5. La<sub>0.2</sub>Sr<sub>0.6</sub>Ti<sub>0.8</sub>Nb<sub>0.2</sub>O<sub>3</sub>; 6. La<sub>0.9</sub>(Mn<sup>4+</sup><sub>0.5</sub>Mn<sup>3+</sup><sub>0.5</sub>)O<sub>3+δ</sub>; 7. La<sub>0.55</sub>Sr<sub>0.4</sub>Co<sup>3+</sup><sub>0.2</sub>Fe<sup>3+</sup><sub>0.8</sub>O<sub>3</sub>; 8. LaNiO<sub>3</sub>, 9. LaCoO<sub>3</sub>. Figure reproduced from Ref. 91, Wiley Publishing Group.

## 1.7 Phase diagram

In the sintering process, the participation of liquid phase can assist densification usually by enhancing grain boundary transport rates and the densification rates. Specific grain boundary properties may also be produced because of the distribution of liquid film on this region. Typically, the amount of liquid involved in the densification is quite small, only a few volume percent, which make the solidified liquid phase difficult to detect and sometimes can only be revealed by high-resolution transmission electron microscopy. The addition of sintering aids for densification in the sintering of ceramic oxide is generally based on the principle of liquid phase sintering.

### 1.7.1 Y<sub>2</sub>O<sub>3</sub>-BaO-CuO system

The study of phase equilibrium diagrams is very useful in optimizing the condition

for calcining, sintering and crystal growth of the superconducting compound  $\text{YBa}_2\text{Cu}_3\text{O}_{6+\delta}$ . The pseudo-binary phase diagram of the  $\text{YCuO}_{2.5}$ - $\text{BaCuO}_2$  constructed by Nevriiva et al.<sup>93</sup> is illustrated in Figure 1-18, where the copper ions were assumed to be divalent and the possible deviation from stoichiometry were neglected. The diagram can roughly be divided into the lower temperature region below 1075 °C and higher temperature region above 1075 °C. At lower temperature, the phases in equilibrium change with the molar ratio of  $\text{BaCuO}_2$ , with  $\text{CuO} + \text{YCuO}_{2.5} + \text{Y}_2\text{BaCuO}_5$  for 33.3 mol% of  $\text{BaCuO}_2$ ,  $\text{CuO} + \text{Y}_2\text{BaCuO}_5 + \text{YBa}_2\text{Cu}_3\text{O}_{6.5}$  for 33.3 – 66.6 mol% of  $\text{BaCuO}_2$  and  $\text{YBa}_2\text{Cu}_3\text{O}_{6.5} + \text{BaCuO}_2$  for 66.6 – 100 mol% of  $\text{BaCuO}_2$ . Peritectic decomposition occurs for 1:2:3 phase at 1000 °C and for 0:1:1 phase at 1025 °C, leading to the new phase equilibria, that is,  $\text{CuO} + 2:1:1 + 0:1:1$  between 1000 °C and 1025 °C,  $\text{CuO} + 2:1:1 + \text{L}$  between 1025 and 1075 °C. Platinum containing phases, X3 and X4, are also present now due to the platinum inserted during sample preparation. Above 1075 °C, liquid phases are formed in the whole range of  $\text{BaCuO}_2$  concentration, making the system more complicated. In the concentration range of  $\text{BaCuO}_2$  below 19 mol%, the co-existence of phases is  $\text{Y}_2\text{O}_3 + 1:0:1 + \text{L}$ . However, phase diagram at higher  $\text{BaCuO}_2$  concentration range is less reliable due to the presence of platinum species.

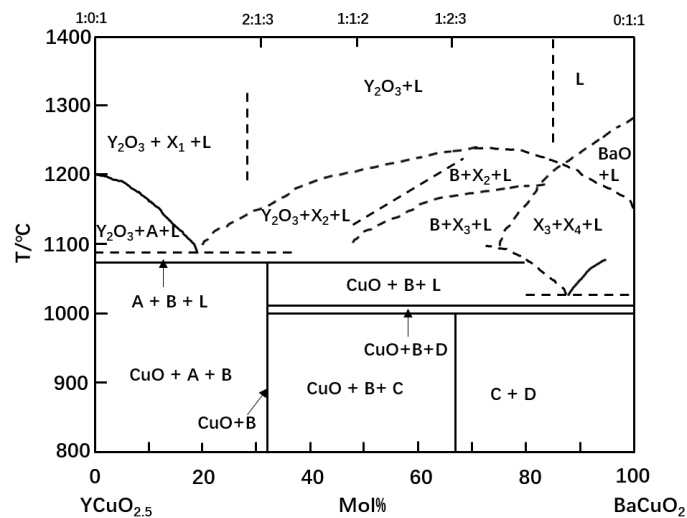


Figure 1-18. Pseudobinary phase diagram of the  $\text{YCuO}_{2.5}$  –  $\text{BaCuO}_2$  system, A-  $\text{YCuO}_{2.5}$ , B- $\text{Y}_2\text{BaCuO}_5$ , C- $\text{YBa}_2\text{Cu}_3\text{O}_{6.5}$ , D- $\text{BaCuO}_2$ . Figure reproduced from Ref. 93.

In the  $Y_2O_3$ -BaO-CuO<sub>x</sub> system, one of the important investigations on the phase equilibrium is the peritectic melting points of quaternary compounds  $Y_2BaCuO_5$  and  $YBa_2Cu_3O_{6+\delta}$  and the ternary eutectic point of  $YBa_2Cu_3O_{6+\delta}$ /BaCuO<sub>2</sub>/CuO/liquid phases. Typically, the liquid phase in the Y-Ba-Cu-O system contains  $Y^{3+}$ ,  $Ba^{2+}$ ,  $Cu^{2+}$ ,  $Cu^+$  and  $O^{2-}$  ions and maintains electrical neutrality by adjusting the relative amounts of the  $Cu^{2+}$ ,  $Cu^+$  and  $O^{2-}$  ions.

### 1.7.2 BaO-CuO system

In the BaO-CuO<sub>x</sub> and BaO<sub>2</sub>-CuO<sub>x</sub> systems, only a few phases were reported, including BaCuO<sub>2-2.12</sub>, BaCuO<sub>2.26-2.39</sub>, BaCuO<sub>2.5</sub>, Ba<sub>2</sub>CuO<sub>3+x</sub>, Ba<sub>2</sub>Cu<sub>3</sub>O<sub>5+x</sub>, BaCu<sub>2</sub>O<sub>2+x</sub>, Ba<sub>3</sub>Cu<sub>5</sub>O<sub>8</sub>, Ba<sub>5</sub>Cu<sub>3</sub>O<sub>6+x</sub>, Ba<sub>3</sub>CuO<sub>4</sub>, BaCu<sub>3</sub>O<sub>4</sub>, Ba<sub>3</sub>Cu<sub>2</sub>O<sub>4+x</sub>, and BaCu<sub>2</sub>O<sub>x</sub>. As indicated by the formulas, many of the phases are nonstoichiometric in terms of the oxygen content.

Roth lab<sup>94</sup> firstly determined the phase equilibrium of BaO-CuO<sub>x</sub> system in air. In this system, two phases were confirmed, BaCuO<sub>2</sub> and Ba<sub>2</sub>CuO<sub>3</sub>. Under the atmosphere of 1 atm oxygen pressure, Nevriva et al.<sup>95</sup> conducted experiments on phase diagram of CuO<sub>x</sub>-BaCuO<sub>2</sub> quasi-binary system. Later, combined with thermal analysis, the diagram is reexamined by Zhang et. al<sup>96</sup> and further completed by Zimmermann et al.,<sup>97</sup> illustrated in Figure 1-19.

Ba<sub>2</sub>CuO<sub>3</sub> melts at 900 °C by the peritectic reaction ( $L + BaO \rightarrow Ba_2CuO_3$ ) at a composition of 35 mol% CuO. Under the finite cooling rate, peritectic reaction does not reach completion and part of the liquid remained unreacted. This liquid is followed by eutectic reaction below. Two eutectic reactions (E3 and E2) accompanied with a slight increase in weight occur at 900 °C and 920 °C, through  $L \rightarrow BaO + Ba_2CuO_3$  and  $L \rightarrow Ba_2CuO_3 + BaCuO_2$ , respectively. The eutectic composition is around 24.5 mol% CuO for E3 and 36.5 mol % CuO for E2. This reaction does not occur in the heating process. A phase transition takes place at 810 °C of the Ba<sub>2</sub>CuO<sub>3</sub>, from tetragonal structure at above 810 °C to an orthorhombic symmetry (Immm) at lower temperature.

Another eutectic reaction ( $L \rightarrow BaCuO_2 + Cu_2O$ ) occurs at 890 °C near 71.5 mol%

CuO, between the phase BaCuO<sub>2</sub> and CuO. The same eutectic point is reported to be at varied temperature and contain a different liquid composition. For example, Roth et al. reported that the eutectic took place at 900 °C and 0.62 mol fraction of CuO at 0.21 atm oxygen pressure, while this reaction occurred at 926 °C and 72 mol% CuO at 1 atm oxygen pressure, investigated by Nevriřa et al<sup>95</sup>. Lay et al<sup>98</sup>. had the similar results on this eutectic reaction as Nevriřa et al., which is about 70 mol% CuO in the liquid composition in air. Based on the experimental date by Nevriřa et al. and Lay et al., Lee and co-authors<sup>99</sup> calculated the thermodynamic data of the BaO-Cu<sub>2</sub>O-CuO system, which shows the CuO/BaCuO<sub>2</sub>/liquid eutectic point at 1 atm oxygen pressure to be at 926 °C with 69.5 mol% CuO and at 0.21 atm oxygen pressure to be at 906 °C with 69.8 mol % CuO. The melting temperature of BaCuO<sub>2</sub> was calculated to be 1028 °C and 1007 °C at 1 atm and 0.21 atm oxygen pressure, respectively. The temperature of this reaction changes with the BaO-CuO composition.

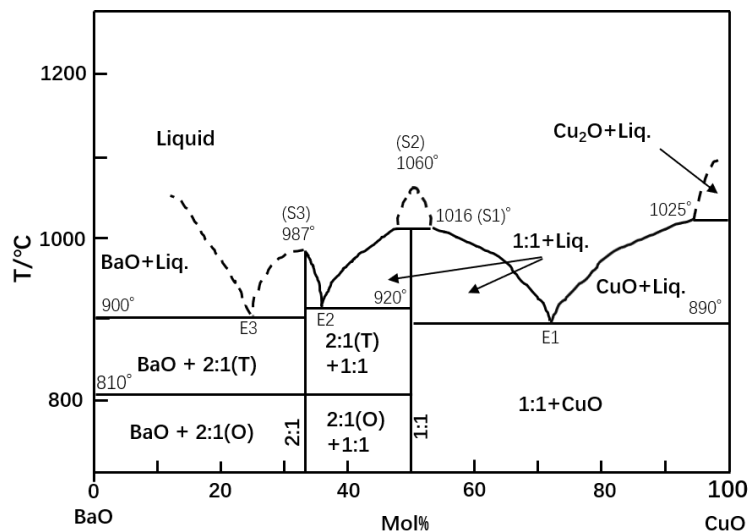


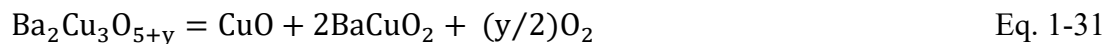
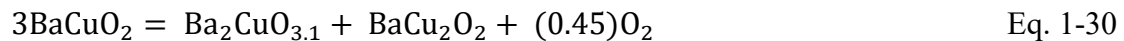
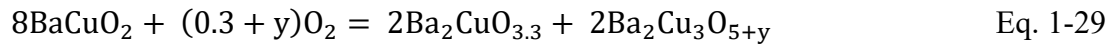
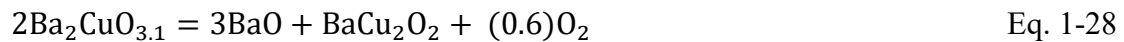
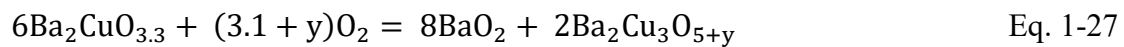
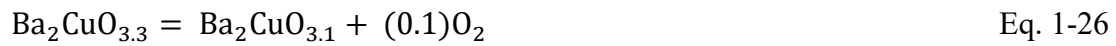
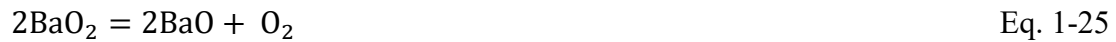
Figure 1-19. Pseudo binary phase diagram BaO-CuO, pO<sub>2</sub> = 0.21 bar. Figure reproduced from Ref. 97.

The behavior of BaCuO<sub>2</sub> phase on heating and on cooling is different. This phase remains stable up to 1016 °C, then melts by the synthetic reaction (L1 + L2 → BaCuO<sub>2</sub>). The temperature of 1060 °C is the highest temperature, below which the two liquids coexist. During cooling, the synthetic reaction dose not take place. The two liquids will

remain at temperature below 1016 °C. Each liquid finally solidifies at the respective eutectic point E1, E2.

CuO transfers into Cu<sub>2</sub>O at 1025 °C, but no observation has been confirmed of the transition.

Another type of phase diagram, shown in Figure 1-20, provides potential functions (oxygen pressure and temperature) on both axes and is exemplified by the so-called stability (or predominance) diagram.<sup>100</sup> Each line in this figure represents the conditions for the corresponding two or three phases in equilibrium, with the phases stable on each side of the line. For example, the 2:1 phase is stable when oxygen pressures and temperatures are between the bold solid lines (1-9), while 1:1 phase remain stable in the condition range of thin solid line (2-8). For 2:3 phase, it can be stabilized at oxygen pressure and temperature condition above the short dash line (4), and for the higher Cu content phase, 1:2 phase, it is only stable below the chained-dot line (6). Below the two dots chain line (10), the barium cuprate phases totally decompose and copper species exist in the form of Cu metal. Overall, the stability fields of the phases in the Ba-Cu-O system are bounded by the following reactions:





It is worth noting that the phase equilibria in this figure only express the thermodynamic instability of a phase but say nothing about the kinetics, which means that it is not known to us that how quickly the unstable phase decomposes.

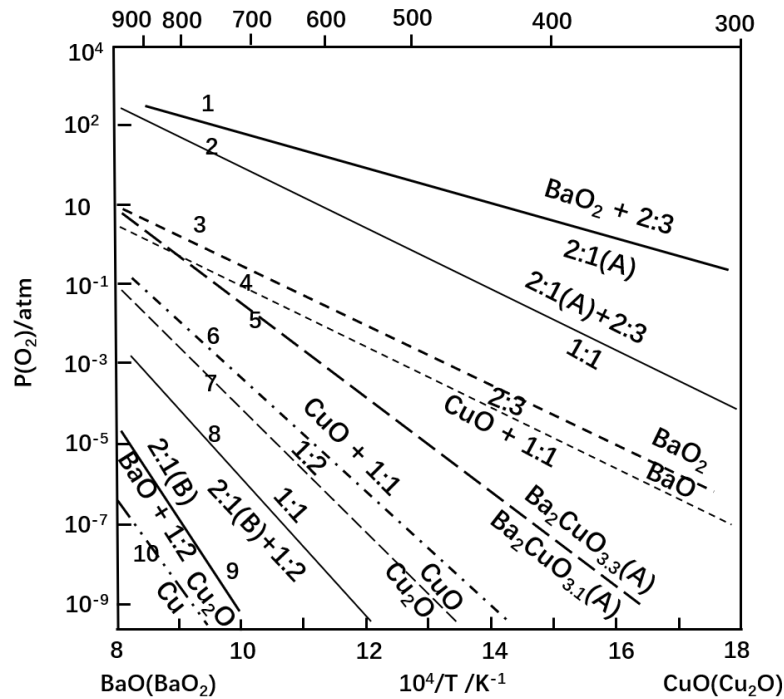


Figure 1-20. Stability diagram of the Ba-Cu-O system. Figure reproduced from Ref. 100.

Although the 1:1 phase is expressed as  $\text{BaCuO}_2$ , evidence shows that the phase is not stoichiometric but can dissolve an excess of oxygen.

### 1.7.3 NiO-BaO system

When BaO and NiO mixtures with different fractions for each component were calcined, two products were observed,  $\text{NiO} \cdot \text{BaO}$  and  $\text{NiO} \cdot 3\text{BaO}$ .  $\text{NiO} \cdot \text{BaO}$  is orthorhombic. In a pseudohexagonal unit cell,  $\text{Ba}^{2+}$  is hexagonally close-packed and nickel ions locate at the center of a square array of  $\text{O}^{2-}$ . The  $\text{NiO} \cdot \text{BaO}$  single crystal can be easily grown at about  $1000^\circ\text{C}$  in  $\text{N}_2$ . A plate-like morphology is usually observed.



This compound is soluble in acid but insoluble in alkali and water. For  $\text{NiO}\cdot 3\text{BaO}$ , it is hexagonal (rhombohedral) with three oxygen ions in triangular arrangement and a nickel ion at the center.  $\text{NiO}\cdot 3\text{BaO}$  is soluble in acid and alkali and rapidly absorbs moisture from air.

Phase diagram of NiO-BaO system<sup>101</sup> is shown in Figure 1-21. There are two eutectic points: one is between NiO and  $\text{NiO}\cdot\text{BaO}$  occurring at 1200 °C, the other one is between  $\text{NiO}\cdot\text{BaO}$  and  $\text{NiO}\cdot 3\text{BaO}$  taking place at about 1080 °C. However, the eutectic compositions are not determined. No eutectic takes place between  $\text{NiO}\cdot 3\text{BaO}$  and BaO. The melting temperature of  $\text{NiO}\cdot\text{BaO}$  and  $\text{NiO}\cdot 3\text{BaO}$  is 1240 °C and 1160 °C, respectively.

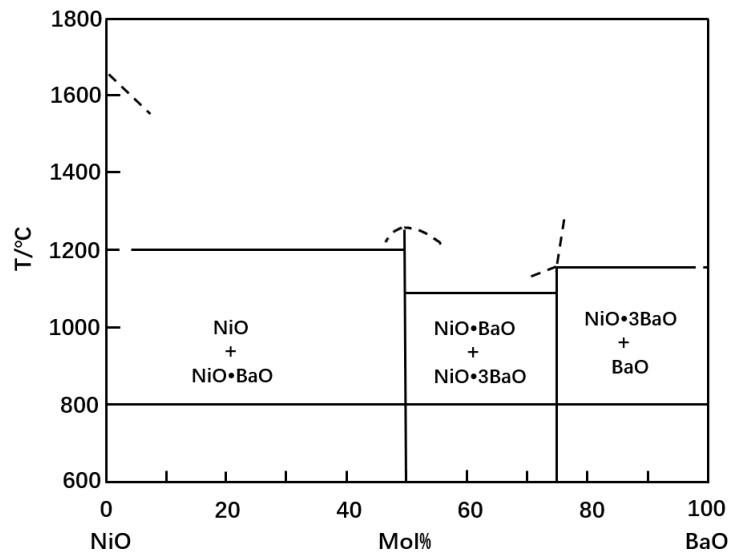


Figure 1-21. Phase diagram of NiO-BaO system. Figure reproduced from Ref. 101.

## 1.8 Aim of this thesis

This thesis aims to investigate the exsolution ability and process for transition metal- doped barium cerate zirconates perovskite oxide. With exsolved nanoparticles socketed on the proton conducting barium cerate and zirconates host, this material can act as a cathode material for the  $\text{CO}_2$  and  $\text{H}_2\text{O}$  co-electrolysis in the SOECs.

- ✓ Investigate the exsolution process of Cu and Ni particles from the doped barium

cerate zirconate oxides.

- ✓ Understand the A-site deficiency effect on the particle exsolution in BCZY.
- ✓ Study the effect of bimetal doping on the material sintering and exsolution from the BCZY perovskite.
- ✓ Know how the A-site deficiency affects the material's proton conductivity.
- ✓ Investigate the catalytic activity of BCZY-supported Cu particles towards CO oxidation.
- ✓ Illustrate the enhanced sinterability with the addition of ZnO in BCZY oxide.
- ✓ Prepare and test electrochemical cells by tape casting method and optimized by screen printing and impregnation methods.

## 1.9 Outline of this thesis

The chapters of the thesis are organized as follow:

Chapter 2 describes the sample and cell preparation method and summarizes the principle of the techniques employed in this project.

Chapter 3 examines the Cu particles exsolution process from doped BCZY perovskite and explores the influence of A-site deficiency and Cu doping level on the lattice constants and lattice hexagonality. The conductivity was dramatically increased after exsolution and exhibited metallic property. The highest conductivity was achieved by modifying A-site non-stoichiometry and Cu doping concentration.

Chapter 4 compares the different Ni exsolution process in doped BCZY oxide by adjusting stoichiometry. Three different types of Ni particles are observed as a result of the existence of impurity at the grain boundary and co-segregation of barium.

Chapter 5 demonstrates the influence of bimetal dopants in the BCZY perovskite. A pure phase is obtained with the bimetallic doping strategy, increasing the solubility of the transition metal in the perovskite structure. Compared with the single metal, the bimetal doped perovskite shows a much nicer exsolution, with smaller particle size and higher population. The native surface exhibits a similar exsolution phenomenon as the cleaved surface. Different from the exsolution phenomenon from lanthanum titanate

based perovskite, A-site rich surface (Ba rich) does not show prohibiting effect on B-site cation exsolution. This chapter also illustrates that the enhanced proton conductivity with the introduction of A-site deficiency in doped BCZY oxide is mainly due to the improved pre-exponential factor at the grain boundary.

Chapter 6 describes the tape casting technique for the BCZY cell fabrication in water or organic system. Screen printing method is also applied for the electrode preparation to optimize the porosity. B-site cation exsolution is probably significantly affected by the material preparation method. Impregnation is finally used for introducing electrode materials on the porous scaffold.

Chapter 7 summarizes the main findings of this thesis.

## 1.10 List of publications

Paper in preparation:

M. Wang, J. Hui, C. Savaniu & J.T.S. Irvine, Influence of cation stoichiometry of Ni exsolution from  $Ba_xCe_{0.5}Zr_{0.3}Y_{0.2-y}Ni_yO_{3-\delta}$ .

## References

1. Outlook, A. E., With Projections to 2035, April 2011, US Energy Information Administration Office of Integrated and International Energy Analysis, US Department of Energy. 2011.
2. Ritchie, H.; Roser, M., CO<sub>2</sub> and Greenhouse Gas Emissions. *Our world in data* **2017**.
3. Utgikar, V.; Thiesen, T., Life cycle assessment of high temperature electrolysis for hydrogen production via nuclear energy. *International Journal of Hydrogen Energy* **2006**, *31* (7), 939-944.
4. Steeneveldt, R.; Berger, B.; Torp, T., CO<sub>2</sub> capture and storage: closing the knowing–doing gap. *Chemical Engineering Research and Design* **2006**, *84* (9), 739-763.
5. Midilli, A.; Dincer, I., Hydrogen as a renewable and sustainable solution in

reducing global fossil fuel consumption. *International Journal of Hydrogen Energy* **2008**, *33* (16), 4209-4222.

6. Olah, G. A., Beyond oil and gas: the methanol economy. *Angewandte Chemie International Edition* **2005**, *44* (18), 2636-2639.

7. Dry, M. E., The fischer–tropsch process: 1950–2000. *Catalysis today* **2002**, *71* (3-4), 227-241.

8. Irvine, J. T.; Connor, P., *Solid oxide fuels cells: facts and figures*. Springer: **2013**, 163-180.

9. Hino, R.; Haga, K.; Aita, H.; Sekita, K., 38. R&D on hydrogen production by high-temperature electrolysis of steam. *Nuclear Engineering and Design* **2004**, *233* (1-3), 363-375.

10. Jensen, S. H.; Larsen, P. H.; Mogensen, M., Hydrogen and synthetic fuel production from renewable energy sources. *International Journal of Hydrogen Energy* **2007**, *32* (15), 3253-3257.

11. Fisher, F.; Tropsch, H., Conversion of methane into hydrogen and carbon monoxide. *Brennst.-Chem.* **1928**, *9*.

12. Kendall, K., Progress in solid oxide fuel cell materials. *International Materials Reviews* **2005**, *50* (5), 257-264.

13. Litzelman, S.; Hertz, J.; Jung, W.; Tuller, H., Opportunities and challenges in materials development for thin film solid oxide fuel cells. *Fuel Cells* **2008**, *8* (5), 294-302.

14. Goodenough, J. B., Oxide-ion electrolytes. *Annual Review of Materials Research* **2003**, *33* (1), 91-128.

15. Yokokawa, H., Understanding materials compatibility. *Annual Review of Materials Research* **2003**, *33* (1), 581-610.

16. Stotz, S.; Wagner, C., Die löslichkeit von wasserdampf und wasserstoff in festen oxiden. *Berichte der Bunsengesellschaft für physikalische Chemie* **1966**, *70* (8), 781-788.

17. Takahashi, T., Solid-state ionics: protonic conduction in perovskite type oxide

solid solutions. **1980**.

18. Iwahara, H.; Uchida, H.; Tanaka, S., High temperature type proton conductor based on SrCeO<sub>3</sub> and its application to solid electrolyte fuel cells. *Solid State Ionics* **1983**, *9*, 1021-1025.

19. Iwahara, H.; Esaka, T.; Uchida, H.; Maeda, N., Proton conduction in sintered oxides and its application to steam electrolysis for hydrogen production. *Solid State Ionics* **1981**, *3*, 359-363.

20. Iwahara, H., High temperature proton conducting oxides and their applications to solid electrolyte fuel cells and steam electrolyzer for hydrogen production. *Solid State Ionics* **1988**, *28*, 573-578.

21. Uchida, H.; Yoshikawa, H.; Iwahara, H., Formation of protons in SrCeO<sub>3</sub>-based proton conducting oxides. Part I. Gas evolution and absorption in doped SrCeO<sub>3</sub> at high temperature. *Solid State Ionics* **1989**, *34* (1-2), 103-110.

22. Iwahara, H.; Uchida, H.; Ono, K.; Ogaki, K., Proton conduction in sintered oxides based on BaCeO<sub>3</sub>. *Journal of the Electrochemical Society* **1988**, *135* (2), 529-532.

23. Iwahara, H.; Uchida, H.; Morimoto, K., High Temperature Solid Electrolyte Fuel Cells Using Perovskite - Type Oxide Based on BaCeO<sub>3</sub>. *Journal of the Electrochemical Society* **1990**, *137* (2), 462-465.

24. Bonanos, N.; Knight, K.; Ellis, B., Perovskite solid electrolytes: structure, transport properties and fuel cell applications. *Solid State Ionics* **1995**, *79*, 161-170.

25. Taniguchi, N.; Hatoh, K.; Niikura, J.; Gamo, T.; Iwahara, H., Proton conductive properties of gadolinium-doped barium cerates at high temperatures. *Solid State Ionics* **1992**, *53*, 998-1003.

26. Bonanos, N.; Ellis, B.; Mahmood, M., Construction and operation of fuel cells based on the solid electrolyte BaCeO<sub>3</sub>: Gd. *Solid State Ionics* **1991**, *44* (3-4), 305-311.

27. Yajima, T.; Kazeoka, H.; Yogo, T.; Iwahara, H., Proton conduction in sintered oxides based on CaZrO<sub>3</sub>. *Solid State Ionics* **1991**, *47* (3-4), 271-275.

28. Iwahara, H., Oxide-ionic and protonic conductors based on perovskite-type

- oxides and their possible applications. *Solid State Ionics* **1992**, 52 (1-3), 99-104.
29. Katahira, K.; Kohchi, Y.; Shimura, T.; Iwahara, H., Protonic conduction in Zr-substituted BaCeO<sub>3</sub>. *Solid State Ionics* **2000**, 138 (1-2), 91-98.
30. Larring, Y.; Norby, T., The equilibrium between water vapour, protons, and oxygen vacancies in rare earth oxides. *Solid State Ionics* **1997**, 97 (1-4), 523-528.
31. Norby, T.; Larring, Y., Concentration and transport of protons in oxides. *Current Opinion in Solid State and Materials Science* **1997**, 2 (5), 593-599.
32. Kreuer, K.-D., Proton-conducting oxides. *Annual Review of Materials Research* **2003**, 33 (1), 333-359.
33. Tanner, C. W.; Virkar, A. V., Instability of BaCeO<sub>3</sub> in H<sub>2</sub>O - Containing Atmospheres. *Journal of The Electrochemical Society* **1996**, 143 (4), 1386-1389.
34. Pasierb, P.; Drożdż-Cieśla, E.; Gajerski, R.; Łabuś, S.; Komornicki, S.; Rękas, M., Chemical stability of Ba (Ce<sub>1-x</sub>Ti<sub>x</sub>)<sub>1-y</sub>Y<sub>y</sub>O<sub>3</sub> proton-conducting solid electrolytes. *Journal of Thermal Analysis and Calorimetry* **2009**, 96 (2), 475-480.
35. Tao, Z.; Zhu, Z.; Wang, H.; Liu, W., A stable BaCeO<sub>3</sub>-based proton conductor for intermediate-temperature solid oxide fuel cells. *Journal of Power Sources* **2010**, 195 (11), 3481-3484.
36. Liu, X.-M.; Gu, Y.-J.; Liu, Z.-G.; Ouyang, J.-H.; Yan, F.-Y. Y.; Xiang, J., Electrical conductivity and chemical stability of BaCe<sub>0.8-x</sub>A<sub>x</sub>Gd<sub>0.2</sub>O<sub>3-δ</sub> (A= In, Zr, Ta; x= 0, 0.1) ceramics. *Bulletin of Materials Science* **2013**, 36 (3), 395-401.
37. Kreuer, K., On the development of proton conducting materials for technological applications. *Solid state ionics* **1997**, 97 (1-4), 1-15.
38. Seakins, J., Electrospray mass spectrometry of highly moisture-sensitive metal alkoxides. *Journal of Materials Chemistry* **1997**, 7 (8), 1553-1558.
39. Veith, M.; Mathur, S.; Lecerf, N.; Huch, V.; Decker, T.; Beck, H. P.; Eiser, W.; Haberkorn, R., Sol-gel synthesis of nano-scaled BaTiO<sub>3</sub>, BaZrO<sub>3</sub> and BaTi<sub>0.5</sub>Zr<sub>0.5</sub>O<sub>3</sub> oxides via single-source alkoxide precursors and semi-alkoxide routes. *Journal of Sol-Gel Science and Technology* **2000**, 17 (2), 145-158.
40. Thongtha, A.; Bongkarn, T., Phase formation and microstructure of barium

zirconate ceramics prepared using the combustion technique. *Ferroelectrics* **2009**, 383 (1), 33-39.

41. Chen, F.; Sørensen, O. T.; Meng, G.; Peng, D., Preparation of Nd-doped barium cerate through different routes. *Solid State Ionics* **1997**, 100 (1-2), 63-72.

42. Tong, J.; Clark, D.; Hoban, M.; O'Hayre, R., Cost-effective solid-state reactive sintering method for high conductivity proton conducting yttrium-doped barium zirconium ceramics. *Solid State Ionics* **2010**, 181 (11-12), 496-503.

43. Orlov, A. V.; Vinokurov, A. L.; Shlyakhtin, O. A.; Tretyakov, Y. D., Low-temperature sintering of BaZrO<sub>3</sub> and BaCeO<sub>3</sub> barrier materials. *Mendeleev Communications* **2004**, 14 (4), 163-165.

44. Gorbova, E.; Maragou, V.; Medvedev, D.; Demin, A.; Tsiakaras, P., Influence of Cu on the properties of gadolinium-doped barium cerate. *Journal of Power Sources* **2008**, 181 (2), 292-296.

45. Roth, R.; Davis, K.; Dennis, a. R., Phase equilibria and crystal chemistry in the system Ba-Y-Cu-O. *Advanced Ceramic Materials* **1987**, 2, 303-312.

46. Yang, C.-F.; Lo, S.-H., Grain growth for CuO-BaO mixtures added BaTi<sub>1+x</sub>O<sub>3+2x</sub> ceramics. *Materials research bulletin* **1997**, 32 (12), 1713-1722.

47. Ricote, S.; Bonanos, N., Enhanced sintering and conductivity study of cobalt or nickel doped solid solution of barium cerate and zirconate. *Solid State Ionics* **2010**, 181 (15-16), 694-700.

48. Babilo, P.; Haile, S. M., Enhanced sintering of yttrium-doped barium zirconate by addition of ZnO. *Journal of the American Ceramic Society* **2005**, 88 (9), 2362-2368.

49. Tao, S.; Irvine, J. T., A stable, easily sintered proton - conducting oxide electrolyte for moderate-temperature fuel cells and electrolyzers. *Advanced Materials* **2006**, 18 (12), 1581-1584.

50. Bi, L.; Tao, Z.; Liu, C.; Sun, W.; Wang, H.; Liu, W., Fabrication and characterization of easily sintered and stable anode-supported proton-conducting membranes. *Journal of Membrane Science* **2009**, 336 (1-2), 1-6.

51. Glazer, A., The classification of tilted octahedra in perovskites. *Acta Crystallographica Section B: Structural Crystallography and Crystal Chemistry* **1972**, 28 (11), 3384-3392.
52. Goodenough, J. B.; Cooper, S., *Localized to itinerant electronic transition in perovskite oxides*. Springer: 2001; Vol. 98.
53. Eng, H. W.; Barnes, P. W.; Auer, B. M.; Woodward, P. M., Investigations of the electronic structure of d0 transition metal oxides belonging to the perovskite family. *Journal of Solid State Chemistry* **2003**, 175 (1), 94-109.
54. Wolfram, T.; Ellialtioglu, S., *Electronic and optical properties of d-band perovskites*. Cambridge University Press: 2006.
55. Woodward, P. M., Octahedral tilting in perovskites. II. Structure stabilizing forces. *Acta Crystallographica Section B: Structural Science* **1997**, 53 (1), 44-66.
56. Kennedy, B. J.; Howard, C. J.; Kubota, Y.; Kato, K., Phase transition behaviour in the A-site deficient perovskite oxide  $\text{La}_{1/3}\text{NbO}_3$ . *Journal of Solid State Chemistry* **2004**, 177 (12), 4552-4556.
57. Ali, R.; Yashima, M., Space group and crystal structure of the perovskite  $\text{CaTiO}_3$  from 296 to 1720 K. *Journal of Solid State Chemistry* **2005**, 178 (9), 2867-2872.
58. Kreuer, K.-D., Proton conductivity: materials and applications. *Chemistry of Materials* **1996**, 8 (3), 610-641.
59. Kreuer, K. D.; Rabenau, A.; Weppner, W., Vehicle mechanism, a new model for the interpretation of the conductivity of fast proton conductors. *Angewandte Chemie International Edition in English* **1982**, 21 (3), 208-209.
60. Münch, W.; Seifert, G.; Kreuer, K.; Maier, J., A quantum molecular dynamics study of proton conduction phenomena in  $\text{BaCeO}_3$ . *Solid State Ionics* **1996**, 86, 647-652.
61. Shimojo, F.; Hoshino, K.; Okazaki, H., First-Principles Molecular-Dynamics Simulation of Proton Diffusion in Sc-Doped  $\text{SrTiO}_3$ . *Journal of the Physical Society of Japan* **1997**, 66 (1), 8-10.



62. Kreuer, K.; Münch, W.; Traub, U.; Maier, J., On proton transport in perovskite-type oxides and plastic hydroxides. *Berichte der Bunsengesellschaft für physikalische Chemie* **1998**, *102* (3), 552-559.
63. Kreuer, K. D., Proton-Conducting Oxides. *Annual Review of Materials Research* **2003**, *33* (1), 333-359.
64. Kreuer, K.; Dippel, T.; Baikov, Y. M.; Maier, J., Water solubility, proton and oxygen diffusion in acceptor doped BaCeO<sub>3</sub>: A single crystal analysis. *Solid State Ionics* **1996**, *86*, 613-620.
65. Larring, Y.; Norby, T., Protons in rare earth oxides. *Solid State Ionics* **1995**, *77*, 147-151.
66. Kreuer, K., Aspects of the formation and mobility of protonic charge carriers and the stability of perovskite-type oxides. *Solid State Ionics* **1999**, *125* (1-4), 285-302.
67. Norby, T.; Widerøe, M.; Glöckner, R.; Larring, Y., Hydrogen in oxides. *Dalton transactions* **2004**, (19), 3012-3018.
68. Münch, W.; Kreuer, K.-D.; Seifertli, G.; Majer, J., A quantum molecular dynamics study of proton diffusion in SrTiO<sub>3</sub> and CaTiO<sub>3</sub>. *Solid State Ionics* **1999**, *125* (1-4), 39-45.
69. Münch, W.; Kreuer, K.-D.; Seifert, G.; Maier, J., Proton diffusion in perovskites: comparison between BaCeO<sub>3</sub>, BaZrO<sub>3</sub>, SrTiO<sub>3</sub>, and CaTiO<sub>3</sub> using quantum molecular dynamics. *Solid State Ionics* **2000**, *136*, 183-189.
70. Münch, W.; Kreuer, K.; Adams, S.; Seifert, G.; Maier, J., The relation between crystal structure and the formation and mobility of protonic charge carriers in perovskite-type oxides: A case study of Y-doped BaCeO<sub>3</sub> and SrCeO<sub>3</sub>. *Phase Transitions* **1999**, *68* (3), 567-586.
71. Kreuer, K.-D.; Münch, W.; Fuchs, A.; Klock, U.; Maier, J., Proton conducting alkaline earth zirconates and titanates for high drain electrochemical applications. *Solid State Ionics* **2001**, *145* (1-4), 295-306.
72. Kreuer, K.; Münch, W.; Ise, M.; He, T.; Fuchs, A., Defect interactions in proton

conducting perovskite-type oxides. *Berichte der Bunsen-Gesellschaft* **1997**, *101* (9), 1344-1350.

73. Karmonik, C.; Udovic, T.; Paul, R.; Rush, J.; Lind, K.; Hempelmann, R., Observation of dopant effects on hydrogen modes in  $\text{SrCe}_{0.95}\text{M}_{0.05}\text{H}_x\text{O}_{3-\delta}$  by neutron vibrational spectroscopy. *Solid State Ionics* **1998**, *109* (3-4), 207-211.

74. Hempelmann, R.; Soetratmo, M.; Hartmann, O.; Wäppling, R., Muon diffusion and trapping in proton conducting oxides. *Solid State Ionics* **1998**, *107* (3-4), 269-280.

75. Scherban, T.; Nowick, A., Bulk protonic conduction in Yb-doped  $\text{SrCeO}_3$ . *Solid State Ionics* **1989**, *35* (1-2), 189-194.

76. Davies, R.; Islam, M.; Gale, J., Dopant and proton incorporation in perovskite-type zirconates. *Solid State Ionics* **1999**, *126* (3-4), 323-335.

77. Neagu, D.; Tsekouras, G.; Miller, D. N.; Menard, H.; Irvine, J. T., In situ growth of nanoparticles through control of non-stoichiometry. *Nature Chemistry* **2013**, *5* (11), 916-923.

78. Nishihata, Y.; Mizuki, J.; Tanaka, H.; Uenishi, M.; Kimura, M., Self-regeneration of palladium-perovskite catalysts in modern automobiles. *Journal of Physics and Chemistry of Solids* **2005**, *66* (2-4), 274-282.

79. Bierschenk, D. M.; Potter-Nelson, E.; Hoel, C.; Liao, Y.; Marks, L.; Poepelmeier, K. R.; Barnett, S. A., Pd-substituted  $(\text{La},\text{Sr})\text{CrO}_{3-\delta}-\text{Ce}_{0.9}\text{Gd}_{0.1}\text{O}_{2-\delta}$  solid oxide fuel cell anodes exhibiting regenerative behavior. *Journal of Power Sources* **2011**, *196* (6), 3089-3094.

80. Jardiel, T.; Caldes, M. T.; Moser, F.; Hamon, J.; Gauthier, G.; Joubert, O., New SOFC electrode materials: The Ni-substituted LSCM-based compounds  $(\text{La}_{0.75}\text{Sr}_{0.25})(\text{Cr}_{0.5}\text{Mn}_{0.5-x}\text{Ni}_x)\text{O}_{3-\delta}$  and  $(\text{La}_{0.75}\text{Sr}_{0.25})(\text{Cr}_{0.5-x}\text{Ni}_x\text{Mn}_{0.5})\text{O}_{3-\delta}$ . *Solid State Ionics* **2010**, *181* (19-20), 894-901.

81. Kobsiriphat, W.; Madsen, B. D.; Wang, Y.; Marks, L. D.; Barnett, S. A.,  $\text{La}_{0.8}\text{Sr}_{0.2}\text{Cr}_{1-x}\text{Ru}_x\text{O}_{3-\delta}-\text{Gd}_{0.1}\text{Ce}_{0.9}\text{O}_{1.95}$  solid oxide fuel cell anodes: Ru precipitation and electrochemical performance. *Solid State Ionics* **2009**, *180* (2-3), 257-264.

82. Kobsiriphat, W.; Madsen, B. D.; Wang, Y.; Shah, M.; Marks, L. D.; Barnett, S. A., Nickel- and Ruthenium-Doped Lanthanum Chromite Anodes: Effects of Nanoscale Metal Precipitation on Solid Oxide Fuel Cell Performance. *Journal of The Electrochemical Society* **2010**, *157* (2), B279-B284.

83. Tanaka, H.; Taniguchi, M.; Uenishi, M.; Kajita, N.; Tan, I.; Nishihata, Y.; Mizuki, J.; Narita, K.; Kimura, M.; Kaneko, K., Self-regenerating Rh- and Pt-based perovskite catalysts for automotive-emissions control. *Angewandte Chemie International Edition* **2006**, *45* (36), 5998-6002.

84. Tanaka, H.; Uenishi, M.; Taniguchi, M.; Tan, I.; Narita, K.; Kimura, M.; Kaneko, K.; Nishihata, Y.; Mizuki, J., The intelligent catalyst having the self-regenerative function of Pd, Rh and Pt for automotive emissions control. *Catalysis Today* **2006**, *117* (1-3), 321-328.

85. Liu, C. Y.; Bard, A. J., Pressure-induced insulator conductor transition in a photoconducting organic liquid-crystal film. *Nature* **2002**, *418* (6894), 162-164.

86. Neagu, D. Materials and microstructures for high temperature electrochemical devices through control of perovskite defect chemistry. University of St Andrews, 2013.

87. Szot, K.; Speier, W., Surfaces of reduced and oxidized SrTiO<sub>3</sub> from atomic force microscopy. *Physical Review B* **1999**, *60* (8), 5909.

88. Kobsiriphat, W.; Madsen, B.; Wang, Y.; Shah, M.; Marks, L.; Barnett, S., Nickel-and ruthenium-doped lanthanum chromite anodes: effects of nanoscale metal precipitation on solid oxide fuel cell performance. *Journal of The Electrochemical Society* **2009**, *157* (2), B279-B284.

89. Neagu, D.; Oh, T. S.; Miller, D. N.; Menard, H.; Bukhari, S. M.; Gamble, S. R.; Gorte, R. J.; Vohs, J. M.; Irvine, J. T., Nano-socketed nickel particles with enhanced coking resistance grown in situ by redox exsolution. *Nature Communications* **2015**, *6*(1), 1-8.

90. Irvine, J. T. S.; Neagu, D.; Verbraeken, M. C.; Chatzichristodoulou, C.; Graves, C.; Mogensen, M. B., Evolution of the electrochemical interface in high-temperature fuel cells and electrolyzers. *Nature Energy* **2016**, *1* (1), 1-13.

91. Konyshva, E. Y.; Xu, X.; Irvine, J. T., On the existence of A-site deficiency in perovskites and its relation to the electrochemical performance. *Advanced Materials* **2012**, *24* (4), 528-532.
92. Shannon, R., Shannon RD & Prewitt C T. Effective ionic radii in oxides and fluorides. *Acta Crystallographica Section B: Structural Crystallography and Crystal Chemistry* **1969**, *25*(5), 925-946.
93. Nevr, M.; Pollert, E.; Mate, L.; Tr, A., Phase diagram of the pseudobinary BaCuO<sub>2</sub>-YBa<sub>2</sub>Cu<sub>3</sub>O<sub>6.5</sub>-YCuO<sub>2.5</sub> system. *Physica C: Superconductivity* **1988**, *153*, 377-378.
94. Roth, R.; Davis, K.; Dennis, a. R., Phase equilibria and crystal chemistry in the system Ba-Y-Cu-O. *Advanced Ceramic Materials* **1987**, *2* (3B), 303-312.
95. Nevřiva, M.; Pollert, E.; Matějková, L.; Tríska, A., On the determination of the CuO-BaCuO<sub>2</sub> and CuO-YCuO<sub>2.5</sub> binary phase diagrams. *Journal of Crystal Growth* **1988**, *91* (3), 434-438.
96. Zhang, W.; Osamura, K.; Ochiai, S., Phase Diagram of the BaO-CuO Binary System. *Journal of the American Ceramic Society* **1990**, *73* (7), 1958-1964.
97. Zimmermann, E.; Hack, K.; Mohammad, A.; Boudéne, A.; Neuschütz, D., Experimental investigation and thermochemical assessment of the system Ba-Cu-O. *Calphad* **1995**, *19* (2), 179-188.
98. Lay, K. W.; Renlund, G. M., Oxygen pressure effect on the Y<sub>2</sub>O<sub>3</sub>-BaO-CuO liquidus. *Journal of the American Ceramic Society* **1990**, *73* (5), 1208-1213.
99. Lee, B. J.; Lee, D. N., Thermodynamic evaluation for the Y<sub>2</sub>O<sub>3</sub>-BaO-CuO<sub>x</sub> system. *Journal of the American Ceramic Society* **1991**, *74* (1), 78-84.
100. Voronin, G.; Degterov, S., Solid state equilibria in the Ba-Cu-O system. *Journal of Solid State Chemistry* **1994**, *110* (1), 50-57.
101. Lander, J., The Phase System BaO-NiO. *Journal of the American Chemical Society* **1951**, *73* (6), 2450-2452.

## 2 Experimental

### 2.1 Sample preparation

#### 2.1.1 Solid state synthesis

BCZY materials with different dopants were prepared via solid state synthesis in this study. The following describes the preparation process taking Cu dopant for example.

1) Powder drying. BaCO<sub>3</sub>, CeO<sub>2</sub>, ZrO<sub>2</sub> and Y<sub>2</sub>O<sub>3</sub> powders were dried in air at 300 °C for 2 h to remove absorbed H<sub>2</sub>O and CO<sub>2</sub>.

2) Powder weighing. Remove the dried powders from the furnace at 300 °C and weigh the chemicals immediately according to the stoichiometry.

3) Powder mixing. Starting materials were dispersed in acetone medium and mixed by an ultrasonic probe (Herslcher UP200S) to break down agglomerates. After that, the acetone was then evaporated under continuous stirring to obtain the dry powder.

4) Pre-calcination. The dried mixture was transferred into a crucible and then calcined at 1000 °C for 12 h in air in a muffle furnace, with a ramping rate of 5 °C /min.

5) Powder mixing. The pre-calcined oxides were mixed with CuO (e.g., 4 mol%) dopants by the ultrasonic probe in acetone media and then dried in air.

6) Pellet pressing. About 2.5 g powder was put into a steel die ( $\phi=2.3$  cm) and pressed under a pressure of 1 ton holding for 20 s.

7) Pellet sintering. The pressed pellet was transferred on an alumina plate and sintered at 1350 °C for 12 h in air with a ramping rate of 5 °C/min. A layer of powder was applied as a buffer layer between the alumina plate and pellet to avoid the reaction between them.

For the preparation of Ni, (Ni, Cu) and Zn doped BCZY, the sintering procedure is the same, using specific precursors of desired transition metal dopants.

#### 2.1.2 Exsolution

Exsolution was achieved by the reduction of samples in tubular furnace supplied

with dry 5% H<sub>2</sub>/Ar (25 ml/min). The reduction temperature varied between 500 – 900 °C for 12 h with a ramping rate of 5 °C /min.

### **2.1.3 Tape casting**

#### 2.1.3.1 A brief overview of tape casting

Tape casting is a well-known technique in the fabrication of thin and flat ceramic films with large area and controlled thickness. The flexibility of the unfired tapes allows them to be either punched with holes or cut into various shapes. Lamination of the green tapes can produce a multi-layer ceramic, which is quite effective for preparing a thick electrode or electrolyte component or the co-firing of the two components. For the electrode tape, in order to achieve a porous structure after sintering, pore formers are needed in the preparation of tape slurry. The pores can be created by reducing the sintering temperature or removal of added pore formers, either by heat treatment or leaching.

In the preparation of the typical tape slurry, the ceramic powders are first dispersed in a solvent to produce a well-dispersed suspension. After that, in order to enhance the plasticity of the slurry for casting into a tape, some plasticizers are used to incorporate with the binder that added in the following step to create the cohesion between the ceramic particles. In addition. After a complete mixing and removing the small bubbles, the slurry is cast into a tape, followed by drying in air for a few hours. The solvent can be an organic system or water and in the case of the latter the system is more complicated by the existence of specific problems such as the limitation of binders/plasticisers available or drying problems.

#### 2.1.3.2 Slurry preparation.

The powder used for slurry preparation was obtained either from grinding the sintered pellet or the mixture of pre-calcined BCZY powder with dopants. The powder was ground in an agate mortar, followed by 500 rpm ball milling for 20 min and 800 rpm ball milling for another 20 min in propanol medium. Here, water-based system and organic-based system were both tried to obtain a dense electrolyte tape and at the same time a porous electrode tape. In the first stage of slurry preparation, the ceramic powder

was mixed with dispersant (Hypermer KD6-LQ-(MV)) and solvent (de-ionised water in the water-based system or binary organic solvent MEK/ethanol in the organic-based system), forming a well-dispersed suspension. The mixture was then subjected to ball milling using 18 zirconia balls ( $\phi=8.8$  mm) under the speed of 160 rpm for 18 h. For porous electrode slurry, pore former in the form of graphite, spherical particles of PMMA or starch was added with ceramic powder in this step. In the second stage, binder (Polyvinyl alcohol, PVA, 15 wt%) was used to ensure the good cohesion of the entire chemical system. In order to improve the plasticity of the slurry, plasticizers (Glycerol and Poly(ethylene glycol)) were added into the dispersed mixture. Because of the formation of foam during ball milling, defoamer 2,4,7,9-tetramethyl-S was also added to the system to produce a homogeneous suspension. After adding all the organics, another ball milling under 100 rpm for 4 h was required to ensure sufficient mixing. For dense electrolyte slurry, ball milling with a low speed of 26 rpm was needed for 18 h for de-aeration. The electrolyte and electrode tape formulations in the water-based and organic-based system are shown in Table 2.1-2.3.

Table 2.1 Formulations of green tapes in a water-based system.

Compositions			Formulations (g)	
			Electrolyte	Electrode
<b>Powder</b>			18	8.7768
<b>Stage 1</b> <b>(18h, 160rpm)</b>	Pore former	PMMA		1.7554
	Dispersant	KD 6	0.54	0.54
	Solvent	DI water	8	8
<b>Stage 2</b> <b>(4h, 100rpm)</b>	Plasticizer	PEG	1.08	1.08
		Glycerol	2.16	2.16
	Binder	PVA (15 wt%)	12	12
	Defoamer	2, 4, 7, 9 – Tetraethyl	0.3	0.3

For the tape prepared in the organic solvent, its slurry formulation can be seen in Table 2.2 (electrolyte) and Table 2-3 (optimized electrode tape by adjusting the

proportion of the chemicals).

Table 2.2 Formulations of green electrolyte tapes in an organic solvent system.

Compositions		Formulations (g)
Powder	BCZY+ZnO	30.6
Solvent	MEK/ethanol	14.5
Dispersant	Triton	0.195
Plasticizer	PEG	2.43
	DBP	2.19
Binder	BUTVAR	3.37

Table 2.3 Optimized formulations of green electrode tapes in an organic solvent system.

Compositons		Formulations (g)		
		Electrode 1	Electrode 2	Electrode 3
Powder	BCZY+ZnO	8.5	8.5	8.5
Pore former	Graphite	5.355 (67.3%)	6.9615 (72.8%)	3.477
	Starch	-	-	2.745
Solvent	MEK/ethanol	10.15	15.225	15.225
Plasticizer	PEG	1.701	2.552	2.552
	DBP	1.531	2.296	2.296
Binder	BUTVAR	2.355	3.533	3.533

### 2.1.3.3 Tape casting process

A TTC-1000 (Richard E Mistler Inc) tape caster was used for casting. As shown in Figure 2-1, for a casting process, the doctor blade was adjusted accordingly to leave a gap between the carrier film and blade. Then the prepared slurry was poured into the reservoir. When the carrier film was moving, the slurry was cast into a tape. Moving speed was set at 4 cm/s. After casting, the tape was left in air to dry for about 4 h.



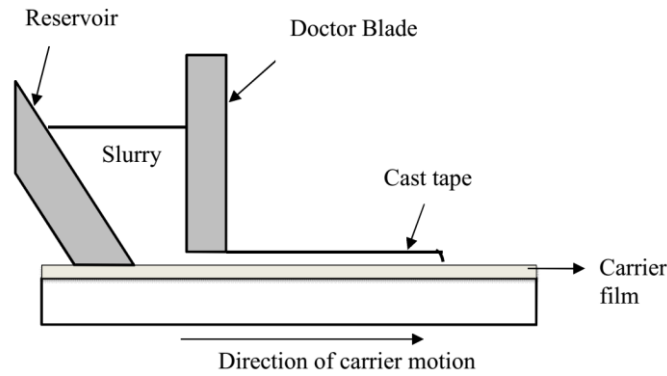


Figure 2-1 Tape casting process.

#### 2.1.3.4 Lamination of green tapes

A thin electrolyte can decrease ohmic resistance to improve electrochemical performance, but it is at the cost of lowering cell's mechanical strength. In this study, the obtained thickness of electrolyte is less than 20  $\mu\text{m}$ , which is quite fragile and has a serious curling edge after sintering. Therefore, the electrode layer needs to be thick enough to provide mechanical strength for the cell. Usually, the green tape surface was dried out and hard to stick together with another tape at room temperature, so during the lamination process, a household iron was applied to heat the tape at  $\sim 50\text{ }^{\circ}\text{C}$  during pressing, to ensure the good adhesion between tapes. Meanwhile, a hand-rubber roller was used to remove the bubbles between tape layers. In most cases, one layer of the porous electrode is about 70  $\mu\text{m}$ , so two layers of porous electrode will be firstly laminated together and then one layer of dense electrolyte is laminated on it. Finally, another three layers of porous tape will be laminated with the previous one to form a sandwich structure with the dense electrolyte being in the middle. In this way, the sintered cell would exhibit sufficient mechanical stability.

#### 2.1.3.5 Sintering temperature program

In order to ensure a high density of the electrolyte and prevent separation between tapes, a sintering program was carried out as in Figure 2-2. Water evaporated before  $270\text{ }^{\circ}\text{C}$ , together with some organic constituents in the tape. Organic additives burnt out completely at  $800\text{ }^{\circ}\text{C}$  using a low heating rate of  $1\text{ }^{\circ}\text{C}/\text{min}$  to avoid edge curling of the tapes. After that, the tape continued to be heated up to the sintering temperature with a

heating rate of 2 °C /min and held for several hours to obtain high density. After high temperature sintering, the temperature was cooled down to room temperature with a slow rate of 2 °C /min.

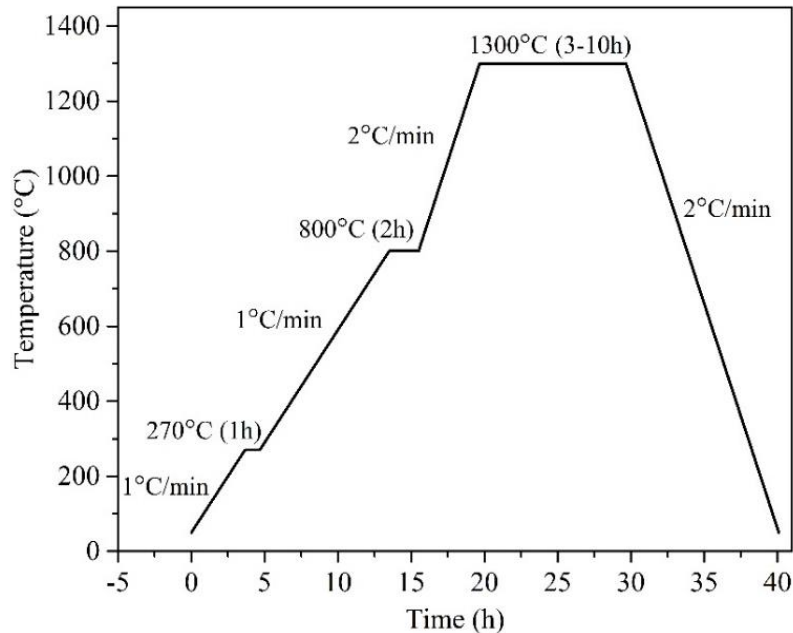


Figure 2-2. Sintering temperature program of laminated tapes.

## 2.1.4 Preparation of solid oxide cell

### 2.1.4.1 Coated electrode scaffold

Apart from the cell being fabricated by lamination of electrolyte and electrode tapes, the porous electrode scaffolds (anode and cathode) are also prepared by a coating technique. As the sintered BCZYZ electrolyte tape is not perfectly flat, enough to coat electrode ink by a screen-printing machine, the electrodes are coated onto the electrolyte using the following procedure in Figure 2-3. A plastic tape having a hole of 6 mm in diameter was attached to the centre of the sintered electrolyte tape, making the hole to be at the centre position of the electrolyte and acting as a mask. The exposed electrolyte area was thus used to coat electrode on top. The electrode ink is made by mixing 80 % electrode powder with 20 % Terpeneol. A toothpick was dipped with some electrode ink and rolled over the exposed electrolyte surface slowly, and a layer of electrode materials with a thickness same as the plastic tape was then applied onto the

electrolyte centre. This rolling process can repeat for a few times until the film was uniform. Afterwards, the electrolyte coated with an electrode was transferred in an oven for drying at 80 °C for 1 h. The plastic tape was then peeled off gently, leaving a layer of electrode with diameter of 6 mm at electrolyte centre. The preparation of the electrode on the other side was the same. The cell was sintered at 1200 - 1350 °C to form an electrode structure and make good contact between the components.

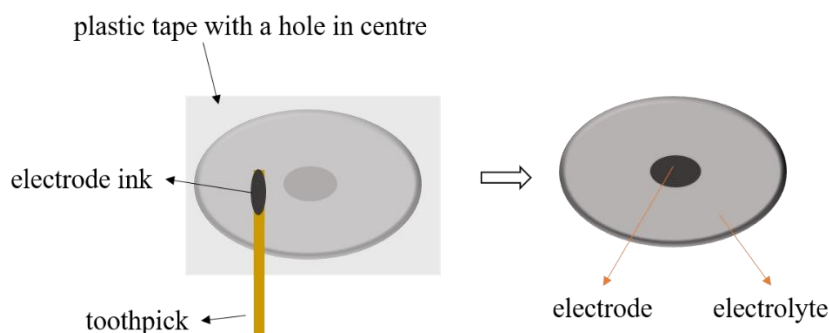


Figure 2-3. Schematic of screen printing by hand.

#### 2.1.4.2 Impregnation of electrode materials

The porous scaffolds of BCZYF were used to further impregnate catalytically active materials that will serve as electrodes. Impregnation solution of the electrode materials was prepared by dissolving the nitrates of electrode precursor in absolute ethanol, e.g.  $\text{La}(\text{NO}_3)_3 \cdot 6\text{H}_2\text{O}$ ,  $\text{Sr}(\text{NO}_3)_2$ ,  $\text{Co}(\text{NO}_3)_2 \cdot 6\text{H}_2\text{O}$  and  $\text{Fe}(\text{NO}_3)_3 \cdot 9\text{H}_2\text{O}$  for  $\text{La}_{0.6}\text{Sr}_{0.4}\text{Co}_{0.2}\text{Fe}_{0.8}\text{O}_3$  (LSCF) anode material and  $\text{Ni}(\text{NO}_3)_2 \cdot 6\text{H}_2\text{O}$  for Ni cathode material in SOEC. The ethanol provides a lower surface tension and more rapid evaporation than water solution. In the preparation of LSCF precursor solution,  $\text{Sr}(\text{NO}_3)_2$  was found to be difficult in dissolving in ethanol, and it was firstly dispersed in ethanediol and then mixed with ethanol dissolved  $\text{La}^{3+}$ ,  $\text{Co}^{2+}$  and  $\text{Fe}^{3+}$  solution. The concentration of LSCF and Ni precursor was 0.5 M and 1 M, respectively. Although a solution of higher concentration may reduce the repeating time for impregnation, it tends to produce agglomerated particles which are likely to deposit on the near-surface of the porous scaffold and block the subsequent solution or even gas diffusion to the inner area of the electrode. It is important to ensure the uniform distribution of the metal

precursor solution on the electrode-electrolyte interface where the electrochemical reactions occur predominantly. The precursor solution was introduced drop-wise onto the porous electrode support using a 1 ml capacity syringe fitted with a needle and dried in an oven at 80 °C for 10 mins. This process was repeated for 2-3 times until the substrate was saturated. Then the impregnated cell was calcined at 800 °C (LSCF) and 650 °C (NiO) for 1 h for the nitrate decomposition and phase formation. The impregnation and calcination processes were repeated for 5-8 times until achieving desired solid loading.

#### 2.1.4.3 Electrochemical test

Silver paste was coated on both electrode sides as a current collector. The cell was sealed by Aremco Ceramabond™ in a home-made testing jig. A reducing atmosphere of hydrogen was applied at the Ni electrode side to reduce the impregnated NiO to Ni metal catalysts at 600 °C for 5 h.

## 2.2 Characterization methods and techniques

### 2.2.1 Powder X-ray diffraction

X-ray diffraction method is widely applied for the material characterisation to analyse crystallographic structure and crystalline phases on an atomic scale. In a crystalline structure, the atoms are arranged regularly in a repeating pattern built up from the smallest unit called unit cell. The array of atoms results in the formation of parallel planes, which are in various orientations and directions with an interplanar distance  $d$ . When a beam of incident X-rays of a certain wavelength strikes these lattice planes, the radiation is scattered due to the interaction with atoms along certain direction and forms a diffraction pattern. When Bragg's law (Eq. 2-1) is satisfied, a set of reflection beams will interfere constructively. Figure 2-4 shows the schematic diagram of Bragg's law. When two incident rays strike on the lattice plane with an angle  $\theta$ , beam bb' travels extra distance  $2d \sin \theta$  (an integral number of wavelengths,  $n\lambda$ ) than beam aa' does. In this case, constructive interference will occur.

$$2d \sin \theta = n \lambda \quad \text{Eq. 2-1}$$

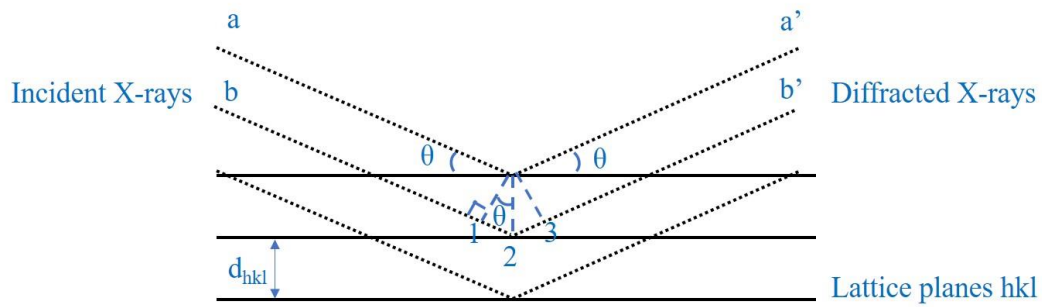


Figure 2-4. Schematic diagram of Bragg's law

Room temperature powder X-ray diffraction patterns were collected on a PANalytical X-ray diffractometer operating with  $\text{CuK}\alpha$  radiation ( $\lambda = 1.5406 \text{ \AA}$ ). The range of  $2\theta$  is  $10\text{-}90^\circ$ . Sintered pellet specimen is ground into powder using agate pestle and mortar, then transferred to a metallic sample disk. A piece of glass is used to press the powder gently and make the powder disk to be at the same plane as the metallic disk. The XRD patterns give the specimen information on phases, structure, and preferred crystal orientations, et. al.

Variable temperature X-ray diffraction (VT-XRD) provides the diffraction peaks under certain temperature and atmosphere, which is very useful for *in situ* monitoring crystal structures and phase transitions as a function of temperature. The VT-XRD characterisation was carried out on a PANalytical Empyrean operating with  $\text{Mo K}\alpha 1$  and  $\text{K}\alpha 2$  radiation. The XRD patterns were collected from a polished pellet from room temperature to  $900^\circ\text{C}$  in  $5\% \text{ H}_2/\text{N}_2$  atmosphere.

### 2.2.2 Scanning electron microscopy

Scanning electron microscopy (SEM)<sup>1</sup> is a very useful characterization technique to provide information about the samples, such as microscopic texture, surface topography, compositions and fracture features of materials. In order to obtain a good microstructure photo from SEM, the samples should be ensured to be conductive. Gold-coating method always be used for providing a conductive surface for the non-conducting materials. In an operating process, electron beams with high energy are generated from an electron gun and interact with the sample surface, emitting several

types of signals. Figure 2-5 presents the various signals that produced from sample-electron beam interaction, which carry the different information of the sample. The grey rectangular is the sample and the blue water drop is the area affected by the electron beam. The signals are emitted from the different parts of the affected area. For example, Auger electrons and secondary electrons (SE) provide information about sample surface and backscattered electrons (BSE) are generated from deeper area. In the even deeper position, characteristic X-ray is produced. These signals are collected by one or more detectors to form images that can be displayed on the computer screen. Generally, the deep and large-affected area gives rise to a low resolution. When the specimen is ultrathin ( $<100$  nm) and the electron beam is very strong, electrons can be transmitted through the solid specimen and different signals can be captured, which are often used in transmission electron microscopy (TEM) characterization.

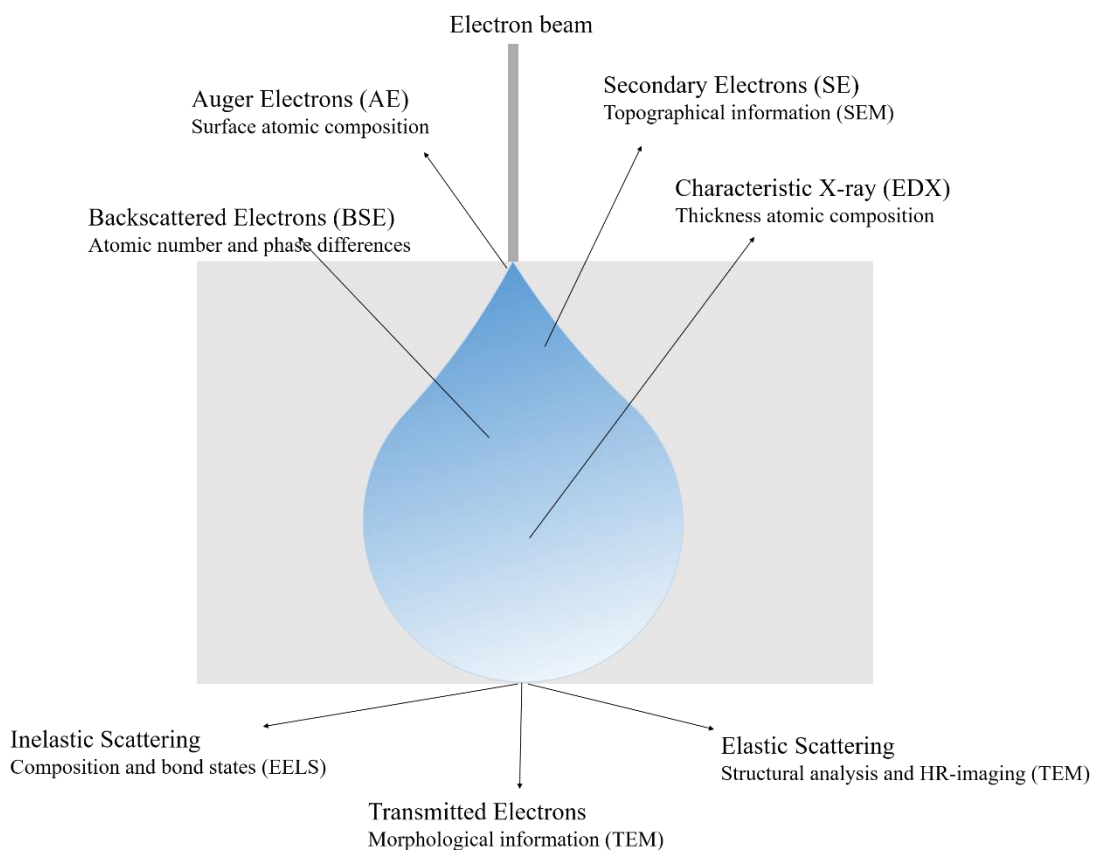


Figure 2-5. Schematic of varied signals emitted from different parts of solid specimen by electron beam.

The main functions of the microscope used in this thesis are introduced in the following.

(1) Secondary electrons (SE). When the electron beam is incident on the surface of the specimen, electrons from the outer shell can be excited, producing free electrons. If the energy of free electrons is large enough to escape from the material, they will become the secondary electrons, which can be detected by a secondary electron detector. The number of the detected secondary electrons, known as the signal intensity, depend on the specimen topography and thus the surface morphology of specimen can be provided.

SE images were recorded on a JSM-6700F Field Emission Gun (FEG) microscope and FEI Scios DualBeam microscope. Both microscopes were operated at an accelerating voltage of 5 kV and working distance of 7 mm.

(2) Back scattered electrons (BSE) are used to detect contrast between areas with different phase or chemical compositions. They are a result of elastic collisions of high-energy electrons with the specimen. Since heavy elements (with a greater atomic number,  $z$ ) backscatter electrons more strongly than light elements, they will produce a higher signal to the detector, shown as a brighter area in the image. Thus, the number of backscattered electrons reaching the detector is proportional to the  $z$  number of samples.

BSE images were recorded on a FEI Scios DualBeam microscope with an in-lens BSE detector.

(3) Energy-dispersive X-ray spectroscopy (EDX). Relying on characteristic X-ray, EDX is widely used to analyse element compositions and distribution in a sample. For the generating of the characteristic X-ray, an incident electron beam with high energy hits the specimen surface, stimulating an electron in an inner shell. Then the electron is ejected from the shell and an electron hole is thus created. In this case, an electron from an outer shell with high energy will fill the hole, and the different energy of the two shells may be released in the form of X-ray. The emitted X-ray can be measured by an energy-dispersive spectrometer. In addition, since the energy level is quantized, the wavelength of X-ray is specified. By detecting characteristic X-ray counts of the

specimen, the qualitative and semi-quantitative properties of elements can be determined.

EDS analysis was carried out on a FEI Scios DualBeam microscope with an EDS analysis system under an accelerating voltage of 20 kV.

In the microscope chamber, there are different detectors to collect various signals, such as the Everhart-Thornley Detector (ETD), the Through-the-lens Detector (TLD), backscatter electrons detector and X-ray detectors, etc. Among these detectors, ETD and TLD primarily collect secondary electrons that carry the topographical information of the sample surface. However, some backscattered electrons and electrons from collision with the chamber wall are also detected by ETD positioned to one side of the SEM column (Figure 2-6) and shows directional shadowing, while the eliminated contributions from these electrons can be done by immersion lens and the Through-the-lens detector which is located inside the column and thus shows non-directional shadowing. The TLD efficiently collects second electrons signal and provides a high contrast of sample's topography.

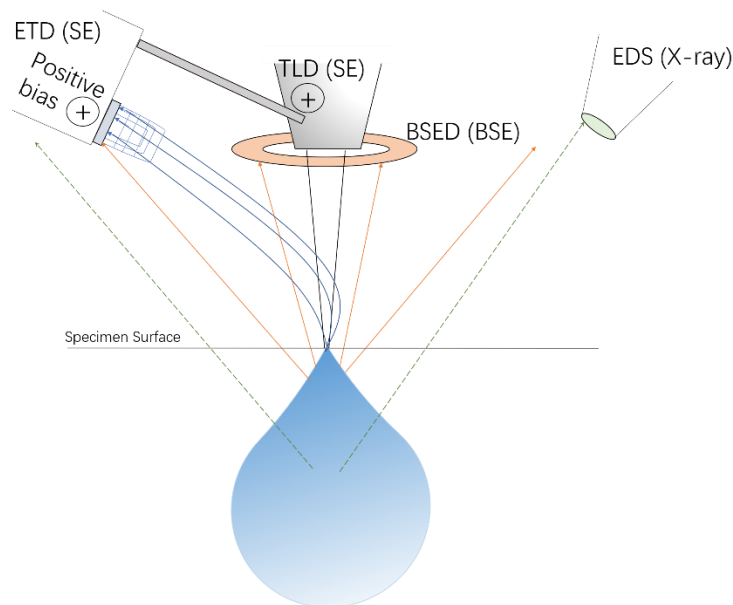


Figure 2-6. Various detectors for collecting signals.



### 2.2.3 Transmission electron microscopy

As illustrated in Figure 2-5, TEM information was collected from the transmitted electron through an ultrathin solid film. Generally, TEM provides two methods for sample observation, image mode and diffraction mode. The two modes are presented in Figure 2-7. The operating principle of the two modes can be described as follows. An electron beam is generated from the electron gun and is focused by the condenser lenses. When the electron beam hits onto the specimen, it can interact with the specimen and pass through it. The transmitted and diffracted electrons are then recombined and focused by the objective lens, forming a diffraction pattern and an intermediate image at the back focal plane. The beam then diverges and is focused by the projector lens to produce the final image. The displaying of an image or an electron diffraction pattern is determined by choosing images from the image plane or the back focal plane.

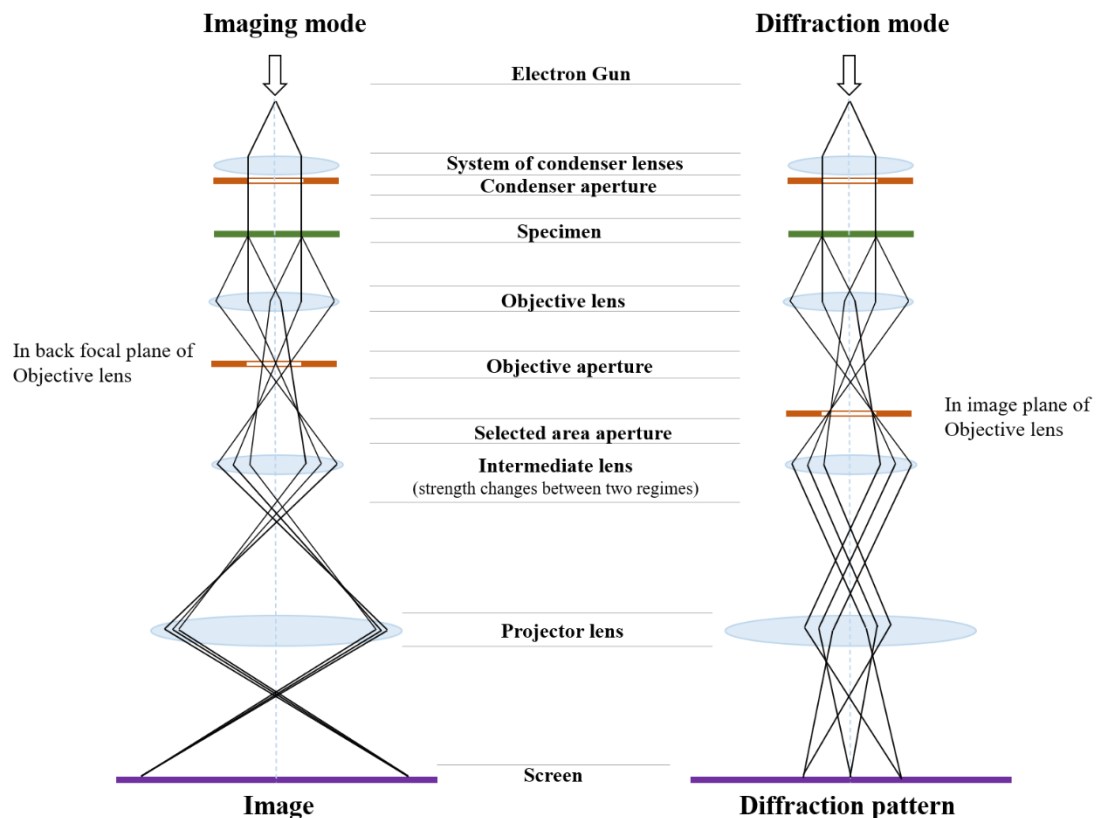


Figure 2-7. Schematic view of imaging and diffraction modes in TEM.

Within the conventional TEM imaging, the contrast at lower magnification arises from different adsorption of electrons by the material due to variations in compositions or thickness of the specimen. Under higher magnification (high-resolution transmission electron microscopy, HRTEM), the intensity of the image is given from complex wave interaction that results from chemical identity, crystal orientation and electronic structure.

Selected area electron diffraction pattern (SAED) can be obtained on the fluorescent screen under the diffraction mode. The pattern is entirely equivalent to the X-ray diffraction pattern: a single crystal produces a pattern of dots and a polycrystalline will give a powder or ring pattern. For the single crystal case, the diffraction pattern can provide information on the space group symmetry and orientation of the specimen.

Scanning transmission electron microscopy (STEM) is a conventional TEM equipped with additional scanning coils, detectors and necessary circuitry. Unlike conventional TEM, STEM is modified by a system that transfers a convergent beam across the sample, making STEM suitable for some analytical techniques such as electron energy loss spectroscopy (EELS), Z-contrast annular dark field imaging (ADF) and EDX spectroscopic mapping.

The series of TEM/STEM characterization were carried out on an FEI Titan Themis, operated at 200 kV and equipped with a Bruker SuperX EDX detector, a CEOS DCOR Cs probe corrector and a Gatan Enfium EEL spectrometer. For the STEM measurements, a probe current of ~100 pA is generally used for imaging or ~300 pA for EDX mapping and a 21 mrad convergence angle. For HAADF images, the inner/outer collection angles are 56.3 and 200 mrad, respectively.

#### **2.2.4 TEM sample preparation via focus ion beam**

When a single nanoparticle socketed on the surface of a ceramic grain needs to be investigated by TEM, the TEM sample was prepared by focused ion beam (FIB), operated on Scios DualBeam microscopy. Protective carbon and platinum layers were firstly deposited onto the selected area to prevent damage from cutting by Ga<sup>2+</sup> ion

beam. Besides the protective area, two rectangle holes were dug to allow the protected sample to be cut off afterwards and picked up by a tungsten needle. The sample slide was then melted onto the TEM grid and finely polished to less than 100 nm in thickness step-by-step using  $\text{Ga}^{2+}$  focused ion beam.

### 2.2.5 X-ray photoelectron spectroscopy

X-ray photoelectron spectroscopy (XPS) is a surface-sensitive quantitative spectroscopic technique that can identify element composition, chemical state and electronic structure in the material. It operates by irradiating a specimen with a beam of X-rays in ultra-high vacuum condition. Simultaneously, electrons that escape from the material surface is measured with regard to their kinetic energy and population. The information from the specimen surface layer up to 10 nm can be detected by XPS.

Here, XPS measurements were carried out using a Kratos Axis Ultra-DLD photoelectron spectrometer and the data were analysed by CasaXPS software.

### 2.2.6 Dilatometry analysis

Dilatometry test is used to analyse the shrinking behaviour of samples. It records the linear dimensional change  $\Delta L/L_0$  of a ceramic as a function of temperature while it is subjected to a controlled temperature procedure. The schematic diagram of the dilatometer is shown in Figure 2-8. During the measurement, pushrod movement resulting from the length change of the sample is detected by a linear variable displacement transducer, producing an electrical signal which is then transmitted to the analogue-to-digital converter in the Thermal Analysis (TA) system controller.

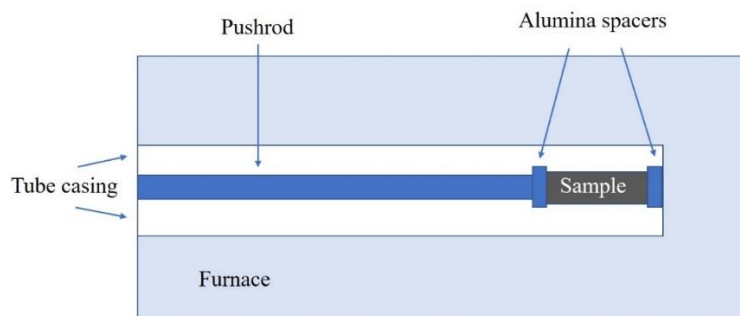


Figure 2-8 Schematic diagram of dilatometer.

Dilatometry tests were carried out on Netzch dilatometer Dil 420C. Pellets were used to take the test with a diameter of 1.3 cm and a thickness of 2 mm in air atmosphere with a ramping rate of 5 °C /min.

### **2.2.7 Thermogravimetry analysis**

Thermogravimetry analysis (TGA) is a technique for measuring the change in mass loss of a substance as a function of temperature or time. The sample is heated at a constant rate and its mass is recorded continuously. The mass change will occur when there is physical adsorption/desorption of volatile components, phase transitions or chemical decomposition at a certain temperature. The plot of mass against temperature depends on variables such as heating rate, nature of the sample and atmosphere being used.

Thermogravimetric was carried out on a Netzch STA 449C Jupiter thermal analyser in 5% H<sub>2</sub>/Ar with temperature ramping rate of 5 °C/min.

### **2.2.8 AC impedance spectroscopy**

AC impedance spectroscopy<sup>2-4</sup> is a powerful technique for characterizing the electrical properties of ceramic materials. It is advantageous in that the measurement can be implemented using arbitrary electrodes and most importantly, resistances from bulk, grain boundary and electrode contributions can be separated. Moreover, when the impedance results are obtained from an electrolyte material, the ionic conductivity property of the grain and grain boundary can be achieved.

Ohm's law states that the current  $I$  flowing in a circuit is proportional to the applied voltage difference  $V$  and the constant of the proportionality is defined as resistance  $R$ :

$$R = \frac{V}{I} \quad \text{Eq. 2-2}$$

However, this relationship can only be used in a circuit containing the ideal resistor. In the real circuits, more complex behaviour would occur, which require a more general circuit parameter, impedance, to express the relationship between potential and current.

Impedance ( $Z$ ) is generally defined as the total opposition to the alternating current (AC) at a given frequency in a device, and it is expressed by a complex quantity which

is graphically shown on a vector plane. An impedance vector consists of two components, a real part (resistance R) and an imaginary part (reactance X). If  $X > 0$ , the reactance is defined to be inductive. If  $X = 0$ , the impedance is purely resistive. If  $X < 0$ , the reactance is capacitive.

The impedance is measured by applying a small sinusoidal voltage perturbation to the cell that is given as:

$$V(t) = V_0 \sin(\omega t) \quad \text{Eq. 2-3}$$

where,  $V(t)$  is the instantaneous voltage,  $V_0$  is the maximum amplitude of the signal,  $\omega$  is the angular frequency,  $t$  is time. The resulted current is thus also a sinusoid with the same frequency but shifted in phase:

$$I(t) = I_0 \sin(\omega t + \varphi) \quad \text{Eq. 2-4}$$

where  $I_0$  is the maximum amplitude of the signal,  $\varphi$  is the phase shift in radians and equals to 0 for purely resistive behaviour. The relationship between  $\omega$  and frequency ( $\nu$ ) is expressed as:

$$\omega = 2 \pi \nu \quad \text{Eq. 2-5}$$

Impedance is given by:

$$Z = \frac{V(t)}{I(t)} \quad \text{Eq. 2-6}$$

Using Euler's relationship,

$$e^{ix} = \cos x + i \sin x \quad \text{Eq. 2-7}$$

The impedance can be expressed as a complex function and the potential is described as:

$$V(t) = V_0 e^{i\omega t} \quad \text{Eq. 2-8}$$

The current is:

$$I(t) = I_0 e^{i(\omega t + \varphi)} \quad \text{Eq. 2-9}$$

The impedance  $Z$  can be then described with the combination of real and imaginary impedance:

$$Z(\omega) = \frac{V_0}{I_0} e^{-i\varphi} = Z_0 (\cos \varphi - i \sin \varphi) = Z' - iZ'' \quad \text{Eq. 2-10}$$

When the real part is plotted on the X axis and the imaginary part on the Y axis, a Nyquist plot is obtained as shown in Figure 2-9.

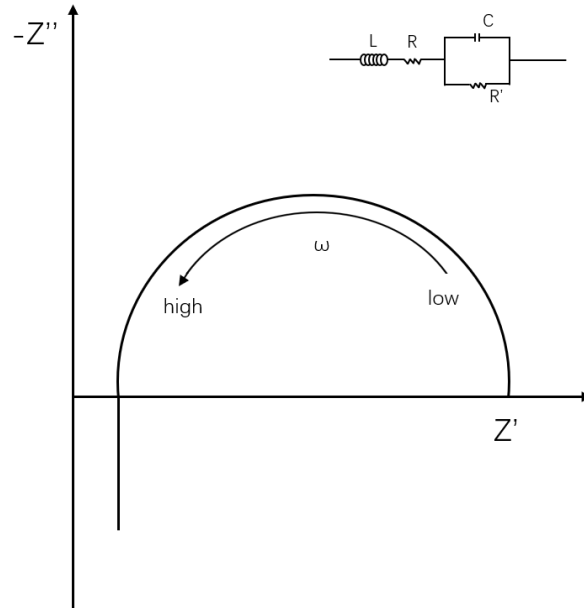


Figure 2-9. Nyquist plot with an equivalent circuit.

The equivalent circuit is commonly used to analyse the Electrochemistry Impedance Spectroscopy (EIS) by interpreting the spectroscopy results into several elements such as ideal resistors, capacitors and inductances. The impedance of the common electrical elements is listed in Table 2-4.

Table 2-4. Impedance of common electrical elements.

Component	Current vs. Voltage	Impedance
Resistor	$E = IR$	$Z = R$
Inductor	$V = LdI / dt$	$Z = i\omega L$
Capacitor	$I = CdV / dt$	$Z = 1/i\omega C$

When an electrochemical process is fitted with a resistance R and a capacitor C in parallel, the impedance is expressed as:

$$\frac{1}{Z} = \sum_i \frac{1}{Z_i} = \frac{1}{R} + i\omega C \quad \text{Eq. 2-11}$$

It can also be described as:

$$Z = \left[ \frac{1}{R} + i\omega C \right]^{-1} = \frac{R}{1+i\omega RC} \times \frac{1-i\omega RC}{1-i\omega RC} = \frac{R}{1+(\omega RC)^2} - \frac{i\omega R^2 C}{1-(\omega RC)^2} \quad \text{Eq. 2-12}$$

In the Nyquist plots, the number of semicircles in the complex plane means the number of varied electrochemical (RC) processes occurring, with each RC process being

associated to a time constant ( $\tau$ ),

$$\tau = RC = \frac{1}{2\pi\nu} \quad \text{Eq. 2-13}$$

Typically, a Nyquist plot has an arc at high frequency (e.g. 1MHz – 4kHz), a second arc at an intermediate frequency (e.g. 4 kHz – 25 Hz) and a linear portion at a lower frequency (e.g. 25 Hz – 0.1 Hz). Depending on the capacitance values associated with the arcs, the three regimes can correspond to the grain interior (bulk), grain boundary and electrode response, respectively. The relative magnitude of capacitance related to the effects is listed in Table 2-5 which can be used in the creating of equivalent circuits for data fitting.

Table 2-5. Capacitance values based on 1 cm cube and their possible interpretation<sup>4</sup>.

Capacitance [F]	Phenomenon Responsible
$10^{-12}$	Bulk
$10^{-11}$	Minor, second phase
$10^{-11} - 10^{-8}$	Grain boundary
$10^{-10} - 10^{-9}$	Bulk ferroelectric
$10^{-9} - 10^{-7}$	Surface layer
$10^{-7} - 10^{-5}$	Sample-electrode interface
$10^{-4}$	Electrochemical reactions

However, in most cases, the semicircle is not symmetric and exhibits depression owing to deviations from the ideal situation. A constant phase element (CPE) is introduced to substitute the capacitance. CPE element can be considered as an illustration of the frequency dispersion of the electrochemical processes occurring in the cell. The impedance of a CPE is:

$$Z_{\text{CPE}} = \frac{1}{C(i\omega)^\alpha} \quad \text{Eq. 2-14}$$

where  $\alpha$  is the ionic correlation index in the range of  $0 \leq \alpha \leq 1$  with  $\alpha = 1$  corresponding to an ideal capacitor.

Conductivity values with respect to varied electrochemical processes can be deduced from the interception of the arcs with the real axis in the Nyquist plot. In routinely studied materials, the temperature dependence property of the conductivity is

also involved due to the nature of the thermally activated process. Conductivity in ceramics occurs by a so-called “hopping” mechanism (Figure 2-10) for the transport of species. In the nonactivated state, the mobile species (ions or electrons) vibrate in its site at a frequency,  $\nu$  (usually around  $10^{12}$  to  $10^{13}$  s<sup>-1</sup>). When they gain sufficient vibrational energy from heating, they are able to escape from the sites and become mobile by hopping to adjacent atoms. The energy is called activation energy,  $E_a$ . This thermally activated process can be expressed as:

$$\sigma T = A \exp\left(-\frac{E_a}{RT}\right) \quad \text{Eq. 2-15}$$

where  $E_a$  is the activation energy,  $A$  is called pre-exponential factor related to the number of carriers per unit volume,  $a_0^2$ . When plotting  $\log \sigma T$  vs.  $(1/T)$ , where  $\sigma$  can be obtained from the Nyquist plot, a straight line is obtained with the activation energy  $E_a$  being calculated from the slop of the line. The graph of  $\log \sigma T$  vs.  $(1/T)$  is called Arrhenius plot.

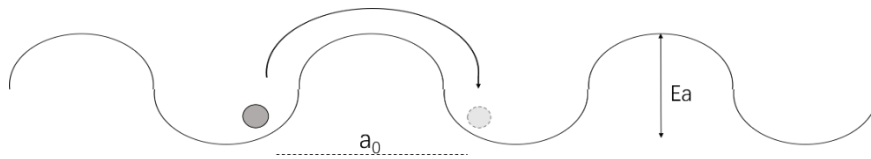


Figure 2-10. Mobile carrier hopping model.

In this work, the ion transport properties of the perovskite pellet were examined by AC impedance spectroscopy with an amplitude of 20 mV over a frequency range of 20 Hz – 1 MHz on an HP 4284 LCR (inductance-capacitance-resistance) meter. Silver electrodes were coated on the opposite sides of the dense pellets. The testing atmosphere is dry/wet air, dry/wet 5% H<sub>2</sub>/Ar.

### 2.2.9 DC Conductivity

When the resistance from the jig design is higher than that of the investigated material, the errors in the conductivity result from AC impedance spectroscopy become unacceptably large. In this case, four-terminal DC measurement is used to determine the total conductivity of material accurately. Different from the AC impedance



technique, DC conductivity test is not able to identify processes from bulk and grain boundary. As shown in Figure 2-11, four strips of gold mesh are attached to the sample long side and end sections with gold paste, fired at 750 °C for 0.5 h. The sample is mounted on the testing jig and a thermocouple and a zirconia pO<sub>2</sub> sensor are equipped in the vicinity of the sample to record the test temperature and oxygen partial pressure. The jig was then inserted in a furnace where the atmosphere can be controlled (e.g., air or 5% H<sub>2</sub>/Ar). During the test, a current (I) is supplied to the sample bar through the two outer gold wires while the generated potential difference (U) is measured from the two inner electrodes. The resistance of the material is thus obtained by Ohm's law, which is recorded with an online multi-meter sensor (Keithley 2000, Digital Multimeter). When the distance between two inner electrode (L) and the cross-section area (A) painted with gold paste at the outer surface are measured, the sample conductivity can be given by equation 2-16.

$$\sigma = \frac{1}{R} \frac{L}{A} \quad \text{Eq. 2-16}$$

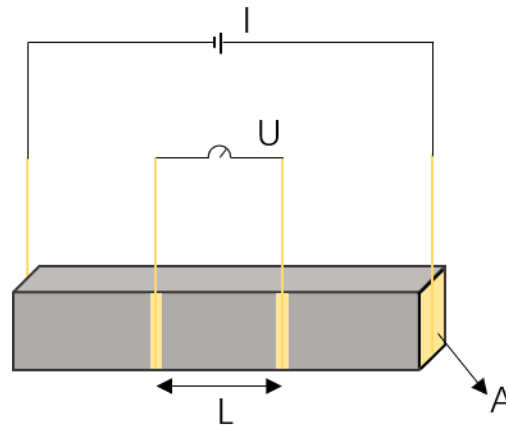


Figure 2-11. Schematic of the four-terminal DC conductivity measurement.

### 2.2.10 Inductively coupled plasma – Optical emission spectrometry

Inductively coupled plasma – Optical emission spectrometry (ICP-OES) is a useful technique for detecting amounts of metals and several non-metals in a liquid sample with very low concentrations. When the measurement is performed, argon is

ionized by the intense electromagnetic field created within the coil by the high-power radio frequency signal, generating high electron density and temperature in the order of 10000 K. Solution sample is delivered into an analytical nebulizer where it is immediately changed into mist due to the high temperature and enters the central channel of the plasma flame. The component elements (atoms) are excited by the high energy of the plasma. When the excited atoms return to low energy position, emission rays (spectrum rays) are released and the corresponded photon wavelength is measured. The position of the photon rays determines the element type and the intensity would give the element content.

Element concentration was measured on Thermo Fisher Scientific ICP-OES iCAP 6000 Series in this work. Ceramic samples were dissolved in nitric acid.

## References

1. Brundle, C. R.; Wilson, L.; Evans, C. A.; Wilson, S.; Wilson, G., *Encyclopedia of materials characterization: surfaces, interfaces, thin films*. Gulf Professional Publishing: 1992.
2. Buchanan, R. C., *Ceramic materials for electronics: processing, properties, and applications*. Marcel Dekker, Inc.: 1986.
3. Macdonald, J. R.; Barsoukov, E., Impedance spectroscopy: theory, experiment, and applications. *History* **2005**, *1* (8), 1-13.
4. Irvine, J. T.; Sinclair, D. C.; West, A. R., Electroceramics: characterization by impedance spectroscopy. *Advanced materials* **1990**, *2* (3), 132-138.

# 3 In situ growth Cu nanoparticles from doped BCZY perovskite

## 3.1 Introduction

Functional nanoparticles (NPs) have generated considerable interest in various fields, and among them, metal NPs dispersed on oxides surface are extensively investigated in catalyst, energy storage and conversion in batteries and fuel cells<sup>1-2</sup>. In the preparation of the NPs, in situ exsolution of B-site cation from perovskite ( $ABO_3$ ) has been found an effective strategy to grow metal NPs on the oxide surface that can be easily achieved by annealing the oxides in a reducing atmosphere (e.g., 5%  $H_2/Ar$ )<sup>3-7</sup>. Particle size can be tailored by varying parameters like reduction temperature and time. Due to the strong interaction with the perovskite substrate, nanoparticles obtained from exsolution are not prone to coarsen and show a high stability in severe environment during operation<sup>8-11</sup>. So far, only limited kinds of cations ( $Ni^{2+}$ ,  $Ru^{2+}$ ,  $Co^{3+}$ ,  $Ag^+$ ,  $Rh^{4+}$ ,  $Pd^{4+}$ ,  $Pt^{2+}$ ,  $Fe^{3+}$ ,  $Cu^{2+}$ )<sup>6, 12-17</sup> were demonstrated to exsolve from the perovskite lattice in the form of metallic NPs, and exsolution from the stoichiometric  $ABO_3$  perovskites is only achieved for the easily reducible cations, preferentially grow in the bulk rather than on the surface due to the surface enrichment of large A-site cations. To overcome these drawbacks, A-site deficient  $A_{1-x}BO_{3-\delta}$  was proposed to promote the hard-to reduce cations to exsolve and allow exsolution to occur on the surface<sup>7</sup>. This is because the non-stoichiometric perovskites with  $A/B < 1$  successfully alleviate the A-site cation segregation and lower the cation diffusion barrier. Moreover, A-site deficiency provides a strong driving force to pull B-site cation out of the lattice to reach a stoichiometric structure.

Here, in our work, copper metal nanoparticles exsolution from proton conducting barium cerate zirconate was investigated. Both stoichiometric and cation deficient materials were prepared. The composition is  $Ba_{1-a}Ce_{0.5}Zr_{0.3}Y_{0.2-b}Cu_bO_{3-\delta}$  ( $a=0, 0.05$ ;  $b=0.02, 0.03, 0.04, 0.06, 0.08$ ). To simplify the compound name, the prepared oxides are named as BCZYCx, where x is the percentage of Cu doping concentration, d-

BCZYC stands for 5% Ba deficient compositions. Different reduction temperatures were applied to better observe metal exsolution process from the perovskites, and the reduced specimen are named as rBCZYCx.

## **3.2 Microstructure and phase identification of Cu-doped BCZY**

### **3.2.1 Microstructure of the as-prepared Cu-doped BCZY**

The observation of microstructure of materials helps in understanding phase formation and structure differences, and the generally used technique is Scanning Electron Microscope (SEM). Figure 3-1 is the SEM images of the native surface of Cu-doped BCZY pellets with different Cu concentration and Ba deficiency sintered at 1350 °C for 12 h in air. All the samples show a dense microstructure except a few isolated pores in 4% and 6% Cu doped oxides. Samples with a lower concentration of Cu, like 2% and 3%, exhibit similar dense morphology and grains connect well with each other forming smooth grain boundaries. But for samples with higher Cu doping level, they display slightly smaller grains and the shape of the grains is almost cuboid, leading to a disordered grain boundary. Observing the microstructure, Ba-deficiency does not change the grain morphology much.

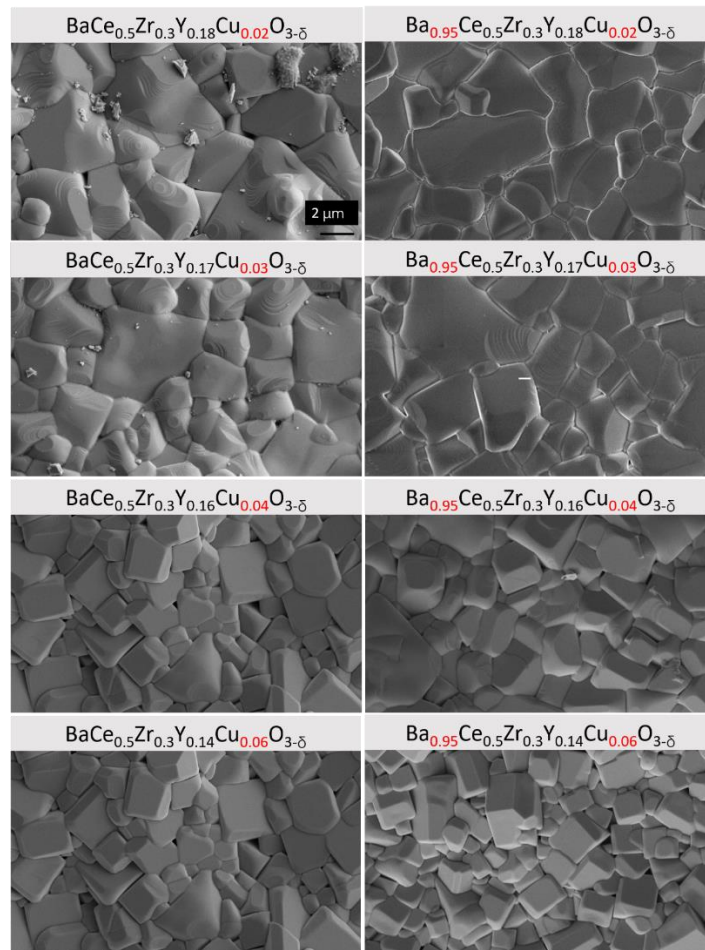


Figure 3-1. SEM images of the native surface of prepared Cu-doped BCYZ pellets sintered at 1350 °C for 12 h with different stoichiometry.

It is known that CuO could promote the densification of BCG or BZY at low sintering temperature<sup>18-22</sup>. Different low melting phases were proposed to be responsible for the increased ability of grain growth and grain boundary mobility, such as CuO, Cu<sub>2</sub>O, Y<sub>2</sub>BaCuO<sub>5</sub> and BaO-CuO eutectic. However, no enough evidence has been found to identify the existence of the liquid phases. Other sintering aids like NiO and ZnO<sup>23-24</sup> were also suggested that the formed BaY<sub>2</sub>NiO<sub>5</sub> and BaY<sub>2</sub>ZnO<sub>5</sub> phase during sintering benefited the grain boundary mobility. Additionally after sintering, these secondary phases (sintering aids-rich phase) most commonly exist at the grain boundary rather than the bulk. In our work, extra phases are also found in the SEM images shown in Figure 3-2. The impurities seem to vary in samples with different Cu doping concentration. EDS line scan and element quantification results indicate that the

impurities are BaO-Y<sub>2</sub>O<sub>3</sub>, Y<sub>2</sub>O<sub>3</sub>, Y<sub>2</sub>O<sub>3</sub>-ZrO<sub>3</sub> and Y<sub>2</sub>BaCuO<sub>5</sub> for BCZYC2, d-BCZYC4 and d-BCZYC6, respectively. It is possible that other phases also existed beyond the limited observation area of SEM.

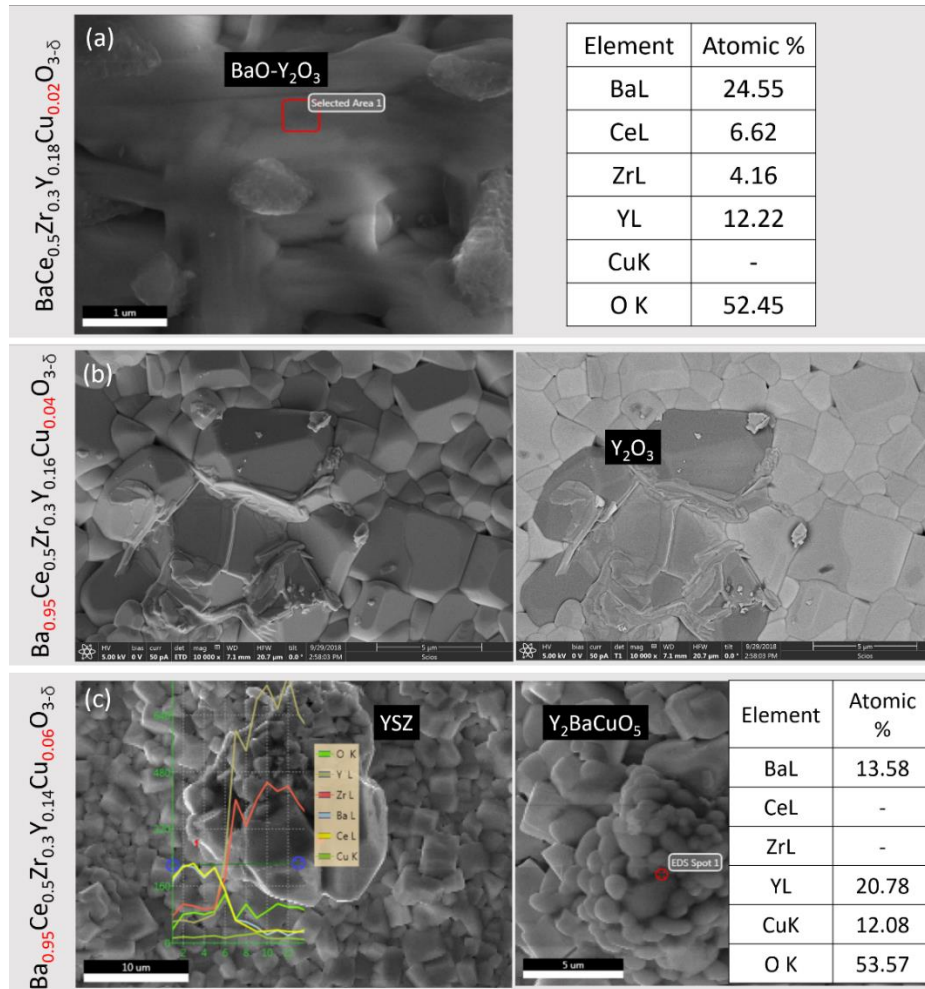


Figure 3-2. (a) SEM image and elemental quantitative results of  $\text{BaCe}_{0.5}\text{Zr}_{0.3}\text{Y}_{0.18}\text{Cu}_{0.02}\text{O}_{3-\delta}$ , (b) SEM images of  $\text{BaCe}_{0.5}\text{Zr}_{0.3}\text{Y}_{0.16}\text{Cu}_{0.04}\text{O}_{3-\delta}$ , (SE in left, BSE in right), (c) EDS line scan (left) and elemental quantitative results (right) of  $\text{BaCe}_{0.5}\text{Zr}_{0.3}\text{Y}_{0.14}\text{Cu}_{0.06}\text{O}_{3-\delta}$ .

### 3.2.2 Phase identification of the as-prepared Cu-doped BCZY

A-site non-stoichiometry effects on barium cerate-based perovskites is still not fully understood by researchers. Ba deficiency can be unintentionally achieved either by the BaO evaporation after exposing the material to a high temperature or deliberately,

by adjusting the initial composition. It was reported that the perovskite structure could not tolerate significant Ba deficiency in undoped BaCeO<sub>3</sub>, which would result in the precipitation of CeO<sub>2</sub><sup>25</sup>. In one sense this is not so critical as an overall Ba deficiency will reduce Ba activity and hence limit degradation, even if not quite single phase. Ma et al.<sup>26</sup> suggested that 5% Ba deficiency could be tolerated in BaCeO<sub>3</sub> and formed a single phase. When dopants were involved in the BeCeO<sub>3</sub> lattice, Ba deficiency was able to be accommodated as much as 4-10 mol% (depending on the dopant ions). For example, a single phase of orthorhombic Ba<sub>x</sub>Ce<sub>0.90</sub>Y<sub>0.10</sub>O<sub>3-δ</sub> was claimed when initial x was between 0.90 and 1.20, considering the likely Ba loss.<sup>27</sup> Among the different stoichiometric materials, Ba<sub>0.95</sub>Ce<sub>0.90</sub>Y<sub>0.10</sub>O<sub>3-δ</sub> exhibited the highest conductivities in dry or wet air and wet H<sub>2</sub><sup>27</sup>. The different behaviour upon A-site deficiency between undoped and doped perovskite implies a defect chemistry mechanism in the applying of dopants. Shima *et al.*<sup>25</sup> proposed that the trivalent dopant Gd<sup>3+</sup> not only substituted Ce<sup>4+</sup> site but also resided on the Ba<sup>2+</sup> site, according to Eq. 3-1 (in terms of Ba deficiency) and 3-2 (in terms of Ce excess, known that Ba deficiency can be regarded as Ce excess).



However, this does not indicate that all the ions can redistribute on the Ba site under Ba deficiency condition. The atomistic study revealed that this redistribution process was energetically favourable over Ba-O vacancy pair formation, and sensitive to the precise Ba/Ce ratio and experimental processing condition. Furthermore, small ions were unfavourable to transfer from the Ce to the Ba site.<sup>28</sup>

Powder X-ray diffraction is used to identify the phase of prepared Cu-doped BCZY, shown in Figure 3-3 (a). On the first sight, the XRD patterns may reflect a cubic structure, however, the rhombohedral and cubic structure have mostly similar patterns in XRD, nevertheless, the rhombohedral structure exhibits an additional reflection at 34.4° attributed to the (113) plane while the cubic structure has no reflection at this scattering angle. Although some peaks are split in the rhombohedral structure especially at high angle, but they cannot be resolved due to the close lattice spacings.<sup>29</sup>

Therefore, all the samples prepared are indexed with the Rhombohedral R-3c space group. Various impurities labeled with different symbols in the high magnification Figure 3-3 (b). A summary of impurities is listed in Table 3-1. Throughout the compositions, single phase was only obtained for BCZYC3, suggesting that Cu has here been incorporated into the perovskite lattice. The ionic radius of six coordinated  $Y^{3+}$  are 0.90 Å and 0.87 Å for  $Ce^{4+}$ , and the sizes of  $Zr^{4+}$  (0.72 Å) and  $Cu^+$  (0.77 Å),  $Cu^{2+}$  (0.73 Å) are quite comparable, while  $Cu^{3+}$  (0.54 Å) seems to be too small compared with the other B-site dopants. It is also known that  $BaZrO_3$  structure has cubic symmetry, however, the doping with  $Y^{3+}$  usually leads to an expansion of the  $BaZrO_3$  cell and causes tetragonal distortion due to the significant ion size mismatch. Therefore, when copper is doped into the perovskite lattice, it may not only occupy Ce and Zr site, but also be prone go into the larger  $Y^{3+}$  site to relieve the octahedra tilting from size mismatch<sup>30</sup>. This is probably the reason why  $Y_2O_3$  impurity is commonly existing in the Cu-BCZY oxides, especially in Ba-deficient samples, e.g., d-BCZYC2 and d-BCZYC3. This is in accordance with the precipitated  $CeO_2$  in Ba-deficient  $BaCeO_3$  mentioned before. Even in stoichiometric oxides, when Cu doping level is more than 4%, the precipitation of  $Y_2O_3$  still occurs. In addition,  $Y_2BaCuO_5$  peaks are found in BCZYC4, d-BCZYC6, BCZYC8 and d-BCZYC8 compositions, and  $mZrO_2$  is detected in BCZYC2, BCZYC4 and d-BCZYC4 samples. The peaks at 32.5° and 32.8° in BCZYC6 are not identified. The impurities in these materials suggest that Ba deficiency did not promote the formation of a pure perovskite phase, on the contrary, the A-site vacancy coupled with oxygen vacancy may destabilize the perovskite lattice, prohibiting the B-site cation from incorporating into the structure, especially the lower valence cation<sup>7</sup>. But this seems not to adapt to the BCZYC4 specimen, where the deficient oxide possibly has less impurity, at least with no  $Y_2BaCuO_5$  peaks and much weaker  $Y_2O_3$  and  $mZrO_2$  peaks if their relative intensities compared with the perovskite peaks are taken into account.



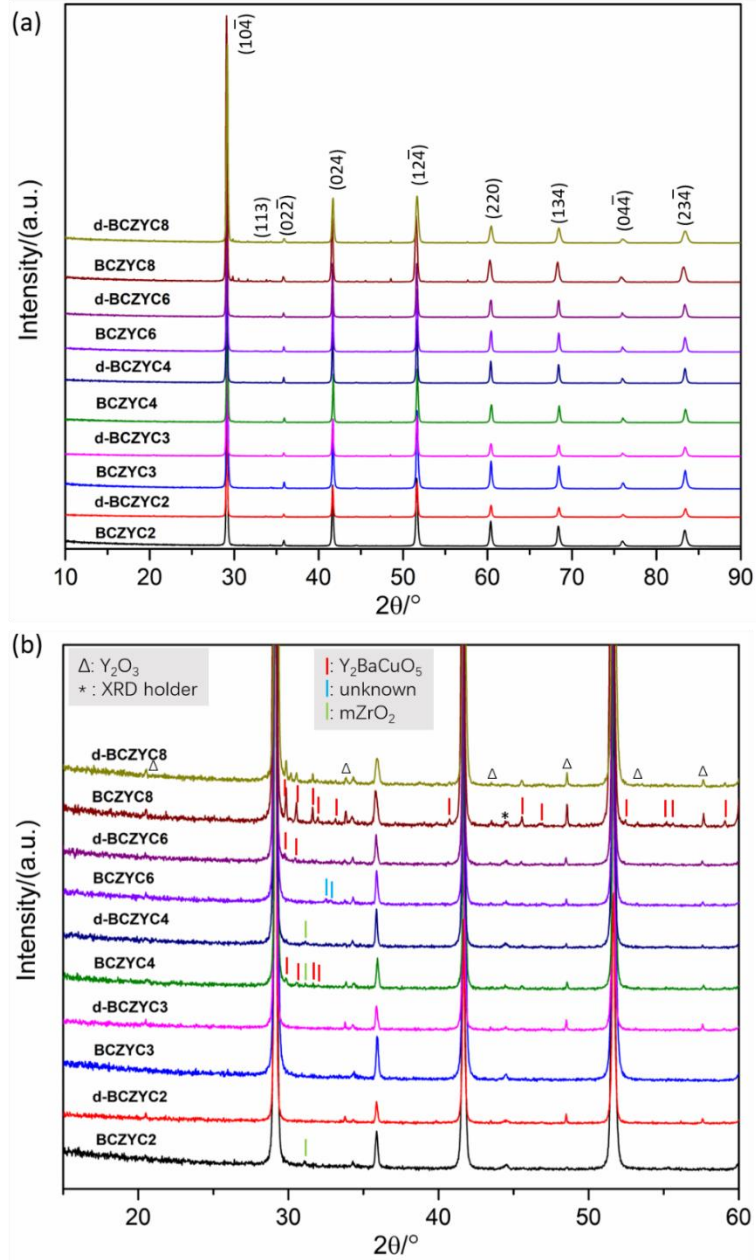


Figure 3-3. (a) RT powder X-ray diffraction patterns of as-prepared BCZYC, and (b) the same XRD patterns as zoomed in selected range.

Table 3-1. Summary of impurities in BCZYC oxides.

composition impurity	BCZYC2	d- BCZYC2	BCZYC3	d- BCZYC3	BCZYC4	d- BCZYC4	BCZYC6	d- BCZYC6	BCZYC8	d- BCZYC-8
Y <sub>2</sub> O <sub>3</sub>		√		√	√	√	√	√	√	√
Y <sub>2</sub> BaCuO <sub>5</sub>					√			√	√	√
mZrO <sub>2</sub>	√				√	√				
Unknown							√			

### 3.2.3 Effect of Cu concentration on the unit cell parameter of BCZYC

Pseudo-cubic unit cell parameter as a function of Cu concentration in stoichiometric and A-site deficient BCZYC is compared in Figure 3-4 (a). Note here the cell parameter without Cu dopant is not listed because the BCZY oxide sintered at 1350 °C is far from a pure phase unless it is fired at over 1500 °C, making it incomparable with the Cu aided oxides. In the stoichiometric compositions, 4% Cu doped BCZY has the smallest lattice constant. Typically, the substitution of smaller sized ion for a larger one causes a contraction in the cell volume, and this well explains the decreased lattice parameter with doping more  $\text{Cu}^{2+}$  in the structure until 4 mol%. It is thus further indicated that  $\text{Cu}^{2+}$  replaced the  $\text{Y}^{3+}$  site. While Cu concentration gradually increases, the lattice is expanding. One possible reason is that 4% Cu reaches its solubility in the perovskite, and the higher concentration leads to the more favourable formation of Cu contained impurities (mainly  $\text{Y}_2\text{BaCuO}_5$ ) but less incorporation in the lattice. Meanwhile, the higher (Y+Cu)/Ba ratio in  $\text{Y}_2\text{BaCuO}_5$  impurity compared with that in the perovskite results in a higher Ba concentration left in the perovskite oxide, which also contributes to a larger unit cell. Another possible reason is the perovskite can tolerate a Cu concentration higher than 4 %, and there is a critical point between 4 % and 6% Cu where repulsive interaction between cations due to the continually introduced oxygen vacancies with the doping of Cu begin to dominate the cell parameter changes and result in lattice expansion<sup>31</sup>. Thus, with doping too much copper, the oxygen vacancy effect dominates the lattice constant change rather than the dopant ionic radius.

When A-site deficiency is introduced, the unit cell parameter changes differently upon the Cu content. The existence of A-site vacancies increases linearly the cell volume of BCZYC doped with up to 6% Cu while leading to a cell contraction at 8% Cu-BCZY. According to the analysis in the stoichiometric samples, if decreased Cu solubility and favourable formation of impurities are considered as the reason for the expanded cell with increasing Cu concentration, one should expect stronger impurity XRD peaks as a function of Cu concentration between 2% - 6% in the deficient samples,

however, much weaker impurity peaks are observed in the deficient 4% Cu-doped oxide. This suggests that the cell parameter change in stoichiometric materials is more possibly attributed to the increased oxygen vacancy concentration in the higher Cu doping level. Back to the deficient perovskites, a cell size contraction compared to stoichiometric composition is observed for 2%. Normally, lattice constant would decrease with the A-site deficiency because of the process of introducing a cation with a smaller radius into the A-site. Thus, for the d-BCZYC2, the cell constant is determined by the ionic radius. However, A-site vacancy would also promote the formation of oxygen vacancy, leading to the critical point where oxygen vacancy effect begins to dominate cell parameter occurring between 2% and 3% Cu dopant. The expansion effect due to oxygen vacancy plays a stronger role with increasing Cu content until 8%, where a cell contraction takes place. There is a relatively high concentration of impurities in d-BCZYC8 by comparing the intensity of XRD characteristic peaks, making it difficult to clarify the reason for cell contraction.

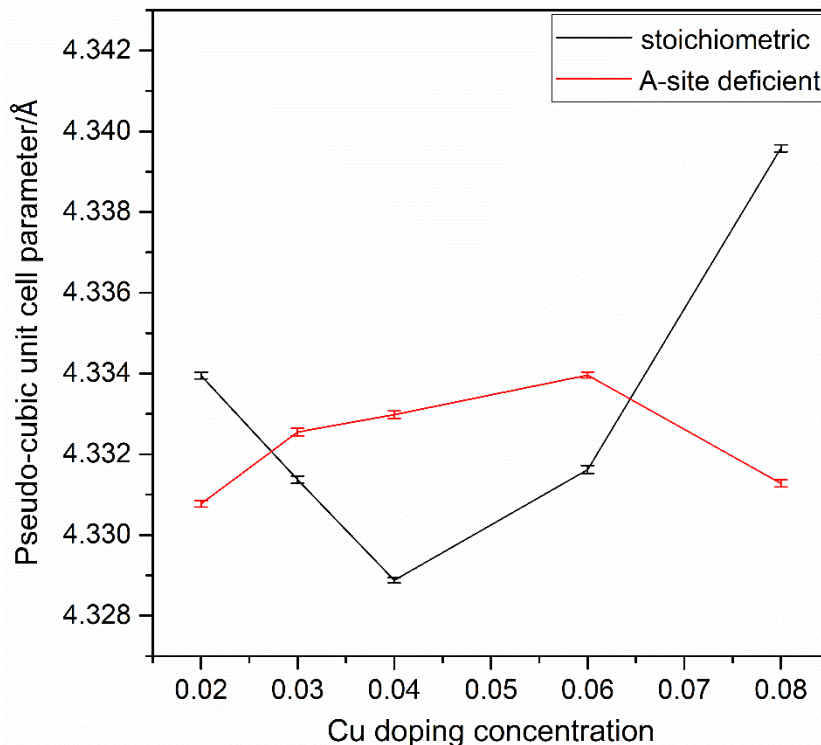


Figure 3-4. Pseudo-cubic unit cell parameter of BCZYC as a function of Cu concentration and A-site deficiency (the symbol size indicates the error size).

### 3.2.4 Axial $c/a$ ratios of as-prepared Cu-doped BCZY oxides

In an ideal hexagonal close packed (hcp) unit cell (Figure 3-5), the atoms of equal size are at the corners with one inside at position  $\left(\frac{1}{3}, \frac{2}{3}, \frac{1}{2}\right)$ . Adjacent atoms are in contact, thus parameter  $a$  is equal to the diameter of the atom and  $c$  is equal to twice the vertical height of a tetrahedron. This determines that:

$$\overline{GD} = \overline{OD} = 2R = a \quad (R \text{ is the atomic radius})$$

$$\overline{OE} = \frac{c}{2}$$

$$\text{In triangle DLE, } \overline{DE} = \overline{DE} \cdot \cos 30^\circ = \frac{a}{\sqrt{3}}$$

While in triangle OED,  $\overline{ED}^2 + \overline{OE}^2 = \overline{OD}^2$ , yielding

$$\left(\frac{a}{\sqrt{3}}\right)^2 + \left(\frac{c}{2}\right)^2 = a^2, \text{ giving}$$

$$\frac{c}{a} = \sqrt{\frac{8}{3}} = 1.633$$

An ideal  $c/a$  ratio of 1.633 in a hexagonal unit cell suggests that the distance between every atom is the same. If the axial  $c/a$  ratio deviates from the ideal value then the distances between nearest neighbouring atoms in the basal plane is different from that between nearest atoms between planes.

The primitive Rhombohedral cell can be expressed with the R-centered hexagonal matrix, as shown in Figure 3-5 (b). The two additional lattice points inside the hexagonal unit cell are at  $\left(\frac{2}{3}, \frac{1}{3}, \frac{1}{3}\right)$  and  $\left(\frac{1}{3}, \frac{2}{3}, \frac{2}{3}\right)$ , respectively. This gives the ideal  $c/a$  ratio to be  $1.633 \cdot (3/2) = 2.4495$ .

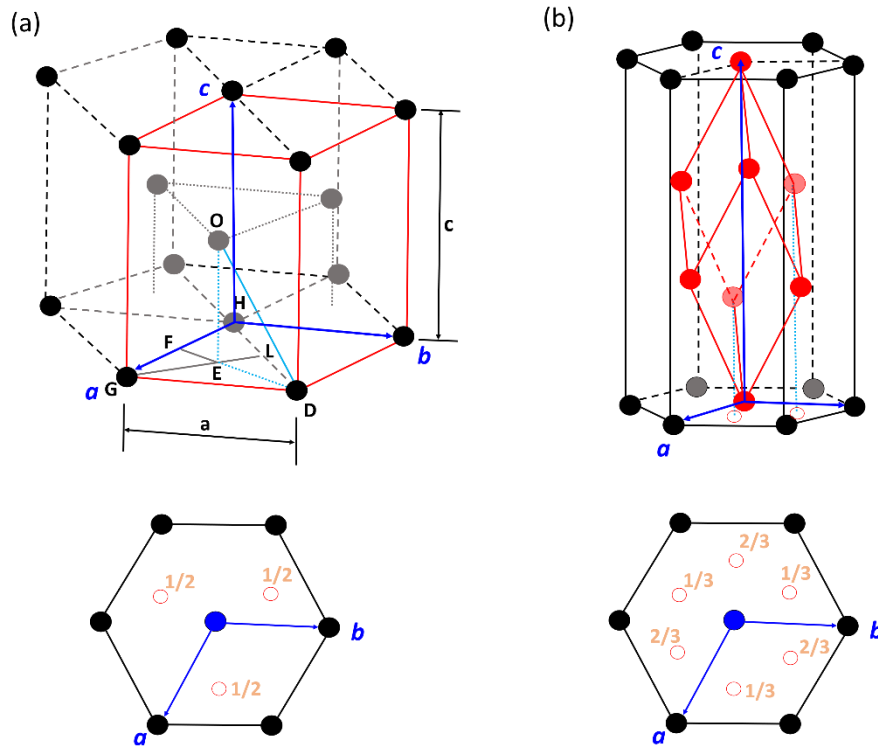


Figure 3-5. (a) hexagonal closed packed unit cell, (b) primitive rhombohedral cell expressed with R-centered hexagonal matrix.

However, in perovskite structures, the atoms in close packing may be pushed apart by ions in the interstitial sites, making the axial  $c/a$  ratio to deviate from the ideal value. Therefore, the  $c/a$  value can reflect how well the ionic sizes match in the solid solution and how close the geometry is to hexagonal matrix. Here,  $c/a$  ratios are calculated to investigate the effect of Cu concentration and Ba deficiency on the lattice changes. As demonstrated in Figure 3-6, in stoichiometric compositions, all the samples show a lattice that deviates from the ideal hexagonal lattice with their  $c/a$  ratio lower than the ideal value. Among them 4% Cu-BCZY has the lowest  $c/a$  value that suggests the most deviation from the ideal hexagonal lattice. Additionally, axial  $c/a$  ratio exhibits the same trend with the pseudo-cubic cell parameter as a function of Cu content in stoichiometric perovskites, indicating that the doping of Cu in fact makes lattice deviate more from ideal hexagonal unit, while expansion effect from oxygen vacancies in oxides with higher Cu doping level (6%) leads to a less distorted hexagonal lattice, and the expansion effect is more obvious along the  $c$  axis than the  $a$  axis.

While 4% Cu-BCZY has the lowest axial  $c/a$  ratio in the stoichiometric compositions, the corresponding deficient oxide exhibits significant improvement. For the other compositions, only BCZYC2 shows a slight increase in the  $c/a$  ratio when applying Ba deficiency, but the rest result in a more distorted hexagonal lattice with lower  $c/a$  ratio. Since oxygen vacancies were suggested to be advantageous for a higher degree of hexagonal matrix, the introduction of A-site deficiency in BCZYC4 creates extra oxygen vacancies in the lattice that expand the cell and give rise to a more hexagonal unit cell. However, in 6% and 8% Cu-doped BCZY, the more oxygen defects in deficient oxides affected reversely. The reason for this probably because lattice oxygen atoms at different positions in the lattice have different energy or property due to their surrounding cation environment.

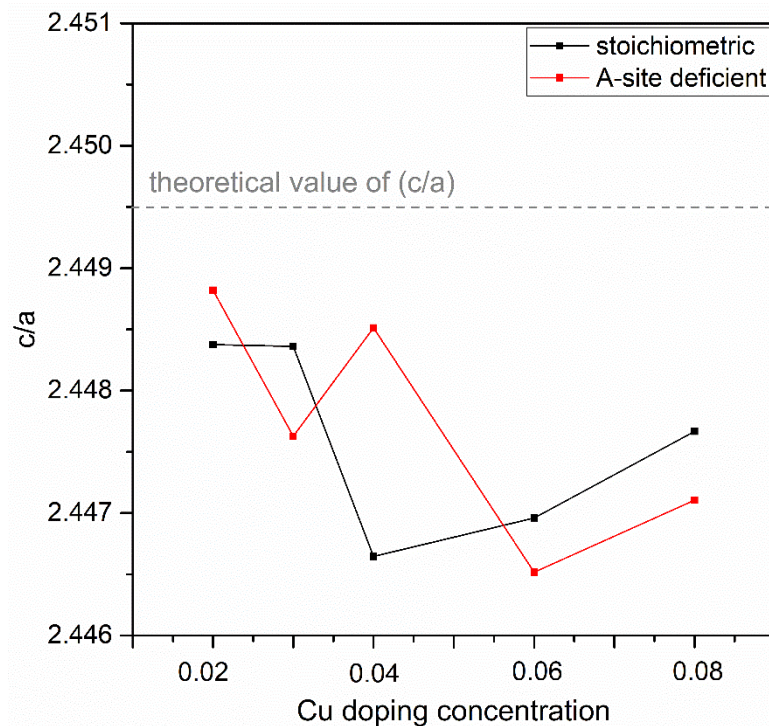


Figure 3-6. Axial ( $c/a$ ) ratio of the hexagonal lattice of BCZYC as a function of copper content and A-site deficiency.

The different oxygen sites have been proposed by Kreuer<sup>32</sup> to explain the varied activation energy for proton transfer in Y-doped BaCeO<sub>3</sub> and SrCeO<sub>3</sub> perovskites. He suggested that the large orthorhombic distortion of Y-SrCeO<sub>3</sub> has tremendous effects

on the arrangement of lattice oxygen, resulting in nonhomogeneous chemical interactions with the cations. It is thus suspected that there are also different lattice oxygens in the BCZYC perovskite structure originating from the octahedra tilting and its surrounded cation environment. As shown in Figure 3-7, the tilting of  $\text{BO}_6$  octahedra may result in different energies in different oxygen sites. The oxygen vacancies in deficient BCZYC4 only located at the sites where cause more expansion along the  $c$  axis, leading to a large unit cell and less deviation from hexagonal unit (defined as O1 site). When more oxygen vacancies exist in the hexagonal lattice of d-BCZYC6 and d-BCZYC8, lattice oxygen has to be removed from the sites where will lead to more expansion along  $a$  axis (defined as O2 site). Therefore, the lattice become to deviate more from an ideal hexagonal unit.

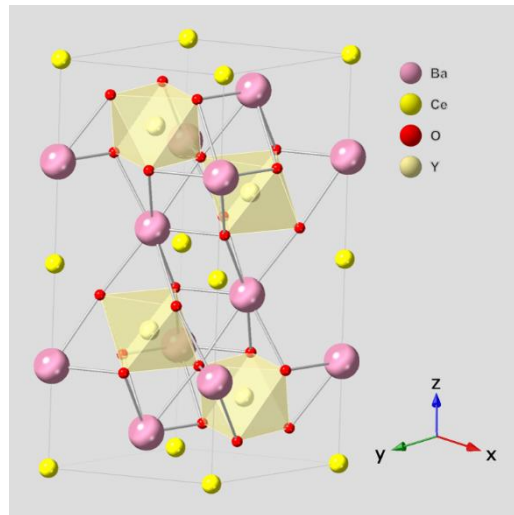


Figure 3-7. BCZY unit cell, space group: R-3cH.

To summarize the copper dopant concentration and Ba-deficiency effect on the cell parameter and deviation from ideal hexagonal lattice, in the low doping concentration range (2% - 4%) of the stoichiometric compositions, the lowered cell volume is determined by the smaller ionic radius of copper, and the lattice becomes less hexagonal with the dopants. Doping more copper results in unit cell expansion and closer lattice to hexagonal matrix due to the dominated oxygen vacancy effect, and the number of oxygen vacancies is in the limit that preventing it from being removed from



O2 site. In deficient perovskites, more oxygen vacancies are created in their corresponding stoichiometric oxides, and among them, deficient BCZYC4 shows the best balance between dopants concentration and oxygen vacancies, producing a large unit cell and less deviation from ideal hexagonal unit. However, simulation of the structure needs to be carried out to confirm the assumption in future work.

XRD can be used to determine the crystallinity by comparing the integrated intensity of the background pattern to that of the sharp peaks. Generally, the crystalline compounds with high crystallinity give well-defined, narrow, sharp and distinct peaks. In our work, all the XRD samples were prepared in the same condition and tested by the same machine. Hence, the relative intensity of the main peak was used to compare the crystallinity of the compositions. In Figure 3-8, the lowest XRD intensity appears in the BCZYC oxide with Cu doping ratio of 4%. However, for the deficient compositions, 4% Cu doped BCZY behaves the highest XRD intensity, indicating a distinct improvement in the crystallinity of the material due to the Ba-deficiency. Conversely, the XRD intensity of all the other samples is lowered by the A-site vacancy. This is somehow consistent with the expanded unit cell and the higher degree of hexagonal lattice in the deficient BCZYC4 oxide we mentioned above, supporting that Ba deficiency is advantageous for 4% Cu-BCZY.

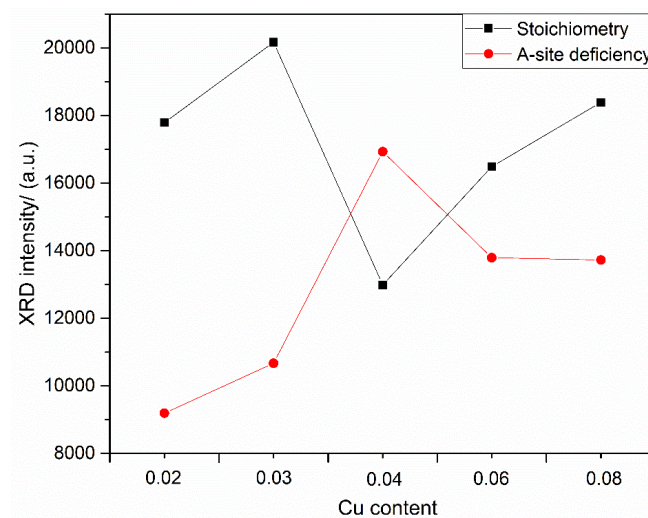


Figure 3-8. (104) XRD peak intensity of BCZYC as a function of Cu concentration and A-site deficiency.



### 3.3 Copper exsolution from BCZYC perovskite

#### 3.3.1 Phase identification of BCZYC oxide after reduction

The as-prepared BCZYC pellets were ground into powder and reduced at 900 °C for 12 h in 5% H<sub>2</sub>/Ar, and phase identification of the resulting powders were analyzed in Figure 3-9 (a letter of 'r' is put in front of the name of samples in redox history to label as the perovskites after reduction). After reduction, the BCZYC perovskite substrates retain a R-3cH symmetry, indicating no distinct decomposition of the parent material occurred during reduction. Peaks at 43.5° and 50.4° corresponding to Cu metal are found in all the compositions, revealing Cu metal were exsolved from the perovskite structure. The absence of Y<sub>2</sub>BaCuO<sub>5</sub> oxide peaks suggests its decomposition and the product of copper is in the form of Cu metal because of the reducing atmosphere, while barium and yttrium are either reintegrated into the perovskite structure or left on the perovskite surface as oxide impurities. There are no peaks of barium oxide shown in all the materials after reduction, and it is either because of its small amount or re-dissolving into the parent oxide. Y<sub>2</sub>O<sub>3</sub> phase still exists in the materials with Cu doping more than 4%, making it difficult to determine the re-doping behaviour of Y<sub>2</sub>O<sub>3</sub> product. Whereas, mZrO<sub>2</sub> peak did not appear in rBCZYC2, demonstrating that the mZrO<sub>2</sub> probably re-dissolved into the perovskite structure due to the B-site deficient after Cu exsolution.

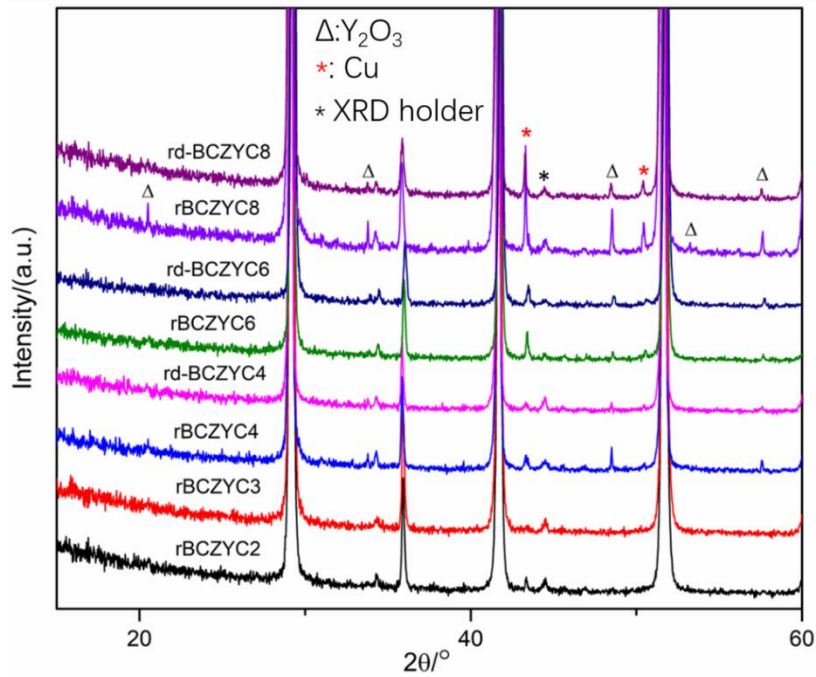


Figure 3-9. RT powder X-ray diffraction patterns of BCZYC samples after reduced at 900 °C for 12 h in 5% H<sub>2</sub>/Ar.

### 3.3.2 Unit cell parameter and axial *c/a* ratios of the reduced BCZYC oxides

It is generally known that reduction of the material gives rise to a cell expansion because the removal of negatively charged lattice oxygen results in the stronger repulsion force between the neighbouring cations ( $O_O^{\times} \rightarrow v_O^{\bullet} + 2e^- + \frac{1}{2}O_2$ )<sup>7, 10</sup>. Moreover, the electrons producing from this process lower the oxidation state of a portion of Ce from Ce<sup>4+</sup> to Ce<sup>3+</sup> according to  $e^- + Ce^{4+} \rightarrow Ce^{3+}$ , which will also reflect into an increase of the cell volume. But when the introduced oxygen vacancies reach the limit  $\delta_{lim}$  ( $\delta$  is the number of lattice oxygen removed per formula unit of the perovskite, standing for the extent of reduction,  $\delta_{lim}$  is the most oxygen vacancies that the perovskite structure can hold) of stabilizing the perovskite structure, further reduction will pull the B-site Cu<sup>2+</sup> out of lattice, creating Cu nuclei ( $2e^- + Cu^{2+} \rightarrow Cu^0$ ). Reverse to cell expansion, this process allows the removal of oxygen vacancies and results in a cell contraction<sup>33</sup>. The unit cell parameter of stoichiometric Cu-doped BCZY perovskite as prepared in air and after reduction at 900 °C are compared in Figure 3-10

(a). A peak cell parameter is observed in the r-BCZYC4 sample among the reduced oxides in the Cu concentration range of 2% - 6%, which indicates the highest amount of oxygen vacancies in it. Compared with materials sintered in air, a decrease in cell parameter is seen after reduction except for 4% Cu doped BCZY. This implies that r-BCZYC4 probably has a larger  $\delta_{lim}$  value among the compositions which means that it can tolerate a higher extent of oxygen vacancies, while the cell contractions in the other compositions are supposed to be due to their decreased ability to tolerate oxygen vacancies accompanied with Cu exsolution. The  $c/a$  ratios of the hexagonal lattice in compositions after reduction are shown in Figure 3-10 (b), presenting a pretty much same trend with the oxidized samples, except that the largest deviation from an ideal hexagonal lattice exists in BCZYC6. Comparing single composition between oxidized state and reduction state, an increased  $c/a$  value is observed in all the compositions after reduction except the BCZYC6. This enhanced  $c/a$  value after reduction is possibly due to the decreased Cu concentration in the lattice after exsolution, which is consistent with the lowering  $c/a$  ratio as a function of Cu doping level in the oxidized perovskite.

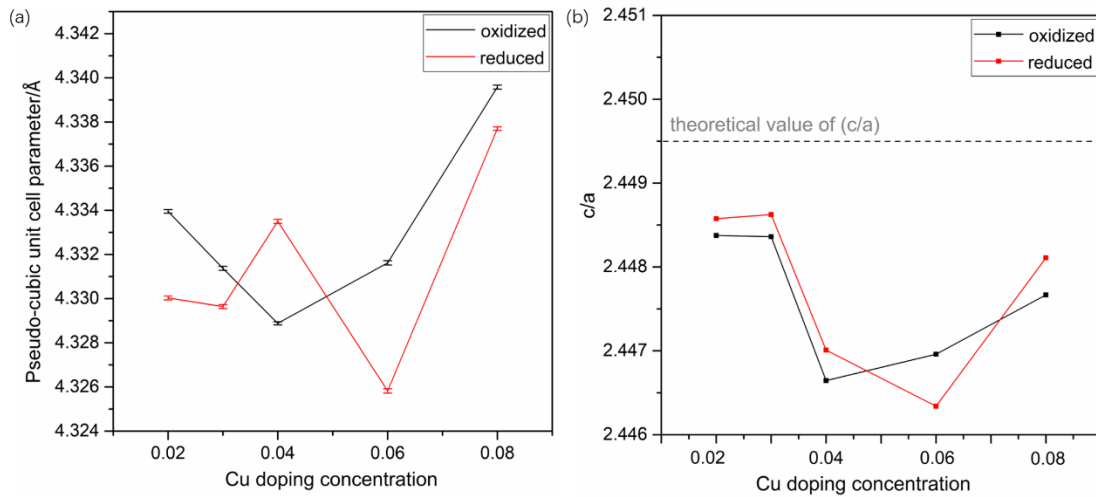


Figure 3-10. (a) Pseudo-cubic unit cell parameter and (b) axial  $c/a$  ratio of the hexagonal lattice of stoichiometric BCZYC as a function of Cu concentration before and after reduction.

In the reduced Ba deficient samples (Figure 3-11 a), the pseudo-cubic cell

parameter follows the same trend with the compositions before reduction, except the large jump in the d-BCZYC6, from the largest cell in oxidized condition to the smallest one after a reduction treatment. It is known that with B-site Cu exsolving, the A-site deficient compositions become more stoichiometric, which allows to accommodate higher amount of oxygen vacancies in the structure, and thus leading to cell expansion. But this seems not apply to the d-BCZYC6, whose lattice contracts a lot in the reduced state, which means the structure has less oxygen vacancies but excessive exsolution. The change in cell parameter is quite complicated, not only a matter of Cu exsolution and oxygen vacancy change, but also accompanied with Ba transportation, which will be illustrated in the following SEM analysis section.

In Figure 3-11 (b), the  $c/a$  value after reduction of the deficient samples also shows a similar trend as the oxidized materials, except the d-BCZYC8. Reverse to the change in the stoichiometric BCZYC, the deficient materials exhibit slightly less perfection in hexagonal unit after reduction. The deviation may be a result that the deficient structures begin to remove lattice oxygen from the O2 site. The expansion of unit cell and improved hexagonality in d-BCZYC8 is probably owing to the composition rearrangement between the impurities and parent perovskite during reduction.

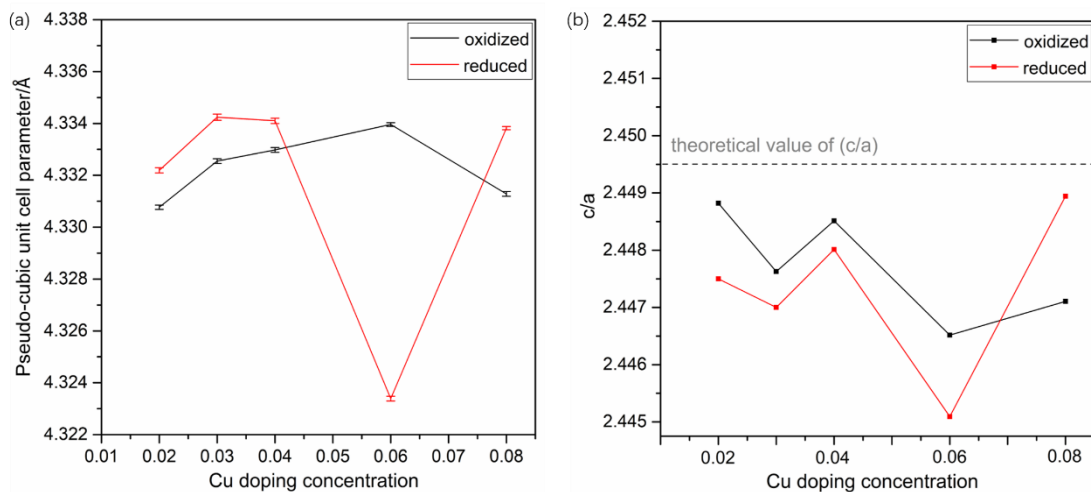


Figure 3-11. (a) Pseudo-cubic unit cell parameter and (b) axial  $c/a$  ratio of deficient BCZYC as a function of Cu content before and after reduction at 900 °C for 12 h in 5%  $H_2/Ar$ .

### 3.3.3 Microstructure of the reduced BCZYC pellets

Normally, to be at the lowest free energy state (most stable), the native surface of the pellet has a different atom arrangement from the bulk due to the dangling bonds of the surface atoms<sup>2</sup>. Thus, the atom rearrangement on the surface or near the surface will take place in the form of typical cation enrichment or depletion in the crystals containing multi-elements with various ion sizes. This segregation can cause a deteriorated effect on the material surface property and functionality. The segregation of the large A-site cation on the surface is found to be the most common phenomenon in stoichiometric perovskite, in the form of AO islands or  $A_{n+1}B_nO_{3n+1}$  Ruddlesden-Popper structures. B-site cation exsolution is severely influenced by the AO segregation even in oxygen deficient perovskites ( $ABO_{3-\delta}$ ). For example, only a few nickel NPs can be found on the  $(La_{0.7}Sr_{0.3})(Cr_{0.85}Ni_{0.15})O_{3-\delta}$  perovskite after reduction<sup>34</sup>. This demonstrates that apart from oxygen deficiency, A-site vacancy plays a key role in the occurrence of exsolution, as first found by Neagu and co-workers<sup>7</sup>. The existence of A-site deficiency restrains the surface A-site enrichment and benefit for the B-site exsolution process. Therefore, in order to alleviate the effect of AO enrichment on the exsolution, a cleaved surface obtained by breaking the pellet or grinding the coarse powder to expose native surfaces was investigated for the exsolution process because of the more representative of the nominal bulk stoichiometry.

Reduction temperature is a very simple and useful parameter in controlling the size, population and dispersion of the exsolved particles, which allows to tailor the microstructure of materials for different applications<sup>10</sup>. Considering this factor, the prepared Cu doped BCZY pellets with different stoichiometry were reduced at 500 – 900 °C for 12 h in 5% H<sub>2</sub>/Ar. The morphology and distribution of the nanoparticles on the cleaved surface were investigated by SEM. All the samples exhibited a similar morphology. In order to minimize Ba segregation during reduction, a deficient sample d-BCZYC6 is chosen for discussion. Basically, a large population of particles can be obtained at each reduction temperature, as shown in Figure 3-12. When reduced at 500 °C, SEM images in Figure 3-12 (a1-a3) indicate the existence of two kinds of

exsolved particles with different size ranges. The larger particles are between 200 nm to 1  $\mu\text{m}$  in size and the smaller ones, distributed randomly on the surface, are approximately 100 nm. In order to distinguish different particles in the following discussion, the large particles are labelled as type I particle and the small ones are type II. Increasing reduction temperature to 600  $^{\circ}\text{C}$ , the dual nature of particles remains the same in size range, but the shape of type I particles becomes more spherical (Figure 3-12 b1-b3). The distribution of particles seemed to be more regular, with the type I particles sitting at the interface of three or four grains and the type II ones orderly distributed along the grain boundaries. It is believed that more crystalline defects are formed at the grain boundaries because of the mismatch of different orientation from two planes, and these defects will be even more present at the interface of several orientations. Meanwhile, the more defects impose the increased instability of the local structure, making it more favourable for metal nucleation due to the lowered nucleation barrier<sup>2</sup>. A large quantity of very small nanoparticles (labelled as type III particle) was found on the surface in high magnification (shown in the red square in b2). It is also noted that a thin layer exists underneath the type I particles (shown in the yellow circle), which is believed to be a crystalline phase formed along with exsolution. This phase can also be observed in samples reduced at 700 and 800  $^{\circ}\text{C}$ . Figure 3-13 shows the EDS results of sample reduced at 600  $^{\circ}\text{C}$ . The quantification analysis of elements implies that the large particle at EDS spot 3 is Cu metal, and the smaller one at EDS spot 1 contains mostly an amount of Cu with less Ba and Zr. It is possible that the Ba and Zr are from the matrix or the particle because the particle size is smaller than the electron beam effect area. For the substrate area at EDS spot 4, the EDS quantitative result is almost identical to the Ba/Ce ratio present in  $\text{Ba}_{0.95}\text{Ce}_{0.5}\text{Zr}_{0.3}\text{Y}_{0.14}\text{Cu}_{0.06}\text{O}_{3-\delta}$  but with less Zr and Y. No Cu was found in this area, suggesting that most copper atoms have already been stripped from the perovskite lattice due to the reduction treatment. When the reduction temperature is increased to 700  $^{\circ}\text{C}$  (Figure 3-12 c1-c3), the numerous type III nanoparticles disappeared. The type I particles became even more spherical while the type II particles grew slightly larger and less present. In addition, the surface of type I particles seems to be composed of many layers, which may indicate its growing process.

When reduced at an even higher temperature 800 °C (Figure 3-12 d1-d3), the number of type II particles tend to be even lower with only a few particles distributed on the grain, and mostly type I large particles are present along the grain boundary. In the yellow square region of (d1), it seems that the largest particles are wrapped in an extra phase that has the same contrast with the particles in the back scattering electron (BSE) image inserted in (d1), suggesting the two phases may have the same element presence in a large percentage. This extra phase can also be found on the pellets reduced at 500-700 °C. EDS analysis of spot 2 in Figure 3-13 indicates that this phase is probably barium cuprate. We suspect that some large particles grow from this extra phase, leaving the phase shown in the yellow circle after copper exsolving. When reduced at 900 °C (Figure 3-12 e1-e3), only the type I particles are found on the surface. There is a significant morphology change on the particles from sphere to polyhedron. Furthermore, another phase with polygonal shape is socketed on the perovskite surface and some of such phases have larger particles sitting on top. From the BSE image inserted in Figure 3-13 (e1), no contrast difference is observed between the polygonal phase and the substrate. EDS quantification result of the polygonal phase inserted in (e2) shows a slightly Ba-excess.

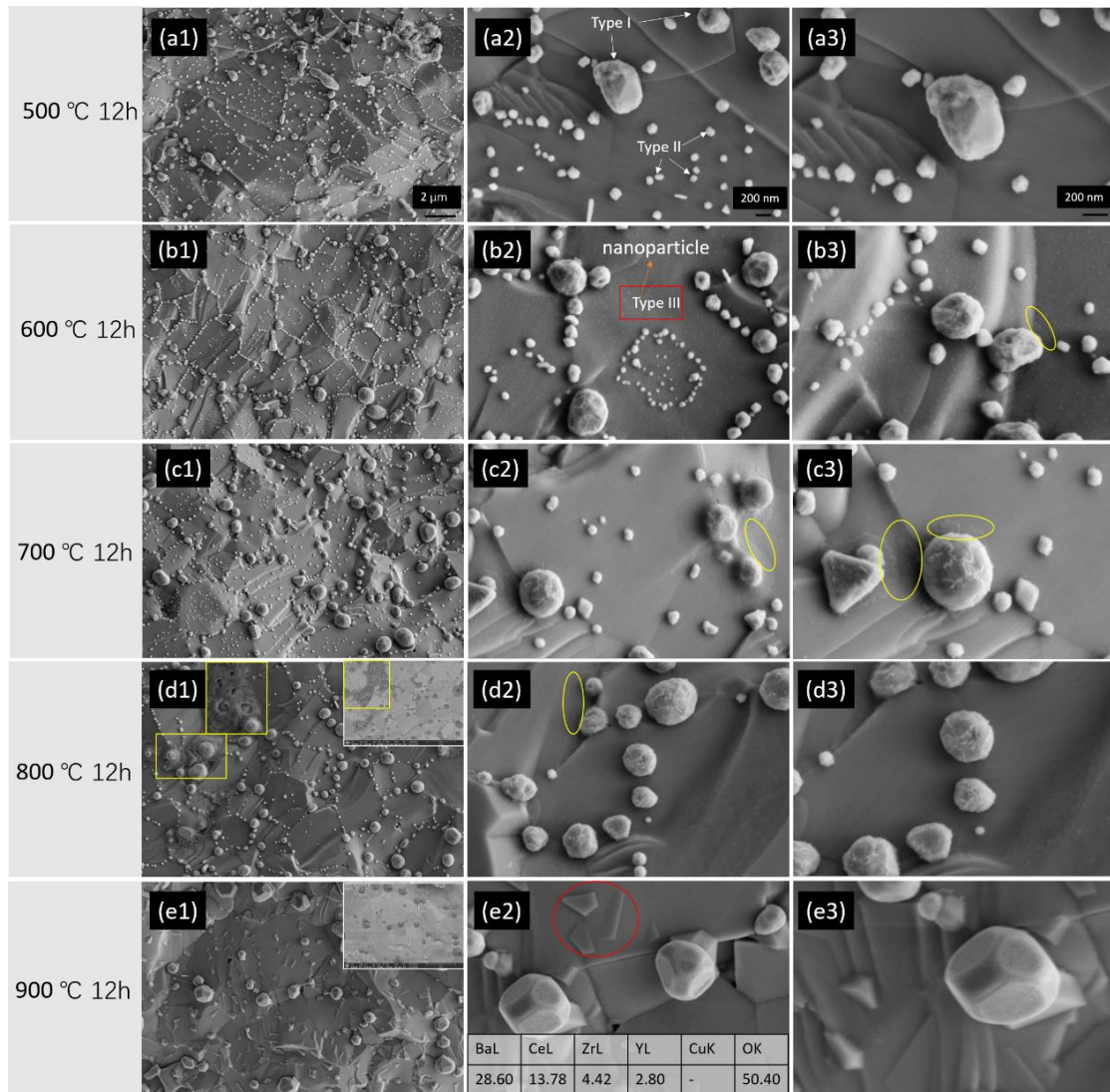


Figure 3-12. SEM images of cleaved surface of  $\text{Ba}_{0.95}\text{Ce}_{0.5}\text{Zr}_{0.3}\text{Y}_{0.14}\text{Cu}_{0.06}\text{O}_{3-\delta}$  pellet reduced at different temperatures for 12 h in 5%  $\text{H}_2/\text{Ar}$ , (a1-a3) 500 °C, (b1-b3) 600 °C, (c1-c3) 700 °C, (d1-d3) 800 °C, (e1-e3) 900 °C. The inset in (d1) and (e1) is back scattered image, and the table in (e2) is the EDS quantification result of the polygonal phase in the red circle. The number 1-3 means different magnification from low to high.



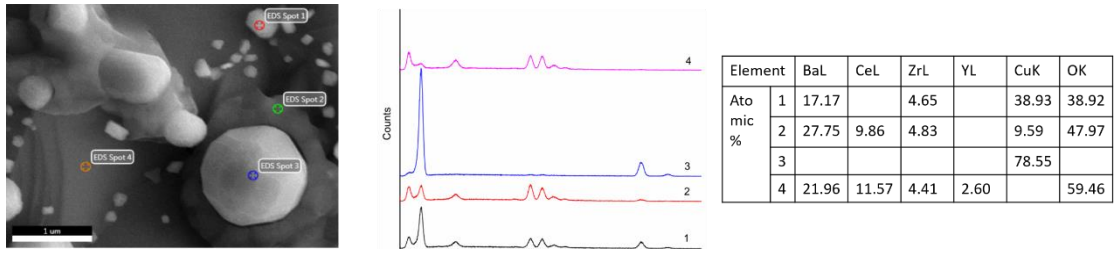


Figure 3-13. EDS spectra and quantitative analysis of particles and phases on pellet reduced at 600 °C for 12 h in 5% H<sub>2</sub>/Ar.

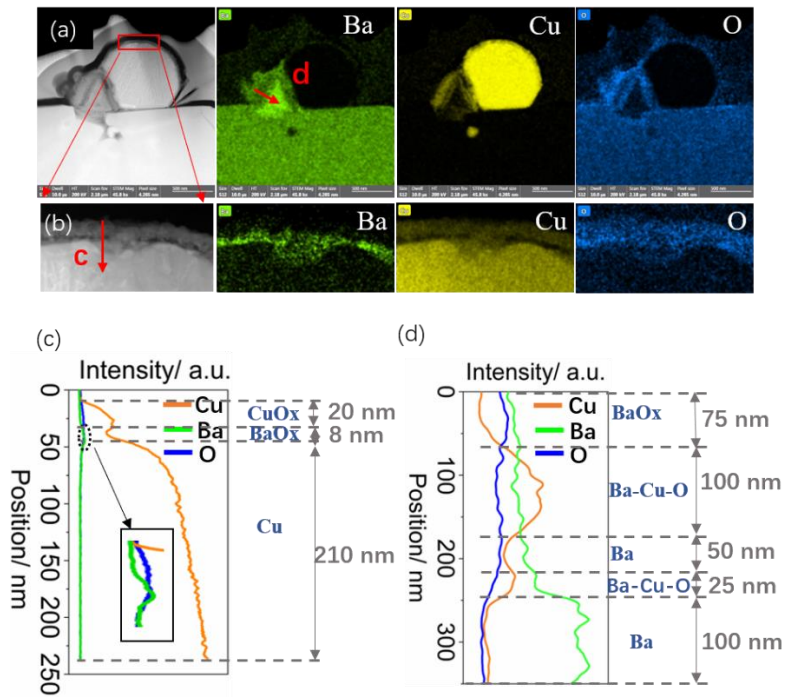


Figure 3-14. Characterization of the sample reduced at 900 °C for 12 h in 5% H<sub>2</sub>/Ar.

(a) HAADF image of the particles and its EDS mappings, (b) surface layer of the particle and EDS mappings, (c) the EDS line scan in area c in (b), (d) the EDS line scan of the area d in (a). (The TEM characterization in this work was carried out by Dr. Aaron Naden except those with extra annotation)

The morphology and chemistry of the exsolved particles obtained after reduction at 900 °C for 12 h were analyzed by the TEM. As shown in Figure 3-14 (a), an extra triangle-shaped phase attaching the particle is observed, which is the same phase as the one underneath the large particle in Figure 3-12 (e3). EDS mappings show that the spherical particle is rich in Cu, further confirming the identification of Cu metal. For

the triangle extra phase, it is accumulated with barium species, especially in the inner triangle area, showing as a Ba metal state. However, a shell structure is displayed in the extra phase, composing several layers that consist of copper and oxygen elements. For the surface layer of the particle, the similar shell structure is also observed. The EDS line scans in Figure 3-14 (c, d) reveal the shell composition from outmost to the inner, which is  $\text{CuO}_x$ ,  $\text{BaO}_x$  for the Cu particle and  $\text{BaO}_x$ , barium cuprate, Ba, barium cuprate for the triangle phase.

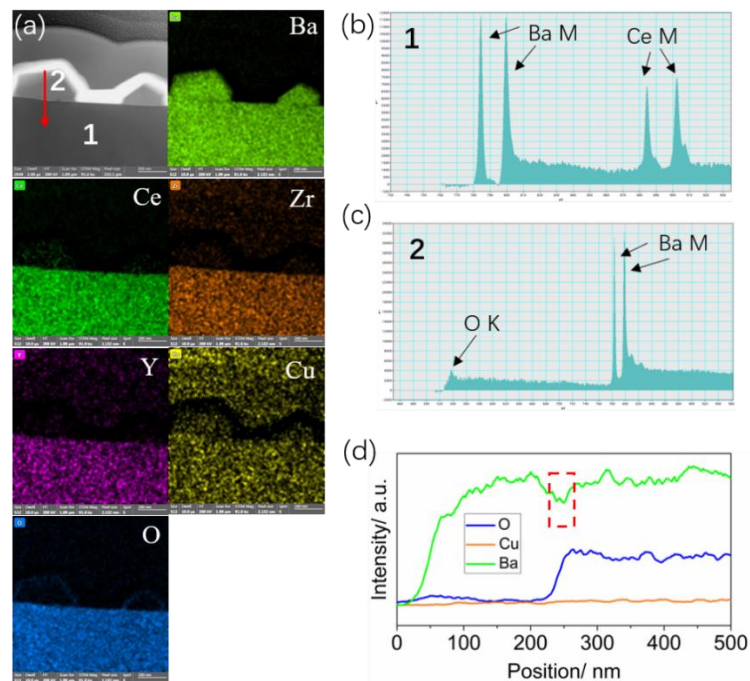


Figure 3-15. (a) HAADF image of the irregular-shaped phase after reduction the cleaved surface at 900 °C for 12 h and its EDS mappings, (b) Ba and Ce EELS spectra of the position 1 in (a), (c) Ba and O EELS spectra of the position 2 in (a), (d) EDS line scan of the area indicated by the red arrow in (a).

For the polygonal-shaped phase obtained at 900 °C in the red circle in Figure 3-12 (e2), the EDS mappings in Figure 3-15 (a) demonstrate that it is significantly rich in barium. The EELS spectrum in Figure 3-15 (c) further confirms the existence of barium but also suggests the presence of a small amount of oxygen. For the perovskite bulk, the EELS spectrum in Figure 3-15 (b) verifies the barium and cerium species, while the

cerium is still in the  $Ce^{4+}$  state after reduction. From the EDS line scan of the area in (a), Figure 3-15 (d) indicates a small barium deficiency in the interface between the barium metal phase and the perovskite substrate, about 50 nm thick, which is probably due to the diffusion of lattice  $Ba^{2+}$  to form the Ba metal phase.

Until now, we may still feel confused about the exsolution process of the Cu particles since there are some other phases present during the period. In the following experiment, the individual particles are followed to have a better observation on the particle evolving and phase change.

It is also worth mentioning that native surface of Cu-BCZY also has the similar Cu exsolution as the cleaved surface, not only in Ba deficient samples but also in Ba stoichiometric compositions. This indicates the AO segregation problem did not hinder the Cu exsolution from the doped BCZY material.

### **3.3.4 Particle tracking for exsolution process study**

The as-prepared d-BCZYC6 pellet was polished in order to obtain a flat and uniform, bulk-like surface for better observing exsolution process. Normally, exsolution is more favourable to occur on the polished surface not only because of the removal of A-site enriched surface but also the creation of more defects for nucleation. Here, individual particles are followed treated with different reduction time and temperature in 5%  $H_2/Ar$ . The microstructures are shown in Figure 3-16.

Before reduction, the pellet surface is clean with a defect at the area labeled 11, seen from Figure 3-16 (a). After reducing the pellet at 600 °C for 2 h (Figure 3-16 b), some nanoparticles (e.g., particles 4, 6, 7, 8, 9) appear on the surface as well as a number of irregular-shaped phases like shown at position 3, 10 and 12. This kind of phase actually also exists underneath the spherical particles, like particle 9. At the defect 11, a mixture of nanoparticles with the irregular-shaped phases underneath is observed. Further reducing the pellet for another 10 h (Figure 3-16 c), the irregular-shaped phases at 1, 2, 3, 5, 10, 12 disappear with nanoparticles exsolving instead at their corresponding position, and their particle size is smaller than the particles achieved after 2 h's reduction. Therefore, the irregular-shaped phases obtained after reduction for 2 h seem

to provide a transient stage for particle exsolution, we name them as “intermediate phase”. For the particles at position 4 and 8, two or three smaller particles are deposited instead of the single one. As this phenomenon is thermodynamically contradictory, it is believed one possible reason is that the single particle is kicked out by the high energy electron beam in the operation of scanning microscope, resulting in the new growth of particles at the corresponding position when reduced at 600 °C for another 10 h. At position 11, a large irregular-shaped phase appears instead of the nanoparticles. EDS mappings in Figure 3-17 indicate that this phase is accumulated with barium and copper, and especially rich in oxygen, suggesting a barium cuprate phase. Moreover, there is a small crack and convex shape around areas 1, 2 and 3 which means more defects are created during exsolution, destabilizing the substrate perovskite. By further reduction of the pellet at 700 °C for another 10 h (Figure 3-16 d), the individual particles at positions 4 and 8 grow into a larger one again, while no morphological changes seems to occur for particles 1, 2, 5, 6, 7, 9 except the expanded size. However, some particles turned out to be much smaller and even diminish, such as the particles 12 and 10. Particle population decreases a great extent at this temperature. Now areas near position 1, 2 and 3 exhibit a new irregular shaped phase, probably being another barium cuprate composition but with different stoichiometry from 11 in Figure 3-16 (c). At position 11, the barium cuprate phase decomposes and the original defect before reduction is exposed now with several particles surrounded. Position 10 seems to become a bit convex as we observed at 1, 2 and 3 before, and it is expected to form a new phase like area 3 after further reduction. Then, reducing the pellet at 800 °C for another 10 h (Figure 3-16 e), we can see that the particles become even less present and grow larger (particles 1, 2, 4, 5, 6, 8, 12). Unsurprisingly, the supposed barium cuprate phase at area 3 decomposes now and a distinguish crack is around there with a large particle on top. The convex area at area 10 is also replaced by a new irregular shaped phase as expected, which is possibly the Ba-Cu-O oxide with different element ratio from the previous ones. Moreover, a large particle is occupied at the defect position 11 with the surrounded particles disappearing. Finally, another reduction treatment at 900 °C for 10 h is carried out, only limited numbers of particles are left (Figure 3-16 f). Some larger

particles, like particle 4, 8 and 9, turn to be smaller but have not diminished. For the Ba-Cu-O oxide like phase at 7, 9 and 10, only spherical particles are achieved without any other defect or new phases appearing. It is also noticed that the crack at position 3 is recovering and attaches better with surroundings, and the defect at position 11 is totally decorated by the particles.

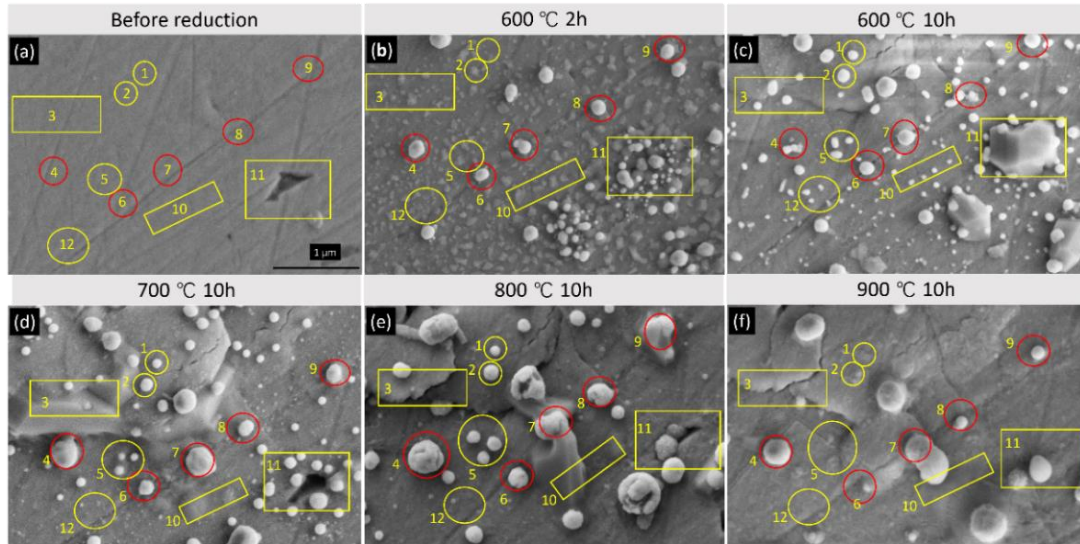


Figure 3-16. SEM images of the polished  $\text{Ba}_{0.95}\text{Ce}_{0.5}\text{Zr}_{0.3}\text{Y}_{0.14}\text{Cu}_{0.06}\text{O}_{3-\delta}$  pellet reduced at different temperature, (a) before reduction, (b) 600 °C for 2 h, (c) 600 °C for 10 h, (d) 700 °C for 10 h, (e) 800 °C for 10 h, (f) 900 °C for 10 h. Note that each SEM image was taken in the same area after the pellet was reduced at each stage.

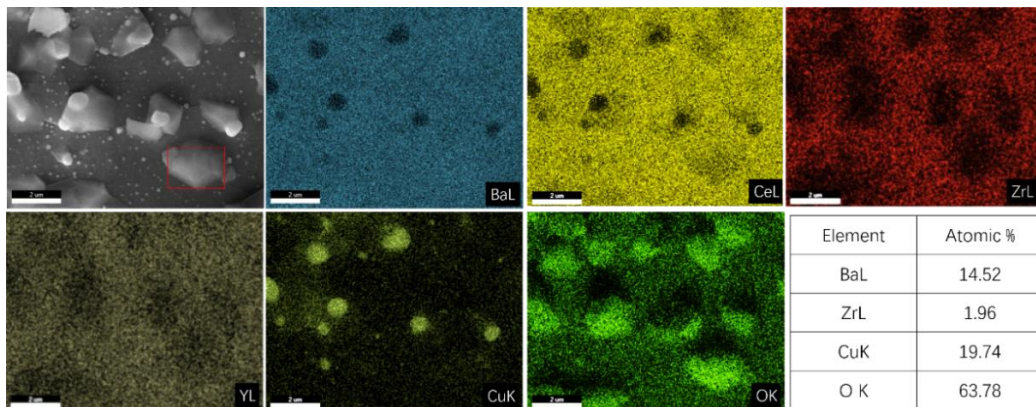


Figure 3-17. EDS mappings and quantitative results of the irregular-shaped phase obtained after reducing the polished  $\text{Ba}_{0.95}\text{Ce}_{0.5}\text{Zr}_{0.3}\text{Y}_{0.14}\text{Cu}_{0.06}\text{O}_{3-\delta}$  pellet at 600 °C for 12 h in 5%  $\text{H}_2/\text{Ar}$ .

In order to identify the “intermediate phase” and the one underneath the particles in Figure 3-16 (b), TEM sample is prepared from the position shown in the inset of Figure 3-18 (a). It is noticed that instead of socketing into the larger irregular-shaped phase, the particle is actually held by it from the side. EDS mappings show that the large irregular-shaped phase is rich in barium and oxygen, probably being  $\text{BaO}_x$ . The large particle on top is copper metal. Below the polished surface, the Cu particle is not embedded in the perovskite oxide neither, instead, it is immersed in another  $\text{BaO}_x$  phase, which is also verified in the EDS quantitative result (1) in Figure 3-17 (b). Note here the oxygen EDS quantification result is less believable due to the limited detection ability of light element by EDS. For the perovskite bulk area 2 in (a), the EDS quantitative result illustrates a similar composition as the designed  $\text{Ba}_{0.95}\text{Ce}_{0.5}\text{Zr}_{0.3}\text{Y}_{0.14}\text{Cu}_{0.06}\text{O}_{3-\delta}$  but with less copper that is resulted from its exsolution. For the small particle immersed in the  $\text{BaO}_x$ , the TEM image in Figure 3-18 (c) demonstrates that there are some even smaller particles surrounding it. While the EDS mappings show a Cu metal composition in this particle, the quantitative result (position 3) in Figure 3-18 (d) reveals the existence of small amount of barium, which is also indicated in the barium EELS spectrum in Figure 3-18 (f). More obviously, the dual composition in the particle can be seen from the BSE image in Figure 3-19 (b), where a different contrast is shown in a single particle, with the dark colour implying light weighed element and the similar white colour as the matrix, indicating the heavy element Ba. For the copper state in the particle, the EELS spectrum in Figure 3-18 (e) shows that copper mostly exists in the state of  $\text{Cu}^0$  with little amount of  $\text{Cu}^{2+}$ , which may be due to the oxidation when handling the sample in air. This oxidation can also be observed in the oxygen mapping in Figure 3-18 (c).



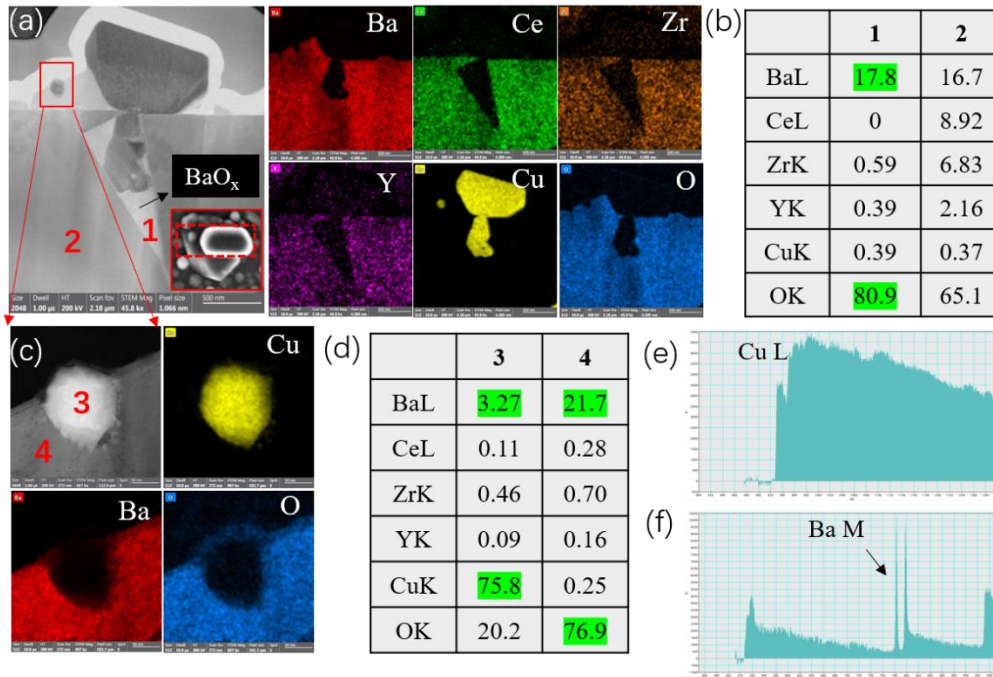


Figure 3-18. TEM characterization of the polished  $\text{Ba}_{0.95}\text{Ce}_{0.5}\text{Zr}_{0.3}\text{Y}_{0.14}\text{Cu}_{0.06}\text{O}_{3-\delta}$  sample reduced at 600 °C for 2 h in 5%  $\text{H}_2/\text{Ar}$ . (a) The TEM image and EDS mappings of the particle with irregular shaped phase, the inset is the SEM image of the TEM sample), (b) EDS quantitative results of area 1 and 2 in (a), (c) TEM image and EDS mappings of the small particles immersed in the irregular-shaped phase, (d) the EDS quantitative results of area 3 and 4 in (c), (e) and (f) the Cu and Ba EELS spectra in the small particle in (c), respectively.

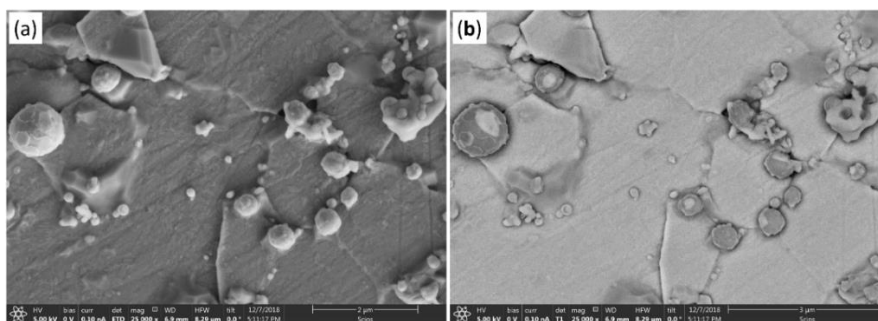


Figure 3-19. SEM (a) and BSE (b) images of the polished  $\text{Ba}_{0.95}\text{Ce}_{0.5}\text{Zr}_{0.3}\text{Y}_{0.14}\text{Cu}_{0.06}\text{O}_{3-\delta}$  pellet reduced at 900 °C for 10 h.

For the small intermediate phase indicated in Figure 3-16 (b), it is characterized in

Figure 3-20. The EDS mappings show that the intermediate phase obtained at 600 °C is rich in barium and oxygen. Although copper seems to exist, it shows a same contrast with the perovskite bulk. While the bulk has been illustrated to contain only a negligible amount of copper in Figure 3-18 (b), position 2, the copper species in the intermediate phase can be neglected. The existence of barium and oxygen is further indicated by the EELS spectra in Figure 3-20 (b).

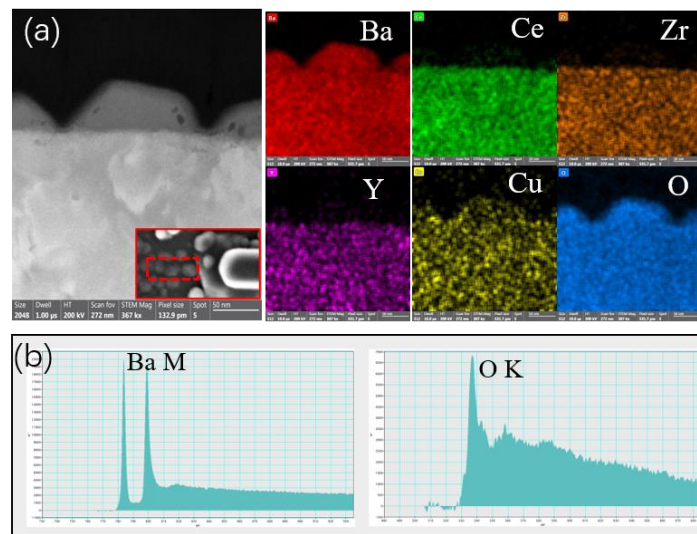


Figure 3-20. (a) TEM image and EDS mappings of the intermediate phase on the polished surface after reduced at 600 °C for 2 h in 5% H<sub>2</sub>/Ar, the inset is the SEM image of the intermediate phase, (b) Ba and O EELS spectra from the intermediate phase.

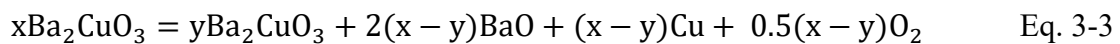
### 3.3.5 Analysis with phase diagram of BaO-CuO system

Conventionally suggested exsolution mechanism is divided into four processes, including diffusion, reduction, nucleation and growth<sup>2, 10-11, 33, 35</sup>. Initially, when the perovskite is reduced, lattice oxygen is stripped creating oxygen vacancies and releasing electrons. As the reduction progresses, the large amount of oxygen vacancies destabilizes the local structure balance, producing the spontaneously B-site metal nucleation at some points by adopting electrons. The nucleation is likely to occur on the surface due to the lower nucleation barrier. The surface nucleation results in deeper ions in the bulk diffusing to the surface to compensate for the compositional gradient



until an equilibrium is reached or the re-organization of surface limits the process. This causes particles growth. The ion diffusion depth can be hundred nanometers.

However, in our work, the Cu exsolution process seems to be different and more complex. In addition to the exsolution from perovskite bulk, there exists a competing process that exsolution occurs from an intermediate phase, that is, the frequently observed barium contained phases. For further analysis, the phase equilibrium between BaO and CuO need to be known. Figure 3-21 (a) presents the phase equilibrium of the BaO-CuO system in air.<sup>36-39</sup> As can be seen, there are three eutectic points (E1, E2, E3) at about 900 °C. Compositions in equilibrium change with the BaO and CuO fraction in the system and temperature. Since in our material, the amount of barium is far more than copper, here we firstly analyze the barium rich region (BaO > 66.7 mol%) of the phase diagram. From high to low temperature, the liquid phase (BaO + Ba<sub>2</sub>CuO<sub>3</sub>) is solidified below 900 °C, followed by a composition change from BaO + Ba<sub>2</sub>CuO<sub>3</sub> (900 – 717 °C), to BaO<sub>2</sub> + Ba<sub>2</sub>CuO<sub>3</sub> (710 – 305 °C), and finally to BaO<sub>2</sub> + Ba<sub>2</sub>Cu<sub>3</sub>O<sub>5</sub> at low temperature (< 305 °C). The schematic of phase change is illustrated in Figure 3-21 (b). However, different from the condition determined in the phase diagram in Figure 3-21 (a), our experiment is conducted in a reducing atmosphere, with an exsolution of Cu particles. In order to simplify the analysis, we firstly assume that the phase equilibrium in the reducing atmosphere is the same as the one in air and the reduction temperature is held at 800 °C. Therefore, Cu will exsolve from the Ba<sub>2</sub>CuO<sub>3</sub> compound that is in equilibrium with BaO at this temperature. The Cu exsolution process will be accompanied with precipitation of BaO, otherwise a phase with richer barium than 2:1 will be obtained, which disobeys the phase equilibrium at 800 °C. This process can be expressed as Eq. 3-3 and Figure 3-21 (c).



With exsolution progresses, BaO proportion in the BaO-CuO system increases, leading to the phase equilibrium left shift parallelly until a limited value of pure BaO, shown as the blue arrow in Figure 3-21 (a). However, if the process of Cu exsolution from Ba<sub>2</sub>CuO<sub>3</sub> is slow, the Ba<sub>2</sub>CuO<sub>3</sub> will not decompose completely when the temperature is held at 800 °C for 12 h. This will lead to a continuous decomposition

during cooling as long as the temperature is high enough for the decomposition reaction. In this case, the equilibrium on cooling does not follow a vertical line but a line with a positive slope, shown as the red arrow in Figure 3-21 (a). This process will finish until a temperature at which the exsolution is thermodynamically limited and followed by a vertical change in phase equilibrium at low temperature. Therefore, the incomplete decomposition of  $\text{Ba}_2\text{CuO}_3$  finally gives rise to a mixture of  $\text{BaO}_2$  and  $\text{Ba}_2\text{CuO}_3$  at room temperature. This may well explain why we observe the barium cuprate phases rich in oxygen in Figure 3-18.

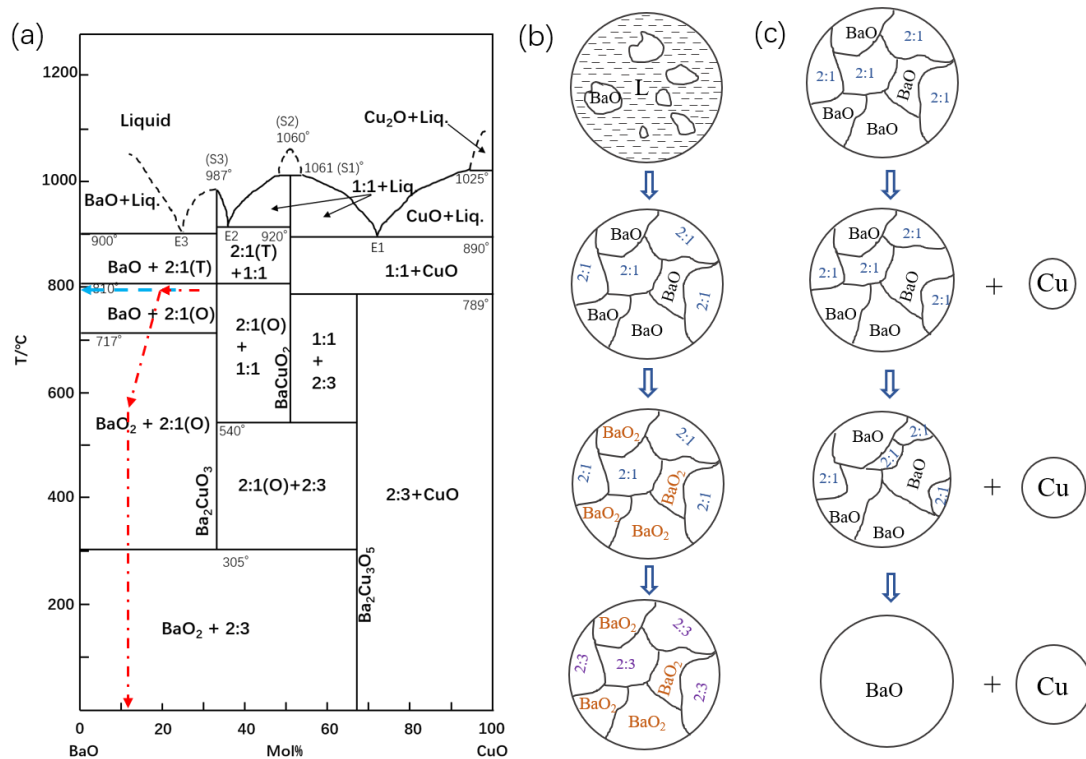
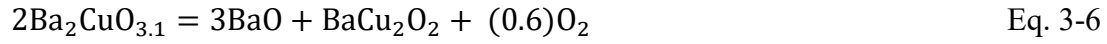
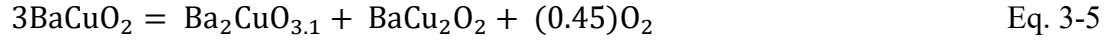
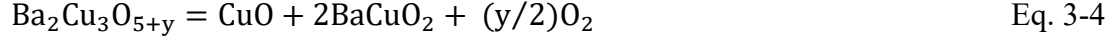


Figure 3-21. (a) Phase diagram of BaO-CuO system (Figure reproduced from Ref. 38 and 39), (b) schematic of phase change on cooling in the BaO rich region ( $\text{BaO} > 66.7 \text{ mol\%}$ ) in air, (c) schematic of phase change on cooling in the BaO rich region ( $\text{BaO} > 66.7 \text{ mol\%}$ ) in 5%  $\text{H}_2/\text{Ar}$  at 800 °C.

The above analysis is based on the assumption that the phase equilibrium in reducing atmosphere is the same as that in air. However, the real equilibrium is changed with oxygen partial pressure. As shown in Figure 3-22, the compositions that can bear

the P(O<sub>2</sub>) from high to low is Ba<sub>2</sub>Cu<sub>3</sub>O<sub>5</sub>, Ba<sub>2</sub>CuO<sub>3</sub>, BaCuO<sub>2</sub> and BaCu<sub>2</sub>O<sub>3</sub>, respectively. The conversion between these phases in the Ba-Cu-O system is related to the following reactions:



Under even lower P(O<sub>2</sub>), the Cu<sub>2</sub>O and BaO can be reduced into the corresponding metal state by the equation 3-9 and 3-10:



However, it is worth to mention that the phase diagram can only express thermodynamically instability of a phase but does not offer kinetic information, which means that it is unknown how quickly the unstable phase decomposes. This indicates that although the P(O<sub>2</sub>) in our experiment may reach a value of 10<sup>-29</sup>, the Ba-Cu-O phase is possible to exist, even the BaO<sub>2</sub> phase. In addition, the migration of lattice Cu<sup>2+</sup> towards the surface at high temperature may cause a local composition change. All these factors will result in a different Ba-Cu-O system but not only the Ba-rich one we discussed before. On reheating the pellet at higher temperature, the previously formed barium cuprate phase has enough time for decomposition, while at some positions a barium cuprate phase is prone to be produced, as observed in Figure 3-16. Apparently, the higher reheating temperature and the local composition change due to ions migration will give rise to the different barium fraction in the barium cuprate phase, which is verified from the varied morphologies in the keep arising large irregular-shaped phase in Figure 3-16. Although the “intermediate phase” on the polished surface reduced at 600 °C for 2 h (Figure 3-16 b) is indicated to be BaO<sub>x</sub> by the TEM analysis, it is believed that lattice Cu<sup>2+</sup> would diffuse towards the BaO<sub>x</sub> phase to form Ba-Cu-O system if the sample is reduced for a longer time.

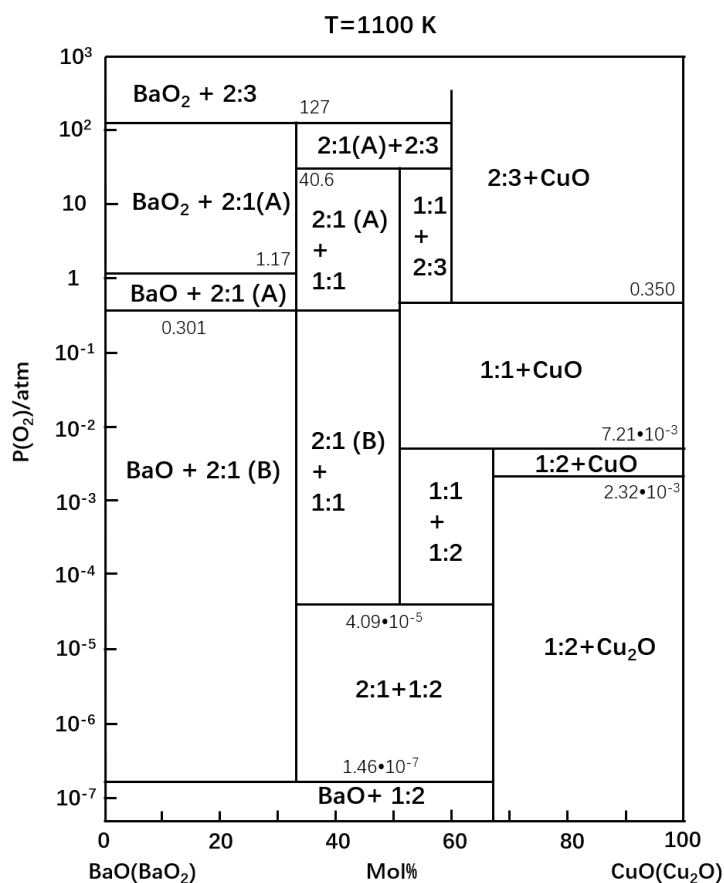


Figure 3-22. Phase diagram of the system BaO(BaO<sub>2</sub>)-CuO(Cu<sub>2</sub>O) at 1100 K. A and B denote the phases Ba<sub>2</sub>CuO<sub>3.3</sub> and Ba<sub>2</sub>CuO<sub>3.1</sub>, respectively. Figure reproduced from Ref. 38.

Overall, Cu exsolving from the doped barium cerate zirconate oxide also undergoes a quite different route: the exsolution of barium cuprate phase from the perovskite and the exsolution of Cu particles from the barium cuprate phase. This process is illustrated as the schematic in Figure 3-23. When the Cu-doped BCZYC pellet is reduced at lower temperature, i.e., 600 °C, Ba<sup>2+</sup> firstly diffuse towards the perovskite surface in the form of BaO<sub>x</sub> precipitates. Afterwards, the lowered migration barrier due to the removal of Ba<sup>2+</sup> from the lattice benefits Cu<sup>2+</sup> to diffuse to the BaO<sub>x</sub>, forming a Ba-Cu-O system contained barium cuprate. When reduced at higher temperature, Cu particle is exsolved from the barium cuprate phase, accompanied with the BaO<sub>x</sub> product. The lattice ions diffusion towards the surface and the exsolution of particles make the local composition to reorganize, and thus producing a new Ba-Cu-O

system in other positions. Since Cu is exsolved from the barium cuprate phase, some barium is possible to exist in the Cu particles due to the incompletely decomposition.

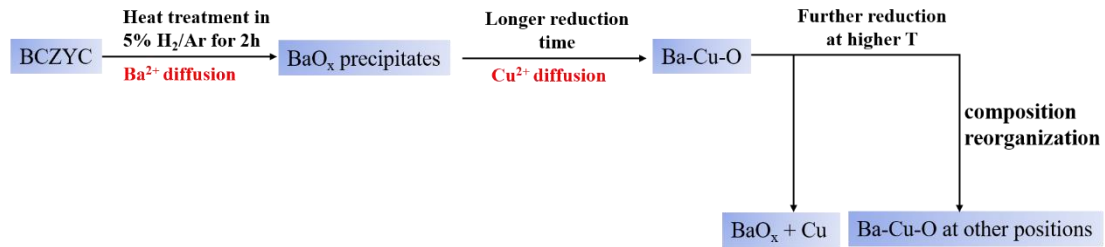


Figure 3-23. Schematic of Cu exsolution process from barium cerate zirconate oxide.

Herein, although B-site exsolution accompanied by A-site enrichment on the surface has been proposed<sup>10, 40</sup>, the phenomenon of co-segregation of A and B-site in the form of eutectic oxide has not been found before. The two-step exsolution mechanism explains the similar exsolution on the native and cleaved surface in this material.

### 3.3.6 VT-XRD characterization of polished BCZYC pellet

Variable temperature powder X-ray diffraction (VT-XRD) is an effective technique to monitor solid phase transitions *in situ* as a function of temperature. Thus, the polished d-BCZYC6 pellet was tested by VT-XRD in 5% H<sub>2</sub>/N<sub>2</sub>. The testing temperature profile is shown as Figure 3-24 that each temperature is held for 6 h and XRD pattern is collected every 2 h (3 times at each temperature) on heating, and only 1 h is held to collect the XRD data at each temperature during cooling down.

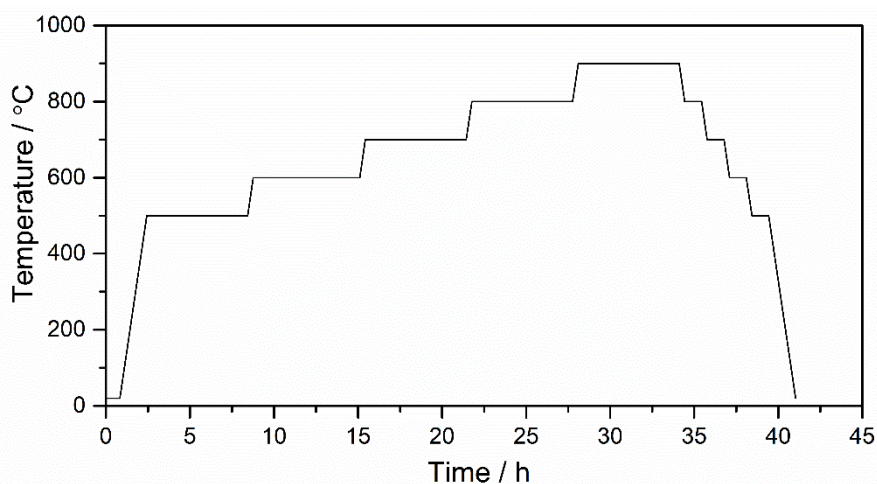


Figure 3-24. Temperature program of the VT-XRD test.

The VT-XRD patterns are collected using MoK $\alpha$  radiation. A shoulder may be observed at each peak in Figure 3-25 (a), and this is due to the stripping of peaks from MoK $\alpha$ 2. The perovskite peaks are indexed with the cubic symmetry. There is no apparent change in the XRD pattern until reducing the pellet at 600 °C for 2 h, distinguished by the apparition of two distinct peaks at 19.45° and 22.47°, corresponding to the (111) and (200) plane of Cu metal, respectively. It is noticed that the peak intensity of Cu metal after reducing at 600 °C for 2 h only increased slightly with temperature and time, indicating that the nucleation process may be time-dependent, but the growth of copper is relatively fast. In addition, another two weak peaks at 11.17° and 12.85° appear at 700 °C, but they are difficult to identify. During cooling, there is no apparent evidence for the phase change in Figure 3-25 (b).

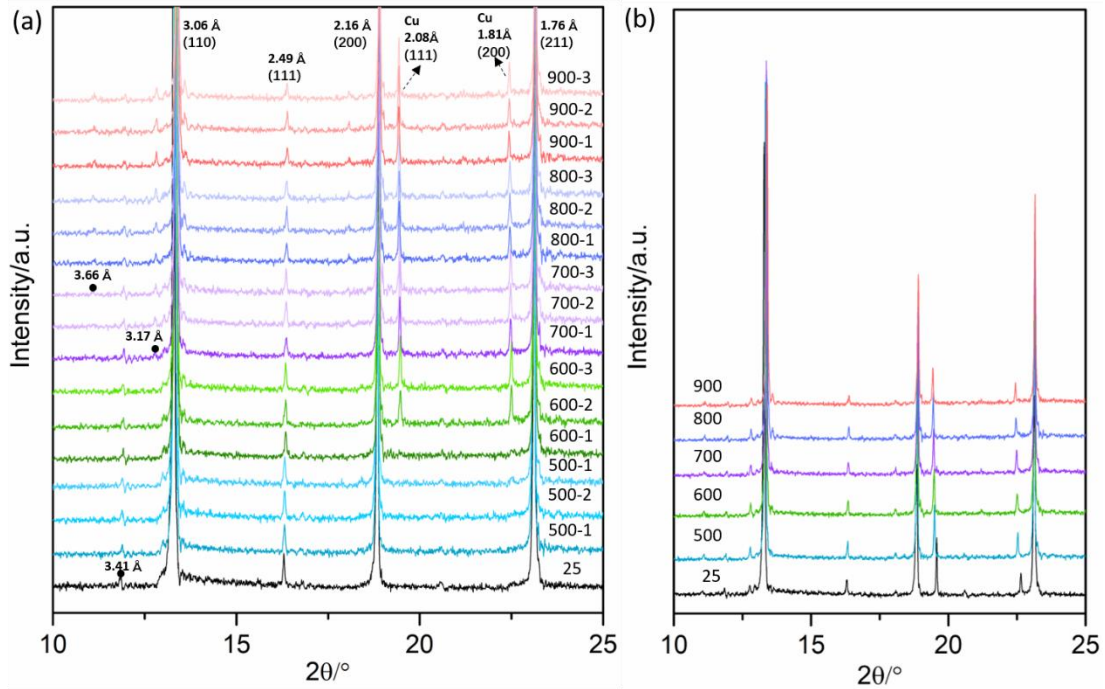


Figure 3-25. VT-XRD results of polished  $\text{Ba}_{0.95}\text{Ce}_{0.5}\text{Zr}_{0.3}\text{Y}_{0.14}\text{Cu}_{0.06}\text{O}_{3-\delta}$  pellet on heating (a) and on cooling (b) in 5%  $\text{H}_2/\text{N}_2$ . (Patterns are collected with MoK $\alpha$  radiation).

As Figure 3-26 (a) displayed, the d-BCZYC6 pellet exhibits a larger unit cell after thermal treatment in the reducing atmosphere than the initial one at room temperature. Cell expansion is supposed to occur with increasing temperature, however, the cell volume of 500 °C is larger than that at 600-900 °C. It is thus suspected that the significant increase of cell volume after being reduced at 500 °C for 2 h (the first XRD collection point at 500 °C) is due to the reduction of surface  $\text{Ce}^{4+}$  to  $\text{Ce}^{3+}$  on the one hand, with ionic radius increasing from 0.87 Å to 1.01 Å for six-fold coordinated cerium. On the other hand, lattice oxygen is gradually stripped from the perovskite structure, creating oxygen vacancies in the corresponding lattices. The removal of lattice oxygen increases the repulsion between highly charged B-site cations and leads to an expansion of the cell. Further reduction at 500 °C results in a dramatic drop in the cell volume. This is supposed to be due to the diffusion of  $\text{Ba}^{2+}$  to form  $\text{BaO}_x$  on the surface and the followed  $\text{Cu}^{2+}$  migration, producing Ba-Cu-O system. The lattice  $\text{Ba}^{2+}$  and  $\text{Cu}^{2+}$  migration process takes place until reducing the pellet at 600 °C for 2 h. After that, with

further reduction at 600 °C until 900 °C, there is only a slow linear increase in the cell volume which is attributed from the thermal expansion of the structure since almost the same tendency is observed in the cell volume on cooling. The thermal expansion effect can be further confirmed by calculating the thermal expansion coefficient between 600 and 900 °C, which is about  $6.8 \times 10^{-6} \text{ K}^{-1}$ , close to the reported value of  $\sim 8 \times 10^{-6} \text{ K}^{-1}$ .<sup>41-42</sup> During this period, only decomposition of the barium cuprate occurs without considerable cation diffusion to the surface that can produce a significant change in the cell volume. Certainly, particle coarsening and mild local composition re-organization keep taking place with the reduction, thus resulting in the slight variation of cell volume.

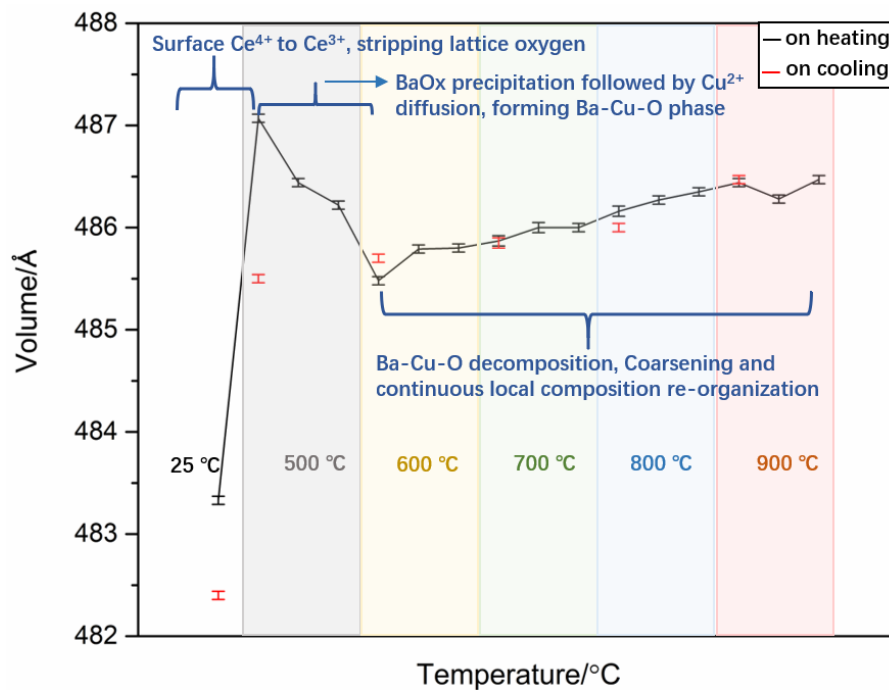


Figure 3-26. Unit cell volume of the polished  $\text{Ba}_{0.95}\text{Ce}_{0.5}\text{Zr}_{0.3}\text{Y}_{0.14}\text{Cu}_{0.06}\text{O}_{3-\delta}$  pellet on heating (black line) and on cooling (red symbols) calculated by the Rietveld refinement of VT-XRD patterns. The symbol size represents the error.

It is noticed that on cooling the cell volume remains similar at temperature between 600 °C and 900 °C as those on heating, however, at 500 °C, it did not change back to the value on heating. This indicates that the segregated barium species is not able to re-dope into the perovskite structure.



### 3.3.7 TGA test on the BCZYC oxide in reducing atmosphere

Considering a stoichiometric perovskite  $ABO_3$ , during reduction, oxygen is stripped from the perovskite lattice, giving rise to a structure with oxygen deficiency  $ABO_{3-\delta}$ , while  $\delta$  can represent the extent of reduction of the material. Because this process is accompanied by a mass change due to the loss of lattice oxygen, the change in oxygen stoichiometry can be monitored by thermogravimetric analysis (TGA). For a perovskite decreasing weight from  $m_{ABO_3}$  to  $m_{ABO_{3-\delta}}$ , its number of moles is conserved, as expressed in the following equation:

$$\frac{m_{ABO_3}}{\mu_{ABO_3}} = \frac{m_{ABO_{3-\delta}}}{\mu_{ABO_{3-\delta}}} \quad \text{Eq. 3-11}$$

where  $\mu_{ABO_3}$  and  $\mu_{ABO_{3-\delta}}$  represent the molar weight of the oxidized and reduced perovskite, respectively. While the reduced perovskite is a product that depicts losing oxygen from the  $ABO_3$  oxide, the  $\mu_{ABO_{3-\delta}}$  can be written as  $\mu_{ABO_3} - \delta \cdot A_o$  ( $A_o$  is the atomic weight of oxygen). Then Eq. 3-7 can be expressed as:

$$\frac{m_{ABO_3}}{m_{ABO_{3-\delta}}} = \frac{\mu_{ABO_3}}{\mu_{ABO_3} - \delta \cdot A_o} \quad \text{Eq. 3-12}$$

Obtaining the extent of reduction:

$$\delta = \frac{\mu_{ABO_3}}{A_o} \cdot \frac{m_{ABO_3} - m_{ABO_{3-\delta}}}{m_{ABO_3}} \quad \text{Eq. 3-13}$$

where  $\frac{m_{ABO_3} - m_{ABO_{3-\delta}}}{m_{ABO_3}}$  is the weight loss can be measured in TGA.  $\delta$  is usually expressed in oxygen atoms per formula unit of perovskite (at./f.u.).

In Figure 3-27 is the TGA results of d-BCZYC4 and d-BCZYC6 measured in 5%  $H_2/N_2$  as a function of temperature. The slower weight loss before 380 °C observed in sample d-BCZYC4 is because of the desorption of adsorbed water, which is about 0.9 wt%. This type of weight loss is not obvious in d-BCZYC6 sample. But for both samples, their mass began to decrease in a more rapid speed after continuous heating above 380 °C, which is attributed to the removal of lattice oxygen in the structure. After reducing at 900 °C for about 8 h, both samples achieved their largest mass loss, indicating the reduction reaches the equilibrium state. The extent of reduction is calculated to be 0.18 at/f.u. for d-BCZYC4 and 0.17 at/f.u. for d-BCZYC6.

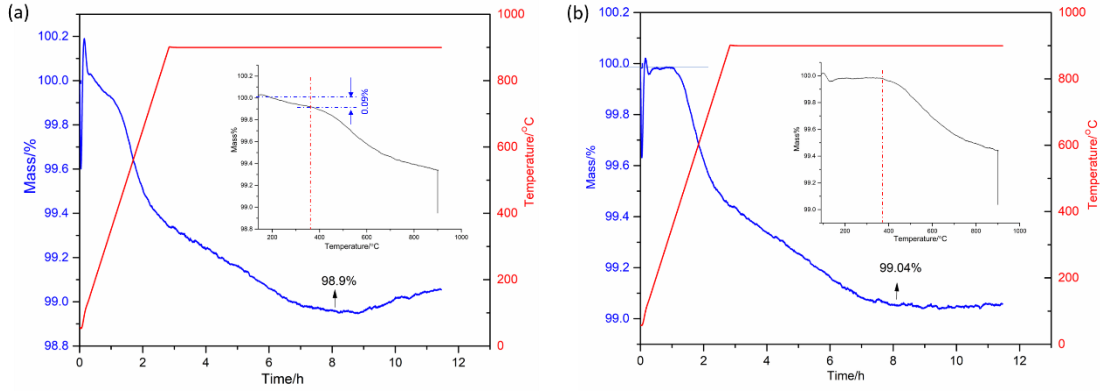


Figure 3-27. Thermal gravimetric analysis of  $\text{Ba}_{0.95}\text{Ce}_{0.5}\text{Zr}_{0.3}\text{Y}_{0.14}\text{Cu}_{0.04}\text{O}_{3-\delta}$  (a),  $\text{Ba}_{0.95}\text{Ce}_{0.5}\text{Zr}_{0.3}\text{Y}_{0.14}\text{Cu}_{0.06}\text{O}_{3-\delta}$  (b) in 5%  $\text{H}_2/\text{N}_2$  as a function of temperature.

In the reduction, the bulk oxygen migration towards the surface is driven by balancing out the gradient that produced from firstly created oxygen vacancies near the perovskite surface. If oxide ions are trapped in the bulk and cannot diffuse to the surface, only limited surface oxygen can be removed, resulting in a low reduction extent. Thus, the diffusion ability of oxide ions can affect the reduction extent of the materials. In the migration process, lattice oxygen transport from one site to a neighbouring oxygen vacancy, leaving behind a new oxygen vacancy and electrons. So, the migration of oxygen vacancies is in the opposite direction to the lattice oxide ions. To accomplish the hopping, the initial B-O bond (B<sub>1</sub>-O<sub>0</sub> bond in Figure 3-28) needs to be broken, and the free oxide ion will migrate through the triangle described by two A-site cations and one B-site cation while remaining equidistant to the B<sub>0</sub>-site cation. This leads to a curved path for the migration. Many researchers have suggested that the mobility of vacancies is higher in lattices that exhibit high symmetry owing to the minimal repulsing effects<sup>43-44</sup>. Looking back the axial *c/a* values for d-BCZYC4 and d-BCZYC6 in Figure 3-6, where d-BCZYC4 exhibits a much closer value to the ideal hexagonal unit cell, meaning a much equal distance between the lattice points and more homogeneous chemical environment in the structure, which promotes better oxide ion mobility. Moreover, as we discussed in the cell parameter and *c/a* ratios section that d-BCZYC6 has excessive oxygen vacancies that leads to more deviation from the ideal hexagonal lattice, the further introduction of oxygen vacancy with reduction treatment

may cause oxide ions trapped in the lattice and thus gives a slightly lower extent of reduction.

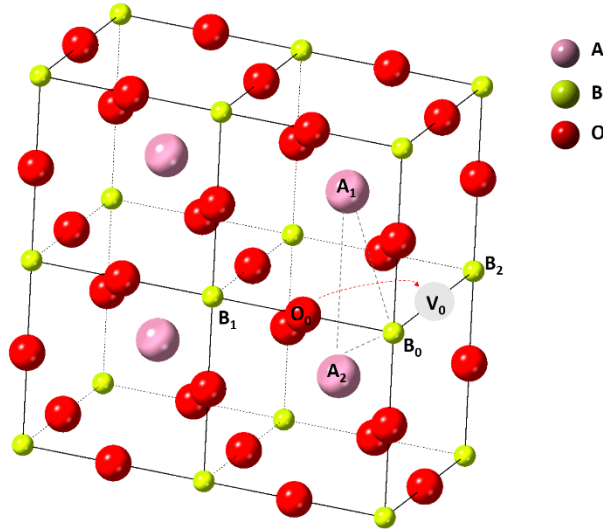


Figure 3-28. Schematic diagram of the migration of the oxide ion in an ideal perovskite.  $V_0$  is the oxygen vacancy.

### 3.4 Plasma treatment on the reduced BCZYC pellet

Copper oxide has been extensively studied as a catalyst in CO oxidation reaction because of its relatively high catalytic reactivity and more cost-effective than other high active noble metals, such as palladium, platinum and rhodium<sup>45-49</sup>. Nanoparticles prepared from *in situ* exsolution from perovskite oxide exhibit high resistance to coking under severe condition because of their strong interaction with the substrate. However, the Cu particles obtained from BCZYC are not small enough and some of the large particles are not nano-scale, providing low surface-to-volume ratios. CuO nanowires (NWs) can be prepared from annealing the copper mesh or plate in the air at 500 °C for two days<sup>50-51</sup>. However, it is quite time-consuming. Plasma was applied a lot in tailoring the surface morphology and function of materials, especially in increasing the specific surface areas<sup>52-54</sup>. Moreover, plasma treatment only takes a few seconds or minutes, which is very flexible and time effective. Herein, 60% oxygen/argon plasma treatment was carried out on the reduced BCZYC pellet to modify the particle surface and be

oxidizing to copper oxide for catalyzing CO oxidation in the future.

The morphology of the metal particles is changed greatly after treating the reduced  $\text{Ba}_{0.95}\text{Ce}_{0.5}\text{Zr}_{0.3}\text{Y}_{0.14}\text{Cu}_{0.06}\text{O}_{3-\delta}$  pellet under oxygen/argon plasma for only 10 mins (Figure 3-29). Instead of a spherical smooth surface, the particle surface looks like an urchin. This change of the morphology not only happened on the larger particles (type I particles) but also the small ones (type II particles). However, different from the type I particles, there seems to be some nanoparticles surrounding the type II particles, which can be seen clearly from the contrast in the image from T2 detector in Figure 3-29 (d), that gather in the black circle with the diameter about 250-350 nm. There is not this kind of black circle in the sample before plasma treatment, suggesting that this phenomenon is caused by the plasma treatment. The tree like pattern in Figure 3-29 (d) is possibly a result of peritectic reaction in the BaO-CuO system during exsolution.

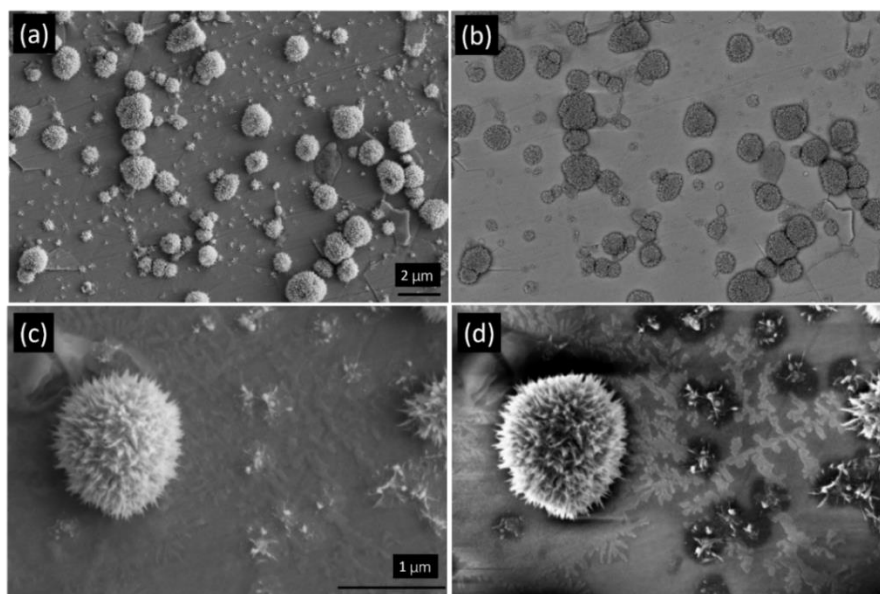


Figure 3-29. SEM images (a, c), BSE image (b) and SEM image obtained from T2 detector (d) of polished  $\text{Ba}_{0.95}\text{Ce}_{0.5}\text{Zr}_{0.3}\text{Y}_{0.14}\text{Cu}_{0.06}\text{O}_{3-\delta}$  pellet reduced at 800 °C for 12 h in 5%  $\text{H}_2/\text{Ar}$  followed by 60% oxygen/argon plasma treatment for 10 mins.

Transmission electron microscope (TEM) characterization was taken on the reduced  $\text{Ba}_{0.95}\text{Ce}_{0.5}\text{Zr}_{0.3}\text{Y}_{0.14}\text{Cu}_{0.06}\text{O}_{3-\delta}$  pellet after plasma treatment to further observe the microstructure of the particles. As shown in the HAADF images and EDS mapping

and spectra results in Figure 3-30 (a), the urchin-like particle contains a dense core and a porous whisker structure grown on top. EDS mapping shows that both the core and whiskers mainly consist of Cu element. Oxygen is also detected in the whole particle, however, EDS spectra in Figure 3-30 (b) showed that compared with the strong Cu peak intensity, oxygen is relatively limited in the core area but is more in the whiskers. Area 2 and 3 have a similar spectrum, suggesting a similar composition between them. Therefore, the dense core is not fully oxidized by plasma. The pellet surface, bulk and interface between the particle and substrate is also compared in the EDS spectra in Figure 3-30 (c). The apparent different one is area 4, whose composition is mostly Cu. For the other four areas, 1, 2, 3, and 5, their compositions are almost the same as the substrate composition.

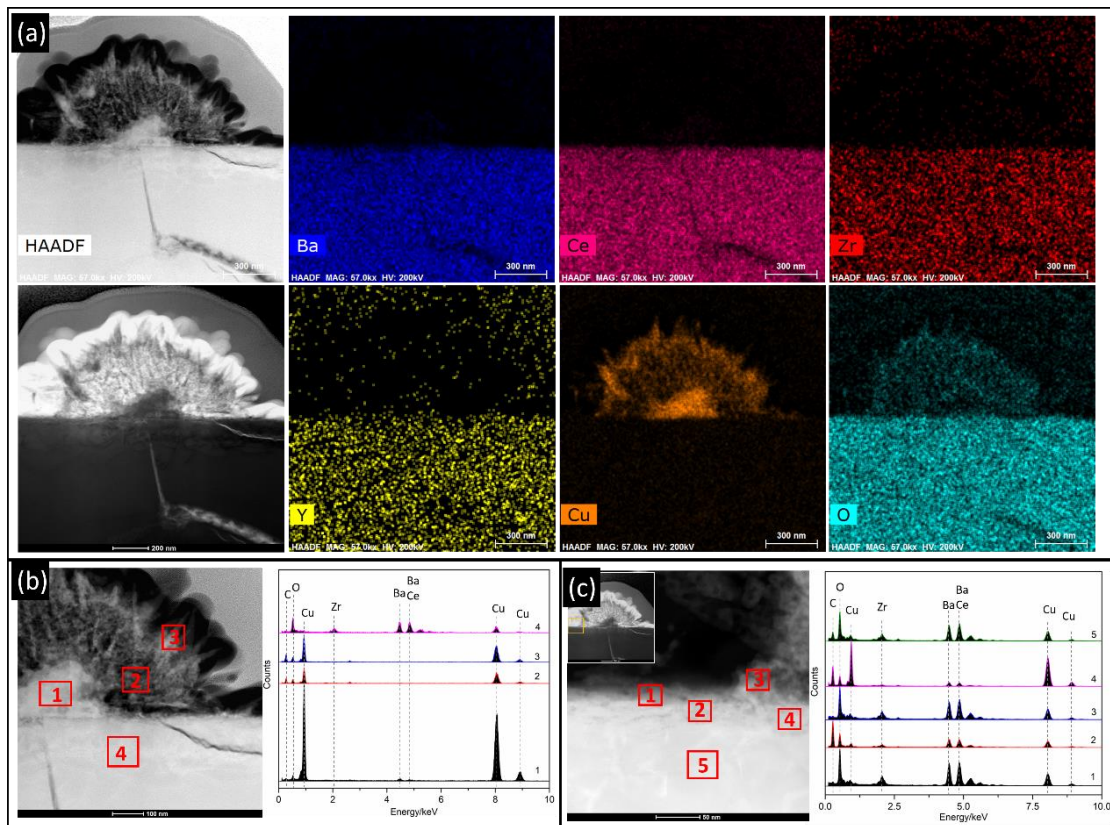


Figure 3-30. (a) EDS mapping of a large particle on  $\text{Ba}_{0.95}\text{Ce}_{0.5}\text{Zr}_{0.3}\text{Y}_{0.14}\text{Cu}_{0.06}\text{O}_{3-\delta}$  pellet after reduction and plasma treatment (60% oxygen plasma for 10 mins), (b, c) EDS spectra of the particles and bulk material. (The TEM characterization for the plasma-treated particle was carried out by Dr. David Miller)

For the oxidation of the copper particles by oxygen plasma, this is because the plasma contains the excited gas atoms and molecules ( $O_2$ ) that carry a large amount of internal energy. The active oxygen species bind to active surface sites (Cu) all over the pellet material. Once the surface of Cu particle is being oxidized by oxygen species with forming numerous oxidized nuclei, the oxidation reaction will move towards the centre of the particle as O species is supposed to diffuse more quickly than Cu. However, we do not investigate more detail here on the formation process of the urchin and whisker morphology.

Instead of growing into an urchin morphology, the type II particles in Figure 3-29 only have a few whiskers on top and have a lot of nanoparticles surrounding them, as revealed by the HAADF image in Figure 3-31. The central spherical particle is about 60 nm and composed of only Cu element indicated from the EDS mapping, suggested being Cu metal. Apart from the 60 nm particle, Cu element is also distributed in the whisker and the clusters on both sides. In fact, the surrounded Cu cluster consists of several nanoparticles with a diameter of 20 nm. But there is a contrast difference on the Cu mapping, with low contrast on the shell of the particles, including both the central particle and the surrounded 20 nm particles. Combined with the EDS mapping of oxygen, it is supposed that only the out layer of Cu particles is oxidized by the plasma and the whisker should be uniformly copper oxide. This core-shell copper-copper oxide structure suggests that before plasma treatment they are supposed to be Cu metal nanoparticles. However, we did not observe the surrounded nanoparticles in the SEM image of samples before plasma treatment. Figure 3-31 (b) is the EDS spectra of the particle and its surroundings, from which we can see area 1 and 4 have the similar composition with the substrate at 9, while area 2, 5, 6 and 8 have a much stronger Cu peak in addition to the substrate peaks. Comparing the peak intensity of Ba and Ba, Ce, Ba peak is relatively stronger at position 2, 5, 6, 8 than at 1, 4, 9. Therefore, it is assumed that areas in 2, 5, 6, 8 is Ba rich and probably has Ba-Cu-O oxide phase. At area 3 and 7, only Cu and very weak O peak is observed without the other elements, suggesting a pure Cu or copper oxide phase here. The bulk area under the particle was also analyzed in Figure 3-31 (c) but did not show much difference with what is observed in Figure 3-

28 (c).

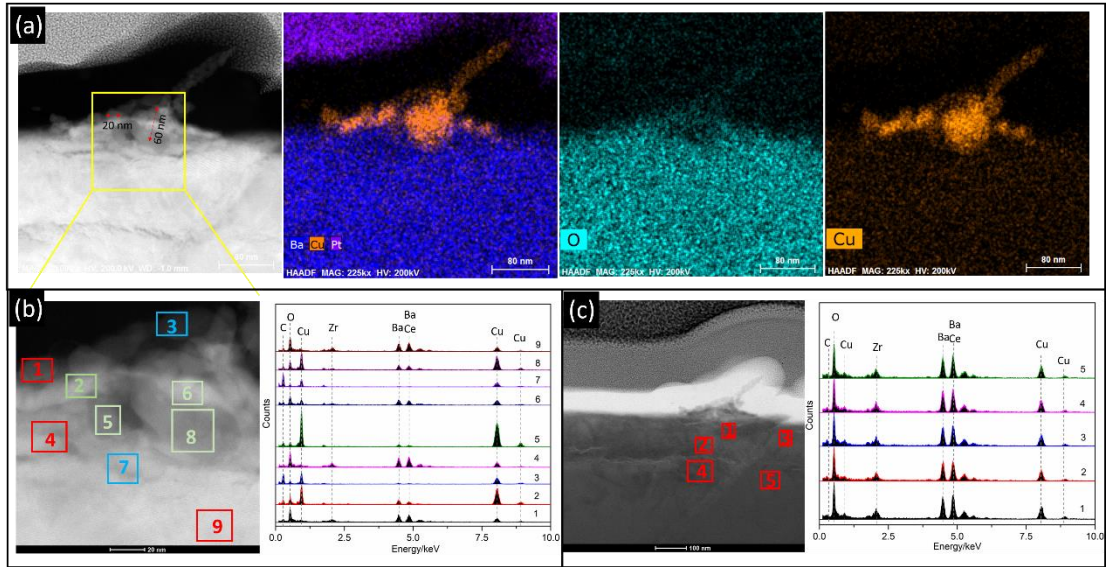


Figure 3-31. (a) EDS mapping of a small particle on reduced  $\text{Ba}_{0.95}\text{Ce}_{0.5}\text{Zr}_{0.3}\text{Y}_{0.14}\text{Cu}_{0.06}\text{O}_{3-\delta}$  pellet after plasma treatment (60% oxygen plasma for 10 mins), (b, c) EDS spectra of the particles and bulk material.

The surrounded nanoparticles can be better observed in another particle shown in Figure 3-32. The size of the central particle is approximately 90 nm while the surrounded particles are around 15 nm. Each 15 nm nanoparticle connects tight and both the 90 nm and 15 nm particles' surface are oxidized by oxygen plasma. We think that these surrounded nanoparticles are the same ones we observed of the black circle in Figure 3-29 (d). A possible reason for the adherent nanoparticles is that the high energy plasma causes some metal species evaporation nearby the large particle and immediately deposition when the plasma supply is stopped. EDS Spectra in Figure 3-32 (b) exhibits strong Cu peak at area 2 mixed with some substrate peaks (Ba peak is stronger than (Ba, Ce), which is the same phenomenon as showed in Figure 3-31 (b). The other four areas, 1, 3, 4 and 5, possess similar composition with parent oxide.



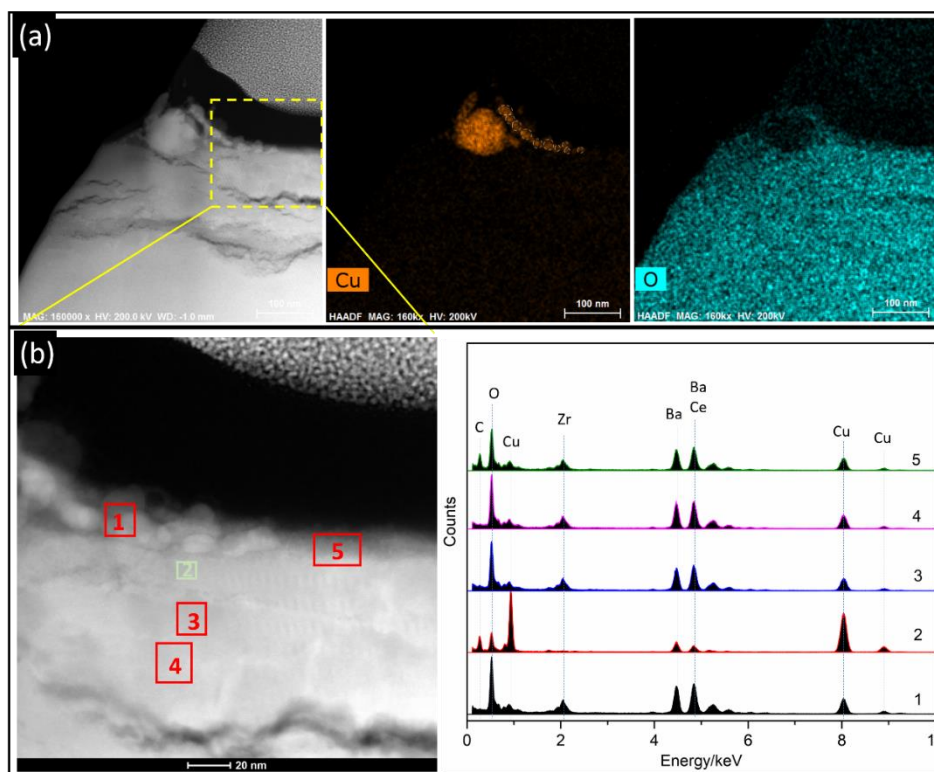


Figure 3-32. (a) EDS mapping of a small particle on reduced  $\text{Ba}_{0.95}\text{Ce}_{0.5}\text{Zr}_{0.3}\text{Y}_{0.14}\text{Cu}_{0.06}\text{O}_{3-\delta}$  pellet after plasma treatment (60% oxygen plasma for 10 mins), (b) EDS spectra of the particles and bulk material.

### 3.5 DC Conductivity tests on BCZYC oxide

#### 3.5.1 DC conductivity tests of BCZYC oxide prepared from two-steps

In solid state fuel cells or electrolysis cells, the electrochemical reaction occurs at the triple phase boundary (TPB) where the reactive gases, oxide ions or protons and electrons meet. In order to maximize the effective area of the TPB, an ideal electrode material should act as a mixed ionic and electronic conductor (MIEC) apart from the higher electrocatalytic activity towards desirable reactions.<sup>2</sup> While exsolved copper particles on our prepared proton conducting electrolyte material BCZYC provide the catalytically active sites for an electrode material, the electronic conductivity was measured by Four-point probe method. The bar for the conductivity test was prepared by grinding the 1350 °C sintered pellet and pressing into bar followed by another heat treatment at 1350 °C for 12 h. The relative density of the sintered bar was measured to



be 80.8% of theoretical density for  $\text{BaCe}_{0.5}\text{Zr}_{0.3}\text{Y}_{0.16}\text{Cu}_{0.04}\text{O}_{3-\delta}$  and 87.3% for  $\text{Ba}_{0.95}\text{Ce}_{0.5}\text{Zr}_{0.3}\text{Y}_{0.14}\text{Cu}_{0.06}\text{O}_{3-\delta}$ . The decreased density of the bar compared with the pellet sintered for one time is possibly due to the lack of liquid phase sintering and solid reactive sintering. The test was carried out at 600 °C in 5%  $\text{H}_2/\text{N}_2$  and the corresponding results are shown in Figure 3-33. The peak conductivity of  $\text{BaCe}_{0.5}\text{Zr}_{0.3}\text{Y}_{0.16}\text{Cu}_{0.04}\text{O}_{3-\delta}$  is about  $0.0045 \text{ S cm}^{-1}$  after reduction at 600 °C for 3.17 h and suddenly drops to  $0.0035 \text{ S cm}^{-1}$ . After leaving the measurement to run for about 15 h, the conductivity remains stable and decreases during cooling until being non-conductive at room temperature (RT). For the  $\text{Ba}_{0.95}\text{Ce}_{0.5}\text{Zr}_{0.3}\text{Y}_{0.14}\text{Cu}_{0.06}\text{O}_{3-\delta}$  sample, its highest conductivity reaches  $1.26 \text{ S cm}^{-1}$  followed by a continuous dropping to  $1.0 \text{ S cm}^{-1}$  after 20 h' reduction. At RT, the conductivity also decreases to almost 0, suggesting that both samples exhibit a semiconductor behaviour. The morphology of the bar is investigated by SEM characterization. Apparently, the population of exsolved Cu nanoparticle in sample  $\text{BaCe}_{0.5}\text{Zr}_{0.3}\text{Y}_{0.16}\text{Cu}_{0.04}\text{O}_{3-\delta}$  is less than that in  $\text{Ba}_{0.95}\text{Ce}_{0.5}\text{Zr}_{0.3}\text{Y}_{0.14}\text{Cu}_{0.06}\text{O}_{3-\delta}$  on the native surface (shown in Figure 3-33 b, e), and the nanoparticle size on the native surface of the two bars is among 30-100 nm. An irregular shaped phase in Figure 3-33 (e) is observed at the grain boundary in sample  $\text{Ba}_{0.95}\text{Ce}_{0.5}\text{Zr}_{0.3}\text{Y}_{0.14}\text{Cu}_{0.06}\text{O}_{3-\delta}$ . In addition to the native surface, the bar is also cracked with the mortar and pestle to check the inner surface. Surprisingly, it is found in Figure 3-33 (c, f) that there are Cu nanoparticles exsolved in the inner surface even if the density of the bars is over 80%, with particle size in the range of 30-100 nm and 150-900 nm for  $\text{BaCe}_{0.5}\text{Zr}_{0.3}\text{Y}_{0.16}\text{Cu}_{0.04}\text{O}_{3-\delta}$  and  $\text{Ba}_{0.95}\text{Ce}_{0.5}\text{Zr}_{0.3}\text{Y}_{0.14}\text{Cu}_{0.06}\text{O}_{3-\delta}$ , respectively. It is supposed that the larger, interconnected particles could have a positive effect on improving the material electronic conductivity.

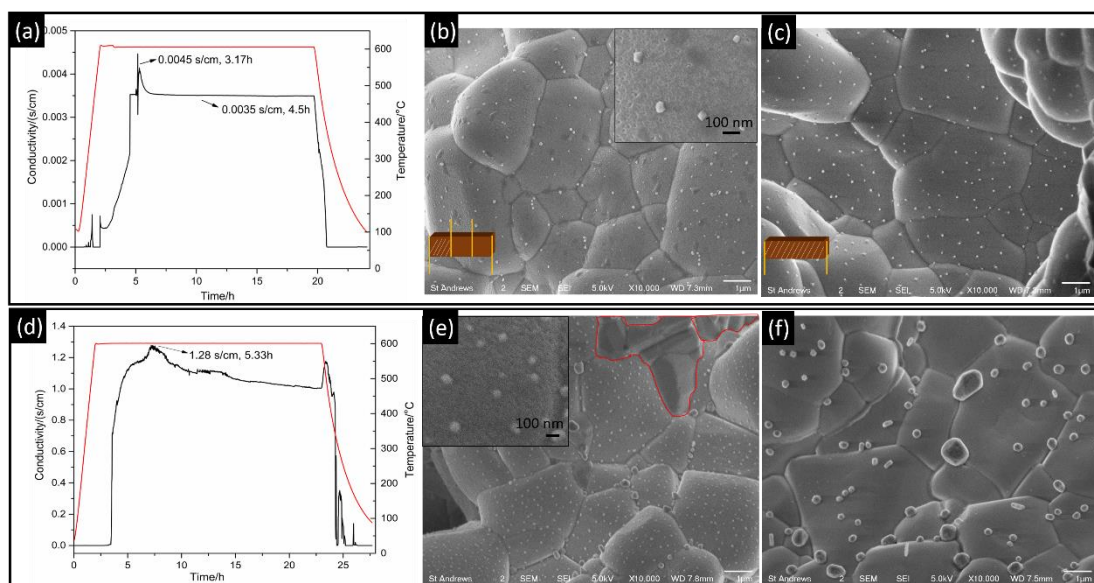


Figure 3-33. Four-point probe conductivity test in 5% H<sub>2</sub>/N<sub>2</sub> at 600 °C for BaCe<sub>0.5</sub>Zr<sub>0.3</sub>Y<sub>0.16</sub>Cu<sub>0.04</sub>O<sub>3-δ</sub> (a) and Ba<sub>0.95</sub>Ce<sub>0.5</sub>Zr<sub>0.3</sub>Y<sub>0.14</sub>Cu<sub>0.06</sub>O<sub>3-δ</sub> (d), SEM image of native and inner surface for Ba<sub>0.95</sub>Ce<sub>0.5</sub>Zr<sub>0.3</sub>Y<sub>0.16</sub>Cu<sub>0.04</sub>O<sub>3-δ</sub> (b) and (c) respectively and for Ba<sub>0.95</sub>Ce<sub>0.5</sub>Zr<sub>0.3</sub>Y<sub>0.14</sub>Cu<sub>0.06</sub>O<sub>3-δ</sub> (e) and (f) respectively. (The native surface is the one exposed in the reducing atmosphere, and the inner surface is the one exposed when the dense bar is cracked by mortar.)

However, the particle size and distribution in Figure 3-33 is different from what was achieved on pellet in Figure 3-12. We think that it is because the bar for conductivity test is sintered from the powder that is already pure phase, which means the material of the bar is sintered twice, causing a different sintering process from the pre-calcined powder with the lack of solid reactive sintering and liquid sintering. This may influence the homogeneity of perovskite composition and even the surface energy and lattice distortion, which further changes the Cu exsolution behaviour.

### 3.5.2 DC conductivity tests on BCZYC oxides prepared from one-step

Follow on from above, the bar was then prepared with pre-calcined powder to make it sinter for only one time (called prepared in one-step), and the relative density of this kind of bar was about 98.5%. DC conductivity test was carried out in air and the results are presented in the following Figure 3-34. Generally, the conductivities of Cu-

doped BCZY in air are not very high, ranging from 0.01 to 0.1 S cm<sup>-1</sup> depend on the Cu concentration and Ba-deficiency. The conductivities in air are quite stable after testing for a long time. All the samples show a semi-conductor property with decreased conductivity during cooling (except the 6% Cu-doped BCZY). Figure 3-34 (b) presents the influence of Cu concentration and Ba-deficiency on the Cu-BCZY conductivity in air. Basically, for the A-site stoichiometric Cu-BCZY, the conductivity increases with Cu doping concentration, but for 5% Ba-deficient samples, the trend is opposite, with slightly change between each other. And the effect of Ba-deficiency seems to be greater on the samples with higher Cu doping level.

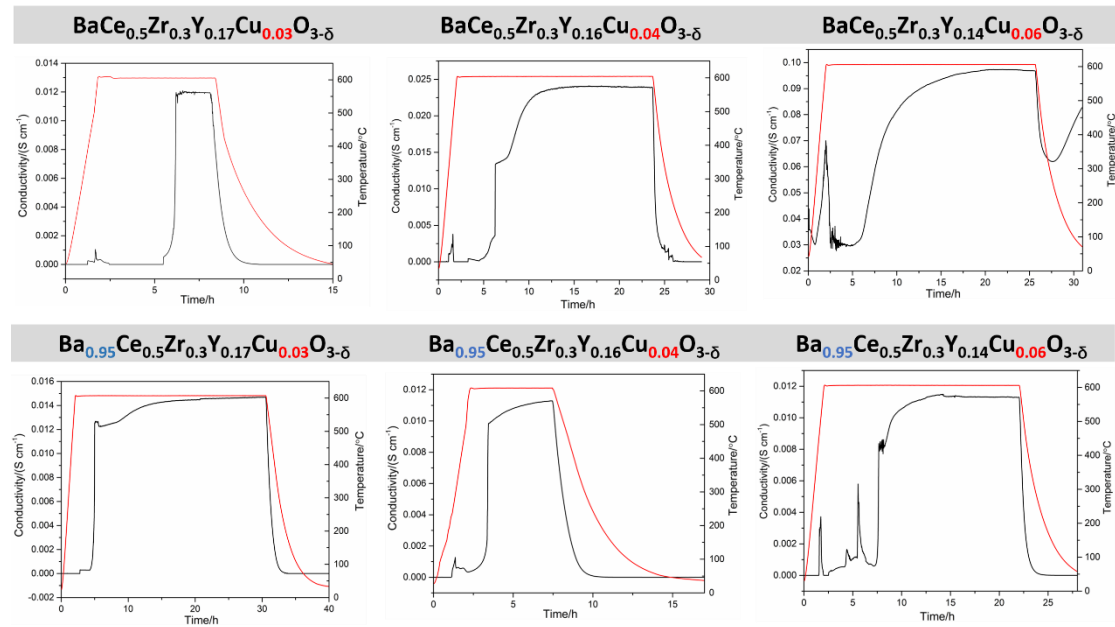


Figure 3-34. DC conductivity test of Cu-doped BCZY (one – step) in air.

Conductivity performed in reducing atmosphere are listed in Figure 3-35 and the comparison between tests in air and H<sub>2</sub> is presented in Table 3-2. Conductivities of Cu-BCZY in 5% H<sub>2</sub>/N<sub>2</sub> are much higher than that achieved in air, and the highest conductivity is obtained in d-BCZYC4, with the peak conductivity at 600 °C reaching 44 S cm<sup>-1</sup> after reduced for about 10 h, which is over 3000 times higher than its conductivity in air. For the stoichiometric samples, the peak conductivity does not change much (6.8 – 7.8 S cm<sup>-1</sup>) with Cu ratio, as clearly seen in Figure 3-35 (b).

However, when introducing 5% Ba deficiency, significant change happens to the 4% Cu-BCZY, with conductivity being the lowest in stoichiometric samples becoming the highest ( $44.0 \text{ S cm}^{-1}$ ) in the deficient ones. This different change is believed to be related with the increased unit cell volume and more ideal hexagonal unit cell we discussed in the previous XRD characterization section, where the Ba-deficiency in BCZYC4 improves the  $c/a$  ratio to closer ideal value that is advantageous for the mobility of ions, and thus gives a higher extent of exsolution, which is responsible for the electronic conductivity. The slightly more oxygen loss in TGA test has also indicated a more exsolution in the deficient BCZYC4 oxide even with less copper doping concentration than 6%.

It can also be observed that the dramatic rising of conductivities for each sample occurred at different reduction times, as it took about 20-35 h reduction for the stoichiometric BCZYC bar and about 10 h for the Ba-deficient compositions. Moreover, in stoichiometric BCZYC, the time acquired for jumping to the peak conductivity decreases with higher Cu doping ratio. This suggests that both A-site deficiency and Cu concentration play a role in accelerating exsolution. It has been reported that A-site deficiency facilitates the formation of oxygen vacancies and thus the release of electrons that participating in the reduction of metal ions. In addition, B-site cation migrated to the adjacent B-site along a curved trajectory in the perovskite, and this trajectory curve is in the (110) planes (Figure 3-36)<sup>10</sup>. When the A-site vacancies are presented, the migration repulsion force from positively charged A-site is lowered, and thus lowers the B-site migration barrier, facilitating its diffusion. In addition, as we proposed that the competing route for Cu exsolution is from the intermediate barium cuprate phase, the deficient samples are expected to require longer time for barium migration to form this intermediate phase at surface and thus a slower exsolution. However, the time-efficient exsolution in the deficient compositions indicates that the barium diffusion is not the exsolution rate control parameter while the exsolution rate is more determined by the copper transportation in the lattice. It is also noticed that conductivities are not so stable after a long time of reduction but gradually decrease (call it decay), and the decay rate is calculated according to Eq. 3-14. Comparing the

decay rate summarized in Table 3-2, Ba deficient samples seem to result in a higher decay rate than the stoichiometric ones, except the 4% Cu-BCZY. The different behaviour in 4% Cu-BCZY is believed to be owing to the improved hexagonal lattice of perovskite lattice after introducing A-site deficiency in it.

$$R_{\text{decay}} = (\sigma_{\text{max}} - \sigma_{\text{min}}) / (\sigma_{\text{max}} \cdot t) \quad \text{Eq. 3-14}$$

Where  $R_{\text{decay}}$  is the decay rate,  $\sigma_{\text{max}}$  is the maximum conductivity at 600 °C,  $\sigma_{\text{min}}$  is the minimum conductivity after dwelling at 600 °C for a long time, which is the value before cooling,  $t$  is the time between the two values.

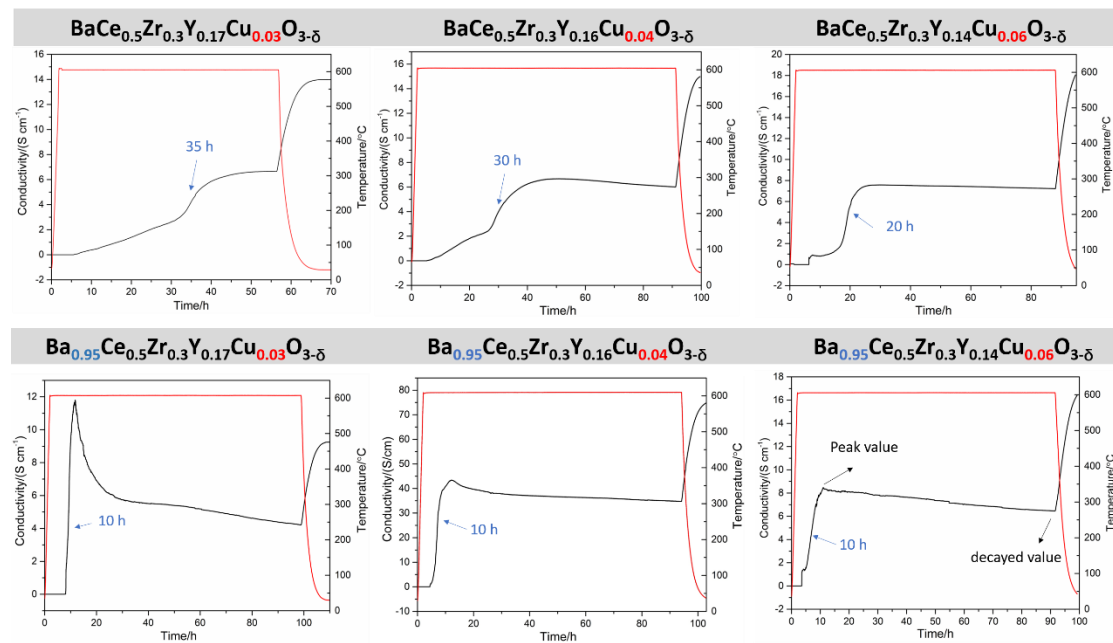


Figure 3-35. DC conductivity test of Cu-doped BCZY (one – step) in 5% H<sub>2</sub>/N<sub>2</sub>.

Furthermore, different from the semi-conductor property achieved in air, the results in 5% H<sub>2</sub>/N<sub>2</sub> reveal a metallic behaviour of the samples during cooling, with the conductivity becoming over twice at room temperature (RT) than that at 600 °C (Figure 3-35). Although the conductivity of d-BCZYC8 (0.32 S cm<sup>-1</sup>) is rather low in 5% H<sub>2</sub>/N<sub>2</sub>, the materials still show a metallic behaviour after exsolution. But when the Cu doping concentration is as low as 2%, Cu exsolution is not able to transform the semiconducting material into a metal property one because of the less population of Cu nanoparticles and very low conductivity.

Table 3-2. DC conductivity results of Cu-BCZY (one – step) in 5% H<sub>2</sub>/N<sub>2</sub>.

stoichiometry Conductivity/(S <sub>cm</sub> <sup>-1</sup> )		d-0.02	0.03	d-0.03	0.04	d-0.04	0.06	d-0.06	d-0.08
		<b>Air</b>		0.024	0.012	0.014	0.023	0.011	0.095
<b>5% H<sub>2</sub>/N<sub>2</sub></b>	<b>peak</b>	0.014	Keep increasing	11.9	6.8	44.0	7.8	8.3	0.42
	<b>decayed</b>	No decay	6.9	4.1	6.0	34.9	7.1	6.5	0.32
	<b>RT</b>	0	14.0	9.2	15.1	75.0	18	16.5	0.61
	<b>Decay rate %/h</b>	0	0	0.75	0.29	0.26	0.15	0.27	0.42

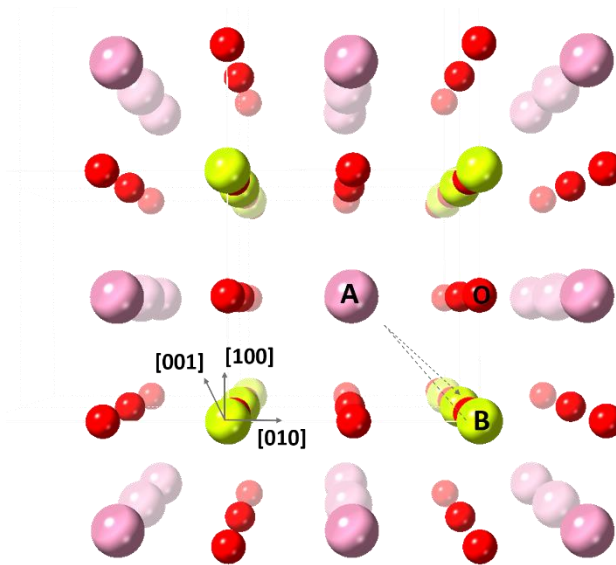


Figure 3-36. B-site cations diffusion trajectory down the [001] direction, according to De Souza et al.<sup>55</sup>

The metallic conduction behaviour of perovskite in reducing atmosphere is believed to be produced from the exsolution of Cu nanoparticles. SEM images of the bar after the conductivity test in Figure 3-37 demonstrate that copper particles are not only exsolved on the native surface but also the inner surface. This was observed after the bar was cracked. On the inner surface, most of the particles are distributed on the grain boundary. Extra phases are also observed on both the native surfaces of d-BCZYC4 and d-BCZYC6, and they are possibly Ba-Cu-O oxide or BaO<sub>x</sub> revealed by EDS quantification analysis and BaCO<sub>3</sub> suggested by XRD. However, this extra phase

at the grain boundaries is found to be a lot on the d-BCZYC6 surface but not on d-BCZYC4, which is considered to have a negative effect on the conductivity and give rise to a lower electrical conductivity in higher Cu doping level. As known before, after plasma treatment, the type II particles are surrounded some 10-20 nm Cu particles, forming a black circle in the SEM image from T2 detector. The SEM images with low magnification can be seen in Figure 3-38. Apparently, the black circle, composed of partially oxidized Cu NPs, forming a connected path on the, especially along the grain boundary.

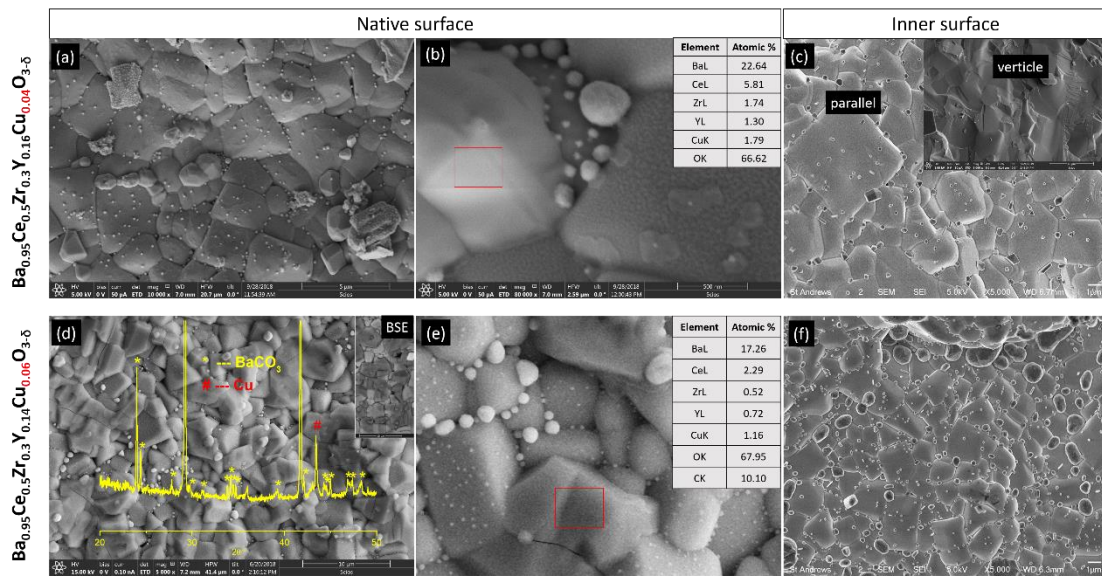


Figure 3-37. SEM images of  $\text{Ba}_{0.95}\text{Ce}_{0.5}\text{Zr}_{0.3}\text{Y}_{0.16}\text{Cu}_{0.04}\text{O}_{3-\delta}$  (a, b, c) and  $\text{Ba}_{0.95}\text{Ce}_{0.5}\text{Zr}_{0.3}\text{Y}_{0.14}\text{Cu}_{0.06}\text{O}_{3-\delta}$  (d, e, f) after conductivity tests in 5%  $\text{H}_2/\text{Ar}$ . (a, b, d, e) are the native surface and (c, f) are the inner surface. The inserted tables in (b, e) are the EDS quantification analysis of the phases in red squares; the inserted SEM images (c, d) are the inner vertical surface; the inserted XRD pattern in (d) is the XRD of the bar.



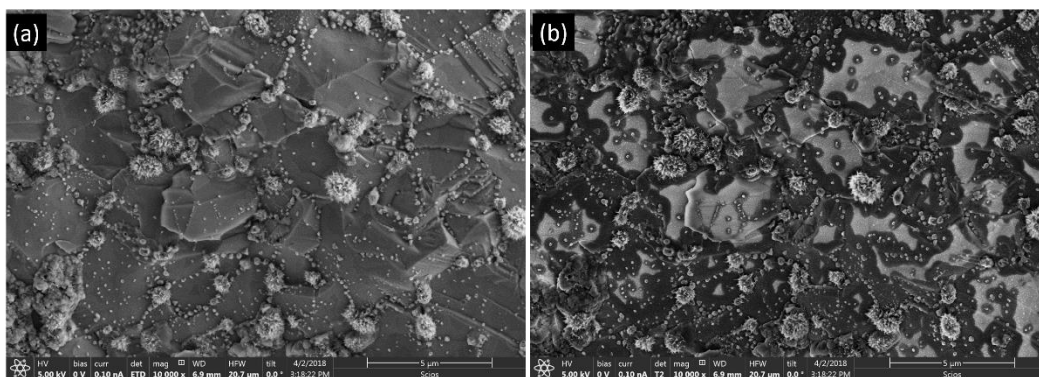


Figure 3-38. SEM images of cleaved surface of  $\text{Ba}_{0.95}\text{Ce}_{0.5}\text{Zr}_{0.3}\text{Y}_{0.14}\text{Cu}_{0.06}\text{O}_{3-\delta}$  with Cu exsolution after 60% oxygen/argon plasma treatment for 10 mins. (a) from ETD detector, (b) from T2 detector.

Conventional exsolution mechanism suggests that the diffusion depth of ions from the bulk to the surface is only about 80-130 nm, and the process would be finally limited by the equilibrium or the surface re-organization<sup>11</sup>. In this case, a ‘core-shell’ structure of perovskite grains after exsolution is formed, with surfaces having depleted B-site cation and the core having unchanged stoichiometry<sup>11</sup>. By using DFT simulations, Gao et al.<sup>35</sup> also suggested that particle nucleation preferred to take place on the native surface rather than in the bulk because of its smaller strain energy  $E_{\text{strain}}$ . Additionally, they revealed that surface morphology had an important influence on nucleation. For example, a higher population of particles were observed at the grain boundary region and concave sites. This was because dihedral angle,  $\varphi$  at these sites was smaller than that at the flat surface ( $\pi$ ), leading to a lowered surface energy and favourable nucleation. However, in our work, Cu exsolution occurred not only on the native surface but also on the inner surface, even the bar prepared in one-step has 98.5% relative density, which means that it is not very likely for hydrogen gas to diffuse into the bulk to create oxygen vacancies that required for exsolution in the bulk. Moreover, we also need to mention here the exsolution on the inner surface of the bar is only observed on the surface that is parallel to the top native surface to some extent but not on the vertical surface, as illustrated in Figure 3-39. Moreover, the inner surface with exsolution exhibits clear grain shape and grain boundary while the surface without exsolution is difficult to see



the grain boundary (seen in Figure 3-37 c). This indicates that the diffusion of oxygen vacancy or copper ions is greatly favoured along with certain facets. The preferential orientation for exsolution has already been proposed by Neagu et al.<sup>10</sup> They believed that in the quasi-cubic structure, the key defects required for exsolution were coplanar, which only happened on (110) orientation, and thus favoured metal nucleation. On the surface that is overall quasi-stoichiometric, exsolution was not prone to occur. This explains why we cannot observe Cu nanoparticles on all the inner surfaces. For the achievement of exsolution in the bulk, it is attributed to the high mobility of oxygen vacancies in the perovskite lattice.

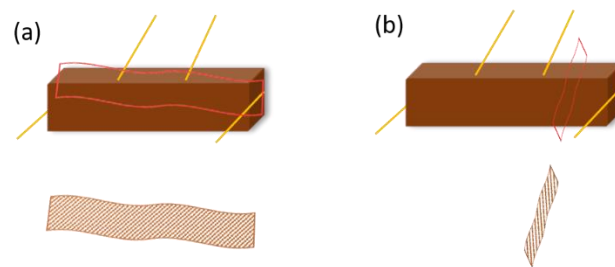


Figure 3-39. (a) the parallel and (b) the vertical inner surface of the bar.

### 3.5.3 TEM analysis of the BCZYC oxide after DC conductivity test

Microstructure and composition of phases in the  $\text{Ba}_{0.95}\text{Ce}_{0.5}\text{Zr}_{0.3}\text{Y}_{0.14}\text{Cu}_{0.06}\text{O}_{3-\delta}$  bar after conductivity test was investigated by TEM, shown in Figure 3-40. Apart from the nanoparticles on the native surface, an extra phase is present at the grain boundaries. EDS mappings in Figure 3-40 (d) display that the concentration of Cu in the nanoparticle is significantly higher than that in the substrate perovskite, suggesting that the particle is Cu metal. For the extra phase at the grain boundary, although the EDS mappings show that it is rich in Ba, Ce and O, the identification of Ce species is unreliable since  $\text{Ba(L}\alpha)$  and  $\text{Ce(L}\alpha)$  peak have an overlap due to the similar excitation energy. On the native surface, a lot of small holes appear, labelled in green arrow in Figure 3-40 (b), and a thin layer of precipitation in yellow sign is observed underneath the particles with about 20 nm in thickness seen from the HAADF image in Figure 3-40 (d). According to our previous discussion, this precipitate is probably barium oxide.

The holes are supposed to be a result of the introduction of a large concentration of defects after about 100 h' reduction and exsolution during the conductivity test. It can also be seen in Figure 3-40 (c) that the contrast in the near-surface layer of the bar is not uniform, with some strips of dark contrast, especially from the 120 nm depth below the surface. This can be attributed to the significantly loss of Ba<sup>2+</sup> in the near surface area during exsolution process and creating significant Ba vacancies.

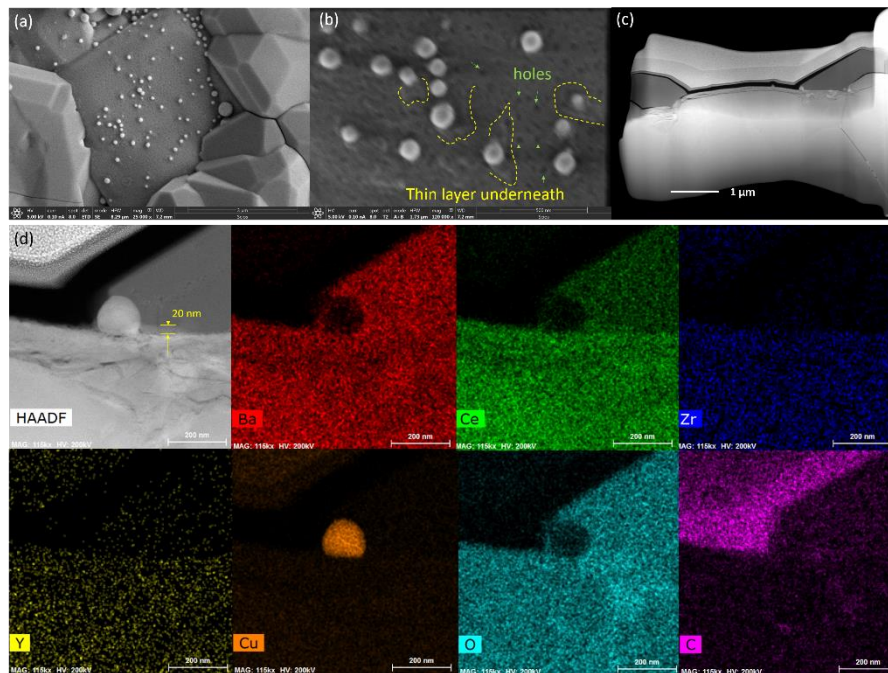


Figure 3-40. (a, b) SEM images of Ba<sub>0.95</sub>Ce<sub>0.5</sub>Zr<sub>0.3</sub>Y<sub>0.14</sub>Cu<sub>0.06</sub>O<sub>3-δ</sub> after conductivity test in 5% H<sub>2</sub>/N<sub>2</sub>, (c) cross section of the FIB sample for TEM analysis, (d) HAADF and EDS mapping of the FIB sample.

The TEM image in Figure 3-41 displays a clear view of the particles and the near-surface layer. Spherical particles are attached on the perovskite surface but not 'socketed' in the substrate. It has been reported that nanoparticles exsolved from perovskite had a strong interaction with the substrate oxide, that one-third of the particles were submerged in the substrate. But this interaction and adhesion between the parent oxide and exsolved particles can possibly diminish with increasing particle size<sup>10</sup>. EDS spectra and quantification analysis were carried out to investigate the

composition of different phases and area of the matrix. The large amount of Cu in Figure 3-41 (d) is from the detected Cu TEM grid.  $K\alpha$  peak was used to analyze the Ba and Ce quantity, confirming the extra phase at the grain boundary (position 4) to be  $BaO_x$ . From the EDS spectra in Figure 3-41 (b), area 1-3 have pretty much identical composition, except that there may be slightly more oxygen in the surface area 1 than the bulk 3 (as see that oxygen peak is relatively more intense compared to the others). Additionally, more yttrium is found to be in position 2 from Figure 3-41 (c), probably coming from the Y-Ba-Cu-O impurity in the material.

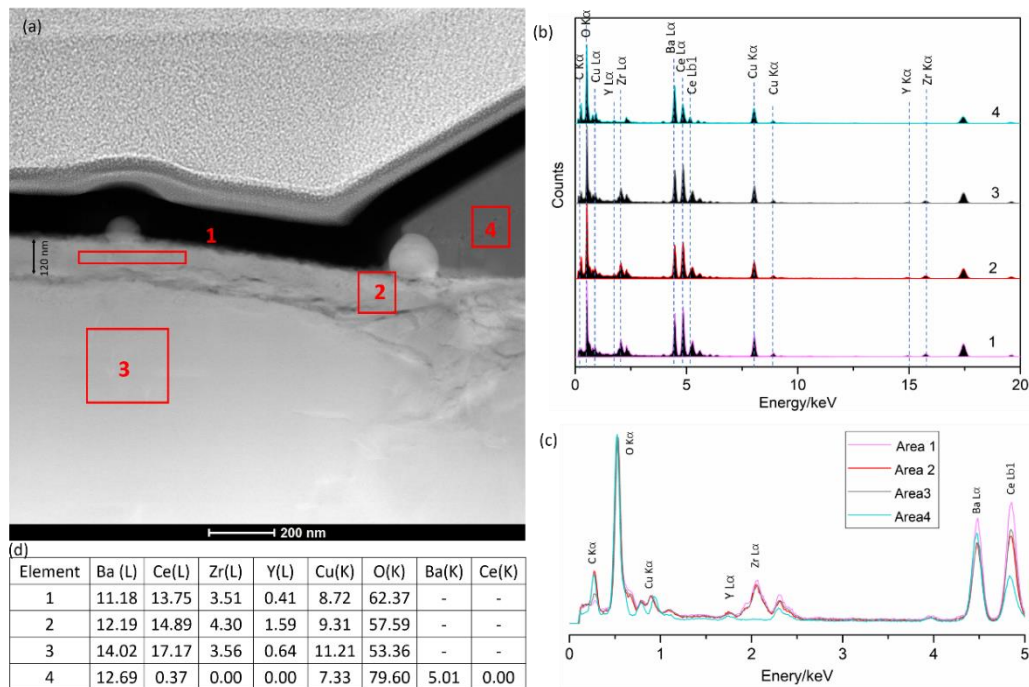


Figure 3-41. (a) TEM image of  $Ba_{0.95}Ce_{0.5}Zr_{0.3}Y_{0.14}Cu_{0.06}O_{3-\delta}$  sample after conductivity test, (b-d) EDS spectra and quantification results of areas indicated in (a). (note that oxygen quantification is not reliable due to the less sensitive of EDS to light elements)

The bright field TEM image in Figure 3-42 (a1) shows the near-surface ‘mystery layer’ and underlying grain structure, the corresponding convergent beam electron diffraction (CBED) patterns are in Figure 3-42 (b1) and (c1), respectively. The crystal structure of the two layers is much the same with only slightly different orientation but

the d-spacings are indistinguishable. These results are consistent with the similar composition observed by EDX. In fact, the surface mystery layer seems to compose of two different layers (Figure 3-42 d1), with the top porous one being about 75 nm in thickness and the bottom one being similar thickness with lighter contrast (Figure 3-42 a2, labelled in blue). (b2), (c2) and (d2) are the FFTs from HRTEM images taken from locations indicated in (a2). The fewer and much weaker reflections in FFT of area (c2) suggest reduced crystallinity and are almost amorphized. (b2) and (d2) are essentially the same, consistent with the CBED data.

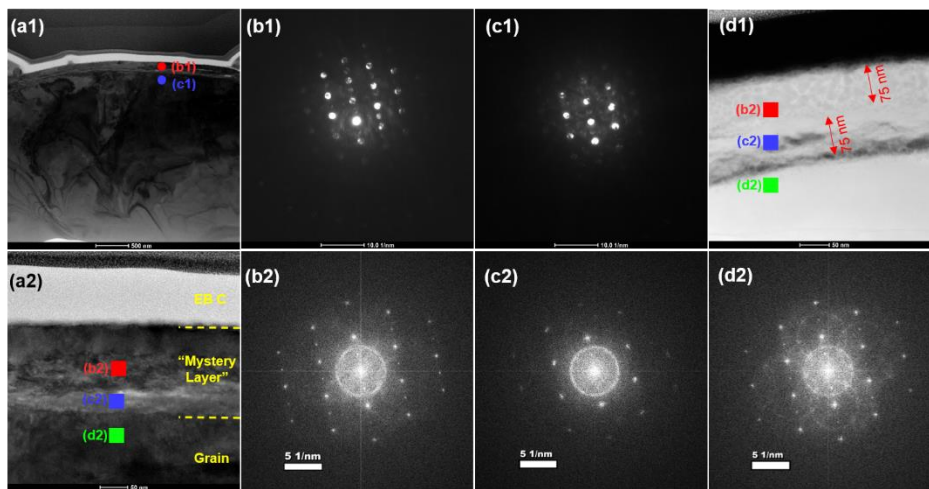


Figure 3-42. (a1) bright field TEM image of  $\text{Ba}_{0.95}\text{Ce}_{0.5}\text{Zr}_{0.3}\text{Y}_{0.14}\text{Cu}_{0.06}\text{O}_{3-\delta}$  sample after conductivity test, (b1, c1) the corresponding convergent beam electron diffraction (CBED) patterns of areas labelled in (a1), (d1) dark field TEM image of the surface layer, (a2) bright field TEM image of the surface layer, (b2-d2) the corresponding FFT from the HRTEM images taken from locations indicated in (a2).

### 3.5.4 Surface etching of the BCZYC sample after DC conductivity test

Samples after conductivity test were etched with 0.01 M aqueous solution of  $\text{HNO}_3$  for various times (2 min, 15 min, 120 min). The same piece of the sample was used for each time of etching, and SEM characterization was taken after each etching. Dilute  $\text{HNO}_3$  solutions with the same concentration were prepared for the three times' etching and the solutions after etching were analyzed by Inductively coupled plasma –

Optical emission spectrometry (ICP-OES). Before the acidic treatment, the SEM image in Figure 3-43 (a) shows a rough surface with particles, precipitates and extra phase ( $\text{BaO}_x$ ) on it. After 2 min etching, the surface seemed to be smooth and the morphology of particles are changed but still attached on the surface. Precipitations are absent now and the number of extra phases at the grain boundary decreases. Figure 3-44 illustrates the ion concentration results for each solution after etching treatment. The graph reveals that after 2 min etching, the removed composition contains relatively more Ba compared with the parent stoichiometry, meaning that the surface is Ba enriched that possibly from the  $\text{BaO}_x$  phase after copper exsolution. Then, the sample is etched for another 15 min, at this stage most of the particles have been removed, corresponding to an increase in the copper relative concentration in the acid solution.  $\text{Y}^{3+}$  is also etched a lot, probably from the  $\text{Y}_2\text{O}_3$  impurity in the material. Cerium does not dissolve much now and even less than the first 2 min treatment. Thus, it is believed that the first 2 min etching dissolves the damaged near-surface layer that contains the perovskite matrix and barium oxide precipitations. BSE image shows a darker contrast at the grain boundary, suggesting that more light elements are distributed at grain boundaries compared with the bulk. SEM image collected by T2 detector in Figure 3-43 (c) demonstrates that although the surface is not as rough as that before etching, a lot of nano-sized precipitations still exist. After another 120 min acidic treatment, the sample surface becomes cleaner without many nano precipitates on top. Grains begin to detach from each other and some grain boundaries show a twisty shape. Additionally, ICP analysis indicates more elements are removed by  $\text{HNO}_3$  in the final 120 min etching, especially  $\text{Y}^{3+}$ , indicating further removal of  $\text{Y}_2\text{O}_3$  impurities.

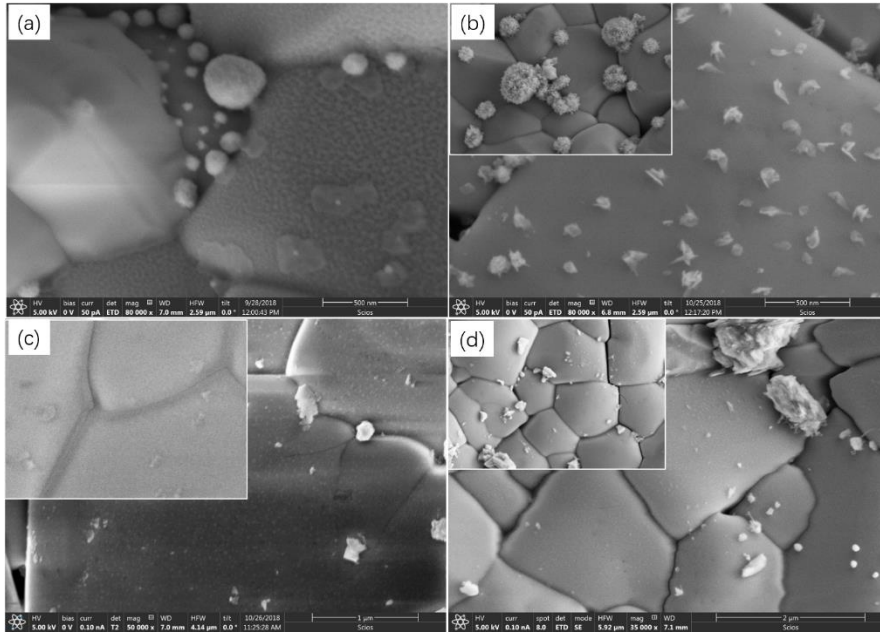


Figure 3-43. SEM images of Ba<sub>0.95</sub>Ce<sub>0.5</sub>Zr<sub>0.3</sub>Y<sub>0.16</sub>Cu<sub>0.04</sub>O<sub>3-δ</sub> after conductivity test in 5% H<sub>2</sub>/N<sub>2</sub> before etching (a), after 2 min (b), 15 min (c) and 120 min (d) etching in 0.01 M aqueous HNO<sub>3</sub> solution.

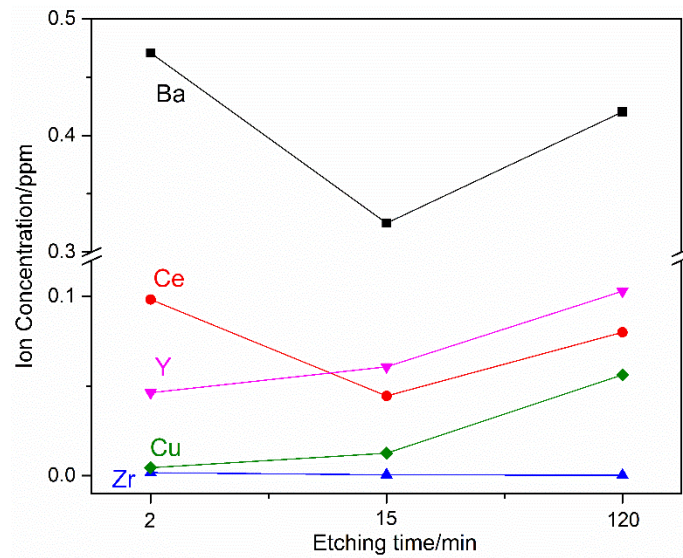


Figure 3-44. Ions concentration after etching for varied time in 0.01 M HNO<sub>3</sub> aqueous solution.



### 3.6 CO oxidation test on BCZYC oxide with copper exsolution

Precious metals have been used as efficient catalysts for CO oxidation due to their high activity and stability. However, the high cost and limited availability of the precious metals required seeking their substitutions for the catalytic reaction. Transition metals and their oxides have been paid considerable attention, and among them copper was found to act as an effective substitute for precious metals in CO oxidation<sup>56-58</sup>.

In our work, CO oxidation test was performed on the exsolved Cu particles from BCZY substrate. The samples after O<sub>2</sub>/Ar plasma treatment were also tested as a comparison, and the results are illustrated in Figure 3-45. Carbon monoxide is hardly oxidized before 240 °C on both exsolved copper catalysts. When gradually increase the temperature, CO conversion on copper particles after plasma treatment rises at a higher speed than that on metallic copper particles. Finally, 100% carbon monoxide is converted at about 330 °C on plasma oxidized copper and at almost 400 °C on metallic copper catalysts. Thus, after O<sub>2</sub>/Ar plasma treatment, the CO oxidation performance is greatly improved on copper particles. It has been reported before by Jernigan and Somorjai<sup>59</sup> that CO oxidation on a thin film of copper is catalyzed by different oxidation states of copper and the rate of the reactions varied upon copper oxidation states. Huang et al.<sup>60</sup> have proposed that the participation of surface lattice oxygen on the copper catalysts attributed to the different performances of CO oxidation on Cu, Cu<sub>2</sub>O and CuO. The reaction progresses according to a Mars-van Krevelen redox mechanism<sup>61</sup> as in Eq. 3-15 and 3-16:



Where O<sub>SL</sub> is the surface lattice oxygen and V<sub>S</sub> is surface oxygen vacancy on the catalysts. In this process, the re-oxidation of the catalysts surface is usually faster than oxygen withdrawal from the metal oxide, determining the oxygen withdrawal step to be rate limited.

In our work, the low temperature restricted the CO conversion to occur for both the samples at the beginning until 240 °C. When the temperature increases, copper

particles with plasma treatment exhibit considerable higher CO conversion than metallic copper particles under the same reaction temperature. This is because only limited number of surface lattice oxygen is obtained from oxidation of non-active metallic copper at low temperature, while plasma-treated copper particles have been partially oxidized to  $\text{Cu}^{1+}$  or  $\text{Cu}^{2+}$  that is able to provide lattice oxygen to react with carbon monoxide. Performing at a higher temperature, the rate of copper oxidation is improved, thus forming more surface oxygen and facilitating CO oxidation. The lower temperature required for 100 % carbon monoxide conversion on plasma-treated catalysts is probably due to the existence of copper oxide and its large specific areas from urchin-like morphology. Therefore, oxidation state and morphology of copper particles have a significant effect on the CO oxidation, and more parameter (e.g. oxygen concentration and time in plasma treatment, CO concentration in the inlet gas) need to be adjusted to obtain the catalysts with the best performance in the future work.

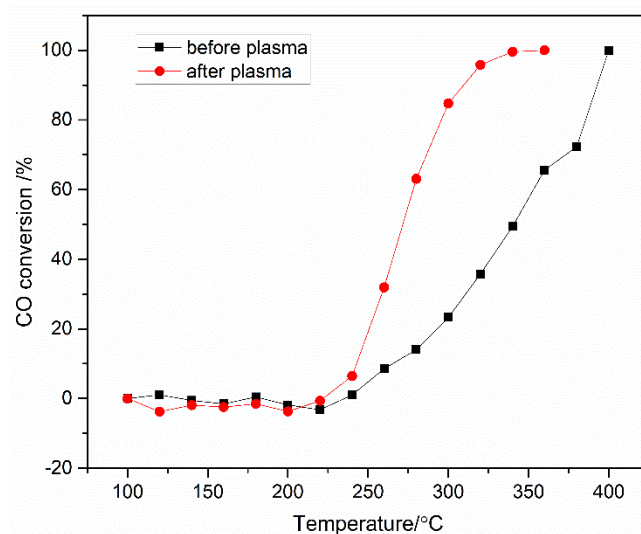


Figure 3-45. CO oxidation on exsolved copper particles from  $\text{Ba}_{0.95}\text{Ce}_{0.5}\text{Zr}_{0.3}\text{Y}_{0.14}\text{Cu}_{0.06}\text{O}_{3-\delta}$  before and after 60%  $\text{O}_2/\text{Ar}$  plasma treatment as a function of temperature. (BCZYC catalysts were reduced at 600 °C for 12 h. The inlet gas flow rate: CO 5 mL/min, air 195 ml/min, catalysts particles size: 250-500  $\mu\text{m}$ , catalysts mass: 0.71 g).



### 3.7 Conclusions

1). The limitation of Cu doping in the barium cerate zirconate is possibly lower than 4 mol%, more doping results in producing impurity phases, such as  $Y_2O_3$ ,  $Y_2BaCuO_5$  and  $mZrO_2$ .

2) BaO-CuO oxides are believed to be the intermediate phase for Cu exsolution from BCZYC perovskites. Continuous composition re-distribution happens between the BaO-CuO phases, substrate perovskites and the exsolved Cu particles.

3) Deficient BCZYC4 oxide exhibited the highest electric conductivity in 5%  $H_2/N_2$ , which is favored from its higher hexagonality in lattice that gives rise to a higher extent of reduction (more oxygen loss and thus more exsolution).

4) The BCZYC oxides ( $Cu \geq 3\%$ ) show metallic property in 5%  $H_2/N_2$  due to the exsolution not only from the surface but also from the bulk in the dense bar.

5) Oxygen/argon plasma treatment oxidizes the exsolved copper particle on BCZYC oxide and changes the copper particles from sphere to urchin-like and whisker shape. This treatment enhances the performance of Cu-BCZY in CO oxidation.

### References

1. Jiang, S. P., A review of wet impregnation—an alternative method for the fabrication of high performance and nano-structured electrodes of solid oxide fuel cells. *Materials Science & Engineering A* **2006**, *418* (1-2), 199-210.

2. Irvine, J. T. S.; Neagu, D.; Verbraeken, M. C.; Chatzichristodoulou, C.; Graves, C.; Mogensen, M. B., Evolution of the electrochemical interface in high-temperature fuel cells and electrolyzers. *Nature Energy* **2016**, *1* (1), 1-13.

3. Neagu, D.; Papaioannou, E. I.; Ramli, W. K. W.; Miller, D. N.; Murdoch, B. J.; Menard, H.; Umar, A.; Barlow, A. J.; Cumpson, P. J.; Irvine, J. T. S.; Metcalfe, I. S., Demonstration of chemistry at a point through restructuring and catalytic activation at anchored nanoparticles. *Nature Communications* **2017**, *8* (1), 1-8.

4. Zhou, J.; Shin, T.-H.; Ni, C.; Chen, G.; Wu, K.; Cheng, Y.; Irvine, J. T., In situ growth of nanoparticles in layered perovskite  $La_{0.8}Sr_{1.2}Fe_{0.9}Co_{0.1}O_{4-\delta}$  as an active and

stable electrode for symmetrical solid oxide fuel cells. *Chemistry of Materials* **2016**, *28* (9), 2981-2993.

5. Konyshva, E.; Irvine, J. T. S., In Situ High-Temperature Neutron Diffraction Study of A-Site Deficient Perovskites with Transition Metals on the B-Sublattice and Structure–Conductivity Correlation. *Chemistry of Materials* **2011**, *23* (7), 1841-1850.

6. Kwon, O.; Sengodan, S.; Kim, K.; Kim, G.; Jeong, H. Y.; Shin, J.; Ju, Y. W.; Han, J. W.; Kim, G., Exsolution trends and co-segregation aspects of self-grown catalyst nanoparticles in perovskites. *Nature Communications* **2017**, *8*(1), 1-7.

7. Neagu, D.; Tsekouras, G.; Miller, D. N.; Menard, H.; Irvine, J. T., In situ growth of nanoparticles through control of non-stoichiometry. *Nature Chemistry* **2013**, *5* (11), 916-923.

8. Nishihata, Y.; Mizuki, J.; Akao, T.; Tanaka, H.; Uenishi, M.; Kimura, M.; Okamoto, T.; Hamada, N., Self-regeneration of a Pd-perovskite catalyst for automotive emissions control. *Nature* **2002**, *418* (6894), 164-167.

9. Cassidy, M.; Gamble, S.; Irvine, J. T., Application of exsolved structures as a route to more robust anodes for improved biogas utilisation in SOFCs. *ECS Transactions* **2015**, *68* (1), 2029-2036.

10. Neagu, D.; Oh, T. S.; Miller, D. N.; Menard, H.; Bukhari, S. M.; Gamble, S. R.; Gorte, R. J.; Vohs, J. M.; Irvine, J. T., Nano-socketed nickel particles with enhanced coking resistance grown in situ by redox exsolution. *Nature communications* **2015**, *6* (1), 1-8..

11. Myung, J. H.; Neagu, D.; Miller, D. N.; Irvine, J. T., Switching on electrocatalytic activity in solid oxide cells. *Nature* **2016**, *537* (7621), 528-531.

12. Tanaka, H.; Uenishi, M.; Taniguchi, M.; Tan, I.; Narita, K.; Kimura, M.; Kaneko, K.; Nishihata, Y., The intelligent catalyst having the self-regenerative function of Pd, Rh and Pt for automotive emissions control. *Catalysis Today* **2006**, *117* (1-3), 321-328.

13. Arandiyan, H.; Wang, Y.; Scott, J.; Mesgari, S.; Dai, H.; Amal, R., In situ exsolution of bimetallic Rh-Ni nanoalloys: a highly efficient catalyst for CO<sub>2</sub> methanation. *ACS Applied Matererials & Interfaces* **2018**, *10* (19), 16352-16357.

14. Arrivé, C.; Delahaye, T.; Joubert, O.; Gauthier, G., Exsolution of nickel nanoparticles at the surface of a conducting titanate as potential hydrogen electrode material for solid oxide electrochemical cells. *Journal of Power Sources* **2013**, *223*, 341-348.
15. Du, Z.; Zhao, H.; Yi, S.; Xia, Q.; Gong, Y.; Zhang, Y.; Cheng, X.; Li, Y.; Gu, L.; Swierczek, K., High-performance anode material  $\text{Sr}_2\text{FeMo}_{0.65}\text{Ni}_{0.35}\text{O}_{6-\delta}$  with in situ exsolved nanoparticle catalyst. *ACS Nano* **2016**, *10* (9), 8660-8669.
16. Qi, W.; Ruan, C.; Wu, G.; Zhang, Y.; Wang, Y.; Xie, K.; Wu, Y., Reversibly in-situ anchoring copper nanocatalyst in perovskite titanate cathode for direct high-temperature steam electrolysis. *International Journal of Hydrogen Energy* **2014**, *39* (11), 5485-5496.
17. Zhu, Y.; Zhou, W.; Ran, R.; Chen, Y.; Shao, Z.; Liu, M., Promotion of oxygen reduction by exsolved silver nanoparticles on a perovskite scaffold for low-temperature solid oxide fuel cells. *Nano Letters* **2016**, *16* (1), 512-518.
18. Gorbova, E.; Maragou, V.; Medvedev, D.; Demin, A.; Tsiakaras, P., Influence of Cu on the properties of gadolinium-doped barium cerate. *Journal of Power Sources* **2008**, *181* (2), 292-296.
19. Choi, S. M.; Lee, J.-H.; Ji, H. I.; Yoon, K. J.; Son, J.-W.; Kim, B.-K.; Je, H. J.; Lee, H.-W.; Lee, J.-H., Determination of proton transference number of  $\text{Ba}(\text{Zr}_{0.84}\text{Y}_{0.15}\text{Cu}_{0.01})\text{O}_{3-\delta}$  via electrochemical concentration cell test. *Journal of Solid State Electrochemistry* **2013**, *17* (11), 2833-2838.
20. Park, K.-Y.; Seo, Y.; Kim, K. B.; Song, S.-J.; Park, B.; Park, J.-Y., Enhanced proton conductivity of yttrium-doped barium zirconate with sinterability in protonic ceramic fuel cells. *Journal of Alloys and Compounds* **2015**, *639*, 435-444.
21. Babilo, P.; Haile, S. M., Enhanced sintering of yttrium-doped barium zirconate by addition of ZnO. *Journal of the American Ceramic Society* **2005**, *88* (9), 2362-2368.
22. Kosasang, O.; Jareun, R.; Phongsathit, S.; Mach-mumas, S., Influence of CuO and ZnO additions on grain growth and proton conductivity of Y-doped  $\text{BaZrO}_3$ . *Journal of the Australian Ceramic Society* **2019**, 1-6.
23. Tong, J.; Clark, D.; Hoban, M.; O'Hayre, R., Cost-effective solid-state reactive

sintering method for high conductivity proton conducting yttrium-doped barium zirconium ceramics. *Solid State Ionics* **2010**, *181* (11-12), 496-503.

24. Zamudio-García, J.; Porras-Vazquez, J. M.; dos Santos-Gómez, L.; Losilla, E. R.; Marrero-Lopez, D., Effect of Zn addition on the structure and electrochemical properties of co-doped  $\text{BaCe}_{0.6}\text{Zr}_{0.2}\text{Ln}_{0.2}\text{O}_{3-\delta}$  (Ln= Y, Gd, Yb) proton conductors. *Ceramics International* **2018**, *44* (12), 14113-14121.

25. Shima, D.; Haile, S., The influence of cation non-stoichiometry on the properties of undoped and gadolinia-doped barium cerate. *Solid State Ionics* **1997**, *97* (1-4), 443-455.

26. Ma, G.; Matsumoto, H.; Iwahara, H., Ionic conduction and nonstoichiometry in non-doped  $\text{Ba}_x\text{CeO}_{3-\alpha}$ . *Solid State Ionics* **1999**, *122* (1-4), 237-247.

27. Ma, G.; Shimura, T.; Iwahara, H., Ionic conduction and nonstoichiometry in  $\text{Ba}_x\text{Ce}_{0.90}\text{Y}_{0.10}\text{O}_{3-\alpha}$ . *Solid State Ionics* **1998**, *110* (1-2), 103-110.

28. Wu, J.; Davies, R.; Islam, M.; Haile, S., Atomistic study of doped  $\text{BaCeO}_3$ : dopant site-selectivity and cation nonstoichiometry. *Chemistry of Materials* **2005**, *17* (4), 846-851.

29. Jo, Y.-R.; Koo, B.; Seo, M.-J.; Kim, J. K.; Lee, S.; Kim, K.; Han, J. W.; Jung, W.; Kim, B.-J., Growth kinetics of individual Co particles ex-solved on  $\text{SrTi}_{0.75}\text{Co}_{0.25}\text{O}_{3-\delta}$  polycrystalline perovskite thin films. *Journal of the American Chemical Society* **2019**, *141* (16), 6690-6697.

30. Gao, D.; Guo, R., Structural and electrochemical properties of yttrium-doped barium zirconate by addition of CuO. *Journal of Alloys and Compounds* **2010**, *493* (1-2), 288-293.

31. Tao, S.; Irvine, J. T., A stable, easily sintered proton-conducting oxide electrolyte for moderate-temperature fuel cells and electrolyzers. *Advanced Materials* **2006**, *18* (12), 1581-1584.

32. Kreuer, K. D., Proton-Conducting Oxides. *Annual Review of Materials Research* **2003**, *33* (1), 333-359.

33. Han, H.; Park, J.; Nam, S. Y.; Kim, K. J.; Choi, G. M.; Parkin, S. S. P.; Jang, H. M.; Irvine, J. T. S., Lattice strain-enhanced exsolution of nanoparticles in thin films.

*Nature Communications* **2019**, *10* (1), 1-8.

34. Hua, B.; Li, M.; Sun, Y. F.; Li, J. H.; Luo, J. L., Enhancing perovskite electrocatalysis of solid oxide cells through controlled exsolution of nanoparticles.

*ChemSusChem* **2017**, *10* (17), 3333-3341.

35. Gao, Y.; Chen, D.; Saccoccio, M.; Lu, Z.; Ciucci, F., From material design to mechanism study: Nanoscale Ni exsolution on a highly active A-site deficient anode material for solid oxide fuel cells. *Nano Energy* **2016**, *27*, 499-508.

36. Voronin, G.; Degterov, S., Solid state equilibria in the Ba-Cu-O system. *Journal of Solid State Chemistry* **1994**, *110* (1), 50-57.

37. Zimmermann, E.; Hack, K.; Mohammad, A.; Boudéne, A.; Neuschütz, D., Experimental investigation and thermochemical assessment of the system Ba-Cu-O. *Calphad* **1995**, *19* (2), 179-188.

38. Zhang, W.; Osamura, K.; Ochiai, S., Phase diagram of the BaO-CuO binary system. *Journal of the American Ceramic Society* **1990**, *73* (7), 1958-1964.

39. Lindemer, T.; Specht, E., The BaO-Cu-CuO system. Solid-liquid equilibria and thermodynamics of BaCuO<sub>2</sub> and BaCu<sub>2</sub>O<sub>2</sub>. *Physica C: Superconductivity* **1995**, *255* (1-2), 81-94.

40. Song, Y.; Wang, W.; Ge, L.; Xu, X.; Zhang, Z.; Juliao, P. S. B.; Zhou, W.; Shao, Z., Rational design of a water-storable hierarchical architecture decorated with amorphous barium oxide and nickel nanoparticles as a solid oxide fuel cell anode with excellent sulfur tolerance. *Advanced Science* **2017**, *4* (11), 1700337.

41. Lyagaeva, Y. G.; Medvedev, D.; Demin, A.; Tsiakaras, P.; Reznitskikh, O., Thermal expansion of materials in the barium cerate-zirconate system. *Physics of the Solid State* **2015**, *57* (2), 285-289.

42. Basbus, J. F.; Arce, M. D.; Prado, F. D.; Caneiro, A.; Mogni, L. V., A high temperature study on thermodynamic, thermal expansion and electrical properties of BaCe<sub>0.4</sub>Zr<sub>0.4</sub>Y<sub>0.2</sub>O<sub>3-δ</sub> proton conductor. *Journal of Power Sources* **2016**, *329*, 262-267.

43. Ishihara, T., *Perovskite oxide for solid oxide fuel cells*. Springer Science & Business Media: 2009.

44. Mogensen, M.; Lybye, D.; Bonanos, N.; Hendriksen, P.; Poulsen, F., Factors

controlling the oxide ion conductivity of fluorite and perovskite structured oxides. *Solid State Ionics* **2004**, *174* (1-4), 279-286.

45. Avgouropoulos, G.; Ioannides, T., Selective CO oxidation over CuO-CeO<sub>2</sub> catalysts prepared via the urea–nitrate combustion method. *Applied Catalysis A: General* **2003**, *244* (1), 155-167.

46. Martinez-Arias, A.; Fernández-García, M.; Gálvez, O.; Coronado, J.; Anderson, J.; Conesa, J.; Soria, J.; Munuera, G., Comparative study on redox properties and catalytic behavior for CO oxidation of CuO/CeO<sub>2</sub> and CuO/ZrCeO<sub>4</sub> catalysts. *Journal of Catalysis* **2000**, *195* (1), 207-216.

47. Manasilp, A.; Gulari, E., Selective CO oxidation over Pt/alumina catalysts for fuel cell applications. *Applied Catalysis B: Environmental* **2002**, *37* (1), 17-25.

48. Qiao, B.; Wang, A.; Yang, X.; Allard, L. F.; Jiang, Z.; Cui, Y.; Liu, J.; Li, J.; Zhang, T., Single-atom catalysis of CO oxidation using Pt1/FeOx. *Nature chemistry* **2011**, *3* (8), 634-641.

49. Chen, M.; Cai, Y.; Yan, Z.; Gath, K.; Axnanda, S.; Goodman, D. W., Highly active surfaces for CO oxidation on Rh, Pd, and Pt. *Surface Science* **2007**, *601* (23), 5326-5331.

50. Zhu, Y.; Moo, A.; Yu, T.; Xu, X.; Gao, X.; Liu, Y.; Lim, C.; Shen, Z.; Ong, C.; Wee, A., Enhanced field emission from O<sub>2</sub> and CF<sub>4</sub> plasma-treated CuO nanowires. *Chemical Physics Letters* **2006**, *419* (4-6), 458-463.

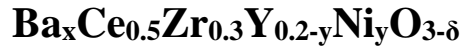
51. Feng, Y.; Zheng, X., Plasma-enhanced catalytic CuO nanowires for CO oxidation. *Nano letters* **2010**, *10* (11), 4762-4766.

52. Kim, S. H.; Na, S. W.; Lee, N.-E.; Nam, Y. W.; Kim, Y.-H., Effect of surface roughness on the adhesion properties of Cu/Cr films on polyimide substrate treated by inductively coupled oxygen plasma. *Surface and Coatings Technology* **2005**, *200* (7), 2072-2079.

53. Vesel, A.; Junkar, I.; Cvelbar, U.; Kovac, J.; Mozetic, M., Surface modification of polyester by oxygen-and nitrogen-plasma treatment. *Surface and Interface Analysis: An International Journal devoted to the development and application of techniques for the analysis of surfaces, interfaces and thin films* **2008**, *40* (11), 1444-1453.

54. Okajima, K.; Ohta, K.; Sudoh, M., Capacitance behavior of activated carbon fibers with oxygen-plasma treatment. *Electrochimica Acta* **2005**, *50* (11), 2227-2231.
55. De Souza, R. A.; Islam, M. S.; Ivers-Tiffée, E., Formation and migration of cation defects in the perovskite oxide LaMnO<sub>3</sub>. *Journal of Materials Chemistry* **1999**, *9* (7), 1621-1627.
56. Kummer, J. T., Catalysts for automobile emission control. *Progress in Energy and Combustion Science* **1980**, *6* (2), 177-199.
57. Nagase, K.; Zheng, Y.; Kodama, Y.; Kakuta, J., Dynamic study of the oxidation state of copper in the course of carbon monoxide oxidation over powdered CuO and Cu<sub>2</sub>O. *Journal of Catalysis* **1999**, *187* (1), 123-130.
58. Huang, T.-J.; Yu, T.-C., Calcination conditions on copper/alumina catalysts for carbon monoxide oxidation and nitric oxide reduction. *Applied Catalysis* **1991**, *71* (2), 275-282.
59. Jernigan, G.; Somorjai, G., Carbon monoxide oxidation over three different oxidation states of copper: metallic copper, copper (I) oxide, and copper (II) oxide-a surface science and kinetic study. *Journal of Catalysis* **1994**, *147* (2), 567-577.
60. Huang, T.-J.; Tsai, D.-H., CO oxidation behavior of copper and copper oxides. *Catalysis Letters* **2003**, *87* (3-4), 173-178.
61. Boreskov, G., Catalytic activation of dioxygen. In *Catalysis*, Springer: 1982, 39-137.

## 4 Influence of cation stoichiometry on Ni exsolution from



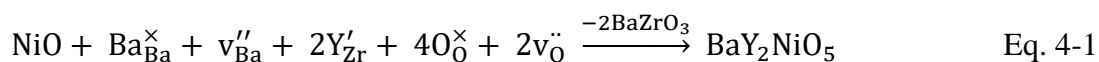
### 4.1 Introduction

Nickel has been extensively investigated as an active catalyst in various fields, such as CO<sub>2</sub> reforming of methane to syngas<sup>1-6</sup>, steam reforming<sup>7-8</sup>, CO methanation<sup>9-11</sup>, etc. Although the catalytic performance of nickel catalyst is not as good as some noble metals such as Rh, Ir and Pt,<sup>12-13</sup> the higher loading amount of Ni is feasible in terms of the catalyst cost in order to increase the activity per volume of the catalyst, making it widely utilized practically and a promising catalyst in comparison with the limited availability and high cost of noble metals. However, nickel suffers severe carbon coking problem, which requires further development of nickel catalysts with less coking deactivation to meet the industrial application. Uniformly distributed nanoparticles prepared by in situ exsolution from the perovskite host are found to exhibit high resistance towards carbon coking due to the strong interaction with the matrix oxides.<sup>14-15</sup> Moreover, nanoparticles can either remain as metallic nanoparticles or reversibly re-dissolve into the perovskite lattice during oxidation, thus avoiding catalysts agglomeration during the redox process, greatly enhancing the lifetime of catalysts<sup>16-17</sup>. Ni exsolution has been reported from various perovskite materials, such as La<sub>0.5</sub>Sr<sub>0.5</sub>Ti<sub>0.75</sub>Ni<sub>0.25</sub>O<sub>3</sub><sup>14, 18</sup>, La<sub>0.4</sub>Sr<sub>0.4</sub>Sc<sub>0.9</sub>Ni<sub>0.1</sub>O<sub>3-δ</sub><sup>19</sup>, PrBaMn<sub>1.7</sub>Ni<sub>0.3</sub>O<sub>5+δ</sub><sup>20</sup>, etc, but only few studies were done on the barium cerate based proton conducting materials, among which only the impact of Ni exsolution on the electrochemical performance of SOFC or SOEC were widely investigated but Ni exsolution process remains unclear.<sup>21-26</sup> Therefore, in this chapter, three samples (BaCe<sub>0.5</sub>Zr<sub>0.3</sub>Y<sub>0.16</sub>Ni<sub>0.04</sub>O<sub>3-δ</sub>, BaCe<sub>0.5</sub>Zr<sub>0.3</sub>Y<sub>0.14</sub>Ni<sub>0.06</sub>O<sub>3-δ</sub>, and Ba<sub>0.95</sub>Ce<sub>0.5</sub>Zr<sub>0.3</sub>Y<sub>0.14</sub>Ni<sub>0.06</sub>O<sub>3-δ</sub>) of nickel doped BCZY oxides were prepared, and the nickel exsolution process was investigated as a function of reduction temperature. In addition, A-site deficiency was applied to study the influence of the non-stoichiometry on the nickel exsolution behavior.



## 4.2 XRD characterization of $\text{Ba}_x\text{Ce}_{0.5}\text{Zr}_{0.3}\text{Y}_{0.2-y}\text{Ni}_y\text{O}_{3-\delta}$ .

The crystalline structures of materials with different stoichiometries were examined using Powder X-ray diffraction (PXRD) technique and the results are shown in Figure 4-1 (a) (a letter ‘r’ is added in front to name the samples after reduction). All the main diffraction peaks of the three compositions, match well with cubic symmetry (space group  $\text{Pm}\bar{3}\text{m}$ ). Broadened and weakened XRD peaks are observed in the A-site deficient composition compared with the stoichiometric  $\text{BaCe}_{0.5}\text{Zr}_{0.3}\text{Y}_{0.14}\text{Ni}_{0.06}\text{O}_{3-\delta}$ , suggesting that A-site deficiency results in smaller crystal size and a decreased crystallinity of the perovskite. A zoom in the XRD peaks between  $30 - 45^\circ$  in Figure 4-1 (b) shows some impurity peaks, including the representative peaks corresponding to NiO species at  $37.2^\circ$  and  $43.2^\circ$  in samples  $\text{BaCe}_{0.5}\text{Zr}_{0.3}\text{Y}_{0.16}\text{Ni}_{0.04}\text{O}_{3-\delta}$  and  $\text{BaCe}_{0.5}\text{Zr}_{0.3}\text{Y}_{0.14}\text{Ni}_{0.06}\text{O}_{3-\delta}$ , and the  $\text{BaNi}_{0.83}\text{O}_{2.5}$ <sup>27-29</sup> phase at  $31.2^\circ$ ,  $\text{Y}_2\text{BaNiO}_5$  impurity at  $32.5^\circ$  in the stoichiometric  $\text{BaCe}_{0.5}\text{Zr}_{0.3}\text{Y}_{0.14}\text{Ni}_{0.06}\text{O}_{3-\delta}$  and deficient  $\text{Ba}_{0.95}\text{Ce}_{0.5}\text{Zr}_{0.3}\text{Y}_{0.14}\text{Ni}_{0.06}\text{O}_{3-\delta}$ , respectively. NiO,  $\text{BaNiO}_x$  and  $\text{Y}_2\text{BaNiO}_5$  phases are generally observed as impurity compounds in the sintering of barium cerate or barium zirconate aided by nickel oxide, with  $\text{Y}_2\text{BaNiO}_5$  being reported as the real sintering promotor for perovskite densification and grain growth that located primarily at grain boundaries.<sup>30-33</sup> Moreover, as simulated by Polfus and co-workers<sup>34</sup>, the enthalpy for exsolution of secondary phase  $\text{Y}_2\text{BaNiO}_5$  in the Ba-deficient material is significantly exothermic,  $-4.43$  eV (HSE), according to reaction 4-1



making the formation of  $\text{Y}_2\text{BaNiO}_5$  to be spontaneous. Nevertheless, the favourable formation of  $\text{Y}_2\text{BaNiO}_5$  does not mean that all the nickel atoms are in the form of this secondary phase, while it has been proved that partial of nickel species are uniformly incorporated in the perovskite lattice.<sup>34</sup>  $\text{BaNiO}_x$  phase is found to form at  $800^\circ\text{C}$  and replaced by  $\text{Y}_2\text{BaNiO}_5$  at  $900^\circ\text{C}$ <sup>32</sup>, however,  $\text{BaNi}_{0.83}\text{O}_{2.5}$  phase still existed in  $\text{BaCe}_{0.5}\text{Zr}_{0.3}\text{Y}_{0.14}\text{Ni}_{0.06}\text{O}_{3-\delta}$  after sintering at  $1350^\circ\text{C}$  in our work, and this barium nickelate in fact is also observed in other reports after high temperature sintering<sup>21</sup>.

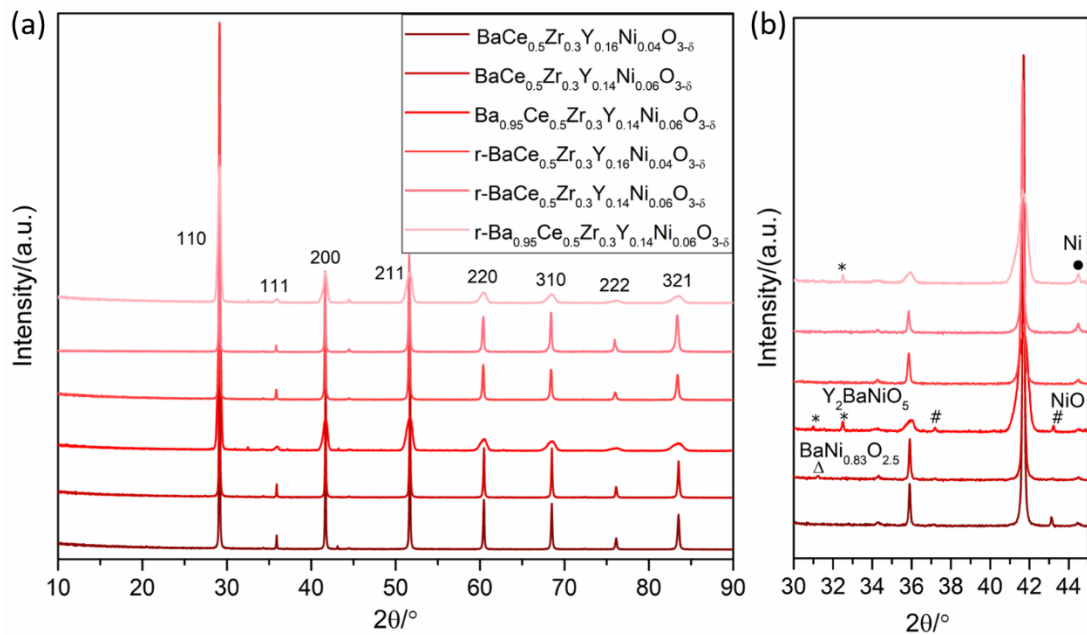


Figure 4-1. (a) XRD patterns of air sintered and reduced  $\text{Ba}_x\text{Ce}_{0.5}\text{Zr}_{0.3}\text{Y}_{0.2-y}\text{Ni}_y\text{O}_{3-\delta}$  samples and a higher magnification between  $30^\circ$  and  $45^\circ$  in (b).

After reduction at  $900^\circ\text{C}$ , peaks at  $44.4^\circ$  corresponded to nickel metal are presented in all three samples. Impurities in the stoichiometric samples are absent now due to decomposition.  $\text{Y}_2\text{BaNiO}_5$  impurity in the deficient oxide still exists.

### 4.3 Microstructure of $\text{Ba}_x\text{Ce}_{0.5}\text{Zr}_{0.3}\text{Y}_{0.2-y}\text{Ni}_y\text{O}_{3-\delta}$ .

#### 4.3.1 Microstructure of the as-prepared $\text{Ba}_x\text{Ce}_{0.5}\text{Zr}_{0.3}\text{Y}_{0.2-y}\text{Ni}_y\text{O}_{3-\delta}$ .

SEM analysis was carried out with the as-prepared samples, shown in Figure 4-2. Here, the sample doped with 3% Ni is also investigated for its morphology. From the native surface images, large grain size and high density is observed in the sintered pellets of 4% and 6% Ni doped stoichiometric BCZY (Figure 4-2 b, c), while either the lower amount of nickel doping of 3% or the introduction of 5% A-site deficiency results in a decreased grain size and lower density, as seen from Figure 4-2 (a, d). The smaller grain size and lower density of the Ba deficient pellet are consistent with its broadened and weakened XRD peaks in Figure 4-1. Observing the cleaved surface of the pellet from the inserted images, a clean cleaved surface is presented in the sample

$\text{BaCe}_{0.5}\text{Zr}_{0.3}\text{Y}_{0.16}\text{Ni}_{0.04}\text{O}_{3-\delta}$  and  $\text{Ba}_{0.95}\text{Ce}_{0.5}\text{Zr}_{0.3}\text{Y}_{0.14}\text{Ni}_{0.06}\text{O}_{3-\delta}$ , but an extra phase is found at the grain boundary area of  $\text{BaCe}_{0.5}\text{Zr}_{0.3}\text{Y}_{0.14}\text{Ni}_{0.06}\text{O}_{3-\delta}$ . It is generally agreed that the densification mechanism of the sintering aids is by forming the liquid phase with a low melting point at the grain boundary that alters both the surface energy and surface diffusion properties of the reactive species during the sintering of the perovskite material.<sup>32</sup> Therefore, the second phase that is observed at the grain boundary in the inserted image in Figure 4-2 (c) is supposed to be the derived from the liquid  $\text{BaNi}_{0.83}\text{O}_{2.5}$  phase formed at elevated sintering temperatures.

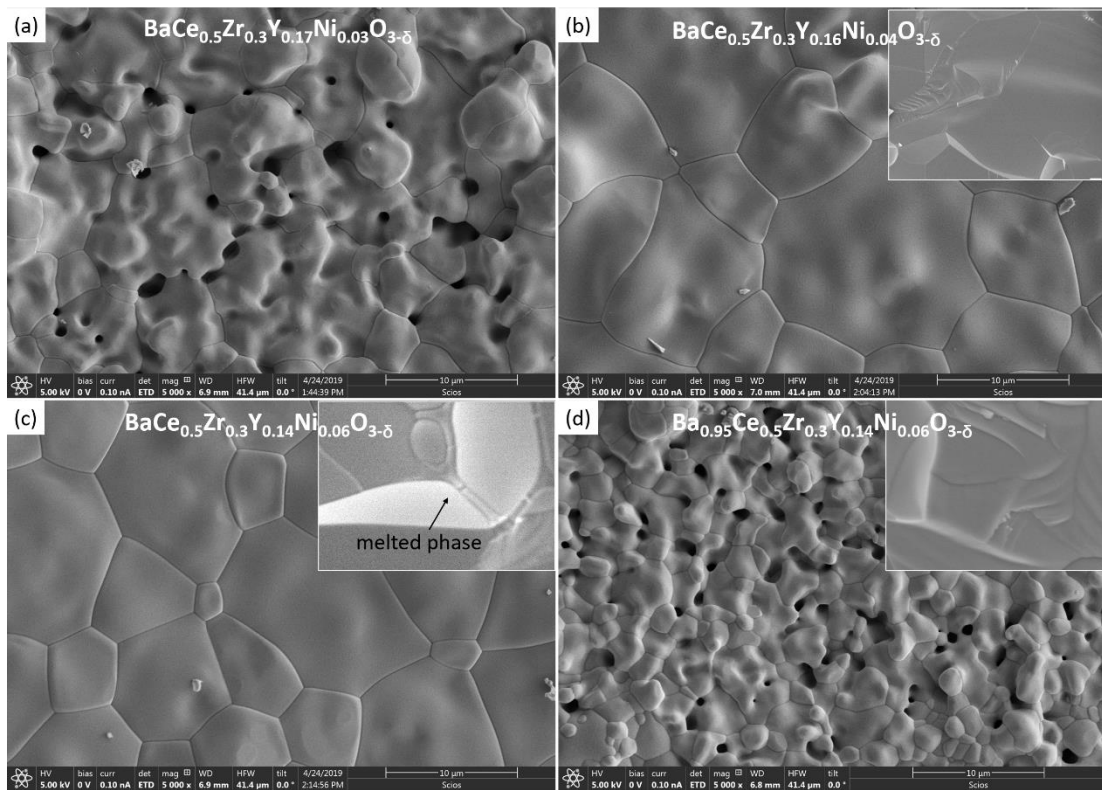


Figure 4-2. SEM micrographs native and cleaved bulk surface of sintered  $\text{Ba}_x\text{Ce}_{0.5}\text{Zr}_{0.3}\text{Y}_{0.2-y}\text{Ni}_y\text{O}_{3-\delta}$  pellets.

The existence of pores in  $\text{BaCe}_{0.5}\text{Zr}_{0.3}\text{Y}_{0.17}\text{Ni}_{0.03}\text{O}_{3-\delta}$  indicates that 3% nickel oxide is not enough to allow the complete densification of the perovskite oxide at 1350 °C, and the less crystalline structure in the deficient 6% doped BCZY also implies the detrimental effect on densification and grain growth of the A-site deficiency. As we suggested above, the densification promoting species are derived from the liquid phases

formed during high temperature sintering, such as the  $\text{BaNi}_{0.83}\text{O}_{2.5}$  or  $\text{Y}_2\text{BaNiO}_5$ . In fact, the second phase already forms at a low temperature of 800 °C, and is reaching its maximum amount at about 1100 °C, followed by gradually decomposition at higher temperature forming barium, yttrium and nickel species incorporating back into the perovskite lattice.<sup>32</sup> However, the second phase does not completely disappear at the final sintering temperature. Moreover, the secondary phase acts as the sintering ‘centres’ which aids in densification and grain growth that occurs at only ~1000 °C, as reported by Tong et al.<sup>32</sup> Therefore, the densification of 3% nickel doped BCZY is restricted by the use of a smaller amount of nickel oxide, producing a limited amount of liquid phase at low temperature that is not enough aiding with the densification and grain growth. On the other hand, in the Ba deficient composition, the less amount of active barium makes it difficult to form enough secondary phase at low temperature to facilitate sintering. A previously suggested possible reason for the less densification in the barium deficient composition is that nickel is doped in the perovskite structure at the octahedral interstice with square planar oxygen coordination that forming a local structure of  $\text{BaNiO}_2$ , as reported by Polfus and co-workers<sup>34</sup> (noting that they add additional NiO to the stoichiometric BZY). Moreover, the existence of barium vacancy promoted the incorporation of nickel to the perovskite structure in the form of  $(\text{Ni}_i\text{V}_{\text{Ba}})^{\times}$  according to Eq. 4-2:



The associate can exist at lower temperatures due to the exothermic binding energies. Hence, it is possible that at low temperature, the NiO species are first dissolved in the perovskite structure with the existence of barium deficiency, while the energetically more favorable process of formation of  $\text{Y}_2\text{BaNiO}_5$  leads to the interstitially dissolved Ni gradually exsolves until Ni reaches equilibrium in  $\text{Y}_2\text{BaNiO}_5$ . However, the  $(\text{Ni}_i\text{V}_{\text{Ba}})^{\times}$  would prevent the formation of  $\text{Y}_2\text{BaNiO}_5$  at lower temperature that aids the surface diffusion of the oxide species. As a consequence, even if  $\text{Y}_2\text{BaNiO}_5$  appears at high temperature it is unable to promote the complete densification of the material. On the other hand, the existence of the interstitial Ni species is expected to produce cation

diffusion barrier, and to some extent also impacting the sintering and grain growth of the perovskite material.

An interesting phenomenon we would like to mention here is that an opposite effect of the A-site deficiency on the sinterability is observed on the Co doped BCZY oxide. When 6% cobalt is doped in the BCZY material, the obtained grain size is quite small, in the range of 1-3  $\mu\text{m}$ , and there are quite a lot of pores in the structure as shown in Figure 4-3 (a). After introducing 5% barium deficiency, grain size increases considerably to 3-8  $\mu\text{m}$  and the sample is densely packed, seen from Figure 4-3 (b). The XRD results of both samples in Figure 4-3 (c) also illustrate the higher crystallinity and larger grain size in the Ba-deficient cobalt doped sample. We suppose that the different effect of the barium deficiency on nickel and cobalt doped BCZY is due to the different sintering mechanism caused by the additives. For the Ni-BCZY, we have explained that nickel oxide plays as a sintering aid in the BCZY oxide by forming the liquid phase  $\text{Y}_2\text{BaNiO}_5$  or barium nickelate at the grain boundary, facilitating the surface diffusion and grain growth. However, the densification aiding effect of cobalt oxide on the host BCZY oxide is assumed not through the formation of similar Ba-Co-O or Ba-Y-Co-O oxide phases, but by the formation of a thin amorphous cobalt rich grain boundary film<sup>35</sup>. It is known that the melting point of  $\text{Co}_2\text{O}_3$  is quite low at about 895  $^\circ\text{C}$  and decompose into CoO at 900  $^\circ\text{C}$ , which determines the intrinsic ability to promote liquid phase sintering of the perovskite oxides without the requirement to form low-melting-point compounds. Therefore, the deficiency of barium would not influence the liquid sintering but leads to higher grain-boundary mobility, grain growth and as a result facilitated the densification. It is also possible that cobalt oxide changes the activation energy for grain growth. However, there are still a lot need to be investigated about the A-site deficiency effect on the densification of BCZY material doped with different transition metal oxides, and we will focus on this field in the future work.

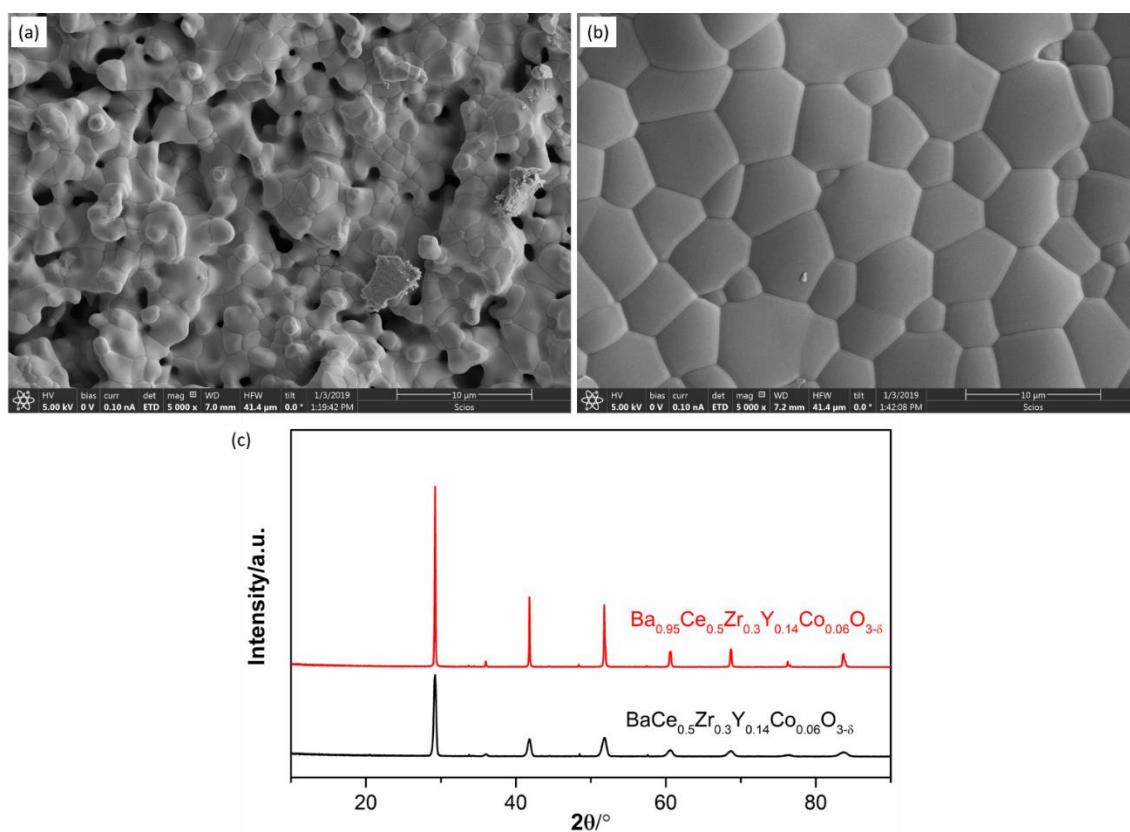


Figure 4-3. SEM micrograph of sintered  $\text{BaCe}_{0.5}\text{Zr}_{0.3}\text{Y}_{0.14}\text{Co}_{0.06}\text{O}_{3-\delta}$  (a) and  $\text{Ba}_{0.95}\text{Ce}_{0.5}\text{Zr}_{0.3}\text{Y}_{0.14}\text{Co}_{0.06}\text{O}_{3-\delta}$  (b), and XRD patterns of the two samples (c).

#### 4.3.2 Characterization of the reduced $\text{BaCe}_{0.5}\text{Zr}_{0.3}\text{Y}_{0.16}\text{Ni}_{0.04}\text{O}_{3-\delta}$ pellet.

Nickel exsolution from the  $\text{BaCe}_{0.5}\text{Zr}_{0.3}\text{Y}_{0.16}\text{Ni}_{0.04}\text{O}_{3-\delta}$  perovskite oxide was investigated as a function of reduction temperature in 5%  $\text{H}_2/\text{Ar}$  for 12 h. SEM micrographs in Figure 4-4 demonstrate that a large number of nanoparticles distribute homogeneously on the substrate native surface. The uniform distribution implies that these nanoparticles are more possibly exsolved from the perovskite lattice and not from the decomposition of the NiO impurity present in the matrix. The average particle size obtained at 600 °C is about 35 nm, and particles grow slightly larger at higher reduction temperature, with the rapid growth occurring at 900 °C and the particle size reaches as large as 90 nm. The exsolution phenomenon happened as a result of oxygen vacancies being created during reduction, which destabilizes the perovskite structure and results in spontaneous exsolution of B-site cations; also, the low Gibbs energy  $\Delta G_r$  for

reduction from oxide to metal ( $-43.48 \text{ kJ/mol}$   $T = 900 \text{ }^\circ\text{C}$ ) is favouring this. This process can be explained by Schottky-type defect reactions shown as follows Eq. 4-3:



where  $Ni_{Ni}$  and  $O_O$  denote nickel and oxygen site with the net charge zero, respectively,  $V_O^{\bullet\bullet}$  denotes the oxygen ion vacancy with the net charge +2, and  $V_{Ni}^{\prime\prime}$  denotes the cation vacancy in the Ni site with the net charge -2.

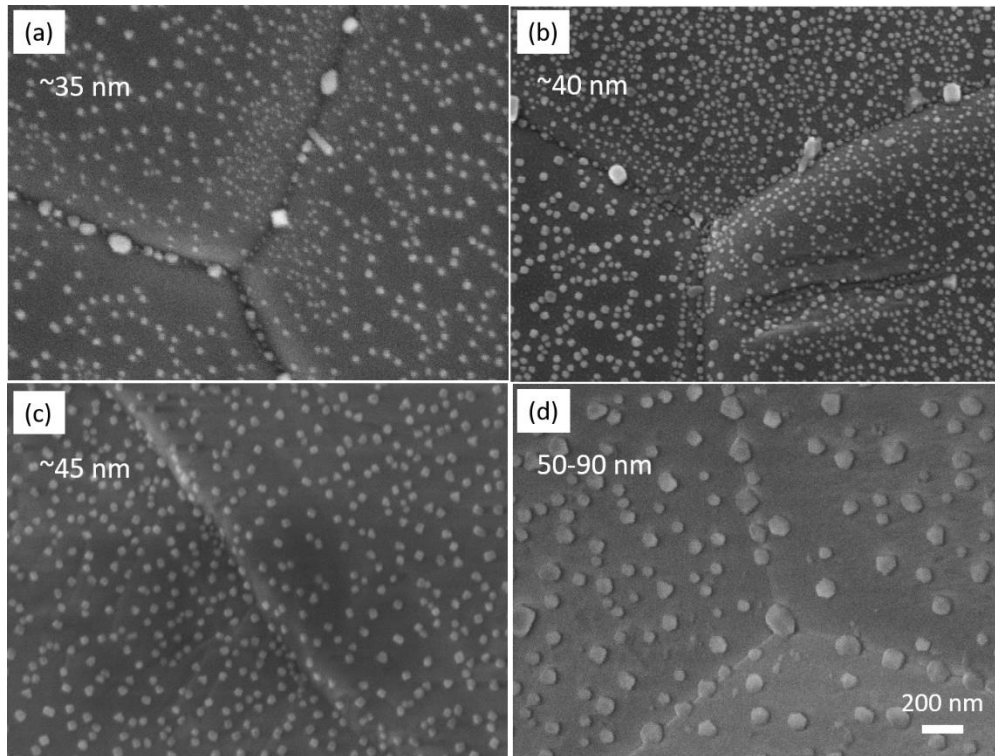


Figure 4-4. SEM micrographs of reduced  $BaCe_{0.5}Zr_{0.3}Y_{0.16}Ni_{0.04}O_{3-\delta}$  pellet at (a)  $600 \text{ }^\circ\text{C}$ , (b)  $700 \text{ }^\circ\text{C}$ , (c)  $800 \text{ }^\circ\text{C}$ , and (d)  $900 \text{ }^\circ\text{C}$  for 12 h in 5%  $H_2/Ar$ .

When the reduced pellet was cracked and the inner surface is exposed to reducing atmosphere at high temperatures, it shows that only several nanoparticles distributed on the grain boundary area of the inner surface (Figure 4-5 a). For the inner area of the pellet, maybe restricted by the slow oxygen migration rate to the surface to compensate the gradient, the oxygen vacancies are not so significant to drive the B-site cation exsolving in a short reduction time, and usually it takes a very long time to achieve oxygen vacancies for inner nickel atoms exsolution. Here, the several observed particles

on the inner surface are probably a result of the inner pores in the pellet that allow the reducing atmosphere to diffuse into the pellet. Energy dispersive X-ray spectrum (EDS) mappings in Figure 4-4 (b-g) clearly confirm the existence of the Ni metal particles from the agglomerated nickel distribution, while uniform Ba, Ce, Zr, Y, and O distribution occurs on the matrix oxide.

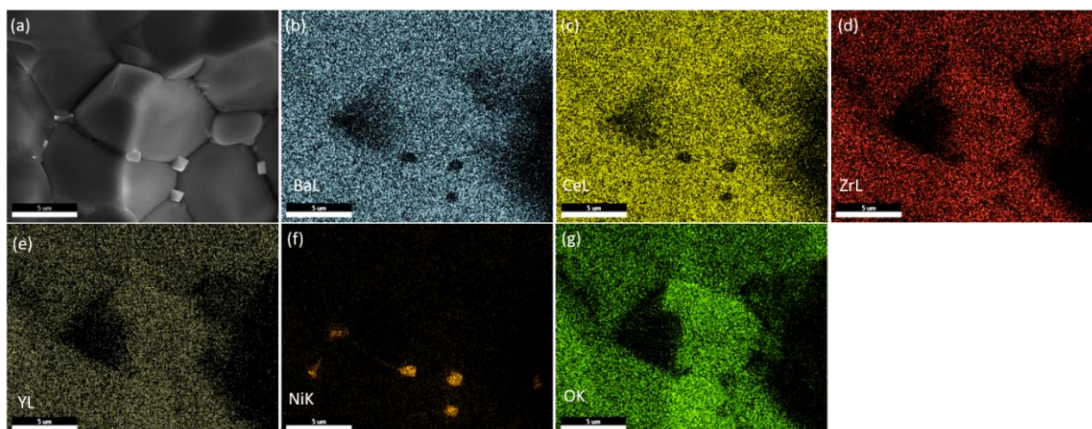


Figure 4-5. EDS mappings of the inner surface of reduced  $\text{BaCe}_{0.5}\text{Zr}_{0.3}\text{Y}_{0.14}\text{Ni}_{0.06}\text{O}_{3-\delta}$  at 900 °C for 12 h.

High-resolution TEM image (HR-TEM) was taken for further characterization of the nanoparticles, shown in Figure 4-6. The measured d-spacings of the exposed particle,  $d_1 = 2.03 \text{ \AA}$  and  $d_2 = 2.50 \text{ \AA}$  with an interplane angle of  $36.25^\circ$ , can be indexed as (111) and (110) planes of cubic Ni metal crystal structure with space group Fm-3m, illustrating the exsolved particles are nickel metal. For the nickel socketed substrate oxide, the distance between the two parallel planes is measured to be  $d_3 = 3.08 \text{ \AA}$ , corresponding to the (110) plane of the cubic BCZY-based perovskite structure as indexed in the XRD patterns (space group: Pm-3m, unit cell parameter:  $4.32 \text{ \AA}$ ).



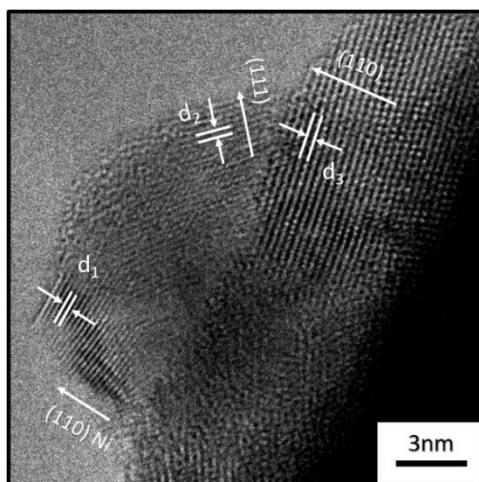
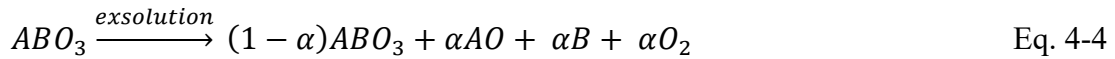


Figure 4-6. TEM image of nanoparticle on  $\text{BaCe}_{0.5}\text{Zr}_{0.3}\text{Y}_{0.16}\text{Ni}_{0.04}\text{O}_{3-\delta}$  reduced at 700 °C for 12 h.

#### 4.3.3 Characterization of reduced $\text{BaCe}_{0.5}\text{Zr}_{0.3}\text{Y}_{0.14}\text{Ni}_{0.06}\text{O}_{3-\delta}$ pellet.

Interestingly, when increasing Ni doping percentage to 6%, apart from exhibiting a large number of nanoparticles, the reduced pellet exhibits quite different morphology at the grain boundary from the one with lower Ni content. Figure 4-7 (a) shows that an extra phase appeared at the grain boundary when the pellet was reduced at 600 °C. Since the intensity of Backscattered Electrons (BSE) is related to the atomic number ( $Z$ ) of the specimen, with heavy elements (high atomic number) backscatter electrons more strongly than light elements (low atomic number) and appear brighter in the image, the insert of BSE image in Figure 4-7 (a) indicates relatively more light weighted elements accumulating at the grain boundary. The additional elements distribution was further investigated by EDS mapping analysis of the area in the black square, and the results are presented in Figure 4-7 (b). Apparently, the grain boundary phase has a higher oxygen to metal ratio than the grain interior, indicated from the bright oxygen distribution at the grain boundary, and this probably accounts for the dark contrast in the BSE image. In addition, Ce, Zr and Y seem to be less distributed at the grain boundary while barium element exists in the grain boundary region and accumulated nickel is found to be on some area of the grain boundary. EDS quantification analysis of the grain boundary phase in Figure 4-7 (a) further implies it is rich in barium and has

a little higher Ni concentration of 13 mol% than 6 mol% in the perovskite if calculated based on Ce. The quantity of Ce, Zr, Y may come from the perovskite substrate signal. We assume that this grain boundary phase could partially originate from the liquid phase of  $\text{BaNi}_{0.83}\text{O}_{2.5}$  in the as-prepared oxide. As proposed by Han et. al.,<sup>36</sup>  $\text{BaY}_2\text{NiO}_5$  decomposed into  $\text{Ba}(\text{OH})_2$ ,  $\text{Y}_2\text{O}_3$  and Ni after heat treatment at 600 °C in dry  $\text{H}_2$ , thus the barium perhaps exists in the form of  $\text{Ba}(\text{OH})_2$  from hydration after the decomposition of  $\text{BaNi}_{0.83}\text{O}_{2.5}$ . The accumulated grain boundary phase could be  $\text{Ba}(\text{OH})_2$ . Furthermore, with the nickel particles exsolution from the perovskite lattice progresses, the substrate perovskite becomes barium excessive and reaches a limit that cannot be tolerated by tilting the structural octahedra, leading to the releasing of excess A-site cation from the perovskite lattice as precipitation on the surface. This process will also facilitate the formation of excess barium phase at the grain boundary region. The release of the A-site cation can be expressed according to Eq. 4-4.



While in the reducing atmosphere, the segregation of BaO may in the form of  $\text{Ba}(\text{OH})_2$ .

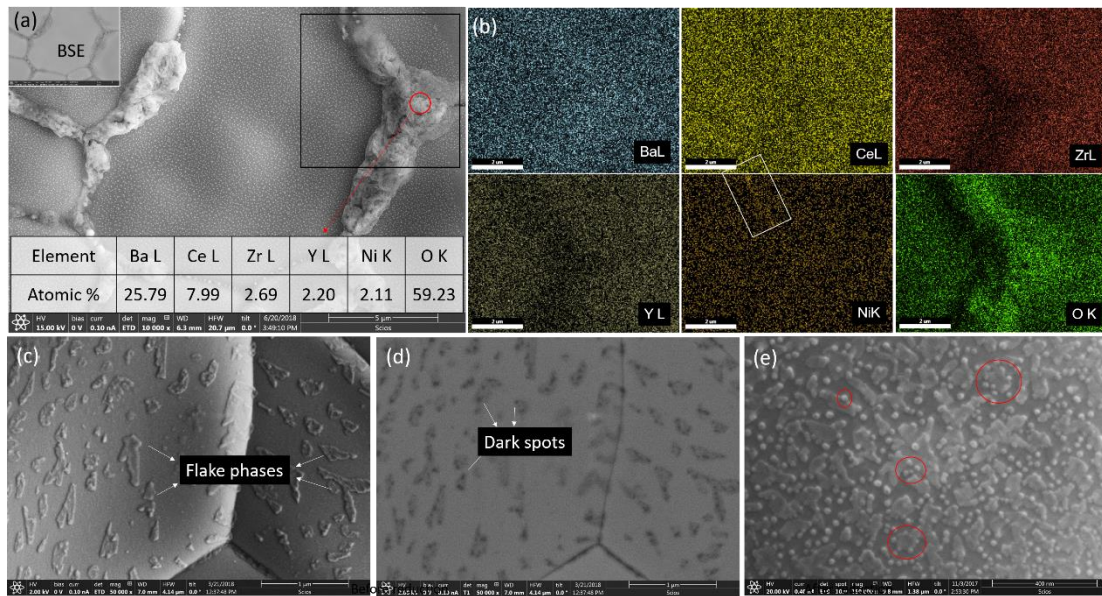


Figure 4-7. (a, c, e) SEM micrographs, (d) BSE images of reduced  $\text{BaCe}_{0.5}\text{Zr}_{0.3}\text{Y}_{0.14}\text{Ni}_{0.06}\text{O}_{3-\delta}$  at 600 °C for 12 h. (b) EDS mappings of the square area in (a). (the table in (a) is the EDS quantification results of the red circle area).

Apart from the phases at the grain boundary, flake-like phases are observed in the bulk area of the perovskite surface, shown in Figure 4-7 (c). The corresponding BSE image in Figure 4-7 (d) illustrates that the flake phases contain a composition of more light atoms in comparison with the substrate oxide. In addition, the elements in the flake phases are distributed unevenly as seen from the dark spots in some areas of the phases, indicating the agglomeration of light atoms in the dark spots. In the SEM image with higher magnification (Figure 4-7 e), nanoparticles of about 30 nm are found to be either isolated on the parent substrate or socketed on the edge of the flake phases with only part of the particle volumes exposing in air. Therefore, it is deduced that nanoparticles grow from the flake phases and the dark spots in the flake phases in the BSE image is a result of the agglomerated nickel atoms that is ready to exsolve from the flake phases. For the flake phases, we suppose that they are the barium nickelate that formed as an intermediate phase for Ni exsolution, the similar process as the formation of barium cuprate in the exsolution of Cu nanoparticles in Chapter 3. Therefore, here in nickel doped BCZY, the intermediate phase barium nickelate also provide an alternative route for Ni nanoparticles exsolution.

We already know that upon exposure to a reducing atmosphere, surface oxygen is first stripped from the perovskite lattice, releasing electrons and creating oxygen vacancies. To examine the chemical state of surface of oxygen and nickel after reduction, X-ray photoelectron spectroscopy (XPS) measurements were performed in the sample  $\text{BaCe}_{0.5}\text{Zr}_{0.3}\text{Y}_{0.14}\text{Ni}_{0.06}\text{O}_{3-\delta}$  either before or after reduction. As can be seen in Figure 4-8 (a), only binding energy peaks of  $\text{Ni}^{2+}$  ( $2p_{3/2}$ ) at 855.1 eV can be detected in the sample before reduction, while peaks of metallic Ni ( $2p_{3/2}$ ) at 861.1 eV and 854.0 eV also appear in the reduced  $\text{BaCe}_{0.5}\text{Zr}_{0.3}\text{Y}_{0.14}\text{Ni}_{0.06}\text{O}_{3-\delta}$  (Figure 4-8 b), which is consistent with the XRD and EDS results that suggest the existence of nickel metal after reduction. For the oxygen O 1s peaks in Figure 4-8 (c, d), the peak at the lower binding energy of 528.9 eV is associated with the surface lattice oxygen, representing the chemical bonding between metal and oxygen ( $\text{O}_{\text{lat}}$ ), whereas the peak at the higher binding energy of 531.6 eV is associated with the surface adsorbed oxygen ( $\text{O}_{\text{ads}}$ ). The relative intensity ratio of  $\text{O}_{\text{lat}}/\text{O}_{\text{ads}}$  thus reflects the surface oxygen vacancy

concentration, with the lower value indicating more existence of oxygen vacancies. Thus, the apparent lower intensity of O 1s<sub>latt</sub> in sample after reduction suggests a richness in surface oxygen vacancies formed with reducing the perovskite.

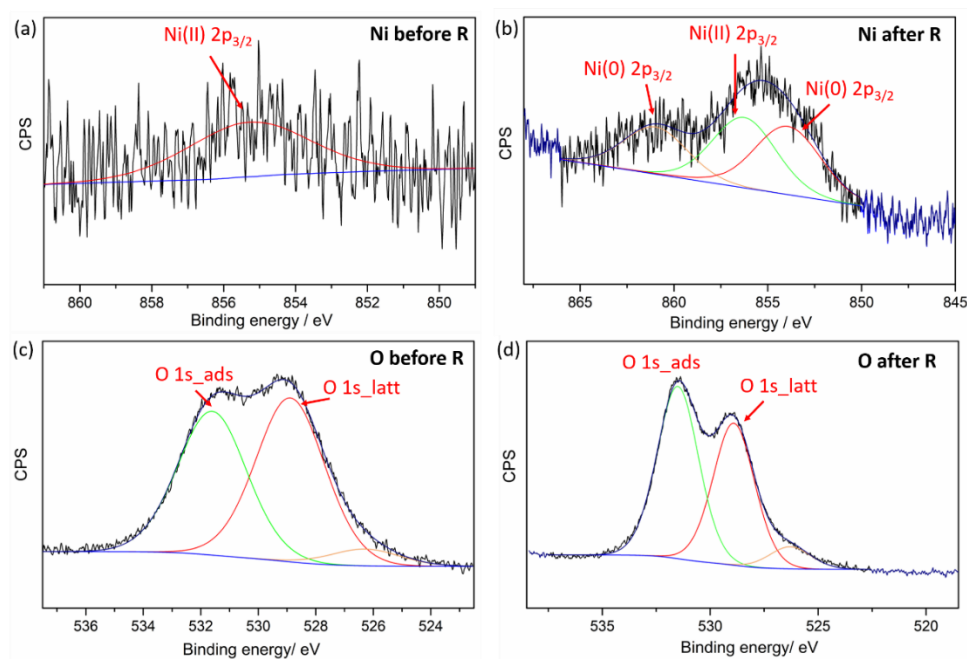


Figure 4-8. XPS results for Ni before reduction (a), Ni after reduction (900 °C for 12 h) (b), O before reduction (c), O after reduction (d) in BaCe<sub>0.5</sub>Zr<sub>0.3</sub>Y<sub>0.14</sub>Ni<sub>0.06</sub>O<sub>3-δ</sub> perovskite.

Analysis of the element content from the XPS results (see Table 4-1) reveals an increased presence of Ba and O after reduction. While surface lattice oxygen is suggested to decrease after reduction from the O 1s spectra, the increased oxygen concentration on the surface is supposed to result from the formation of Ba(OH)<sub>2</sub>. Besides Ba and O, the percentage of Ni also increased on the surface compared to nominal content, confirming that part of Ni in the bulk migrates to the sample surface.<sup>14</sup>

Table 4-1 Quantification of the XPS spectra.

Element/%	Ba	Ce	Zr	Y	Ni	O
BaCe <sub>0.5</sub> Zr <sub>0.3</sub> Y <sub>0.14</sub> Ni <sub>0.06</sub> O <sub>3-δ</sub>						
Before reduction	12.45	4.34	3.13	2.04	0.33	77.72
After reduction	13.03	3.53	2.77	1.13	0.37	79.17

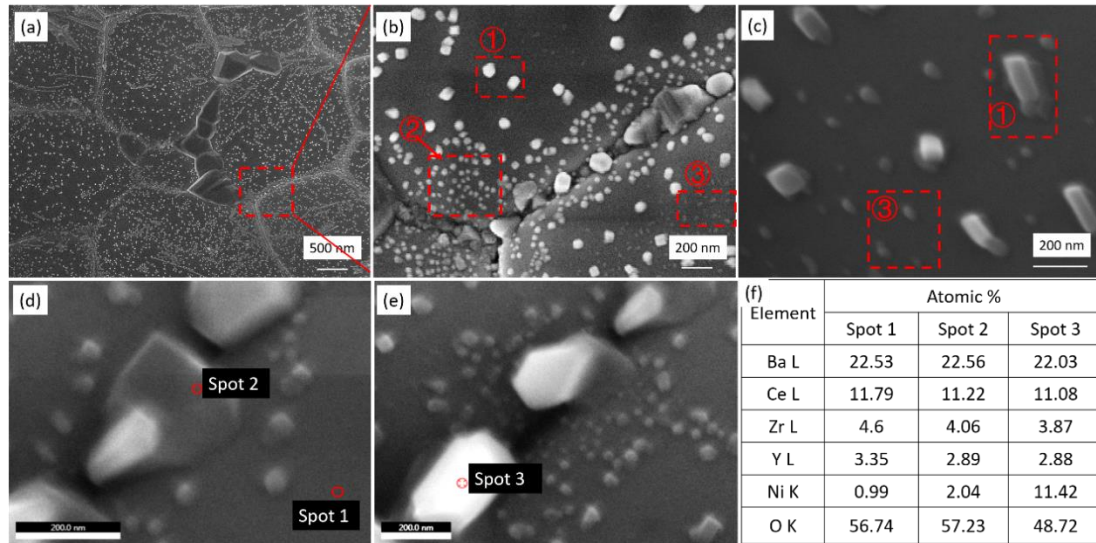


Figure 4-9. (a) SEM micrographs of  $\text{BaCe}_{0.5}\text{Zr}_{0.3}\text{Y}_{0.14}\text{Ni}_{0.06}\text{O}_{3-\delta}$  reduced at  $700\text{ }^{\circ}\text{C}$  for 12 h with a low magnification, showing large extra phases on the grain boundary and a lot of accumulated particles surrounding the grain boundary, (b) a magnified SEM image of the grain boundary area, (c) a magnified SEM image of the grain interior, (d, e) SEM images of particles on the grain boundary, and (f) EDS quantification results of the spots in (d) and (e).

When the pellet was reduced at  $700\text{ }^{\circ}\text{C}$ , the grain boundary phases are only observed occasionally and the flake phases on the grain interior no longer exist, seen in Figure 4-9 (a). Surrounding the grain boundary, a lot of nanoparticles seem to gather there. Zoom in the SEM image in Figure 4-9 (b, c), three types of nanoparticles are presented on the surface, with sizes of around 90 nm, 40 nm, and 30 nm, labelled as ①, ②, and ③, respectively. In terms of morphology, it seems that type ② particles are regularly distributed surrounding the grain boundary and each particle of type ① sits on a substrate, as seen in Figure 4-9 (c). EDS element composition analysis of spots 1, 2 and 3 in Figure 4-9 (d, e) is listed in Figure 4-9 (f), demonstrating that the supported phase beneath the particle at spot 2 has a little more nickel compared with the substrate of spot 1, whereas the particle at spot 3 has a high amount of nickel. We thus hypothesize three different nickel exsolution routes: one is the exsolution of type ① particles from the intermediate barium nickelate phases, similar to the proposed mechanism for Cu exsolution in Chapter 3. For the particles ③, they are formed either



directly by the nucleation from the perovskite lattice or from the early stage of decomposition of the intermediate barium nickelate. Meanwhile, for particles ② surrounding grain boundary, they are exsolved after the volatilization of  $\text{Ba}(\text{OH})_2$  due to its lower boiling point ( $780\text{ }^\circ\text{C}$ ). The latter makes the particles around the grain boundary area smaller in size than the average particles obtained by reduction at  $600\text{ }^\circ\text{C}$ .

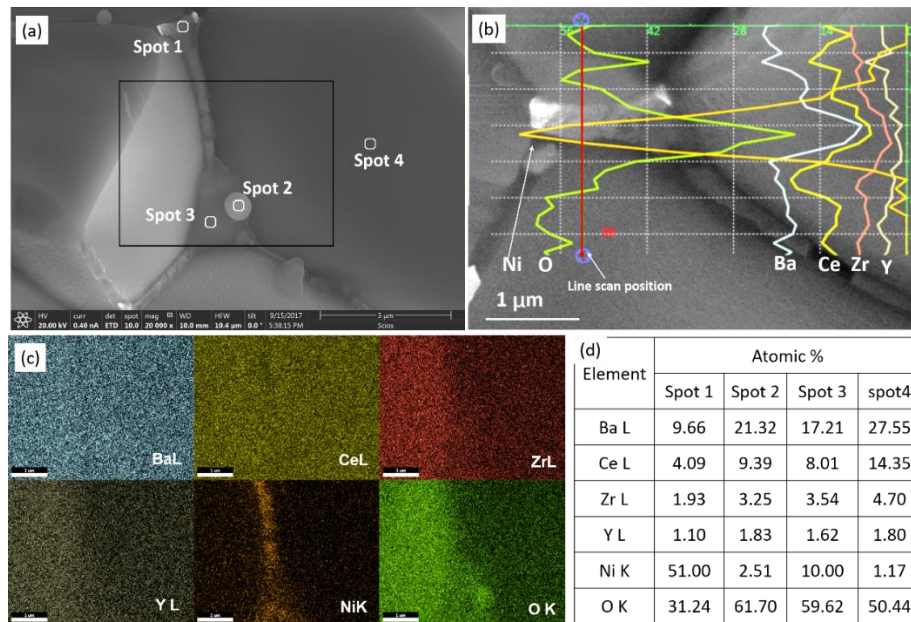


Figure 4-10. (a) SEM micrograph of the inner surface of  $\text{BaCe}_{0.5}\text{Zr}_{0.3}\text{Y}_{0.14}\text{Ni}_{0.06}\text{O}_{3-\delta}$  reduced at  $700\text{ }^\circ\text{C}$  for 12 h, (b) EDS line scanning across the grain boundary as indicated by the red solid line, (c) EDS mapping of the square area in (a), and (d) EDS quantification results of spots in (a)

When the inner surface is investigated after reduction at  $700\text{ }^\circ\text{C}$  (Figure 4-10), distinct melted-like phase at grain boundary is observed that is much obvious than the one we found on the cleaved surface of the as-prepared  $\text{BaCe}_{0.5}\text{Zr}_{0.3}\text{Y}_{0.14}\text{Ni}_{0.06}\text{O}_{3-\delta}$  in Figure 4-2 (c). EDS line scan in Figure 4-10 (b) and the mappings in Figure 4-10 (c) reveal that the grain boundary phase is rich in nickel. Quantification analysis (Figure 4-10 d) shows that spots 1 and 3 consist of a high amount of nickel. A little amount of barium may also exist if compared with the Ba/Ce ratio in the bulk area of spot 4. For the spherical particle (spot 2) on the grain boundary phase, it is a little bit rich in barium and nickel compared with the substrate at spot 4, probably being a barium nickelate

phase. The melted-like phase at grain boundary is supposed to come from the decomposition of  $\text{BaNi}_{0.83}\text{O}_{2.5}$ .

When reduced at 800 °C (Figure 4-11 a), the distribution of particle sizes (30-50 nm) is quite homogeneous. The disappearance of the intermediate phases beneath particles ① and smaller particles sizes than particles ① obtained at 700 °C suggest that Ni exsolution from the suggested barium nickelate has not been completed at 700 °C. When the sample was reduced at 900 °C, larger particles ranging from 60 to 80 nm are detected in the SEM image in Figure 4-11 (b), and it is also consistent with the rapid coarsening of nanoparticles exsolved on  $\text{BaCe}_{0.5}\text{Zr}_{0.3}\text{Y}_{0.16}\text{Ni}_{0.04}\text{O}_{3-\delta}$  at 900 °C.

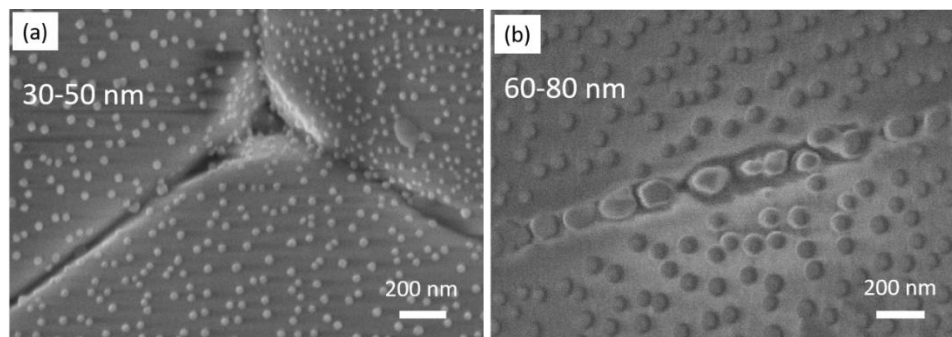


Figure 4-11. SEM micrographs of  $\text{BaCe}_{0.5}\text{Zr}_{0.3}\text{Y}_{0.14}\text{Ni}_{0.06}\text{O}_{3-\delta}$  reduced at (a) 800 °C and (b) 900 °C for 12 h in 5%  $\text{H}_2/\text{Ar}$ .

#### 4.3.4 Characterization of reduced $\text{Ba}_{0.95}\text{Ce}_{0.5}\text{Zr}_{0.3}\text{Y}_{0.14}\text{Ni}_{0.06}\text{O}_{3-\delta}$ pellet.

When reducing the samples with A-site deficiency at 600 °C, flake phases also appear but no extra phase at grain boundary is present (as shown in the micrographs from Figure 4-12). This is due to the fact that not all the areas on the surface are likely to be A-site deficient, thus leading to the formation of the intermediate phases for the nickel exsolution. Another possible reason is that nickel exsolution from the intermediate phases of barium nickelate is probably more energetic saving than exsolving directly from the perovskite lattice, leading to the result that even in the A-site deficient oxide, the co-segregation of barium cannot be eliminated but only weakened. When reduction temperature was increased to 700 °C, Ni nanoparticles with sizes around 30 nm are distributed evenly on the sample surface, and the particles size

did not change much when reduced at 800 °C. Further increasing the reduction temperature to 900 °C, nanoparticles grow larger to a size range of 60-90 nm.

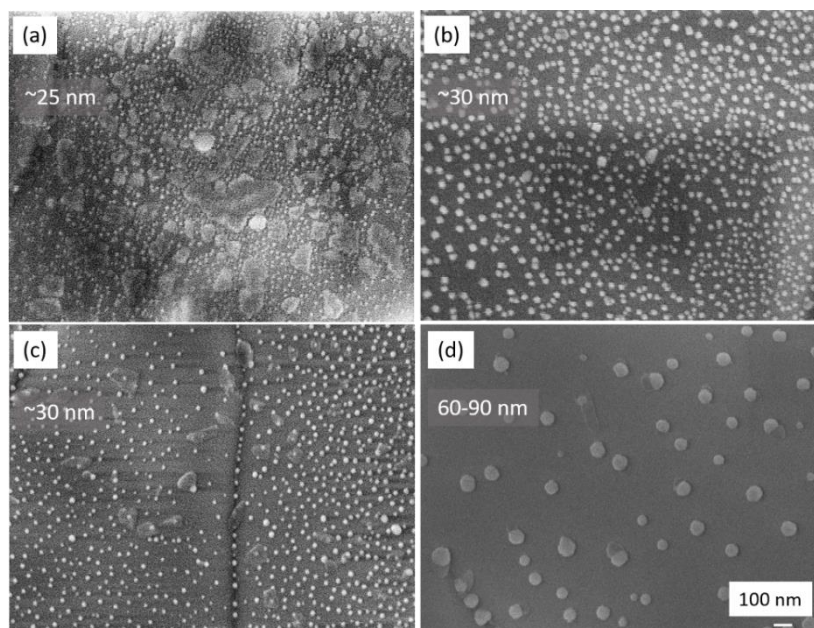


Figure 4-12. SEM micrographs of  $\text{Ba}_{0.95}\text{Ce}_{0.5}\text{Zr}_{0.3}\text{Y}_{0.14}\text{Ni}_{0.06}\text{O}_{3-\delta}$  pellet reduced at (a) 600 °C, (b) 700 °C, (c) 800 °C, and (d) 900 °C for 12 h in 5%  $\text{H}_2/\text{Ar}$ .

#### 4.4 DC conductivity test

As a potential candidate of electrode material in SOFC or SOEC, high electronic conductivity is one of the requirements for its application. Therefore, the electric conductivity of the Ni-doped BCZY was measured using the four-point probe DC method. Figure 4-13 displays the measurement of electrical conductivity for the 6% Ni doped sample in reducing atmosphere (5%  $\text{H}_2/\text{N}_2$ ), with increasing temperature up to 900 °C. Two  $\text{BaCe}_{0.5}\text{Zr}_{0.3}\text{Y}_{0.14}\text{Ni}_{0.06}\text{O}_{3-\delta}$  dense samples were tested, one is the bar prepared from the grinding a sintered Ni-BCZY pellet, followed by another high temperature sintering treatment at 1350 °C (similar to the two-step sintering in the preparation of Cu-BCZY bar in Chapter 3). The other sample is made directly from a sintered Ni-BCZY pellet by cutting it into a square shape. The prepared bar and pellet for conductivity test are shown in the inserted images in Figure 4-13 (a, c). As it can be



seen, the maximum conductivity of the bar reaches 0.02 S/cm within 48 hours of maintaining the sample at 900 °C (Figure 4-13 a), followed by a slight decrease. When the temperature is decreased to room temperature, the conductivity decreases with temperature, as shown in Figure 4-13 (b). The inserted image presents the conductivity at 900 °C as a function of  $pO_2$ , demonstrating that when switching to an atmosphere of lower  $PO_2$ , the material conductivity exhibits a small decrease, indicating the p-type hole conduction mechanism. However, in Figure 4-13 (c), when the pellet prepared from one-step sintering, its conductivity (3 S/cm) in 5%  $H_2/N_2$  is much higher than one for the bar (0.02 S/cm) at 900 °C. Moreover, when the temperature is decreased, an enhancement in the conductivity is observed, showing metallic behaviour.

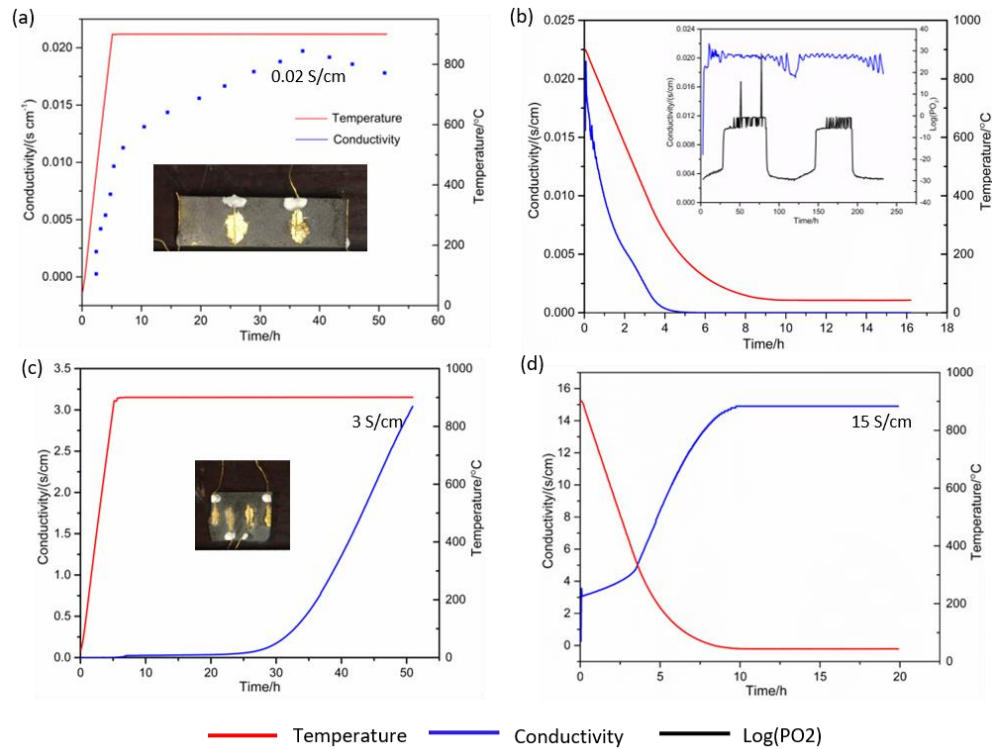


Figure 4-13. DC conductivity measurement of  $BaCe_{0.5}Zr_{0.3}Y_{0.14}Ni_{0.06}O_{3-\delta}$  bar (two-step sintering) in 5%  $H_2/Ar$  on heating (a) and cooling (b), the inserted picture in (b) is the conductivity as a function of  $pO_2$  at 900 °C. (c) and (d) are the conductivity results of the  $BaCe_{0.5}Zr_{0.3}Y_{0.14}Ni_{0.06}O_{3-\delta}$  pellet (one-step sintering) on heating and cooling, respectively.

The microstructures of the bar and pellet after conductivity test were investigated, shown in Figure 4-14. A large distribution of exsolved nanoparticles are observed on the native surface of both samples, but the bar seems to be a bit more porous. When the samples were cracked, micrographs were taken on the inner surface, as presented in Figure 4-14 (b, d). Due to the more porous structure of the bar (Figure 4-14 b), the inner surface that has a large number of exsolutions is the surface exposed to the reducing atmosphere and in fact resembles the native surface, while the surface without distribution of nanoparticles is the ‘real’ inner surface. For the pellet, the dense structure makes it unable to exsolve nanoparticles in the inner surface at least in a short reduction time, therefore, a clean inner surface is observed in Figure 4-14 (d). Even without exsolutions in the inner surface, the pellet still exhibits a metal property after exsolution in reducing atmosphere, which is different from the exsolution of Cu-BCZY bar, where Cu metal particles are observed in the dense inner surface after the test. Therefore, the metallic behaviour of the Ni-BCZY pellet here is assumed to result from the applying of four gold wires on the same plane, and the percolation from the surface nickel particles finally contributes to the higher conductivity and metal property of the dense pellet sample.

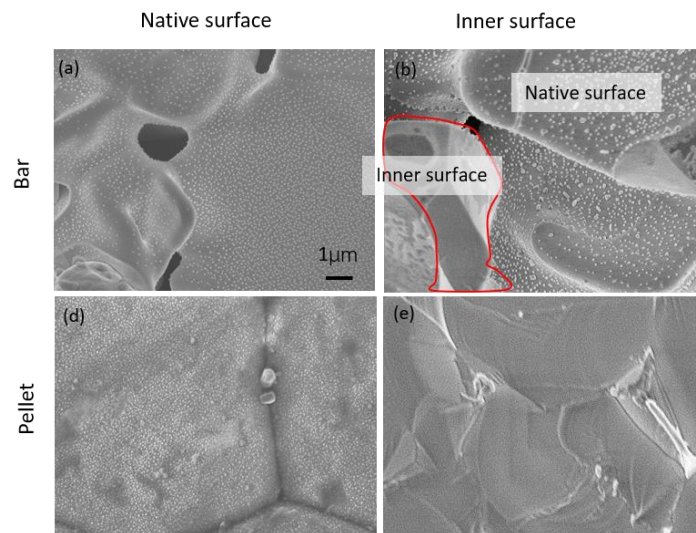


Figure 4-14. (a) native surface and (b) the inner surface of the  $\text{BaCe}_{0.5}\text{Zr}_{0.3}\text{Y}_{0.14}\text{Ni}_{0.06}\text{O}_{3-\delta}$  bar after conductivity test; (c) and (d) are the native surface and inner surface of the pellet after test, respectively.

Another phenomenon that is different from the copper doped sample is while there is only limited number and smaller size of exsolutions occurs in the two-step sintered Cu-BCZY bar after conductivity test, the exsolutions on the Ni-BCZY surface prepared from two-step sintering is quite uniform and with a large quantity. This is probably something to do with the structural stability of the sample after sintering for two times. For the copper doped BCZY, the grains packed much densely after the second time's sintering than that sintered only for one time, indicating a better crystallization and probably higher structure stability, which may cause more difficulty for copper migration. However, the Ni exsolution might not be influenced strongly by the sintering time as good packed and crystallized oxides has already been obtained after the first time's sintering. In order to well understand the difference, we need to carry out XRD measurements after sintering the oxides for the second time and the unit cell parameter is needed to analyze the perovskite structure change.

Although the electric conductivity of nickel doped BCZY tested here is not high enough to be applied as electrode material in SOC, in real electrode preparation, the electrode should be a porous structure, which may have exsolutions occurred on a larger area and result in an improved electronic conductivity.

## 4.5 Conclusion

1. Ni doped BCZY cubic phase was prepared at 1350 °C, but a small amount of NiO, BaNi<sub>0.83</sub>O<sub>2.5</sub> and Y<sub>2</sub>BaNiO<sub>5</sub> appeared as impurities. 4% and 6% nickel oxide dopants in a stoichiometric composition gave rise to a close packed microstructure, while 3% nickel oxide is not enough to accomplish the complete densification of the BCZY oxides. A-site deficiency was detrimental to the sinterability of the BCZY oxides and lead to smaller grain size, less crystallized and porous structure.

2. Numerous Ni nanoparticles were exsolved from the doped BCZY perovskite reduced at 600 °C, and began to have a rapid growth at 900 °C.

3. The BaNi<sub>0.83</sub>O<sub>2.5</sub> phase at the grain boundary area in the as-prepared BaCe<sub>0.5</sub>Zr<sub>0.3</sub>Y<sub>0.14</sub>Ni<sub>0.06</sub>O<sub>3-δ</sub> decomposed into Ba(OH)<sub>2</sub> and nickel metal after reduction at 600 °C for 12 h. Meanwhile, a lot of barium nickelates flakes were observed on the

native surface after reduction. When reduced at 700 °C, there were three types of nickel particles, standing for three types of exsolution process. One is directly exsolving from the perovskite lattice, one is the spontaneous exsolving at the near grain boundary area after the volatilization of Ba(OH)<sub>2</sub>, the third one is the exsolving from the segregated barium nickelate flakes. Reduced at temperatures above 800 °C, the distribution of particles became uniform.

4. A-site deficiency in Ba<sub>0.95</sub>Ce<sub>0.5</sub>Zr<sub>0.3</sub>Y<sub>0.14</sub>Ni<sub>0.06</sub>O<sub>3-δ</sub> did not eliminate the segregation of barium in the form of barium nickelate, but it may weaken the segregation.

## References

1. Li, Y.; Zhang, B.; Xie, X.; Liu, J.; Xu, Y.; Shen, W., Novel Ni catalysts for methane decomposition to hydrogen and carbon nanofibers. *Journal of Catalysis* **2006**, *238* (2), 412-424.

2. Muroyama, H.; Tsuda, Y.; Asakoshi, T.; Masitah, H.; Okanishi, T.; Matsui, T.; Eguchi, K., Carbon dioxide methanation over Ni catalysts supported on various metal oxides. *Journal of Catalysis* **2016**, *343*, 178-184.

3. Pompeo, F.; Nichio, N.; Ferretti, O.; Resasco, D., Study of Ni catalysts on different supports to obtain synthesis gas. *International Journal of Hydrogen Energy* **2005**, *30* (13-14), 1399-1405.

4. Takenaka, S.; Umebayashi, H.; Tanabe, E.; Matsune, H.; Kishida, M., Specific performance of silica-coated Ni catalysts for the partial oxidation of methane to synthesis gas. *Journal of Catalysis* **2007**, *245* (2), 392-400.

5. Wang, S.; Lu, G. M., CO<sub>2</sub> reforming of methane on Ni catalysts: Effects of the support phase and preparation technique. *Applied Catalysis B: Environmental* **1998**, *16* (3), 269-277.

6. Wang, S.; Lu, G., Reforming of methane with carbon dioxide over Ni/Al<sub>2</sub>O<sub>3</sub> catalysts: Effect of nickel precursor. *Applied Catalysis A: General* **1998**, *169* (2), 271-280.

7. Avci, A., Hydrogen production by steam reforming of n-butane over supported

Ni and Pt-Ni catalysts. *Applied Catalysis A: General* **2004**, 258 (2), 235-240.

8. Zhang, B.; Tang, X.; Li, Y.; Cai, W.; Xu, Y.; Shen, W., Steam reforming of bio-ethanol for the production of hydrogen over ceria-supported Co, Ir and Ni catalysts.

*Catalysis Communications* **2006**, 7 (6), 367-372.

9. Jia, C.; Gao, J.; Li, J.; Gu, F.; Xu, G.; Zhong, Z.; Su, F., Nickel catalysts supported on calcium titanate for enhanced CO methanation. *Catalysis. Science. & Technology*. **2013**, 3 (2), 490-499.

10. Le, T. A.; Kim, M. S.; Lee, S. H.; Kim, T. W.; Park, E. D., CO and CO<sub>2</sub> methanation over supported Ni catalysts. *Catalysis Today* **2017**, 293-294, 89-96.

11. Alstrup, I., On the kinetics of CO methanation on nickel surfaces. *Journal of Catalysis* **1995**, 151 (1), 216-225.

12. Hickman, D.; Schmidt, L. D., Synthesis gas formation by direct oxidation of methane over Pt monoliths. *Journal of Catalysis* **1992**, 138 (1), 267-282.

13. Au, C.-T.; Ng, C.-F.; Liao, M.-S., Methane dissociation and syngas formation on Ru, Os, Rh, Ir, Pd, Pt, Cu, Ag, and Au: a theoretical study. *Journal of Catalysis* **1999**, 185 (1), 12-22.

14. Neagu, D.; Oh, T. S.; Miller, D. N.; Menard, H.; Bukhari, S. M.; Gamble, S. R.; Gorte, R. J.; Vohs, J. M.; Irvine, J. T., Nano-socketed nickel particles with enhanced coking resistance grown in situ by redox exsolution. *Nature Communications* **2015**, 6(1), 1-8.

15. Neagu, D.; Papaioannou, E. I.; Ramli, W. K. W.; Miller, D. N.; Murdoch, B. J.; Menard, H.; Umar, A.; Barlow, A. J.; Cumpson, P. J.; Irvine, J. T. S.; Metcalfe, I. S., Demonstration of chemistry at a point through restructuring and catalytic activation at anchored nanoparticles. *Nature Communications* **2017**, 8 (1), 1-8.

16. Sun, Y.; Li, J.; Zeng, Y.; Amirkhiz, B. S.; Wang, M.; Behnamian, Y.; Luo, J., A-site deficient perovskite: the parent for in situ exsolution of highly active, regenerable nano-particles as SOFC anodes. *Journal of Materials Chemistry A* **2015**, 3 (20), 11048-11056.

17. Adijanto, L.; Padmanabhan, V. B.; Küngas, R.; Gorte, R. J.; Vohs, J. M., Transition metal-doped rare earth vanadates: a regenerable catalytic material for SOFC

anodes. *Journal of Materials Chemistry* **2012**, 22 (22), 11396-11402.

18. Arrivé, C.; Delahaye, T.; Joubert, O.; Gauthier, G., Exsolution of nickel nanoparticles at the surface of a conducting titanate as potential hydrogen electrode material for solid oxide electrochemical cells. *Journal of Power Sources* **2013**, 223, 341-348.

19. Gao, Y.; Chen, D.; Saccoccio, M.; Lu, Z.; Ciucci, F., From material design to mechanism study: Nanoscale Ni exsolution on a highly active A-site deficient anode material for solid oxide fuel cells. *Nano Energy* **2016**, 27, 499-508.

20. Kwon, O.; Sengodan, S.; Kim, K.; Kim, G.; Jeong, H. Y.; Shin, J.; Ju, Y. W.; Han, J. W.; Kim, G., Exsolution trends and co-segregation aspects of self-grown catalyst nanoparticles in perovskites. *Nature Communications* **2017**, 8(1), 1-7.

21. Caldes, M. T.; Kravchyk, K. V.; Benamira, M.; Besnard, N.; Gunes, V.; Bohnke, O.; Joubert, O., Metallic nanoparticles and proton conductivity: improving proton conductivity of  $\text{BaCe}_{0.9}\text{Y}_{0.1}\text{O}_{3-\delta}$  Using a Catalytic Approach. *Chemistry of Materials* **2012**, 24 (24), 4641-4646.

22. Duan, C.; Kee, R. J.; Zhu, H.; Karakaya, C.; Chen, Y.; Ricote, S.; Jarry, A.; Crumlin, E. J.; Hook, D.; Braun, R.; Sullivan, N. P.; O'Hayre, R., Highly durable, coking and sulfur tolerant, fuel-flexible protonic ceramic fuel cells. *Nature* **2018**, 557 (7704), 217-222.

23. Liu, Y.; Jia, L.; Chi, B.; Pu, J.; Li, J., In situ exsolved Ni-decorated  $\text{Ba}(\text{Ce}_{0.9}\text{Y}_{0.1})_{0.8}\text{Ni}_{0.2}\text{O}_{3-\delta}$  perovskite as carbon-resistant composite anode for hydrocarbon-fueled solid oxide fuel cells. *ACS Omega* **2019**, 4 (25), 21494-21499.

24. Liu, Y.; Jia, L.; Li, J.; Chi, B.; Pu, J.; Li, J., High-performance Ni in-situ exsolved  $\text{Ba}(\text{Ce}_{0.9}\text{Y}_{0.1})_{0.8}\text{Ni}_{0.2}\text{O}_{3-\delta}/\text{Gd}_{0.1}\text{Ce}_{0.9}\text{O}_{1.95}$  composite anode for SOFC with long-term stability in methane fuel. *Composites Part B: Engineering* **2020**, 193, 108033.

25. Liu, Z.; Zhou, M.; Chen, M.; Cao, D.; Shao, J.; Liu, M.; Liu, J., A high-performance intermediate-to-low temperature protonic ceramic fuel cell with in-situ exsolved nickel nanoparticles in the anode. *Ceramics International* **2020**, 46 (12), 19952-19959.

26. Stange, M.; Stefan, E.; Denonville, C.; Larring, Y.; Rørvik, P. M.; Haugrud,

R., Development of novel metal-supported proton ceramic electrolyser cell with thin film BZY15–Ni electrode and BZY15 electrolyte. *International Journal of Hydrogen Energy* **2017**, *42* (19), 13454-13462.

27. Caldes, M. T.; Kravchyk, K. V.; Benamira, M.; Besnard, N.; Joubert, O.; Bohnke, O.; Gunes, V.; Jarry, A.; Dupré, N., Metallic nanoparticles and proton conductivity: improving proton conductivity of  $\text{BaCe}_{0.9}\text{Y}_{0.1}\text{O}_{3-\delta}$  and  $\text{La}_{0.75}\text{Sr}_{0.25}\text{Cr}_{0.5}\text{Mn}_{0.5}\text{O}_{3-\delta}$  by Ni-doping. *ECS Transactions* **2012**, *45* (1), 143.

28. Lee, J. G.; Hwang, J.; Hwang, H. J.; Jeon, O. S.; Jang, J.; Kwon, O.; Lee, Y.; Han, B.; Shul, Y.-G., A new family of perovskite catalysts for oxygen-evolution reaction in alkaline media:  $\text{BaNiO}_3$  and  $\text{BaNi}_{0.83}\text{O}_{2.5}$ . *Journal of the American Chemical Society* **2016**, *138* (10), 3541-3547.

29. Campá, J.; Gutiérrez-Puebla, E.; Monge, M.; Rasines, I.; Ruiz-Valero, C., Nickel supermixed valence in stoichiometric  $\text{BaNi}_{0.83}\text{O}_{2.5}$ . *Journal of Solid State Chemistry* **1994**, *108* (2), 230-235.

30. Fang, S.; Wang, S.; Brinkman, K. S.; Chen, F., A sinteractive Ni– $\text{BaZr}_{0.8}\text{Y}_{0.2}\text{O}_{3-\delta}$  composite membrane for hydrogen separation. *Journal of Materials Chemistry A* **2014**, *2* (16), 5825-5833.

31. Ran, S.; Winnubst, L.; Wiratha, W.; Blank, D. H. A., Sintering behavior of 0.8 mol%–CuO–Doped 3Y–TZP ceramics. *Journal of the American Ceramic Society* **2006**, *89* (1), 151-155.

32. Tong, J.; Clark, D.; Bernau, L.; Sanders, M.; O'Hayre, R., Solid-state reactive sintering mechanism for large-grained yttrium-doped barium zirconate proton conducting ceramics. *Journal of Materials Chemistry* **2010**, *20* (30), 6333-6341.

33. Tong, J.; Clark, D.; Hoban, M.; O'Hayre, R., Cost-effective solid-state reactive sintering method for high conductivity proton conducting yttrium-doped barium zirconium ceramics. *Solid State Ionics* **2010**, *181* (11-12), 496-503.

34. Polfus, J. M.; Fontaine, M.-L.; Thøgersen, A.; Riktor, M.; Norby, T.; Bredesen, R., Solubility of transition metal interstitials in proton conducting  $\text{BaZrO}_3$  and similar perovskite oxides. *Journal of Materials Chemistry A* **2016**, *4* (21), 8105-8112.

35. Jud, E.; Zhang, Z.; Sigle, W.; Gauckler, L. J., Microstructure of cobalt oxide

doped sintered ceria solid solutions. *Journal of Electroceramics* **2006**, *16* (3), 191-197.

36. Han, D.; Otani, Y.; Noda, Y.; Onishi, T.; Majima, M.; Uda, T., Strategy to improve phase compatibility between proton conductive  $\text{BaZr}_{0.8}\text{Y}_{0.2}\text{O}_{3-\delta}$  and nickel oxide. *RSC Advances* **2016**, *6* (23), 19288-19297.



## **5 Exsolution of Ni-Cu alloy from the co-doped BCZY perovskite**

### **5.1 Introduction**

Nickel and copper both have fcc structures with lattice parameters of 3.54 and 3.62 Å, respectively, making them possible to incorporate into a solid solution, crystallized in a cubic close-packed lattice according to the phase diagram. The catalytic activity of the host monocatalyst material has been proposed to be improved by adding the second metal through altering and modifying the electronic, structural parameters or the active surfaces of the host metal.<sup>1-5</sup> For example, while Ni is an effective catalysts for high WGS activity, the addition of Cu in Ni catalysts suppresses the undesirable methanation side-reaction successfully in the WGS reaction.<sup>6</sup> In steam methane reforming and hydrocarbon decomposition, the presence of Cu in the bimetallic catalysts prevents not only the carbon formation but also the sintering of the active phase.<sup>7</sup> Moreover, such alloy catalysts have also been used in the preparation of fuel cell electrodes and exhibited highly efficient performance.<sup>8-14</sup> Therefore, in this chapter, nickel and copper are co-doped into the BCZY perovskite structure, and nanoparticle exsolution experiments are carried out to investigate the influence of the nickel on the copper exsolution process. Furthermore, catalytic tests on CO oxidation or RWGS reaction will also be performed in future work to see the different performance on single metal catalysts and the alloy catalysts.

### **5.2 Phase identification and microstructure of Ni, Cu co-doped BCZY**

#### **5.2.1 Phase identification of Ni, Cu co-doped BCZY**

Single-phase perovskites were obtained in the Ni, Cu co-doped BCZY oxides within the whole composition range prepared by high temperature solid state synthesis at 1350 °C for 12 h (Figure 5-1). All the compositions can be indexed with R-3c space

group due to the existence of (113) lattice plane scattered at  $34.4^\circ$ . Compared with the BCZY perovskite doped with single Ni or Cu, where impurities appeared when the dopant concentration reaches 4%, in the co-doped oxides, single phase can be achieved with the total dopants concentration reaching at least as high as 5%. The sintering aids-rich impurity is actually very frequently observed in the barium cerate zirconate sintering, and the generally suggested amount in adding the sintering aids is about 1 wt% (which is about 4 mol%) without impacting too much on the perovskite property. The pure phase of Ni and Cu co-doped BCZY indicate that the bimetallic doping strategy enhances the perovskite solubility for the transition metals and promotes a stable perovskite structure. This provides an effective way in aiding material sintering without introducing impurity phases.

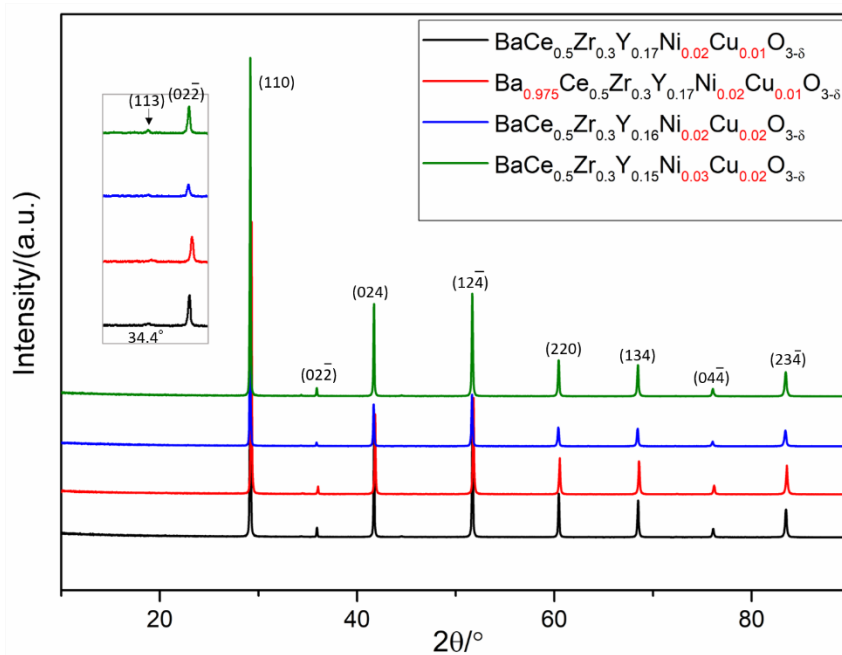


Figure 5-1. RT powder X-ray diffraction patterns of the prepared Ni, Cu co-doped BCZY perovskites sintered at  $1350^\circ\text{C}$  for 12 h.

### 5.2.2 Microstructure of Ni, Cu co-doped BCZY

The microstructure of the prepared Ni, Cu co-doped BCZY pellets is shown in Figure 5-2. All the samples have a very clean surface without impurity phases on the grain boundaries. In addition, grains are packed densely but not like the rectangle-

shaped grains in Cu-doped oxides, suggesting that the co-doping of nickel and copper improves the sintering behaviour of the perovskites. The inserted micrographs of higher magnification of  $\text{Ba}_{0.975}\text{Ce}_{0.5}\text{Zr}_{0.3}\text{Y}_{0.17}\text{Ni}_{0.02}\text{Cu}_{0.01}\text{O}_{3-\delta}$  (Figure 5-2b) and  $\text{BaCe}_{0.5}\text{Zr}_{0.3}\text{Y}_{0.15}\text{Ni}_{0.03}\text{Cu}_{0.02}\text{O}_{3-\delta}$  (Figure 5-2 d) sample demonstrate a rough grain surfaces with various patterns while only part of the gains display a terrace-shaped surface in sample  $\text{BaCe}_{0.5}\text{Zr}_{0.3}\text{Y}_{0.17}\text{Ni}_{0.02}\text{Cu}_{0.01}\text{O}_{3-\delta}$  (Figure 5-2a) and  $\text{BaCe}_{0.5}\text{Zr}_{0.3}\text{Y}_{0.16}\text{Ni}_{0.02}\text{Cu}_{0.02}\text{O}_{3-\delta}$  (Figure 5-2c). In fact, in the later microscope characterization of samples after reduction, the same rough surface with various patterns can also be observed in the two samples, and the absence of rough surface here is due to the limited observation area in the microscope.

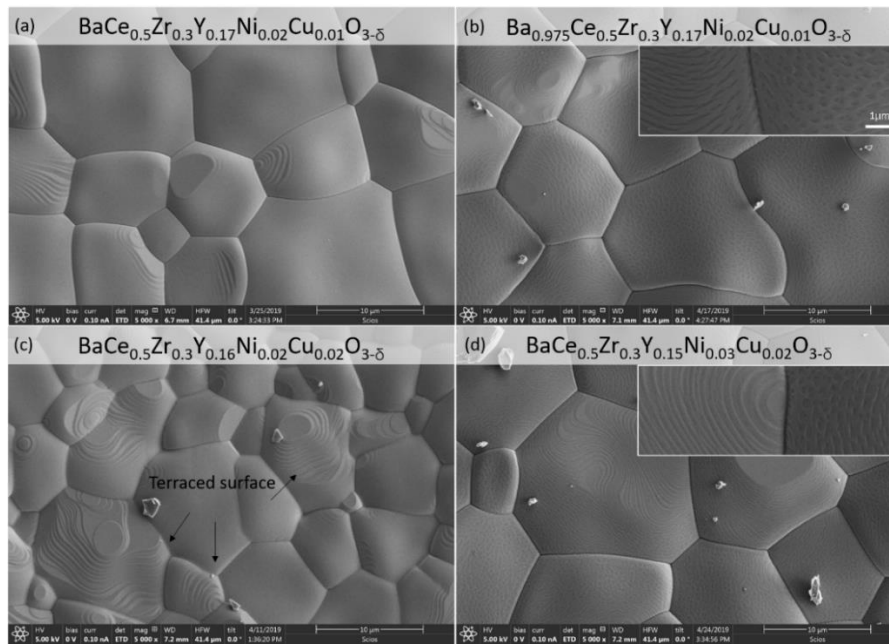


Figure 5-2. Native surface microstructure of the prepared Ni, Cu-doped BCZY pellets sintered at 1350 °C for 12h.

## 5.3 Exsolution from the Ni, Cu co-doped BCZY

### 5.3.1 Microstructure of exsolutions as a function of stoichiometry and temperature

Neagu et al.<sup>15</sup> proposed defect chemistry-based mechanism in the B-site cation

exsolution from perovskite. While no nanoparticles were observed on the native surface of the  $ABO_{3+\gamma}$  (A-site stoichiometric, O-excess) composition after reduction, numerous exsolutes were distributed on the native surface of  $A_{1-\alpha}BO_3$  (A-site-deficient, O-stoichiometric) and  $A_{1-\alpha}BO_{3-\delta}$  (A-site-deficient, O-deficient) type samples (Figure 5-3 a-c). When observing the cleaved surface (bulk surface), a few particles can be obtained in  $ABO_{3+\gamma}$ -type pellet (Figure 5-3 d), but a much higher amount of nanoparticles were found in  $A_{1-\alpha}BO_3$ -type materials (Figure 5-3 e). In addition, the commonly developed A-site surface enrichment phenomenon, which is detrimental to exsolution, can even be observed in the A-site deficient oxides ( $A_{0.8}BO_3$ :  $La_{0.52}Sr_{0.28}Ni_{0.06}Ti_{0.94}O_3$ ), in which the real composition at the native surface was  $A_{1.30}BO_{3.86}$  while the cleaved surface remained the nominal  $A_{0.8}BO_3$  stoichiometry.

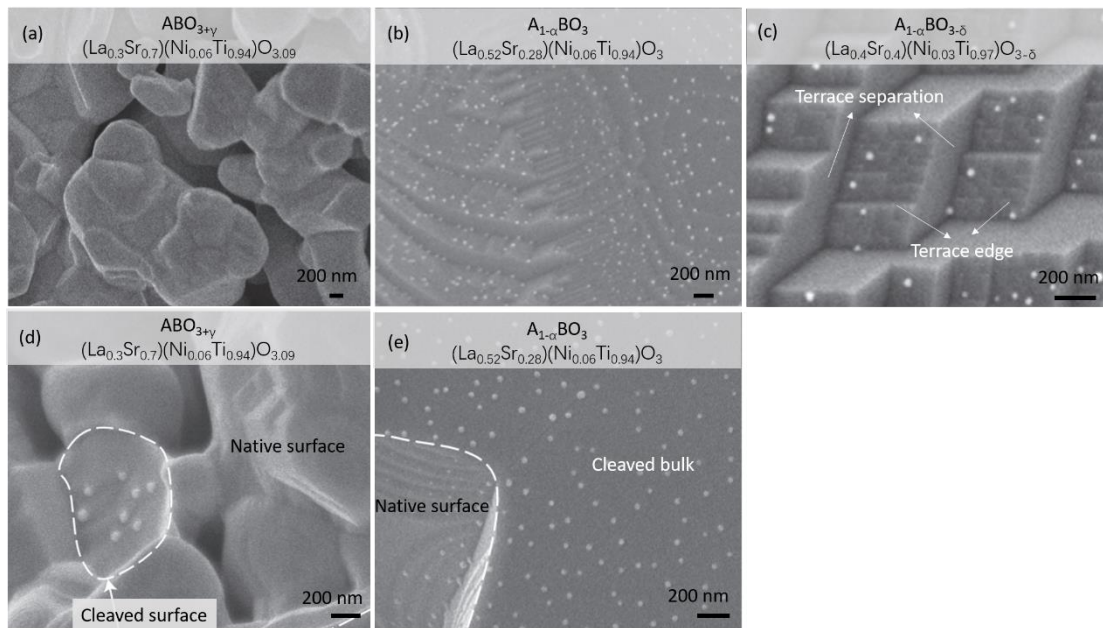


Figure 5-3. Exsolutions from native surface of (a) A-site-stoichiometry, O-excess ( $ABO_{3+\gamma}$ )  $La_{0.3}Sr_{0.7}Ni_{0.06}Ti_{0.94}O_{3.09}$ , (b) A-site-deficient, O-stoichiometric ( $A_{1-\alpha}BO_3$ )  $La_{0.52}Sr_{0.28}Ni_{0.06}Ti_{0.94}O_3$  reduced at 930 °C for 20 h in 5%  $H_2/Ar$ , (c) A-site-deficient, O-deficient ( $A_{1-\alpha}BO_{3-\delta}$ )  $La_{0.4}Sr_{0.4}Ni_{0.03}Ti_{0.97}O_{3-\delta}$  reduced at 930 °C for 20 h and then aged in 3%  $H_2O/5\%H_2/Ar$  at 900 °C for 100 h. Exsolutions from cleaved surface of (d)  $La_{0.3}Sr_{0.7}Ni_{0.06}Ti_{0.94}O_{3.09}$  ( $ABO_{3+\gamma}$ ) and (e)  $La_{0.52}Sr_{0.28}Ni_{0.06}Ti_{0.94}O_3$  ( $A_{1-\alpha}BO_3$ ) reduced at 900 °C for 15 h in 5%  $H_2/Ar$ . Figure reproduced from Ref. 15.

Based on the proposed defect chemistry, the exsolution behaviour was investigated on the native and cleaved surface of the Ni, Cu co-doped BCZY pellets after reduction at 600 °C for 12 h in 5% H<sub>2</sub>/Ar, and the morphologies are displayed in Figure 5-4. In the preparation of ABO<sub>3+γ</sub>-type perovskite, the excess oxygen is generally introduced by doping trivalent cations on the A<sup>2+</sup>-site; however, in our experiments, only Ba is positioned on the A-site, making it not possible to adjust the stoichiometries to be ABO<sub>3+γ</sub>, thus, this type of perovskite will not be discussed here. It can be seen that both the native and cleaved surface are decorated with a large number of nanoparticles, but the average particle size and density vary with the perovskite stoichiometry, grains size, and even the different areas on the same grain. Overall, the nanoparticles on the native surface are slightly smaller in size than those on the cleaved surface, and the particle density is on the opposite trend. But this does not apply to sample BaCe<sub>0.5</sub>Zr<sub>0.3</sub>Y<sub>0.15</sub>Ni<sub>0.03</sub>Cu<sub>0.02</sub>O<sub>3-δ</sub>, who exhibit exsolved particles with a smaller particle size but a higher population on the cleaved surface, as shown in Figure 5-4 (g, h). It is noticed that while the particle size of the Cu metal from BaCe<sub>0.5</sub>Zr<sub>0.3</sub>Y<sub>0.16</sub>Cu<sub>0.04</sub>O<sub>3-δ</sub> (described in Chapter 3) is about ~100 nm (or even 1 μm) at 600 °C, and the Ni metal particles from BaCe<sub>0.5</sub>Zr<sub>0.3</sub>Y<sub>0.16</sub>Ni<sub>0.04</sub>O<sub>3-δ</sub> are around 35 nm, most of the Ni-Cu alloy particles on the native surface of BaCe<sub>0.5</sub>Zr<sub>0.3</sub>Y<sub>0.16</sub>Ni<sub>0.02</sub>Cu<sub>0.02</sub>O<sub>3-δ</sub> are smaller, i.e. 22-25 nm, indicating that the introducing of the second metal significantly modifies the exsolved nanoparticles' size, suppressing the coarsening for Cu metal particles. The strong coarsening effect of Cu due to its high atomic diffusion constants did not make the Ni-Cu alloy particles grow larger than pure Ni metal particles but retained a smaller particle size. This probably arises from the strong interaction between nickel and copper atoms that prevent sintering of the bimetallic particles.<sup>6</sup>

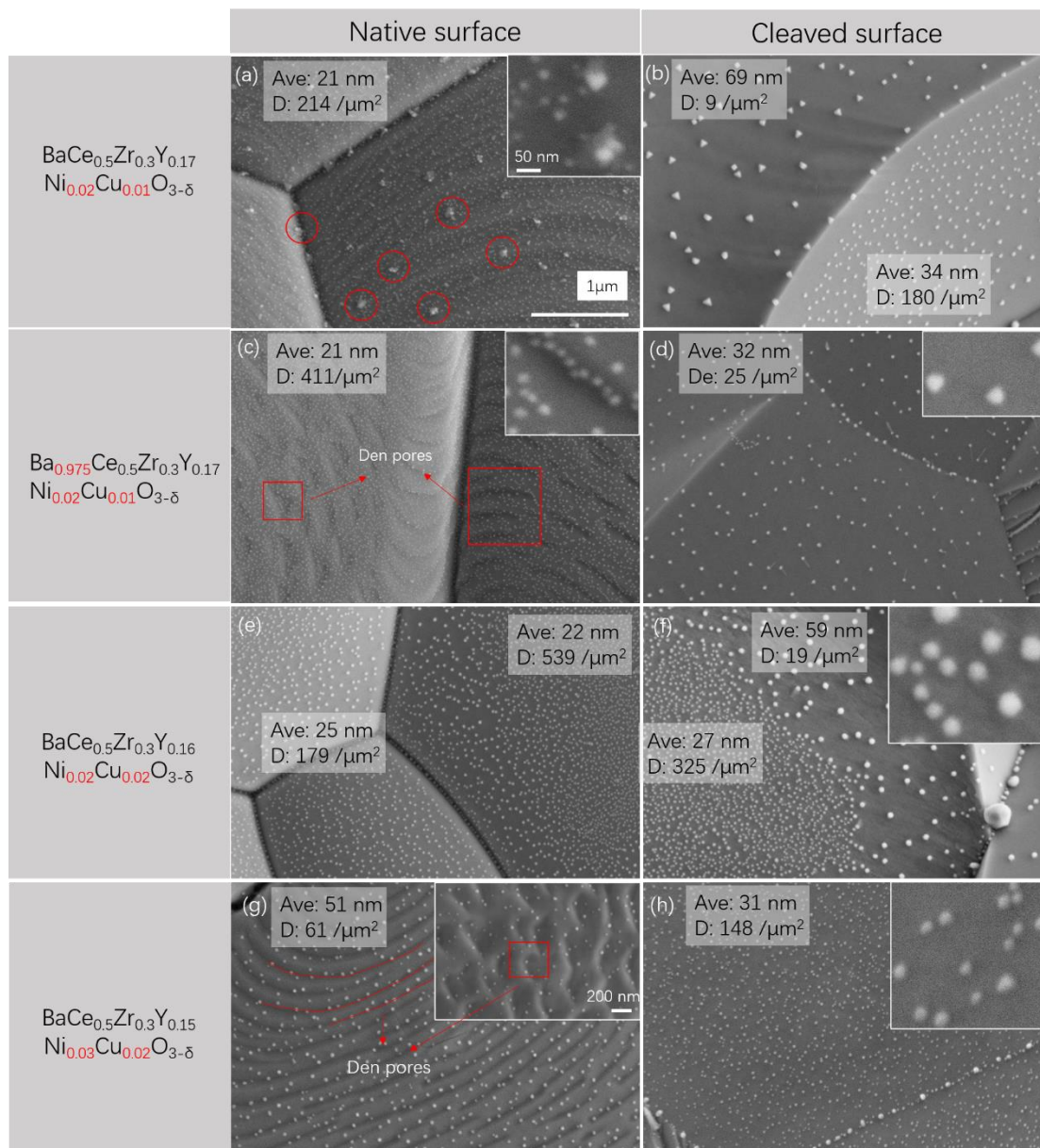


Figure 5-4. Microstructures of the nanoparticles after reducing the Ni, Cu co-doped BCZY at 600 °C for 12 h in 5% H<sub>2</sub>/Ar. (Ave: average particle size, D: particle density)

As the phenomenon of a large number of exsolved particles on the native surface is somehow inconsistent with the defect chemistry proposed before, it stimulates us to investigate the compositional stoichiometry on the parent oxide surface. As shown in Figure 5-5 (b), the EDS mappings of the oxidized  $\text{BaCe}_{0.5}\text{Zr}_{0.3}\text{Y}_{0.16}\text{Ni}_{0.02}\text{Cu}_{0.02}\text{O}_{3-\delta}$  sample reveal a homogeneous distribution of all the elements without distinct element

agglomeration. The high-angle annular dark-field (HAADF) image in Figure 5-5 (a) clearly displays two grains with different surface roughness separated by the grain boundary. The grain on the left side has a slightly terraced surface (the terrace in Figure 5-2 c) while the one on the right shows a rather smooth surface. The lattice space of 3.01 Å in the HRTEM of the bulk in Figure 5-5 (c) is corresponding to the (110) plane of the Rhombohedral crystalline structure of the doped BCZY perovskite (space group R-3c,  $a = b = 6.1258$  Å,  $c = 15.001$  Å) determined by the XRD analysis. Compositions at different positions were investigated by EDS quantification analysis and the results are listed in Figure 5-5 (d). Because  $L\alpha$  of Ba and Ce X-ray emission peaks are overlapping, this leads to inaccurate relative quantitative results of Ba and Ce. Here, the relative quantity ratio between Ba and Ce were obtained from the peak intensity of Ba  $K\alpha$  and Ce  $K\alpha$ . As in  $BaCe_{0.5}Zr_{0.3}Y_{0.16}Ni_{0.02}Cu_{0.02}O_{3-\delta}$ , the nominal stoichiometry of Ba and Ce is 1 and 0.5, respectively, and here  $Ba/(2Ce)$  was calculated to estimate their relative content. Because barium oxide may suffer evaporation upon high temperature sintering, Ce content is assumed to be the accurate value, and the value of  $Ba/(2Ce)$  represents the non-stoichiometry extent of barium, where the value smaller than 1 suggesting barium deficient and larger than 1 meaning barium excess. Surprisingly, the grain with terraced surface shows a Ba-deficient composition, especially at the near-surface area of position 1 and 2, with a slightly more deficiency at the surface area 1. However, the extent of Ba-deficiency decreases considerably at the bulk position 3 with  $Ba/(2Ce)$  being 0.95. On the opposite, the grain with a smooth surface (position 4, 5) demonstrates a significant Ba-excess composition, which is more serious on the surface and the bulk perovskite (position 6) shows a nominal Ba/Ce stoichiometry. Moreover, oxygen content seems to be slightly higher in the smooth grain than in the rough one. It is therefore considered that the terraced surface or the surface with other kinds of patterns, e.g., the rough surface in Figure 5-2 (b, d), is a result of A-site and oxygen non-stoichiometry effect. Similarly, the oxygen non-stoichiometry effect on the surface morphology has already be observed by Neagu. et al.<sup>15</sup> (Figure 5-3 a-c), where oxygen excess ( $ABO_{3+\gamma}$ ) LSNT developed a smooth surface, while terrace-like motifs appeared in the oxygen stoichiometric ( $A_{1-\alpha}BO_3$ ) sample and it became more distinct in both



oxygen and A-site deficient ( $A_{1-\alpha}BO_{3-\delta}$ ) LSNT material. While the surface of different roughness was observed in the different LSNT sample, in our work, the evolution of different morphologies occurs on the same pellet, which is assumed to attribute to the nucleation process and uneven cation diffusion during the perovskite sintering process.

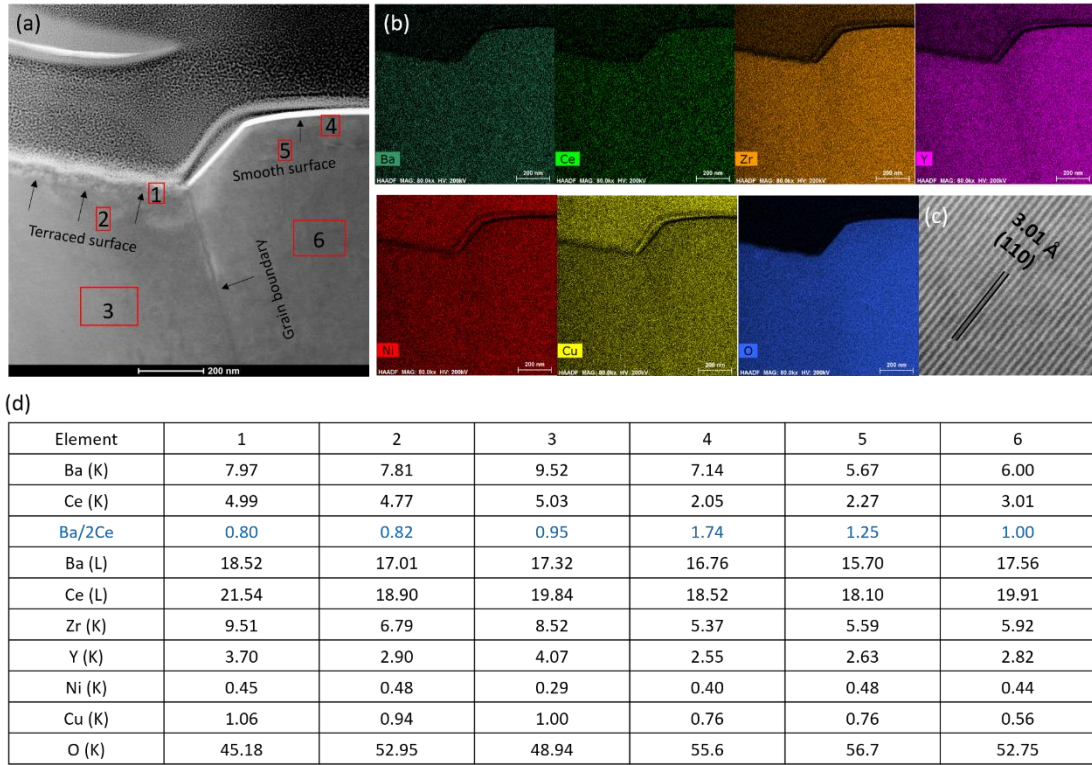


Figure 5-5. (a) EDS mapping, (b) HAADF image and (c) EDS quantification analysis of the prepared  $BaCe_{0.5}Zr_{0.3}Y_{0.16}Ni_{0.02}Cu_{0.02}O_{3-\delta}$  oxide.

Back to the exsolutions observed in Figure 5-4 (a, e), numerous exsolutions are distributed on the smooth native surface of  $BaCe_{0.5}Zr_{0.3}Y_{0.16}Ni_{0.02}Cu_{0.02}O_{3-\delta}$  regardless of barium enrichment of the smooth surface. On the native surface of A-site stoichiometric  $BaCe_{0.5}Zr_{0.3}Y_{0.17}Ni_{0.02}Cu_{0.01}O_{3-\delta}$ , apart from the nanoparticles that are embedded directly into the parent perovskite oxide, some larger particles are located on top of an extra phase, displayed in the red circle in Figure 5-4 (a) and the inserted image of higher magnification. As discussed in the single Cu and Ni doped BCZY, where we also observe an extra phase beneath the Cu and Ni particles that is believed to be Ba-Cu-O and Ba-Ni-O phases, here, this extra phase is supposed to be the mixture of these



two phases. In this case, barium is removed from the perovskite lattice due to the formation of Ba-M-O (M: transition metal, determine this kind of phase as intermediate phase) during reduction, resulting in the alleviation of the detrimental effect of excess A-site cation to the B-site exsolution, providing the possibility for exsolution even on the A-site enriched native surface.

In addition, for the supposed A-site deficient rough surface, exsolution behavior varies upon the extent of the roughness. On the native surface with mild roughness in Figure 5-4 (c), the distribution of nanoparticles is quite homogeneous, while on the surface with distinct patterns in Figure 5-4 (g), particles preferentially grow in the deep pores. This is also the similar phenomenon observed in Figure 5-2 (b, c) where samples with smaller separation between terraces give rise to more uniformly distributed nanoparticles on the parent oxide surface, and exsolutions are prone to occur on the facets of the terrace edges. The varied facets were reported by Neagu et al.<sup>16</sup> to represent different orientations, where the smooth facets (terrace separation in Figure 5-3 c) are A-site terminated (100) and (111) orientations, and the rough surfaces (terrace edges in Figure 5-4 c) correspond to  $ABO^{4+}/O_2^{4-}$  terminated (110) orientations, the preferred termination for exsolution. Moreover, the rough morphology could also facilitate nucleation due to its low surface energy that lowers the nucleation barrier.<sup>17</sup> The nanoparticles distribution on the rough surface is somehow consistent with the above discussed reported results.

Looking at the cleaved surface of  $BaCe_{0.5}Zr_{0.3}Y_{0.17}Ni_{0.02}Cu_{0.01}O_{3-\delta}$  in Figure 5-4 (b), a considerable difference on particle distribution (particle size and density) is observed on different grains. The same inhomogeneous distribution is also observed on the grain interior and around grain boundary of the native (Figure 5-4 e) and cleaved surface (Figure 5-4 f) of  $BaCe_{0.5}Zr_{0.3}Y_{0.16}Ni_{0.02}Cu_{0.02}O_{3-\delta}$ . The inhomogeneous distribution of particles is believed to be related with the orientation of the plane and lattice strain on the local area, and probably also determined by the uneven distribution of compositions between the bulk and grain boundary.

When increasing the reduction temperature to 700 °C, particles grow a little bit larger and the surface coverage decreases than at 600 °C, as seen from Figure 5-6. Same

as the previous observation, native surface achieved smaller but the higher density of nanoparticles than the cleaved surface after reduction. In addition, the intermediate phases (Ba-Ni-Cu-O) become more present along with exsolution, not only on the native surface of the  $\text{BaCe}_{0.5}\text{Zr}_{0.3}\text{Y}_{0.17}\text{Ni}_{0.02}\text{Cu}_{0.01}\text{O}_{3-\delta}$  oxide, but also the cleaved surface of all the four compositions and in particular the stoichiometric samples. It is supposed that the intermediate phases are favorable to form at 700 °C in reducing atmosphere, and Ba deficiency weakens the formation of the phases. The varied morphology of the Ba-Ni-Cu-O phases on the perovskites with different compositions is due to the existence of different stoichiometries, depending on each amount of co-segregation of barium, nickel and copper. Looking carefully at the large particle (~50 nm) in the red circle of the dashed line in Figure 5-6 (f), they are almost in the circle centre that surrounded by some smaller particles, and the diameter of the circle is pretty much the same of ~250 nm. It is thus supposed that ions ( $\text{Ba}^{2+}$ ,  $\text{Ni}^{2+}$ ,  $\text{Cu}^{2+}$ ) from about 250 nm distance diffuse to the nuclei and contribute to the growth of the intermediate phases and particles. Additionally, the particles with the intermediate phases are larger than the surrounding ones that socketed directly into the perovskite, the same phenomenon as observed in Cu-doped BCZY that Cu particles where the extra phase present underneath after reduction at 600 °C for 10 h is much larger.

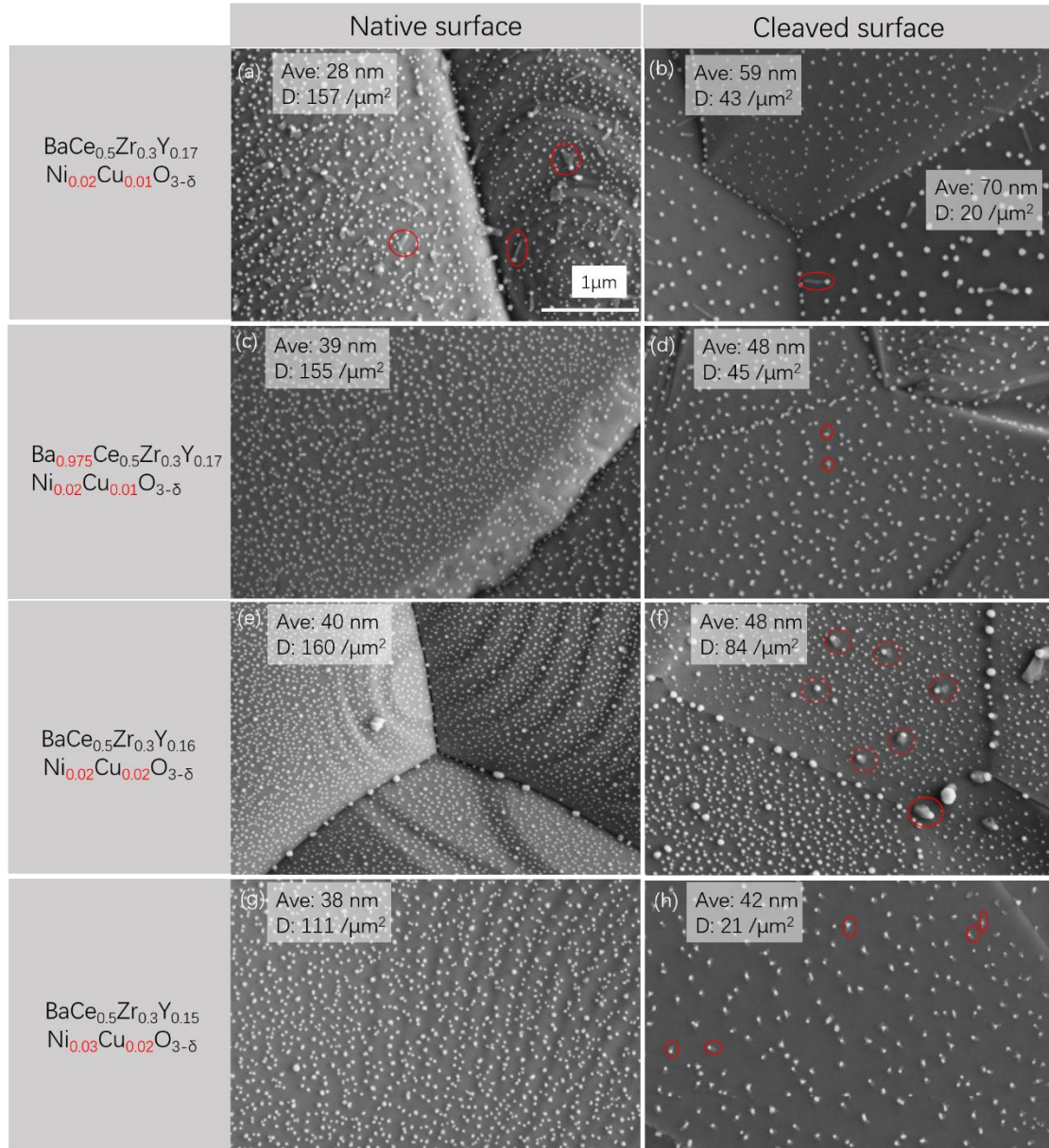


Figure 5-6. Microstructures of the nanoparticles after reducing the Ni, Cu co-doped BCZY at 700 °C for 12 h in 5% H<sub>2</sub>/Ar. (Ave: average particle size, D: particle density)

In order to confirm the exsolution of Ni-Cu alloy nanoparticles, scanning transmission electron microscopy (STEM) along with EDX analysis is conducted on the  $\text{BaCe}_{0.5}\text{Zr}_{0.3}\text{Y}_{0.16}\text{Ni}_{0.02}\text{Cu}_{0.02}\text{O}_{3-\delta}$  sample reduced at 700 °C for 12 h. The EDS mappings in Figure 5-7 (c, f) illustrate the exsolution of Ni-Cu alloy nanoparticles on the perovskite substrate as indicated from the agglomerated Ni and Cu element

distribution in the particles, while the substrate contains uniform Ba, Ce, Zr, Y and O distribution. In the STEM image and the inset of SAED diffractogram of the triangle and cubic-shaped particle (Figure 5-7a, b), the lattice can be indexed with the (200), (020) and (220) planes of the cubic Ni-Cu alloy structure (space group Fm-3m), further proving the formation of the alloy nanoparticles. A thin layer of oxide is presented on the nanoparticle surface, indicated from the oxygen mapping on the out layer of the cubic-shaped particle, which is probably due to the partial re-oxidation of nanoparticles during handling in air. Unexpectedly, quantitative results in Figure 5-7 d show that the Ni/Cu ratio in the triangle and cubic-shaped particle is 3.71 and 3.76, respectively.

Barium EDS mapping in Figure 5-7 c demonstrates that barium-contained phases at position 1 and 3 in Figure 5-7 a, b are located between the nanoparticle and the parent perovskite, wrapping the particles at the bottom area. We believed that this barium contained compound is the extra phase that binds with the particle observed in Figure 5-6. EDS quantification results in Figure 5-7 d show that the extra phases contain mainly Ba, Cu, Ni and O elements with little amount of Zr and Y, which may come from the perovskite matrix as EDS mappings of the corresponding elements show no distribution in the extra phases. The extra phases are thus supposed to be Ba-Ni-Cu-O. Additionally, quantification table illustrates that nickel is around three times the amount of copper in the solid solution, which is close to the Ni/Cu ratio in the alloy particles. Therefore, we suspect that the Ni/Cu ratio in the alloy particles is determined by their values in the extra phase which is further controlled by their co-segregation ability with barium ions during high temperature reduction. Apparently, nickel has more preference in co-segregating with barium than copper ions, leading to the Ba-Cu-Ni-O intermediate phases containing a higher amount of nickel.

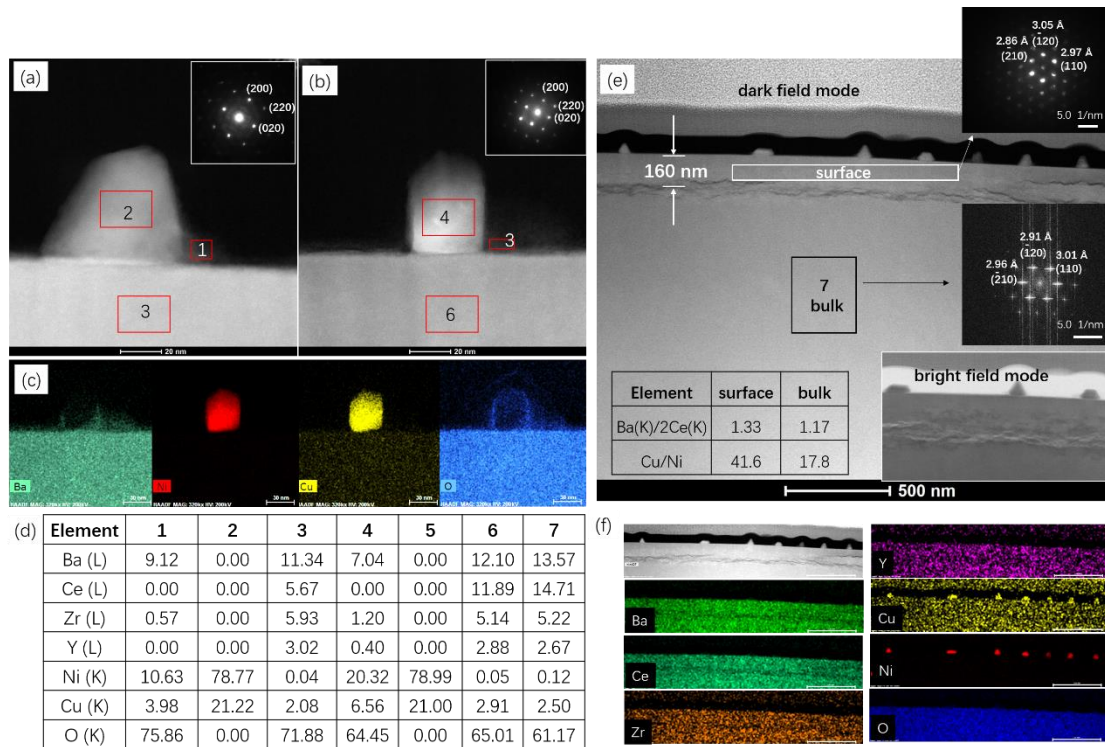


Figure 5-7. TEM characterization of  $\text{BaCe}_{0.5}\text{Zr}_{0.3}\text{Y}_{0.16}\text{Ni}_{0.02}\text{Cu}_{0.02}\text{O}_{3-\delta}$  cleaved pellet after reduced at 700 °C for 12 h. (a, b) STEM images of the triangle and cubic-shaped particles and the corresponding SAED pattern in the inserted images, (c) EDS mappings (Ba, Ni, Cu and O elements) of the cubic-shaped particle, (d) EDS quantitative results in the labelled position in (a), (b) and (e), noting that the quantity of Ba and Ce may not reliable due to the overlapping of  $L\alpha$  of Ba and Ce X-ray emission peaks, (e) Dark field HAADF image of the specimen inserted with bright field image, SAED pattern of the near surface area and FFT pattern of the bulk area, Ba/Cu and Cu/Ni ratio in the surface and bulk area, (f) EDS mappings of the top area in (e).

For the supported perovskite oxide in Figure 5-7 e, a layer with dark contrast is formed at about 160 nm below the surface area and no apparent difference is observed in the EDS mappings between the near surface area and bulk (Figure 5-7 f). The inset of bright field image reveals that the above mentioned dark layer still exhibits a dense structure. In dark field image, the areas with heavier atoms are brighter, indicating that the dark layer at near surface regions contains less number of heavy atoms than the bulk area. This phenomenon is same as the considerable defects in the near surface layer of the reduced Cu-BCZY. Therefore, it is believed that significantly cations diffusion to the surface, especially the large  $\text{Ba}^{2+}$ , occurred from 160 nm beneath the surface. SAED

and FFT patterns show that the near surface layer and the bulk perovskite have the same structure of R-3c symmetry and no severe structure decomposition occurred as a result of exsolution.

It should be also noticed that this TEM sample was prepared from the cleaved surface with reduction treatment, the new native surface of the sample thus belongs to the bulk of the as-prepared oxidized perovskite, which is shown to be barium stoichiometric in the previous characterization. However, the inset EDS quantification table in Figure 5-7 e reveals that the near-surface area of the supported perovskite after reduction contains relatively more barium than the bulk area, further indicating the diffusion of barium to the surface during exsolution. In addition, compared with the as-sintered perovskite in Figure 5-5 c, copper is far more present in the substrate perovskite than nickel after reduction, with Cu/Ni ratio being 41.6 and 17.8 at the near surface area and bulk area, respectively. The higher amount of incorporated copper left in the perovskite lattice is in accordance with the larger Ni ratio in the nanoparticles and intermediate phases. Comparing the Cu/Ni ratio at the near-surface area and the bulk, nickel is much more depleted in the near-surface layer.

The above results also indicate that the formation of Ba-Ni-Cu-O phases is not a result of original surface barium enrichment but of providing an energy saving route for metal particle exsolution. In this case, one can suspect that even on the original A-site enriched native surface, the B-site Ni and Cu cations can also exsolve from the perovskite structure by forming Ba-Ni-Cu-O phases, and this has already been verified as exsolutions occurred on the smooth native surface where Ba is excess (Figure 5-4, 5-6). Recalling that nanoparticles on the native surface have a smaller size and higher density than those on the cleaved surface, except for the surface with distinct den pores on  $\text{BaCe}_{0.5}\text{Zr}_{0.3}\text{Y}_{0.15}\text{Ni}_{0.03}\text{Cu}_{0.02}\text{O}_{3-\delta}$ , which is more determined by the surface energy. Because the smooth native surface is originally barium excess, it provides short diffusion path for the co-segregation of cations to form the intermediate phases. Numerous intermediate nuclei are able to form in a short time, resulting in smaller and highly populated particles distributed on the surface. While on the stoichiometric cleaved surface, barium ions need to migrate from the near-surface layer to segregate

on the surface, and this process is more controlled by barium diffusion. The less frequency in nucleation on surface makes the further cation diffusion towards the firstly formed nucleus at active sites, producing relatively larger intermediate phases. For the slightly rough native surface with barium deficiency, Ni-Cu particle exsolution is facilitated by the lower migration barrier due to the A-site vacancy and the driving force producing from the A-site and oxygen deficiency. However, on the native surface with distinct den pores, nucleation barrier is greatly lowered at the positions of den pores due to the low surface energy, leading to the much more favourable formation of nuclei and higher concentration of ions diffusion. Finally, particles are regularly distributed along the den pores with larger size and less population than the uniformly distributed particles. Thus, in this work, the A-site enrichment seem to produce a quite different effect on exsolutions compared to the well investigated LSNT titanate-based material.

Further increasing the reduction temperature to 800 °C (Figure 5-8), particles become even larger but still uniformly distributed on the surface. Particles on the native surface of the perovskite are still smaller and more populated than those exsolved on the cleaved surface. There are not distinct intermediate phases observed on the surface except for a small amount on the  $\text{BaCe}_{0.5}\text{Zr}_{0.3}\text{Y}_{0.16}\text{Ni}_{0.02}\text{Cu}_{0.02}\text{O}_{3-\delta}$  cleaved surface, as seen in Figure 5-8 (f). Thus, the intermediate Ba-Ni-Cu-O phases are supposed to decompose around 800 °C.



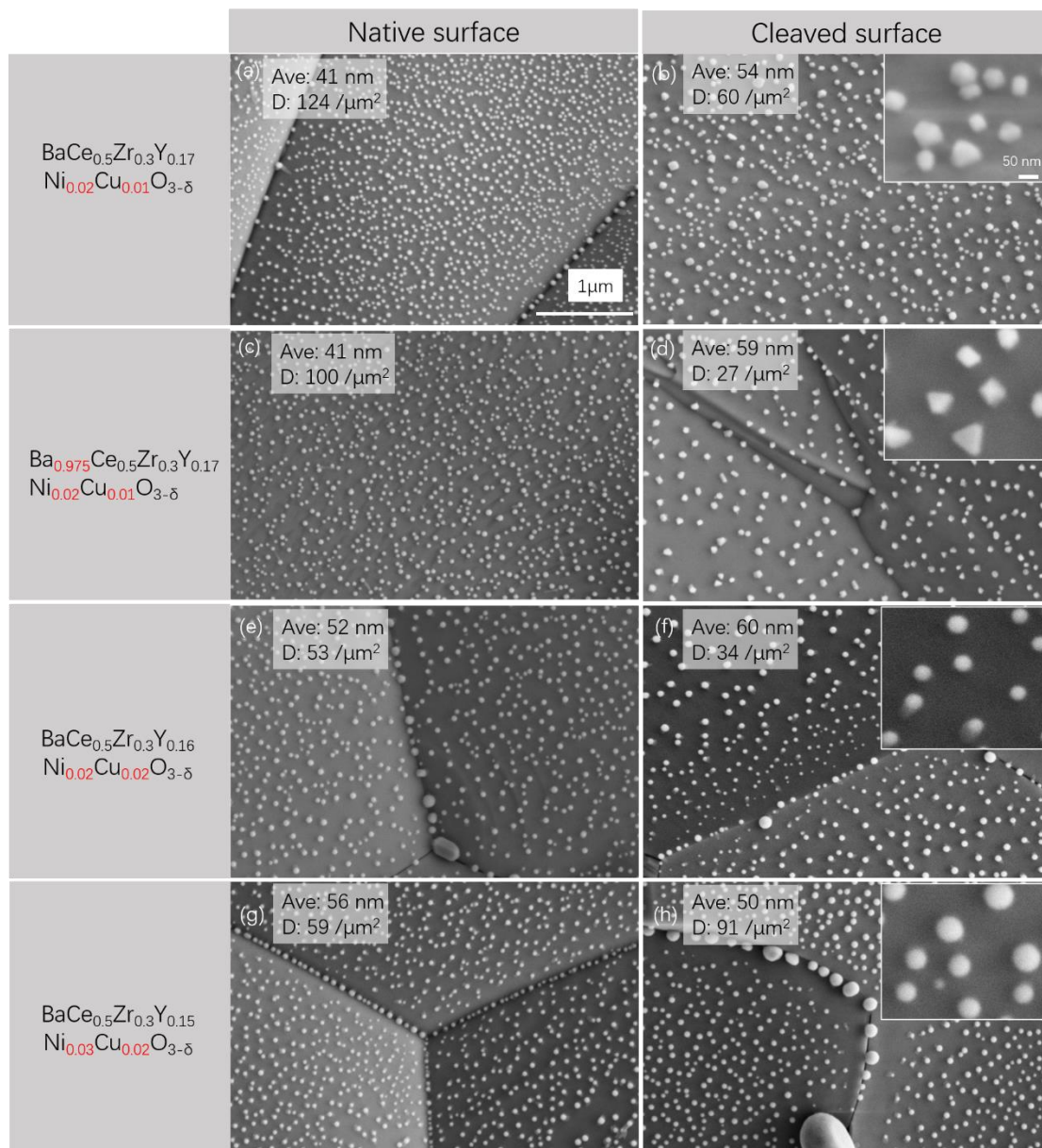


Figure 5-8. Microstructure of the nanoparticles after reducing the Ni, Cu co-doped BCZY at 800 °C for 12 h in 5% H<sub>2</sub>/Ar. (Ave: average particle size, D: particle density)

Apart from the particle size and density, we also noticed that particle shape varies with the nickel and copper stoichiometry in the perovskite. As summarized in Figure 5-9, the shape of the exsolved particles tends to be triangular, cubic and pyramid in shape, for stoichiometric and Ba-deficient  $\text{BaCe}_{0.5}\text{Zr}_{0.3}\text{Y}_{0.17}\text{Ni}_{0.02}\text{Cu}_{0.01}\text{O}_{3-\delta}$  (and some triangular ones observed in  $\text{BaCe}_{0.5}\text{Zr}_{0.3}\text{Y}_{0.15}\text{Ni}_{0.03}\text{Cu}_{0.02}\text{O}_{3-\delta}$ ), while spherical particles



are generally distributed on the cleaved surface of  $\text{BaCe}_{0.5}\text{Zr}_{0.3}\text{Y}_{0.16}\text{Ni}_{0.02}\text{Cu}_{0.02}\text{O}_{3-\delta}$  and  $\text{BaCe}_{0.5}\text{Zr}_{0.3}\text{Y}_{0.15}\text{Ni}_{0.03}\text{Cu}_{0.02}\text{O}_{3-\delta}$  oxides. It is thus deduced that nickel and copper concentration can somehow determine the shape of the exsolved nanoparticles, with Ni-rich ones promoting the formation of a triangular or cubic shape and Cu-rich determining the spherical shape. This provides a way for tailoring particle shape and properties for different applications by simply modifying the metal ions concentration in the alloy.

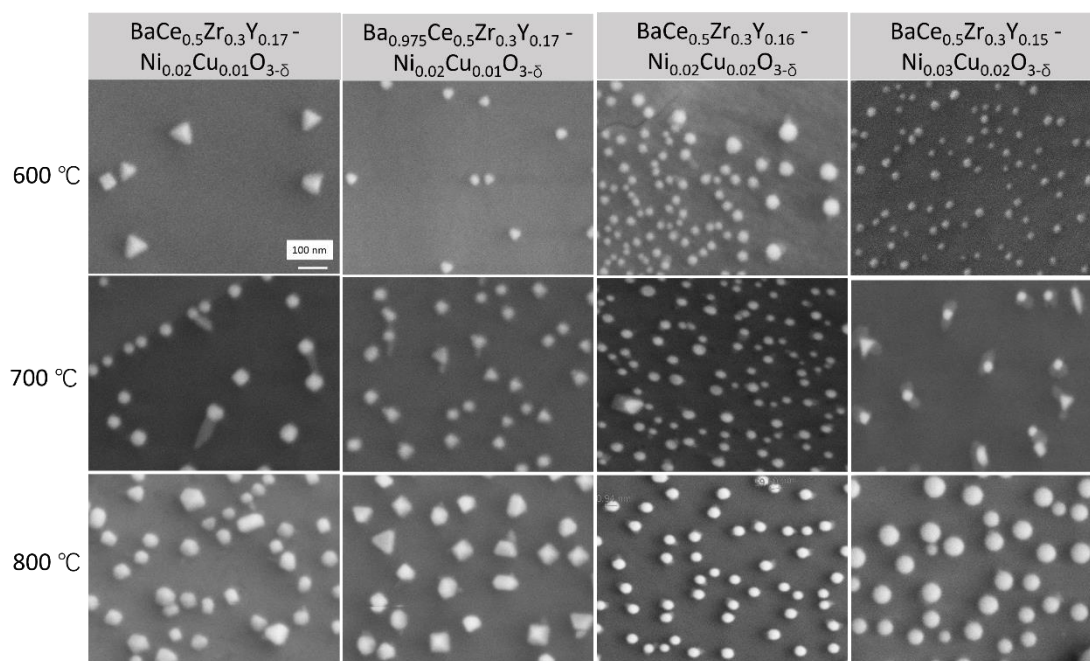


Figure 5-9. Summary of particle shape in Ni, Cu co-doped BCZY as a function of stoichiometry and reduction temperature.

### 5.3.2 The influence of Ni and Cu doping concentration on the Ni/Cu ratio of the exsolved alloy particles

The previous TEM characterization results have shown that although the doping concentration of nickel and copper in BCZY is 2% for each, the resulted exsolved alloy nanoparticle contains a Ni/Cu ratio about 3.7, suggesting a lower exsolution tendency of copper in the presence of Ni. To prove this even further, we prepared two compositions,  $\text{BaCe}_{0.5}\text{Zr}_{0.3}\text{Y}_{0.15}\text{Ni}_{0.03}\text{Cu}_{0.02}\text{O}_{3-\delta}$  and  $\text{BaCe}_{0.5}\text{Zr}_{0.3}\text{Y}_{0.15}\text{Ni}_{0.02}\text{Cu}_{0.03}\text{O}_{3-\delta}$ , to check if nickel would still be the dominating component in the exsolved alloy

nanoparticles even for a Ni/Cu ratio of 2/3. Both samples as powders resulted from grinding in initial pellets were reduced at 700 °C for 12 h. STEM and EDS mapping images in Figure 5-10 demonstrate the exsolution of Ni-Cu alloy nanoparticles on the surface of the doped BCZY perovskite. The existence of Ni-Cu alloy is clearly confirmed by the elemental mappings, which show agglomerated Ni and Cu distribution. Additionally, the nanoparticles exsolved from the matrix with Ni/Cu ratio of 3/2 are smaller than particles with the opposite ratio, indicating that copper is more likely to facilitate particle growth than nickel. The high-angle annular dark-field (HAADF) images clearly present the socketing nature of the particle in the substrate, especially looking at the bottom right particle in Figure 5-10 (a) where almost half of its volume is immersed in the substrate material. Furthermore, a core-shell structure of the alloy particle is presented in all the four nanoparticles. For the core area of the particles, it is found that exsolutions from the perovskite  $\text{BaCe}_{0.5}\text{Zr}_{0.3}\text{Y}_{0.15}\text{Ni}_{0.03}\text{Cu}_{0.02}\text{O}_{3-\delta}$  (Ni/Cu=3:2) result in a significant high Ni/Cu ratio between 32 to 43 in the alloy particles, while  $\text{BaCe}_{0.5}\text{Zr}_{0.3}\text{Y}_{0.15}\text{Ni}_{0.02}\text{Cu}_{0.03}\text{O}_{3-\delta}$  (Ni/Cu=2:3) produces alloy particles with Ni/Cu ratio being in the range of 1.7 - 4. The Ni/Cu ratio in the alloy particle varies with the nanoparticle size, with larger particle containing more Cu in the alloy, which further verifies the coarsening effect of copper on nanoparticles. In fact, it has been investigated in literature by the temperature-programmed reduction (TPR) results that the reduction temperature of the unsupported pristine CuO is 230 °C, which is substantially lower than that of NiO, 430 °C. This result is also in agreement with thermodynamics that the  $\Delta G_r^0$  for CuO and NiO reduction to corresponding metals is  $-132 \text{ kJ mol}^{-1}$  and  $-49.4 \text{ kJ mol}^{-1}$ , respectively, suggesting that the reducibility of CuO is higher than NiO.<sup>5</sup> Therefore, copper tends to grow larger than nickel, leading to the Cu-rich larger particles.

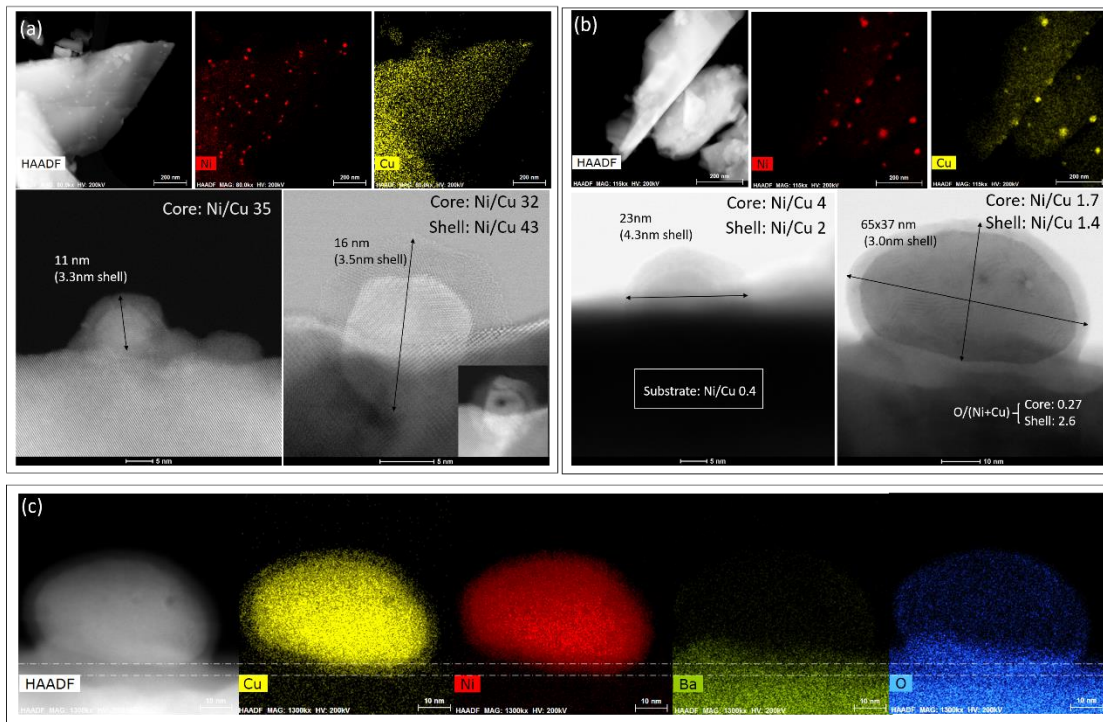


Figure 5-10. EDS mapping and HAADF images of exsolutions on  $\text{BaCe}_{0.5}\text{Zr}_{0.3}\text{Y}_{0.15}\text{Ni}_{0.03}\text{Cu}_{0.02}\text{O}_{3-\delta}$  (a) and  $\text{BaCe}_{0.5}\text{Zr}_{0.3}\text{Y}_{0.15}\text{Ni}_{0.02}\text{Cu}_{0.03}\text{O}_{3-\delta}$  (b), EDS mapping of Ni-Cu particle from (b) on (c).

The shell of the structure is believed to be an oxide layer, as illustrated by the much higher oxygen content ( $\text{O}/(\text{Ni}+\text{Cu}) = 2.6$ ) than in the core ( $\text{O}/(\text{Ni}+\text{Cu}) = 0.27$ ) for the particle in Figure 5-10 (b). For all the four particles, the oxide layer is about 3-4 nm thick and is independent on the particle size. One reason for the formation of this layer is the native formation while handling the sample in air. Another possibility is that the oxide shell is formed during the exsolution process as positively charged Cu or Ni were also found in the catalyst preparation process in the reduction atmosphere. For example, by adding potassium as catalytic promoter towards reverse water-gas shift reaction, positively charged  $\text{Cu}^+$  was induced at the near interfacial area with potassium ions, which was resulted from the electron withdrawing from Cu by  $\text{K}_2\text{O}$ <sup>18-19</sup>. This kind of stabilization effect was also found in copper catalysts supported by some oxides, such as  $\text{Cu}/\text{ZrO}_2$  or  $\text{Cu}/\text{ZnO}$ .<sup>20</sup> Similarly, in the  $\text{Ni}_x\text{Cu}_y$  alloy supported on  $\text{CeO}_2$ , a fraction of  $\text{Cu}^+$  and  $\text{Ni}^{2+}$  were proved to exist in the catalysts by XPS characterization.<sup>21</sup> It is

believed that the existence of copper or nickel oxide species was due to the strong metal-support interaction induced by the redox properties of CeO<sub>2</sub>. The synergistic effects keeps a portion of copper or nickel in the positively charged state.<sup>22-23</sup> Additionally, the reaction between nickel and copper was proposed by Smironov et al. to account for the nickel oxide traces in the alloys from the incomplete reduction of nickel when supported on SiO<sub>2</sub>. In their work, Ni-Cu alloy formation process was suggested to occur according to Eq. 5-1 and 5-2:



The produced CuO via Eq. 5-2 is re-reduced by H<sub>2</sub> and the resulted Cu<sup>0</sup> diffuses into NiO, reducing it to metallic Ni and incorporating into the Ni lattice to yield the alloy. As the diffusion and reduction progresses, Cu metal would deposit on the surface and hinder the transport of hydrogen to the metal oxides. Moreover, the heterogeneity of the sample prevents the diffusion of Cu<sup>0</sup> to NiO and thus giving rise to the incomplete reduction of NiO. In our work, since the oxide layer is not observed on the single Ni particles exsolved from the correspondingly doped BCZY oxides, the oxidation effect induced from the interaction with the oxide supports is less concerning, while the introducing of the second metal atom to the lattice of the host particle structure alters the property of the particles, probably by modifying the electronic or structural parameters.

As it can be seen in the inset in Figure 5-10 (a) that the shell layer probably exists also in the embedded part of the particle that is not exposed to air or the particle is behind the observed substrate plane but not embedded. In the Cu mapping of the particle in Figure 5-10 (c), the interface between the particle and the substrate shows a less agglomerated copper than in the core area and forms a smooth extension from the shell structure. Oxygen mapping shows its distribution at the supposed shell structure at the interface, with similar contrast as the substrate area but more distinct than the shell exposed in air. Additionally, a uniform distribution of barium is also found at the interface shell area and the substrate oxide from the mapping, indicating that the supposed interface shell structure is actually the perovskite matrix with accumulated

copper due to the ongoing exsolution process. It is therefore more convincing that the shell layer is simply due to the oxidation from air and probably this behaviour is more obvious for the NiCu alloy particles.

Afterwards, comparing the Ni/Cu ratio in the shell and core, for the particles with significant more Ni in Figure 5-10 (a), the Ni/Cu ratio gets to be even higher in the outer layer than in the core, while for the particles with relatively more Cu in Figure 5-10 (b), the shell contains more copper than the core. For the phase separation at the surface, the copper enriched surface was observed in some Ni-Cu alloy catalysts as investigated by several researchers, suggesting that this is a consequence of the relatively lower surface free energy of copper rather than nickel that allowing the system to minimize its total free energy.<sup>3-4, 21, 24</sup> However, nickel presence more on the surface than in the bulk was reported to occur in Ni<sub>5</sub>Cu<sub>85</sub>-SiO<sub>2</sub><sup>3</sup>, Ni<sub>8</sub>Cu<sub>1</sub>-CeO<sub>2</sub> catalysts<sup>21</sup> and in the circumstances of a lower reduction temperature that determined by the kinetic factor<sup>4</sup>. Li et al.<sup>4</sup> suggested that although Cu segregation to the surface is thermodynamically favoured at relatively low temperature, the segregation is kinetically dominated. This is because the reducibility of the copper precursor is higher than the one of nickel precursor, leading to reduced samples containing more Cu metal species in the early reduction stage. Furthermore, the lower Tamman temperature of Cu and CuO than Ni and NiO makes copper species diffuse faster than nickel, forming Cu crystals on the support, while the slower diffusion of nickel towards the Cu-rich nuclei leads to a final Cu-rich core and Ni-rich shell structure. The metastable structure with Ni-rich shell would reach the equilibrium when higher temperature (>700 °C) is used, producing a Cu-rich surface with lower surface energies. In addition, as suggested in phase diagram, the Ni-Cu shows a continuous solid alloy solution in all composition ranges above the critical temperature of 354 °C, while in-situ XRD reveals the existence of two phases of Cu-rich and Ni-rich alloy supported on CeO<sub>2</sub> between 300-550 °C, indicating that the strong metal-support interactions probably prevented the complete interdiffusion of Ni and Cu atoms.<sup>6</sup> Thus, the phase separation on the surface can be attributed to three possible reasons: Ni/Cu ratios in the particle, reduction temperature and the interaction with the supports.

In our work, the reduction temperature for the  $\text{BaCe}_{0.5}\text{Zr}_{0.3}\text{Y}_{0.15}\text{Ni}_{0.03}\text{Cu}_{0.02}\text{O}_{3-\delta}$  and  $\text{BaCe}_{0.5}\text{Zr}_{0.3}\text{Y}_{0.15}\text{Ni}_{0.02}\text{Cu}_{0.03}\text{O}_{3-\delta}$  samples is 700 °C, and the support is both Ni, Cu co-doped BCZY perovskite, therefore the reduction temperature is not the factor that determines the surface enrichment phenomenon here but the other two factors mentioned above. Due to the intricate aspects required for investigating these aspects, we did not explore them within the timeframe of this research study. Some other experiments are required, including electron microscopy along with modelling to understand this process.

### 5.3.3 EBSD investigation on exsolutions from Ni, Cu co-doped BCZY oxide

In previous observation of the distribution of nanoparticles exsolved from the doped BCZY perovskite oxide (Figure 5-4), particles size and population demonstrated a nonuniformity between different grains. The varied grains are believed to correspond to the different orientation of the cubic perovskite structure, motivating us to study the relationship between the exsolved particle distribution and the crystalline orientation of the substrate structure.

Electron backscatter diffraction (EBSD) is a technique for microstructural-crystallographic characterization used in conjunction with the scanning electron microscope.<sup>25-26</sup> This technique can be used for providing information about the crystal structure<sup>25</sup>, grain orientation<sup>25</sup>, phase<sup>25</sup> or strain<sup>27</sup> in the material. In order to obtain an analyzable EBSD orientation map, the crystalline specimen placed in the SEM chamber is required to be flat and carefully prepared. Herein, the  $\text{BaCe}_{0.5}\text{Zr}_{0.3}\text{Y}_{0.16}\text{Ni}_{0.02}\text{Cu}_{0.02}\text{O}_{3-\delta}$  pellet sample in our work was finely polished and finally showed a very clean and flat surface. Then, the polished pellet was gently placed in a crucible boat and reduced at 800 °C for 12 h in a tube furnace with 5%  $\text{H}_2/\text{Ar}$ . After that, EBSD orientation map was collected on the reduced pellet.

Figure 5-11 is the SEM image of the polished  $\text{BaCe}_{0.5}\text{Zr}_{0.3}\text{Y}_{0.16}\text{Ni}_{0.02}\text{Cu}_{0.02}\text{O}_{3-\delta}$  surface after reduction. It can see that nanoparticles at the grains 1 and 2 seem to be smaller than those on grains 3 and 4, which further illustrates the influence of orientation on the nanoparticles exsolution on the perovskite material.

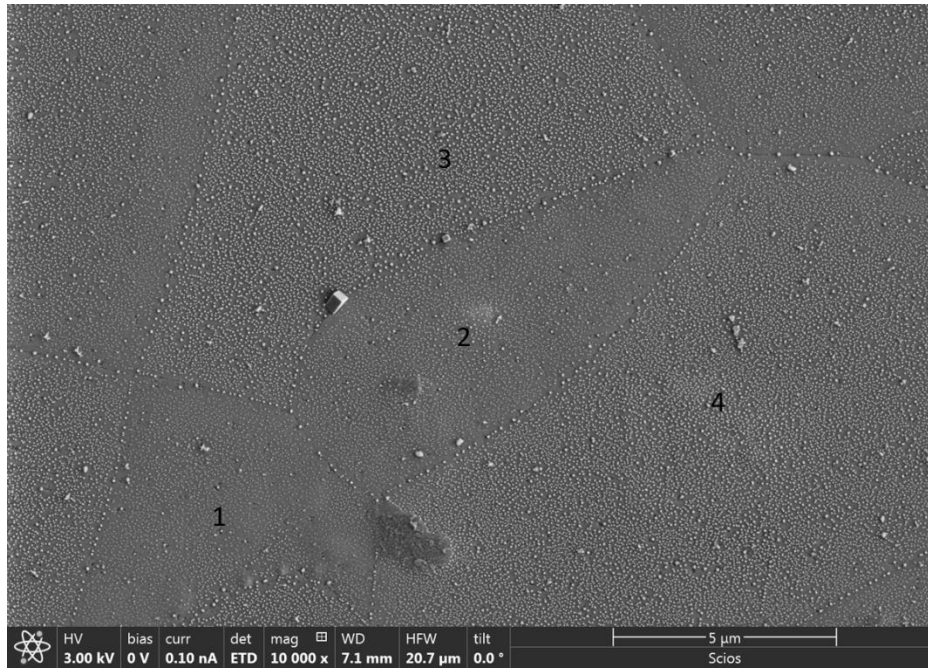


Figure 5-11. SEM image of the polished  $\text{BaCe}_{0.5}\text{Zr}_{0.3}\text{Y}_{0.16}\text{Ni}_{0.02}\text{Cu}_{0.02}\text{O}_{3-\delta}$  surface after reduction at 800 °C for 12 h in 5%  $\text{H}_2/\text{Ar}$ .

After collecting the EBSD map, SEM images were taken on some grains of a certain orientation, including (001), (111), (101) and the orientations in the middle of the two of them. Note that the orientation is roughly estimated according to its position in the colour key (Figure 5-12 c). The nanoparticles average diameter (particles are regarded as spheres) and population were counted and summarized in Figure 5-12 (c), with D representing particle diameter and P representing population per  $\mu\text{m}^2$ . The SEM image in Figure 5-12 (a) clearly reveals the existence of individual grain and the grain boundary, suggesting the well-prepared surface. Orientation map in Figure 5-12 (b) demonstrates the differently oriented grains indicated from their different colours, and their orientation can be known by matching their colour with the position in the colour key. Generally, except the three corner points (red, blue and green), the other positions stand for the mixed orientation. In the areas of the holes, which cannot be indexed, are shown to be black in the orientation map.<sup>28</sup> Apart from the large black holes in Figure 5-12 (b), the other small black dots are probably the defects created during the sample polishing process.



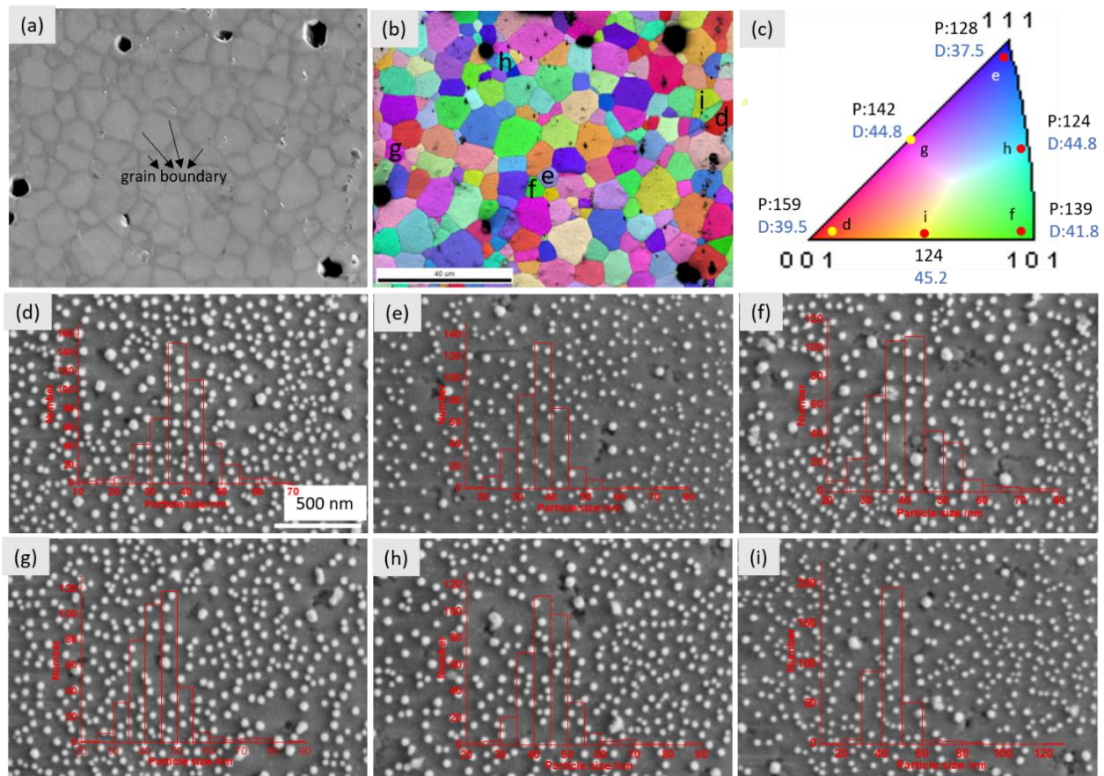


Figure 5-12. (a) SEM image of the polished  $\text{BaCe}_{0.5}\text{Zr}_{0.3}\text{Y}_{0.16}\text{Ni}_{0.02}\text{Cu}_{0.02}\text{O}_{3-\delta}$  surface after reduction and (b) the corresponding EBSD orientation map, (c) the EBSD orientation color key and the summarization of the particle average size and population at different positions (P represents population and D represents particle diameter), the positions are signed in (b) with the same letter, (d-i) SEM images of the grains that at the corresponding position in (b) and (c), the inserted red figures are the particle size and proportion on the grain.

As summarized in Figure 5-12 (c), nanoparticles exsolved from (111) direction seem to be smaller (37.5 nm) and less present than the ones exsolved from (001) (39.5 nm) and (101) (41.8 nm), while the mix of the two planes by half and half results in larger particle size of around 45 nm. This proved that the orientation of the grain has a certain influence on the nanoparticle exsolution. In fact, researchers have already calculated the segregation energy on different orientations by DFT simulation to verify the preferential particle growth on specific terminations.<sup>17</sup> For the Ni metal exsolution on  $\text{La}_{0.4}\text{Sr}_{0.4}\text{Sc}_{0.9}\text{Ni}_{0.1}\text{O}_{3-\delta}$ , four main surfaces, (001), (010), (100), (121) are chosen for the calculation because of their relative high intensity in the XRD pattern. The results



show that all the four surfaces have a negative nickel segregation energy, but the segregation energy on the (010) surface is the smallest, followed by (100), (121), and (001). The difference in segregation energy may come from different nickel concentration near the surfaces, which would further impact the exsolution kinetics.<sup>17</sup> In order to understand more on the effect of structure orientation on the particle exsolution, beside the six grains investigated in this experiment, more grains need to be investigated in future work to offer a more complete picture.

## 5.4 Thermogravimetric analysis

Oxygen loss during reduction was estimated from the TGA measurement. All the four compositions were tested at 800 °C for 12 h in 5% H<sub>2</sub>/N<sub>2</sub> and the results were presented in Figure 5-13 (a). Weight loss occurs at about 350 °C for all the stoichiometries and it continues to decrease as the temperature increase. When the temperature reaches 800 °C, the materials do not show apparent weight loss any longer. The extent of reduction ( $\delta$ ) was calculated according to the previous equation in Chapter 3, expressed in lost oxygen atoms per formula unit of perovskite (at./f.u.). As can be seen from the plot in Figure 5-13 (b) that the extent of reduction increases slightly as a function of total transition metal doping concentration, while decreases with the introduction of 0.025 Ba deficiencies. This further proves that the A-site vacancy will not improve the B-site cation exsolution in the Ni, Cu co-doped BCZY perovskite, and the promoting effect of the formation of the Ba-Ni-Cu-O phases is more beneficial for the Ni-Cu alloy exsolution.

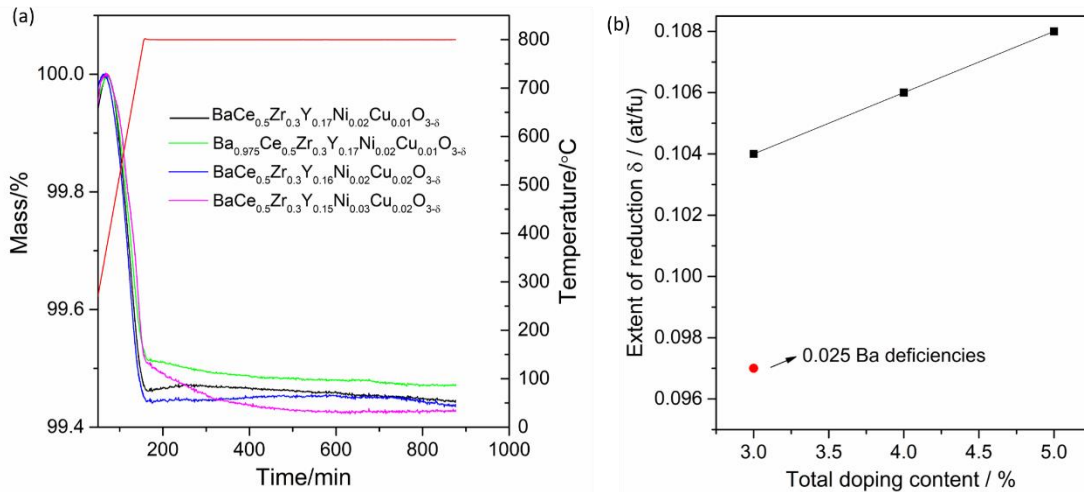


Figure 5-13. (a) Thermogravimetric analysis (TGA) of Ni, Cu co-doped BCZY in 5%  $\text{H}_2/\text{N}_2$  as a function of temperature, (b) calculated extent of reduction at 800 °C as a function of total transition metal doping content.

## 5.5 Electric conductivity and ionic transport number tests

### 5.5.1 DC conductivity test

The total conductivity of the four Ni, Cu co-doped compositions was measured by DC conductivity test in air and 5%  $\text{H}_2/\text{N}_2$  at 600 °C. The values in Figure 5-14 are obtained after the conductivity remains stable at 600 °C. All the four samples present very low conductivity both in air and reducing atmosphere, with conductivity on reduction smaller than that in air. The decrease of the conductivity value on reduction suggests p-type hole conduction of the material and occurs due to the oxygen loss from the perovskite lattice, as predicted by Eq. 5-3:<sup>29</sup>



For the conductivities in air, the co-doped samples exhibited pretty much the same values as the single nickel or copper doped oxides, in the range of 0.01-0.02  $\text{S cm}^{-1}$ . However, unlike the performance of the single Cu-doped BCZY, the conductivity of the Ni, Cu co-doped oxide did not show an increase in value and metal behaviour upon exsolution (n-type), indicating that the introduction of nickel into the Cu-doped compound greatly affects the particle exsolution, which is responsible for the perovskite

electric property.

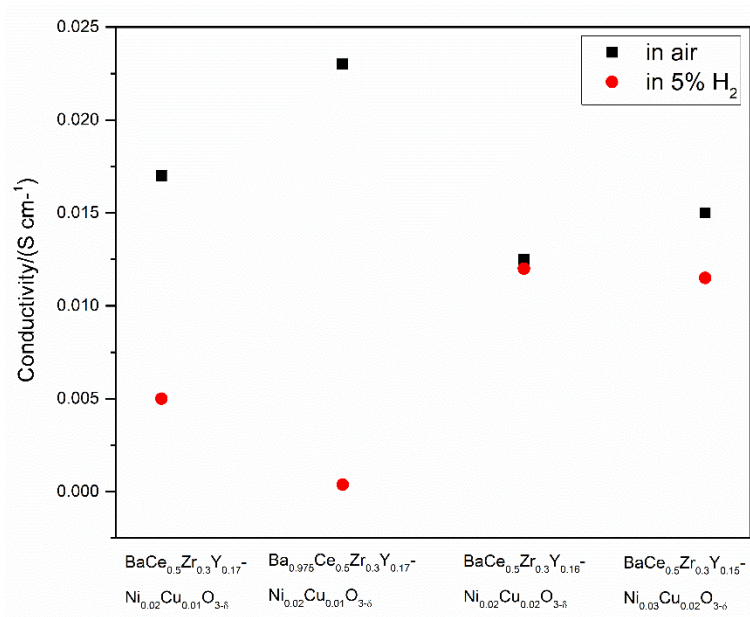


Figure 5-14. Total conductivity values of Ni- Cu co-doped BCZY in air and 5% H<sub>2</sub>/N<sub>2</sub> measured by DC-conductivity test.

### 5.5.2 AC conductivity test

In a typical AC impedance measurement, the complex impedance of a sample, including the real and imaginary components, is measured as a function of frequency. Due to the different relaxation time for ion transfer through the electrolyte, the ideal Nyquist plot of a solid electrolyte is composed of three separate and distinct semicircles at high frequency, intermediate frequency and low frequency, attributed to bulk, grain boundary and electrode performance, respectively (Figure 5-15).<sup>30</sup> The identification of the bulk or grain boundary behaviour in a semicircle is determined from evaluating its capacitance. As revealed in Table 5-1, a capacitance value of  $\sim 1 \times 10^{-12}$  F cm<sup>-1</sup> is expected to be the bulk property and  $\sim 1 \times 10^{-11}$ - $10^{-8}$  F cm<sup>-1</sup> attributes to the grain boundary behavior. For the capacitance value of  $\sim 1 \times 10^{-7}$  - $10^{-5}$  F cm<sup>-1</sup>, it is related to the interaction at sample-electrode interface. To a first approximation, the effective resistance of each of three regions can be estimated from the diameter of each of these arcs, from one (extrapolated) intercept with the x axis to another. For the more accurate

resistance value, the arcs need to be fitted with an equivalent circuit, and one can calculate the conductivity from the fitted resistance by accounting for the sample geometry according to equation 5-4:

$$\sigma = \frac{1}{R} \frac{L}{A} \quad \text{Eq. 5-4}$$

where L is the sample thickness, A is its cross-sectional area, and R is the electrical resistance of the corresponding contribution.

The activation energy ( $E_a$ ) and pre-exponential term (A) can then be determined from a fit of the data to the Arrhenius equation Eq. 5-5:

$$\sigma T = A \exp(-E_a/k_b T) \quad \text{Eq. 5-5}$$

where A is a pre-exponential factor, T and  $k_b$  are temperature (K) and the Boltzman constant, respectively.

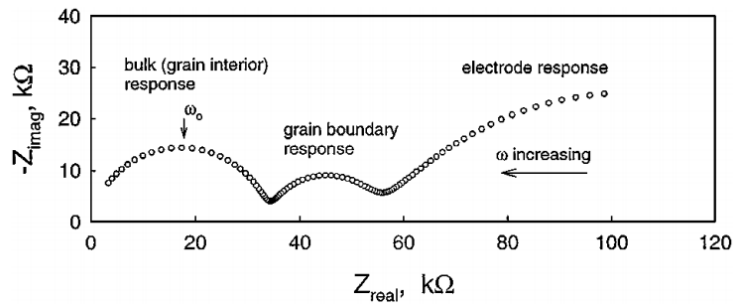


Figure 5-15. Schematic impedance plot in the Nyquist representation of a typical polycrystalline material.

Table 5-1. Capacitance values based on 1 cm cube and their possible interpretations.

(reference<sup>31</sup> [31])

Capacitance [F]	Phenomenon Responsible
$10^{-12}$	Bulk
$10^{-11}$	Minor, second phase
$10^{-11} - 10^{-8}$	Grain boundary
$10^{-10} - 10^{-9}$	Bulk ferroelectric
$10^{-9} - 10^{-7}$	Surface layer
$10^{-7} - 10^{-5}$	Sample-electrode interface
$10^{-4}$	Electrochemical reactions

Figure 5-16 shows the complex impedance plots of  $\text{BaCe}_{0.5}\text{Zr}_{0.3}\text{Y}_{0.17}\text{Ni}_{0.02}\text{Cu}_{0.01}\text{O}_{3-\delta}$  measured at 150, 200 and 300 °C in dry air. The impedance spectra in Figure 5-16 (a) presents the typical high-frequency bulk semicircle and intermediate-frequency grain boundary semicircle at 150 °C, while at higher temperature 200 °C, the bulk response shows an incomplete semicircle (Figure 5-16 b) and is no longer accessible at 300 °C (Figure 5-16 c). This unavailability to collect the bulk response at high temperature is because its characteristic frequency reaches a value greater than the maximum frequency of EIS.<sup>32</sup>

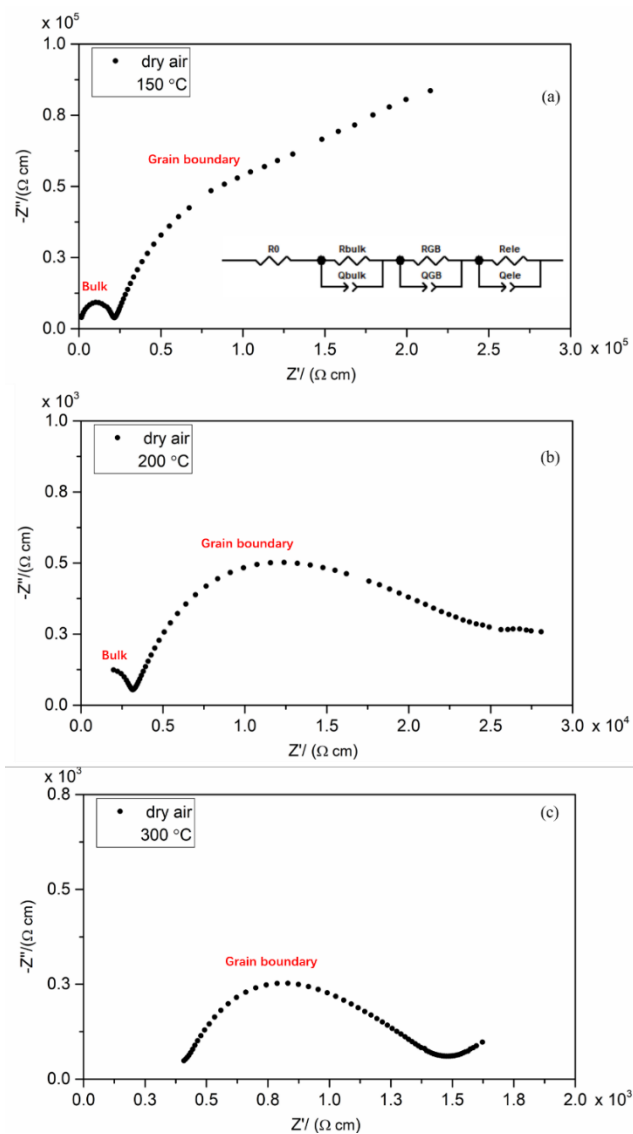


Figure 5-16. Complex impedance plots of  $\text{BaCe}_{0.5}\text{Zr}_{0.3}\text{Y}_{0.17}\text{Ni}_{0.02}\text{Cu}_{0.01}\text{O}_{3-\delta}$  measured at (a) 150 °C, (b) 200 °C and (c) 300 °C in dry air.

The total conductivity of the BCZY-based electrolyte material may be given by possibly four different charge carriers, electrons, holes, oxygen ions and protons. Typically, at high temperature, the contribution of the p-type conductivity and oxygen ion conduction to the total conductivity is relatively large in air. When water vapour is introduced, proton ion conduction could be the dominant charge carrier, but the proton conductivity will decrease at a temperature higher than 500 or 600 °C due to the desorption of water. Here, four different atmosphere conditions were employed in the EIS test, including dry air, wet air (3% H<sub>2</sub>O), dry 5% H<sub>2</sub>/Ar, wet 5% H<sub>2</sub>/Ar. Figure 5-17 shows the Arrhenius plots for the stoichiometric BaCe<sub>0.5</sub>Zr<sub>0.3</sub>Y<sub>0.17</sub>Ni<sub>0.02</sub>Cu<sub>0.01</sub>O<sub>3-δ</sub> and A-site deficient Ba<sub>0.975</sub>Ce<sub>0.5</sub>Zr<sub>0.3</sub>Y<sub>0.17</sub>Ni<sub>0.02</sub>Cu<sub>0.01</sub>O<sub>3-δ</sub> electrolytes, the conductivities are obtained by fitting the impedance spectra with the equivalent circuit shown in Figure 5-16 (a). It is apparent that the total conductivities for both samples in dry air (high pO<sub>2</sub>) are higher than those in a dry hydrogen atmosphere (low pO<sub>2</sub>), indicating the predominant p-type electron-hole conduction, consistent with the DC conductivity test. While the total conductivity for both samples in wet hydrogen is higher than those in dry hydrogen containing atmosphere, especially at a temperature higher than 450 °C, the difference is not so pronounced in air. The enhancement in conductivity under wet atmosphere is a typical characteristic of the proton conductivity, but this effect is normally eclipsed in high pO<sub>2</sub> because hole conductivity increases as a function of (pO<sub>2</sub>)<sup>1/4</sup>, while proton conductivity is independent of pO<sub>2</sub>. The deviation of conductivities from a linear relationship with temperature in hydrogen containing atmosphere when temperature rises is due to the desorption of water from the perovskite structure.

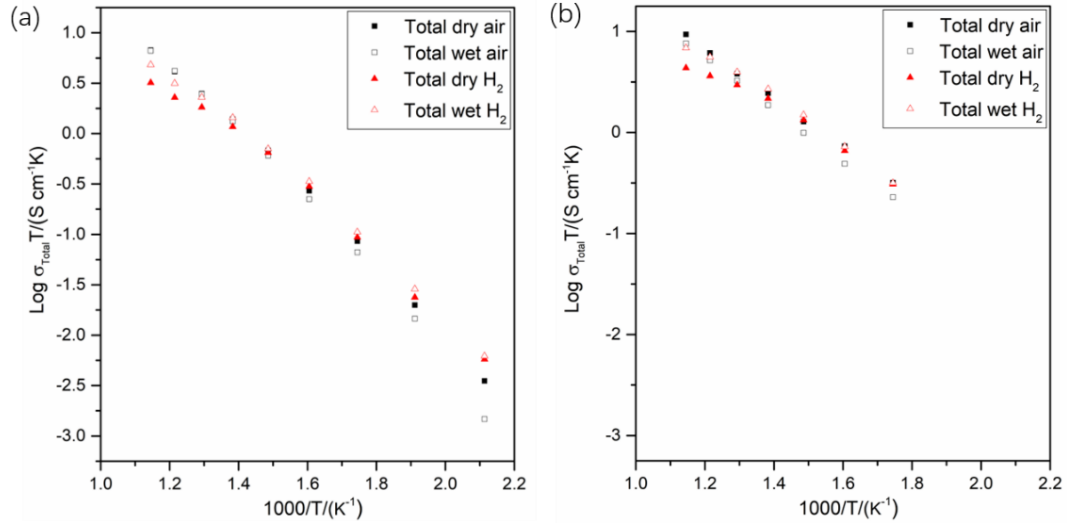


Figure 5-17. Arrhenius plots for total conductivity of  $\text{BaCe}_{0.5}\text{Zr}_{0.3}\text{Y}_{0.17}\text{Ni}_{0.02}\text{Cu}_{0.01}\text{O}_{3-\delta}$  (a) and  $\text{Ba}_{0.975}\text{Ce}_{0.5}\text{Zr}_{0.3}\text{Y}_{0.17}\text{Ni}_{0.02}\text{Cu}_{0.01}\text{O}_{3-\delta}$  (b) as a function of temperature in different atmospheres.

Table 5-2. Total conductivity values of  $\text{BaCe}_{0.5}\text{Zr}_{0.3}\text{Y}_{0.17}\text{Ni}_{0.02}\text{Cu}_{0.01}\text{O}_{3-\delta}$  (stoichiometric) and  $\text{Ba}_{0.975}\text{Ce}_{0.5}\text{Zr}_{0.3}\text{Y}_{0.17}\text{Ni}_{0.02}\text{Cu}_{0.01}\text{O}_{3-\delta}$  (deficient) at 600 °C and 450 °C and their activation energy (Ea) at different atmosphere conditions (The data used for fitting the linearity is in the temperature range of 300 – 500 °C).

Atmosphere	$\sigma_{600^\circ\text{C}}$ (mS cm <sup>-1</sup> )		$\sigma_{450^\circ\text{C}}$ (mS cm <sup>-1</sup> )		Ea <sub>total</sub> / eV	
	Stoichiometric	Deficient	Stoichiometric	Deficient	Stoichiometric	Deficient
Dry air	7.7	10.7	1.9	3.4	0.65	0.47
Wet air	7.6	8.7	1.8	2.6	0.69	0.51
Dry 5% H <sub>2</sub>	3.7	5.0	1.6	3.0	0.56	0.44
Wet 5% H <sub>2</sub>	5.5	7.9	2.0	3.7	0.59	0.49

Overall conductivities of  $\text{BaCe}_{0.5}\text{Zr}_{0.3}\text{Y}_{0.17}\text{Ni}_{0.02}\text{Cu}_{0.01}\text{O}_{3-\delta}$  and  $\text{Ba}_{0.975}\text{Ce}_{0.5}\text{Zr}_{0.3}\text{Y}_{0.17}\text{Ni}_{0.02}\text{Cu}_{0.01}\text{O}_{3-\delta}$  at 600 and 450 °C are listed in Table 5-2, where an enhancement of the total conductivity is observed in the A-site deficient sample compared with the stoichiometric one under the same temperature and atmosphere condition. In wet 5% H<sub>2</sub>, the conductivity is 5.5 mS cm<sup>-1</sup> and 7.9 mS cm<sup>-1</sup> at 600 °C and 2.0 mS cm<sup>-1</sup> and 3.7 mS cm<sup>-1</sup> at 450 °C for  $\text{BaCe}_{0.5}\text{Zr}_{0.3}\text{Y}_{0.17}\text{Ni}_{0.02}\text{Cu}_{0.01}\text{O}_{3-\delta}$  and  $\text{Ba}_{0.975}\text{Ce}_{0.5}\text{Zr}_{0.3}\text{Y}_{0.17}\text{Ni}_{0.02}\text{Cu}_{0.01}\text{O}_{3-\delta}$ , respectively. In addition, the activation energy,

0.59 eV and 0.49 eV for the stoichiometric and deficient samples, respectively, are also consistent with values reported for analogous proton conducting perovskite ceramic.<sup>33</sup> Thus, A-site deficiency effectively decreases the activation energy of the material.

In order to specify the reason for the improved conductivity in Ba-deficient oxide, bulk conductivity and total (effective) grain boundary conductivity are compared between the two samples individually, presented in Figure 5-18. The contribution from the bulk conductivity is not so significantly different with regards to the stoichiometry of the perovskite oxide as demonstrated in Figure 5-18 (a) although bulk conductivity in A-site deficient sample is slightly higher in every testing atmosphere. In contrast, grain boundary conductivities in the Ba-deficient sample are much higher than those in the stoichiometric oxide under each gas condition, indicating that the A-site deficiency dramatically changes the grain boundary property by influencing the microstructure of the sample (sintering behavior).

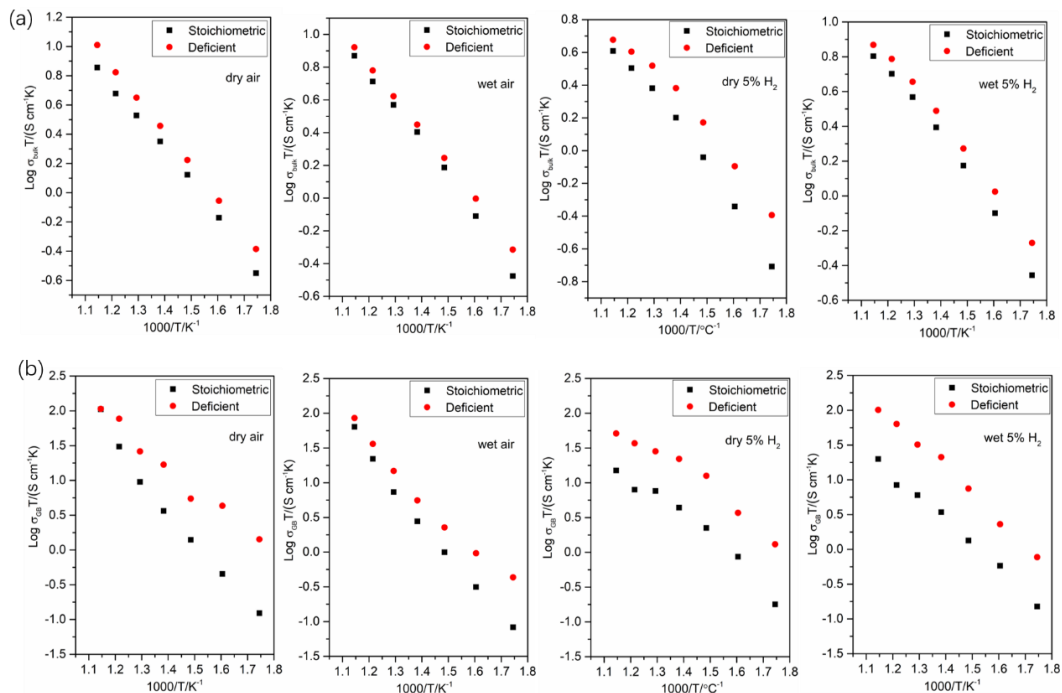


Figure 5-18. Comparison of the bulk conductivity (a) and effective grain boundary conductivity (b) plotted in Arrhenius form between  $\text{BaCe}_{0.5}\text{Zr}_{0.3}\text{Y}_{0.17}\text{Ni}_{0.02}\text{Cu}_{0.01}\text{O}_{3-\delta}$  (stoichiometric) and  $\text{Ba}_{0.975}\text{Ce}_{0.5}\text{Zr}_{0.3}\text{Y}_{0.17}\text{Ni}_{0.02}\text{Cu}_{0.01}\text{O}_{3-\delta}$  (deficient) in different atmosphere.



The activation energy and pre-exponential term for the stoichiometric and deficient samples with respect to their bulk and grain boundary regions under different atmospheres are listed in Table 5-3. It clearly shows that generally the activation energy of the grain boundary is much higher than that in the bulk, in agreement with the observation by Stevenson<sup>34</sup> that grain boundary conduction typically has a much greater activation enthalpy than the grain interior. Comparing the two compositions, the more distinct differences always occur on the grain boundary factors, either of the activation energy or the pre-exponential term. The pre-exponential term A is directly proportional to the concentration of the charge carriers in an ideal case.<sup>35</sup> Therefore, in dry or wet air, the decreased pre-exponential factor of the grain boundary is actually a controversial effect on the improved grain boundary conductivity in the deficient sample, and the increase of the conductivity is derived from the significant decrease in the activation energy. However, the effect of the pre-exponential term on the grain boundary conductivity is different when testing in hydrogen containing atmosphere, where the pre-exponential factor is larger in the Ba-deficient oxide, especially when measured in wet 5% H<sub>2</sub>. Additionally, the activation energy of the deficient sample is still smaller than the stoichiometric one in dry hydrogen, but it gets greater when testing in wet hydrogen. Thus, it is apparent that the pre-exponential factor contributes dramatically to the enhanced grain boundary conductivity in the hydrogen atmosphere, especially in the wet 5% H<sub>2</sub>, indicating that the A-site deficiency is more effective in improving the protonic charge carriers than the hole conduction of the grain boundary area. Noting that the bulk pre-exponential factors are still lower in the deficient sample under hydrogen condition, further implying the advanced property in promoting proton ion charge carriers along grain boundary, and this is in accordance with the previous suggestion from other researchers that grain boundary conductivity is more sensitive to the composition and microstructure than the bulk conductivity.<sup>36</sup>

Table 5-3. Activation energy and pre-exponential factor of the bulk and grain boundary in BaCe<sub>0.5</sub>Zr<sub>0.3</sub>Y<sub>0.17</sub>Ni<sub>0.02</sub>Cu<sub>0.01</sub>O<sub>3-δ</sub> (stoichiometric) and Ba<sub>0.975</sub>Ce<sub>0.5</sub>Zr<sub>0.3</sub>Y<sub>0.17</sub>Ni<sub>0.02</sub>Cu<sub>0.01</sub>O<sub>3-δ</sub> (deficient) under different atmosphere. (The data used for fitting the linearity is in the temperature range of 300 – 500 °C).

Atmosphere	E <sub>a,bulk</sub> / eV		E <sub>a,GB</sub> / eV		Log(A <sub>bulk</sub> ) / (Ω <sup>-1</sup> cm <sup>-1</sup> K)		Log(A <sub>GB</sub> ) / (Ω <sup>-1</sup> cm <sup>-1</sup> K)	
	Stoichiometric	Deficient	Stoichiometric	Deficient	Stoichiometric	Deficient	Stoichiometric	Deficient
Dry air	0.47	0.46	0.82	0.55	3.65	3.63	6.33	4.99
Wet air	0.46	0.41	0.85	0.67	3.62	3.32	6.40	5.43
Dry 5% H <sub>2</sub>	0.48	0.40	0.71	0.62	3.55	3.30	5.57	5.58
Wet 5% H <sub>2</sub>	0.45	0.40	0.70	0.74	3.53	3.33	5.41	6.42

### 5.5.3 Ionic proton transference number

The identification of proton transference number is a key parameter to predict whether the electrolyte material would work promisingly in the fuel cell performance. One of the simple and classical methods to determine the proton transference number is measuring the electromotive force (EMF) in an electrochemical concentration cell. In the preparation of the concentration cell in our work, dense disks of Ni, Cu co-doped BCZY were pasted with porous Pt electrodes on both sides, and the prepared cell was affixed to the end of an alumina tube sealed with Ceramabond™. An open circuit voltage (OCV) was generated by exposing the two electrodes to different atmospheres, one is humidified H<sub>2</sub> and the other is compressed air. The cell configuration is shown below:



The chemical reaction with this cell is simply H<sub>2</sub> and O<sub>2</sub> combining to form water according to Eq. 5-6:



The theoretical voltage, E<sub>N</sub>, is calculated according to the Nernst's equation Eq. 5-7:

$$E_N = E_0 + \frac{RT}{2F} \ln \left( \frac{P_{\text{O}_2}^{0.5} P_{\text{H}_2}}{P_{\text{H}_2\text{O}}} \right) \quad \text{Eq. 5-7}$$

where E<sub>0</sub> = ΔG<sub>0</sub> / 2F, ΔG<sub>0</sub> is the Gibbs free energy of the reaction under standard conditions (T = 273 K, P = 1 bar)<sup>37</sup>, R is the universal gas constant, T is the temperature, F is Faraday's constant, p<sub>H<sub>2</sub></sub>, p<sub>O<sub>2</sub></sub>, p<sub>H<sub>2</sub>O</sub> are the partial pressure of hydrogen, oxygen

and water, respectively. The proton ion transference number is calculated from the ratio of the measured EMF to the theoretical value under the same temperature,  $t_{ion} = E_{meas}/E_N$ .

The results of the EMF measurement and the calculated proton transference number of the Ni, Cu co-doped BCZY are summarized in Table 5-4. The data reveals that the measured EMF for all the compositions is close to the theoretical value below 550 °C, with the proton transference number over 0.98, indicating an almost pure proton conductor at this temperature range, with negligible electron conductivity. Then, on increasing the temperature, all the samples present a decrease in the EMF value and  $t_{ion}$ , which may stem from the loss of water from the structure and the higher mobility of electron holes. However, even the smallest  $t_{ion}$  of 0.92 for  $BaCe_{0.5}Zr_{0.3}Y_{0.17}Ni_{0.02}Cu_{0.01}O_{3-\delta}$  at 700 °C is still higher than most of the reported values for the doped BCZY oxides<sup>38-40</sup>, suggesting that the ionic transport number of the Ni, Cu co-doped BCZY is large enough for the satisfactory utilization in a fuel cell. Comparing the  $t_{ion}$  between the stoichiometric and A-site deficient  $BaCe_{0.5}Zr_{0.3}Y_{0.17}Ni_{0.02}Cu_{0.01}O_{3-\delta}$ , the transference number is slightly higher in the deficient oxide, which is in accordance with the previously observed increased pre-exponential factor in the deficient oxide in wet hydrogen atmosphere.

Table 5-4. Proton transference number of Ni, Cu co-doped BCZY of different stoichiometries as a function of temperature.

T(°C)	Theoretical EMF (mV)	Measured EMF (mV)				$t_{ion}$			
		$BaCe_{0.5}Zr_{0.3}Y_{0.17}Ni_{0.02}Cu_{0.01}O_{3-\delta}$	$Ba_{0.975}Ce_{0.5}Zr_{0.3}Y_{0.17}Ni_{0.02}Cu_{0.01}O_{3-\delta}$	$BaCe_{0.5}Zr_{0.3}Y_{0.16}Ni_{0.02}Cu_{0.02}O_{3-\delta}$	$BaCe_{0.5}Zr_{0.3}Y_{0.15}Ni_{0.03}Cu_{0.02}O_{3-\delta}$	$BaCe_{0.5}Zr_{0.3}Y_{0.17}Ni_{0.02}Cu_{0.01}O_{3-\delta}$	$Ba_{0.975}Ce_{0.5}Zr_{0.3}Y_{0.17}Ni_{0.02}Cu_{0.01}O_{3-\delta}$	$BaCe_{0.5}Zr_{0.3}Y_{0.16}Ni_{0.02}Cu_{0.02}O_{3-\delta}$	$BaCe_{0.5}Zr_{0.3}Y_{0.15}Ni_{0.03}Cu_{0.02}O_{3-\delta}$
500	1152	1141	1141	1145	1129	0.99	0.99	0.99	0.98
550	1144	1121	1127	1144	1133	0.98	0.99	1	0.99
600	1136	1082	1108	1105	1098	0.95	0.98	0.97	0.97
650	1128	1054	1077	1069	1060	0.93	0.95	0.95	0.94
700	1120	1025	1056	1044	1041	0.92	0.94	0.93	0.93

## 5.6 Conclusions

1. Single phase was obtained in the Ni, Cu co-doped BCZY sintered at 1350 °C, and the bimetallic co-doping approach enhanced the transition metal solubility in the perovskite structure with Ni and Cu total concentration reaching at least 5 mol%.

2. The observed rough surface of the pellets possesses a barium deficient composition in the as-prepared Ni, Cu-BCZY perovskite oxide and the smooth surface exhibited barium enrichment.

3. Numerous Ni-Cu alloy nanoparticles were exsolved from perovskite lattice after reduction at elevated temperature. They have a smaller particle size and higher population than the single nickel or copper particles, suggesting the effective approach in modifying exsolutions by introducing a second transition metal.

4. Exsolving from the intermediate phase of Ba-Ni-Cu-O is an observed alternative route for the NiCu alloy exsolution, probably because it was a more energetically saving process.

5. Nickel significantly prohibited the exsolution of copper and was more easily exsolved than copper as seen from the higher nickel concentration in the alloy nanoparticles when they had the same concentration as in the as-prepared perovskite oxide.

6. Unlike the metal property of Cu doped BCZY in reducing atmosphere, the co-doping of Ni and Cu led to p-type hole conduction.

7. 2.5% A-site deficiency increased the conductivity of  $\text{BaCe}_{0.5}\text{Zr}_{0.3}\text{Y}_{0.17}\text{Ni}_{0.02}\text{Cu}_{0.01}\text{O}_{3-\delta}$  as observed by the AC impedance measurements in dry/wet air and dry/wet 5%  $\text{H}_2/\text{N}_2$ . The improvement was mainly due to the modified property on the grain boundary area. Specifically, the enhancement in air atmosphere was attributed to the lower activation energy of the grain boundary in the deficient sample, while in hydrogen atmosphere, especially wet hydrogen, the higher conductivity in the deficient oxide was owing to its larger pre-exponential factor, which suggested more charge carriers and the charge carrier in wet hydrogen was mainly proton carrier. It is therefore indicated that the A-site deficiency enhanced the proton conductivity by increasing the pre-exponential factor of the grain boundary.

8. EMF measurements revealed high proton transference number ( $\geq 0.92$  at  $700\text{ }^\circ\text{C}$ ) in the Ni, Cu co-doped BCZY perovskite with varied stoichiometry, and A-site deficiency increased the transference number of  $\text{BaCe}_{0.5}\text{Zr}_{0.3}\text{Y}_{0.17}\text{Ni}_{0.02}\text{Cu}_{0.01}\text{O}_{3-\delta}$  at a temperature higher than  $550\text{ }^\circ\text{C}$ .

## References

1. Tao, F. F., Synthesis, catalysis, surface chemistry and structure of bimetallic nanocatalysts. *Chemical Society Reviews* **2012**, *41* (24), 7977-7979.
2. Kitla, A.; Safonova, O. V.; Föttinger, K., Infrared studies on bimetallic copper/nickel catalysts supported on zirconia and ceria/zirconia. *Catalysis letters* **2013**, *143* (6), 517-530.
3. Smirnov, A. A.; Khromova, S. A.; Bulavchenko, O. A.; Kaichev, V. V.; Saraev, A. A.; Reshetnikov, S. I.; Bykova, M. V.; Trusov, L. I.; Yakovlev, V. A., Effect of the Ni/Cu ratio on the composition and catalytic properties of nickel-copper alloy in anisole hydrodeoxygenation. *Kinetics and Catalysis* **2014**, *55* (1), 69-78.
4. Li, P.; Liu, J.; Nag, N.; Crozier, P. A., In situ preparation of Ni–Cu/TiO<sub>2</sub> bimetallic catalysts. *Journal of Catalysis* **2009**, *262* (1), 73-82.
5. Naghash, A.; Etsell, T.; Xu, S., XRD and XPS study of Cu– Ni interactions on reduced copper–nickel–aluminum oxide solid solution catalysts. *Chemistry of Materials* **2006**, *18* (10), 2480-2488.
6. Lin, J.-H.; Biswas, P.; Gulians, V. V.; Misture, S., Hydrogen production by water–gas shift reaction over bimetallic Cu–Ni catalysts supported on La-doped mesoporous ceria. *Applied Catalysis A: General* **2010**, *387* (1-2), 87-94.
7. Reshetenko, T. V.; Avdeeva, L. B.; Ismagilov, Z. R.; Chuvilin, A. L.; Ushakov, V. A., Carbon capacious Ni-Cu-Al<sub>2</sub>O<sub>3</sub> catalysts for high-temperature methane decomposition. *Applied Catalysis A: General* **2003**, *247* (1), 51-63.
8. Liu, S.; Liu, Q.; Luo, J.-L., Highly stable and efficient catalyst with in situ exsolved Fe–Ni Alloy nanospheres socketed on an oxygen deficient perovskite for direct CO<sub>2</sub> electrolysis. *ACS Catalysis* **2016**, *6* (9), 6219-6228.
9. Du, Z.; Zhao, H.; Yi, S.; Xia, Q.; Gong, Y.; Zhang, Y.; Cheng, X.; Li, Y.; Gu, L.; Swierczek, K., High-performance anode material Sr<sub>2</sub>FeMo<sub>0.65</sub>Ni<sub>0.35</sub>O<sub>6-δ</sub> with in situ exsolved nanoparticle catalyst. *ACS Nano* **2016**, *10* (9), 8660-8669.
10. Liu, S.; Chuang, K. T.; Luo, J.-L., Double-layered perovskite anode with in situ exsolution of a Co–Fe alloy to cogenerate ethylene and electricity in a proton-

conducting ethane fuel cell. *ACS Catalysis* **2015**, *6* (2), 760-768.

11. Liu, S.; Liu, Q.; Luo, J.-L., CO<sub>2</sub>-to-CO conversion on layered perovskite with in situ exsolved Co-Fe alloy nanoparticles: an active and stable cathode for solid oxide electrolysis cells. *Journal of Materials Chemistry A* **2016**, *4* (44), 17521-17528.

12. Sun, Y. F.; Li, J. H.; Cui, L.; Hua, B.; Cui, S. H.; Li, J.; Luo, J. L., A-site-deficiency facilitated in situ growth of bimetallic Ni-Fe nano-alloys: a novel coking-tolerant fuel cell anode catalyst. *Nanoscale* **2015**, *7* (25), 11173-11181.

13. Yang, C.; Li, J.; Lin, Y.; Liu, J.; Chen, F.; Liu, M., In situ fabrication of CoFe alloy nanoparticles structured (Pr<sub>0.4</sub>Sr<sub>0.6</sub>)<sub>3</sub>(Fe<sub>0.85</sub>Nb<sub>0.15</sub>)<sub>2</sub>O<sub>7</sub> ceramic anode for direct hydrocarbon solid oxide fuel cells. *Nano Energy* **2015**, *11*, 704-710.

14. Zhang, L.; Yang, C.; Frenkel, A. I.; Wang, S.; Xiao, G.; Brinkman, K.; Chen, F., Co-generation of electricity and chemicals from propane fuel in solid oxide fuel cells with anode containing nano-bimetallic catalyst. *Journal of Power Sources* **2014**, *262*, 421-428.

15. Neagu, D.; Tsekouras, G.; Miller, D. N.; Menard, H.; Irvine, J. T., In situ growth of nanoparticles through control of non-stoichiometry. *Nature Chemistry* **2013**, *5* (11), 916-923.

16. Neagu, D.; Oh, T. S.; Miller, D. N.; Menard, H.; Bukhari, S. M.; Gamble, S. R.; Gorte, R. J.; Vohs, J. M.; Irvine, J. T., Nano-socketed nickel particles with enhanced coking resistance grown in situ by redox exsolution. *Nature Communication* **2015**, *6*, 1-8.

17. Gao, Y.; Chen, D.; Saccoccio, M.; Lu, Z.; Ciucci, F., From material design to mechanism study: Nanoscale Ni exsolution on a highly active A-site deficient anode material for solid oxide fuel cells. *Nano Energy* **2016**, *27*, 499-508.

18. Sheffer, G. R.; King, T. S., Differences in the promotional effect of the group IA elements on unsupported copper catalysts for carbon monoxide hydrogenation. *Journal of Catalysis* **1989**, *116* (2), 488-497.

19. Chen, C.-S.; Cheng, W.-H.; Lin, S.-S., Study of reverse water gas shift reaction by TPD, TPR and CO<sub>2</sub> hydrogenation over potassium-promoted Cu/SiO<sub>2</sub> catalyst. *Applied Catalysis A: General* **2003**, *238* (1), 55-67.

20. Spencer, M., The role of surface oxygen on copper metal in catalysts for the synthesis of methanol. *Catalysis letters* **1999**, *60* (1-2), 45-49.
21. Saw, E. T.; Oemar, U.; Tan, X. R.; Du, Y.; Borgna, A.; Hidajat, K.; Kawi, S., Bimetallic Ni–Cu catalyst supported on CeO<sub>2</sub> for high-temperature water–gas shift reaction: methane suppression via enhanced CO adsorption. *Journal of Catalysis* **2014**, *314*, 32-46.
22. Force, C.; Belzunegui, J. P.; Sanz, J.; Martínez-Arias, A.; Soria, J., Influence of precursor salt on metal particle formation in Rh/CeO<sub>2</sub> catalysts. *Journal of Catalysis* **2001**, *197* (1), 192-199.
23. Kondarides, D. I.; Verykios, X. E., Effect of chlorine on the chemisorptive properties of Rh/CeO<sub>2</sub> catalysts studied by XPS and temperature programmed desorption techniques. *Journal of Catalysis* **1998**, *174* (1), 52-64.
24. Studt, F.; Abild-Pedersen, F.; Wu, Q.; Jensen, A. D.; Temel, B.; Grunwaldt, J.-D.; Nørskov, J. K., CO hydrogenation to methanol on Cu–Ni catalysts: theory and experiment. *Journal of Catalysis* **2012**, *293*, 51-60.
25. Schwartz, A. J.; Kumar, M.; Adams, B. L.; Field, D. P., *Electron backscatter diffraction in materials science*. Springer: 2009; Vol. 2.
26. Engler, O.; Randle, V., *Introduction to texture analysis: microtexture, microtexture, and orientation mapping*. CRC press: 2009.
27. Wright, S. I.; Nowell, M. M.; Field, D. P., A review of strain analysis using electron backscatter diffraction. *Microscopy and Microanalysis* **2011**, *17* (3), 316-329.
28. Humphreys, F. J., Characterisation of fine-scale microstructures by electron backscatter diffraction (EBSD). *Scripta Materialia* **2004**, *51* (8), 771-776.
29. Tao, S.; Irvine, J. T., Synthesis and characterization of (La<sub>0.75</sub>Sr<sub>0.25</sub>)Cr<sub>0.5</sub>Mn<sub>0.5</sub>O<sub>3-δ</sub>, a redox-stable, efficient perovskite anode for SOFCs. *Journal of the Electrochemical Society* **2004**, *151* (2), A252-A259.
30. Haile, S.; Staneff, G.; Ryu, K., Non-stoichiometry, grain boundary transport and chemical stability of proton conducting perovskites. *Journal of Materials Science* **2001**, *36* (5), 1149-1160.
31. Irvine, J. T.; Sinclair, D. C.; West, A. R., Electroceramics: characterization by

impedance spectroscopy. *Advanced materials* **1990**, 2 (3), 132-138.

32. Park, K.-Y.; Seo, Y.; Kim, K. B.; Song, S.-J.; Park, B.; Park, J.-Y., Enhanced proton conductivity of yttrium-doped barium zirconate with sinterability in protonic ceramic fuel cells. *Journal of Alloys and Compounds* **2015**, 639, 435-444.

33. Kreuer, K.-D., Proton-conducting oxides. *Annual Review of Materials Research* **2003**, 33 (1), 333-359.

34. Stevenson, D.; Jiang, N.; Buchanan, R.; Henn, F., Characterization of Gd, Yb and Nd doped barium cerates as proton conductors. *Solid State Ionics* **1993**, 62 (3-4), 279-285.

35. Shima, D.; Haile, S., The influence of cation non-stoichiometry on the properties of undoped and gadolinia-doped barium cerate. *Solid State Ionics* **1997**, 97 (1-4), 443-455.

36. Barison, S.; Battagliarin, M.; Cavallin, T.; Daolio, S.; Doubova, L.; Fabrizio, M.; Mortalò, C.; Boldrini, S.; Gerbasi, R., Barium non-stoichiometry role on the properties of  $\text{Ba}_{1+x}\text{Ce}_{0.65}\text{Zr}_{0.20}\text{Y}_{0.15}\text{O}_{3-\delta}$  proton conductors for IT-SOFCs. *Fuel cells* **2008**, 8 (5), 360-368.

37. Bard, A. J.; Faulkner, L. R., Fundamentals and applications. *Electrochemical Methods* **2001**, 2 (482), 580-632.

38. Babilo, P.; Haile, S. M., Enhanced sintering of yttrium-doped barium zirconate by addition of ZnO. *Journal of the American Ceramic Society* **2005**, 88 (9), 2362-2368.

39. Choi, S. M.; Lee, J.-H.; Ji, H. I.; Yoon, K. J.; Son, J.-W.; Kim, B.-K.; Je, H. J.; Lee, H.-W.; Lee, J.-H., Determination of proton transference number of  $\text{Ba}(\text{Zr}_{0.84}\text{Y}_{0.15}\text{Cu}_{0.01})\text{O}_{3-\delta}$  via electrochemical concentration cell test. *Journal of Solid State Electrochemistry* **2013**, 17 (11), 2833-2838.

40. Gao, D.; Guo, R., Structural and electrochemical properties of yttrium-doped barium zirconate by addition of CuO. *Journal of Alloys and Compounds* **2010**, 493 (1-2), 288-293.



## 6 Cell fabrication and optimization

### 6.1 Introduction

For an electrochemical cell, its performance is greatly influenced by many factors, such as ohmic losses, activation losses and concentration losses. Specifically, the ohmic losses are mainly related with the ionic conduction of the electrolyte and electronic conduction of electrode material. Based on literature studies, we used here a BCZYZ electrolyte and its processing optimization in terms of enhanced sinterability was further investigated. As mentioned before Zr-doping into BaCeO<sub>3</sub> materials represent a good compromise in terms of sinterability, conductivity and stability. Moreover, the use of sintering aids such as Ni<sup>2+</sup>, Cu<sup>2+</sup>, Zn<sup>2+</sup> is found to be effective in decreasing the sintering temperature and improving stability without impairing conductivity.<sup>1-5</sup> While the activation losses originate from the reaction kinetics, concentration losses are limited by the transportation of the reactants and products species. In the fabrication of a robust and performant cell, ohmic losses can be effectively weakened by decreasing the electrolyte thickness, and the less activation losses require higher electrocatalytic activity on the electrode and maximizing the length of the triple-phase boundary (TPB) where the electrochemical reactions take place. For the minimization of concentration losses, an optimization of the porous microstructure of the electrode materials is necessary. In this work, tape casting method is used for fabricating the dense electrolyte and porous electrode raw materials, and the porosity of the electrodes can be tailored by the pore former additives. When fabricating the cell, the electrode and electrolyte tape are laminated and experience a co-firing procedure, which requires a well-matched thermal expansion coefficient for the two configurations. Generally, a composite of electrolyte and electrode material is utilized to eliminate the thermal expansion mismatch. However, the co-sintering of the composite requires a similar sintering temperature of the composite materials, limiting the choice for the electrolyte and electrode materials. In addition, the high temperature sintering would also give rise the undesired reactions between the composite components. An alternative way in the

fabrication of electrode component is ion impregnation (infiltration), which is simply by introducing the solutions of metal salts precursors to a porous scaffold made from the electrolyte material. Compared with the co-sintering of the composite, this method requires a lower firing temperature to deposit the electrode material on the electrolyte framework, which effectively avoids the undesired reaction. In this work, the cell configuration is designed as BCZYZ-LSCF (cathode)/BCZYZ/Ni,Cu-BCZY (anode), where impregnation method is used for the preparation of the electrode components. In addition, in situ exsolution is also trialled to obtain nano-catalysts on the electrode material.

## 6.2 Influence of ZnO sintering aid on the sinterability of BCZY

### 6.2.1 Phase characterization of the prepared BCZY

Figure 6-1 is the X-ray diffraction pattern of the prepared BCZY sample by solid state synthesis at 1400 °C. The strong main peaks match well with the cubic crystal system of Pm3m space group. However, a weak peak can be found at the shoulder site of each of the main peak, marked with an arrow, which indicates incomplete sintering of the BCZY oxide at 1400 °C. Moreover, the sintered BCZY pellet still appears white in colour without shrinkage, and is easy to grind, suggesting a porous structure and poor sinterability.

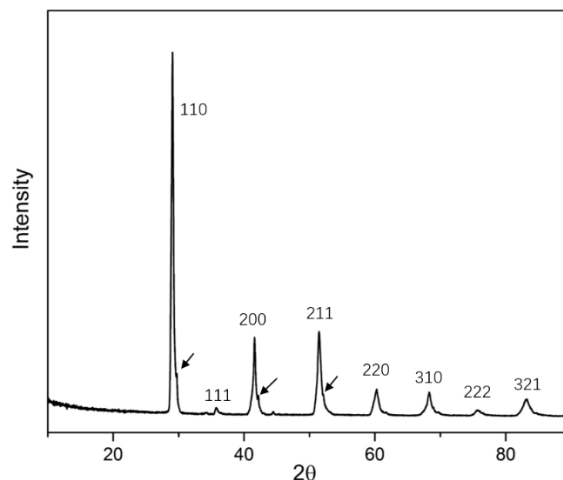


Figure 6-1 XRD pattern of BCZY oxide sintered at 1400 °C for 12h.

## 6.2.2 Preparation of BCZY with the addition of ZnO

Figure 6-2 is the BCZYZ pellet prepared with the addition of 4% ZnO after sintering at 1350 °C for 12 h. Compared to the colour of the sintered BCZY pellet, the BCZYZ pellet exhibits a uniform dark colour and is without cracks,. The pellet shrinks about 16% after firing measured from the diameter of the pellet, and relative density of 92% is achieved, indicating a much better sinterability with the ZnO sintering aid.



Figure 6-2 Typical sintered BCZYZ pellet.

The microstructure of the synthesized BCZYZ pellet was characterised by SEM. As shown in Figure 6-3, the BCZYZ pellet is quite dense with several isolated pores. Between grains there are some fracture paths which are called transgranular fractures, indicating excellent bonding between grain boundaries of well sintered ceramic which may be assisted by the presence of the liquid phase sintering. The dense BCZYZ oxide reveals that ZnO greatly improved the sinterability of the ceramic material.

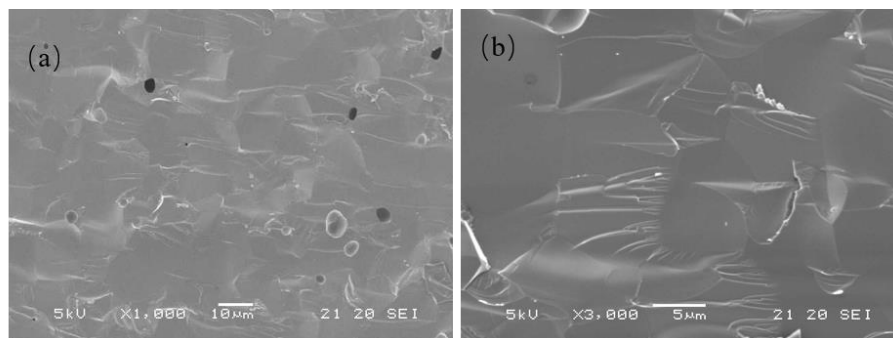


Figure 6-3 Cleaved surface of BCZYZ pellet sintered at 1350 °C for 12 h.

The phase of sintered BCZYZ pellet was identified by XRD characterization. As revealed in Figure 6-4, a single cubic perovskite phase was obtained after sintering the pellet at 1350 °C for 12 h, and no splitting peaks are observed, which further verifies the enhanced sinterability of the BCZY oxide by adding 4% ZnO additives.

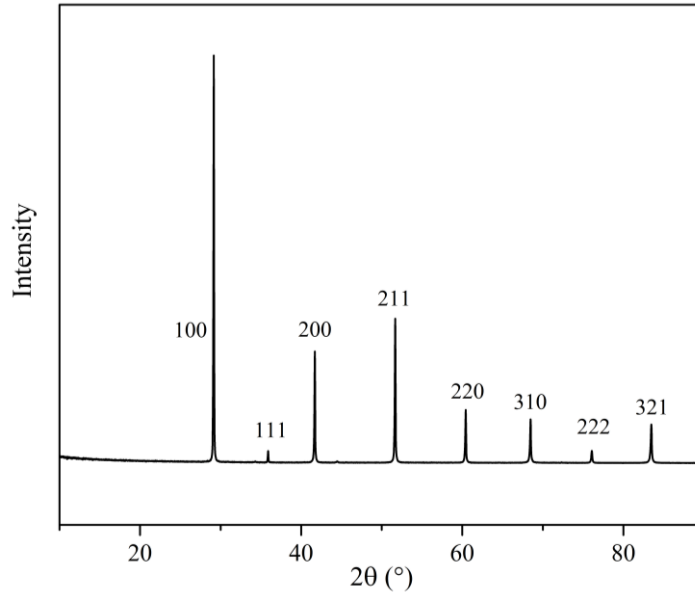


Figure 6-4 XRD pattern of BCZYZ sintered at 1350 °C for 12 h.

Shrinkage behaviour of the sample was measured by dilatometry test. As shown in Figure 6-5, the pellet made from pre-calcined BCZYZ powder begins to shrink at about 1000 °C followed by a rapid shrinkage with temperature rising to 1350 °C. As sintering is a thermally activated process, it is very sensitive to temperature due to the changing factors of diffusivity, viscosity, etc. For a given degree of sintering, the required time can be expressed as exponential functions of temperature.<sup>6</sup> The temperature sensitive property thus leads to the suddenly shrinking of pellet at over 1000 °C, and shrinkage in thickness of the analysed body of about 16% is obtained at 1350 °C. Afterwards, a slight expansion occurs by further heating to 1400 °C. When the temperature is held at 1400 °C, a small shrinkage of the pellet is recorded. The dilatometry test suggests that 1350 °C is an optimized sintering temperature for achieving sufficient densification.

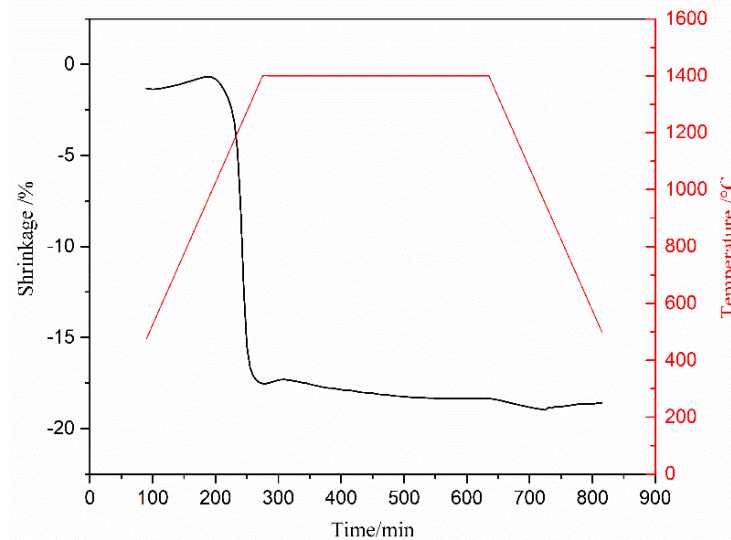


Figure 6-5 Dilatometry test of the pellet ( $\phi 13$  mm x 2 mm) made from the pre-calcined BCZYZ powder.

In order to better observe the shrinking process of the BCZY pellet with ZnO sintering aid, micrographs were taken after sintering at different temperatures for how 12h. As shown in Figure 6-6, the samples become denser with increasing sintering temperature. When sintering at a temperature higher than 1280 °C, the prepared BCZYZ evolved into an extremely dense phase. Additionally, from the native surface of the sintered pellet at 1350 °C, we see that the grain size is about 5  $\mu\text{m}$  in average with regular geometrical shape and clear grain boundary, suggesting excellent sintering at this temperature.

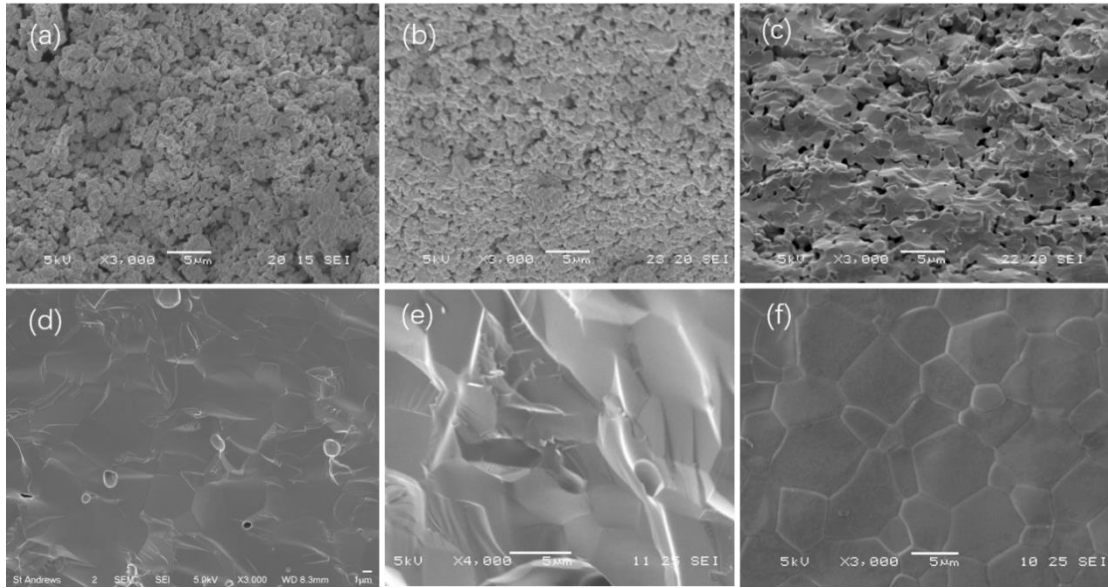


Figure 6-6 Cleaved surface of fracture surface of BCZYZ pellets sintered at different temperatures for 12 h (a) 1000 °C, (b) 1100 °C, (c) 1200 °C, (d) 1280 °C, (e) 1350 °C, and (f) native surface of the pellet obtained at 1350 °C

The phase evolution of the BCZYZ samples as a function of sintering temperature was investigated by XRD measurements. As the graphs in Figure 6-7 implies, all the samples present a cubic structure within all the main peaks. But when observing the detailed XRD peak at 29.2° in the inserted image, a weak secondary phase can be observed with peaks located at the shoulder of the main ones. Rising sintering temperature, the splitting peaks become more apparent because of grain growth and higher crystallinity of the main phase, shown as narrow and more intense peaks. The secondary phase peaks get weaker and finally disappear at 1350 °C, resulting in a single pure phase. It is possible that the secondary phase is very similar in structure to the main one, that is the main phase is in rich with cerium and the secondary phase rich in zirconium due to the higher sinterability of barium cerate than barium zirconate, which was also revealed in the split XRD peaks of BZY after sintering with a BCY shell reported by Savaniu and Irvine<sup>7</sup>. Moreover, Ce<sup>4+</sup> (0.87 Å, six coordinated) is larger than Zr<sup>4+</sup> (0.72 Å, six coordinated), making the higher concentration of cerium in the perovskite structure to exhibit a larger unit cell, shown as a shift to lower angles in the

XRD peaks. This can also be illustrated by the change of the unit cell parameter of the main phase, presented in Figure 6-8, where the unit cell parameter of the main phase gradually decreases with higher sintering temperature. This further suggests that when increasing the sintering temperature, cation diffusion is significantly facilitated and the composition in the oxides becomes gradually uniform with more  $Zr^{4+}$  diffusing from the secondary phase towards the main phase. Meanwhile, the concentration of secondary phase decreases and the highly active diffusion of cations makes the secondary phase contain higher  $Ce^{4+}$  ratio. As a result, a single phase with homogeneous composition is produced at 1350 °C. It is therefore concluded once again that the addition of ZnO effectively improved the sinterability of the BCZY perovskite oxide and single phase can be obtained by sintering the pellet at 1350 °C.

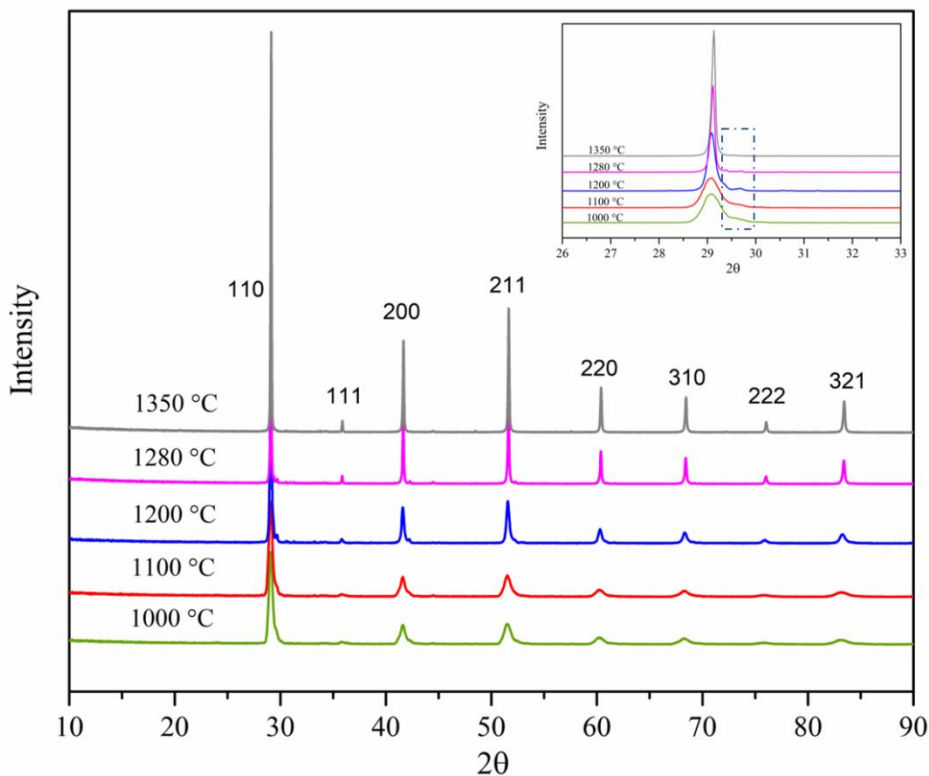


Figure 6-7. XRD patterns of the BCZYZ samples as a function of sintering temperature.

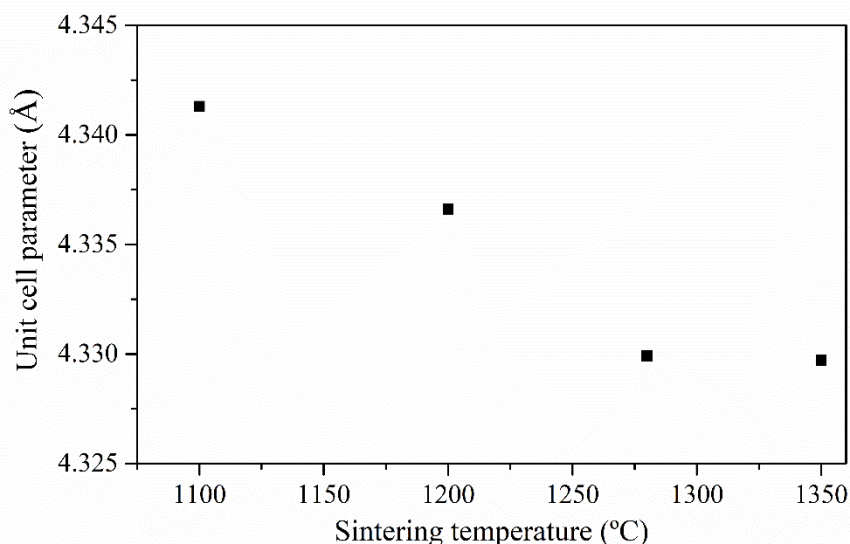


Figure 6-8 Unit cell parameter of BCZYZ main phase as a function of temperature.

## 6.3 Optimisation of tape recipe and sintering procedure

### 6.3.1 BCZYZ tape using water as a solvent

Electrochemical reactions that produce reduction and oxidation of gaseous species occur at the triple phase boundary of the electrodes, thus a good porosity of the electrodes is required. For the electrolyte material, it should be dense enough to isolate gas transfer between anode and cathode. In addition, in order to reduce the ohmic resistance, one of the approaches is to make the electrolyte thinner. Tape casting shows to be a flexible way to prepare thin electrolyte material and is suitable for large scale preparation. When the cell component is fabricated by tape casting, a general way is laminating the electrode and electrolyte tape and co-sintering the laminated cell with optimized sintering procedure.

Here, single-phase BCZYZ powder was used for the preparation of tape slurries of electrode and electrolyte. Water solvent required the use of specific binders and plasticisers in the form of polyethylene glycol and polyvinyl alcohol. In addition, a defoamer is used to prevent foam formation. In the preparation of the electrode tape, 350 nm diameter-PMMA was added in the tape slurry as pore former to prevent a dense structure of the electrode after high temperature sintering. Figure 6-9 presents the cross



section of the co-sintered cell laminated by one layer of electrolyte and two layers of electrode tapes at 1300 °C. This temperature has been chosen to preserve the required porosity in the electrode after sintering. It appears that the electrode layer is about 150  $\mu\text{m}$  thick while the electrolyte is only 15  $\mu\text{m}$  in thickness. Higher magnification of the electrode layer (Figure 6-9 c) shows that there are many small pores existed in the material, which would support the diffusion of reactive gases. However, numerous pores are also observed in the electrolyte material, and it is apparently not dense enough for the cell to work.

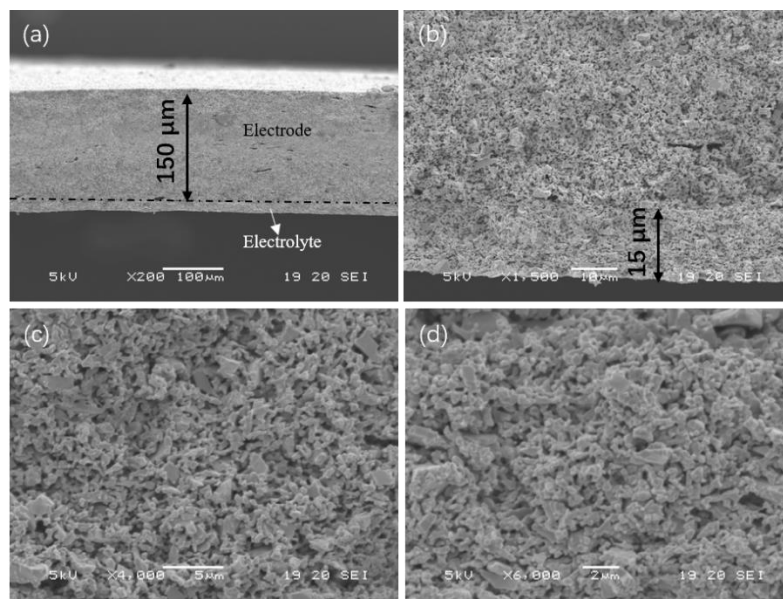


Figure 6-9 Cross section of (a, b) the laminated BCZYZ tape co-sintered at 1300 °C for 3 h, (c) the electrode layer and (d) the electrolyte layer

### 6.3.2 Optimization of the sintering procedure

Since we have established that the pure BCZYZ powders are likely not to be effective for making a dense electrolyte in combination with a porous tape, we attempted to improve the densification of the electrolyte tape by using a mixture of pre-calcined BCZY and 4 mol% ZnO for the tape slurry preparation. As shown in Figure 6-10, after co-sintering at 1300 °C for 3 h, the laminated structure is 170  $\mu\text{m}$  thick in total with the electrolyte layer of only 8  $\mu\text{m}$ . With regard to the electrolyte layer, SEM image

in Figure 6-10 d suggests the agglomeration of the grains of 1  $\mu\text{m}$  in diameter and it seems that the grain growth has not yet been completed.

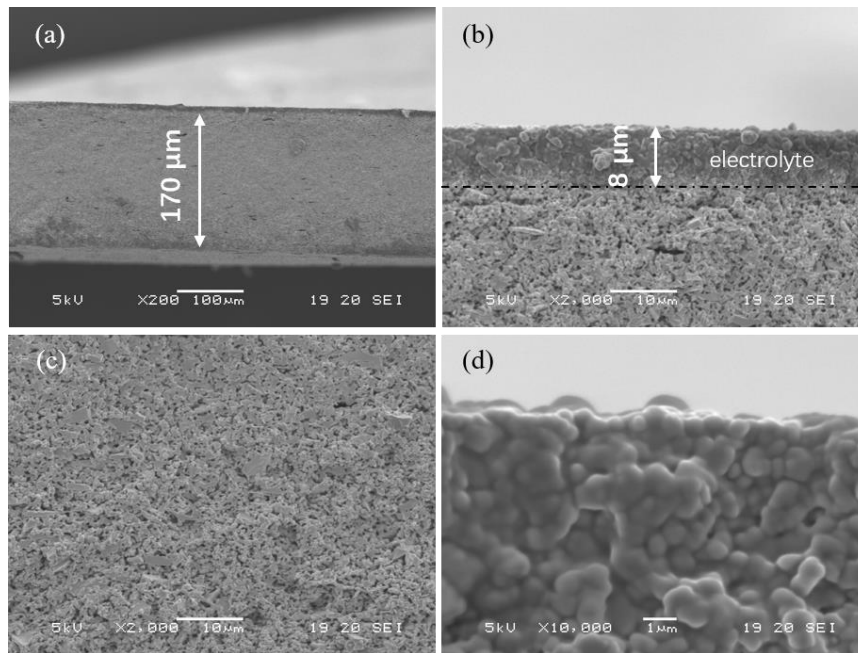


Figure 6-10 SEM images of (a, b) the laminated tape sintered at 1300  $^{\circ}\text{C}$  for 3 h, (c) the electrode layer and (d) the electrolyte layer.

It is known that sintering during solid state synthesis is usually divided into three overlapping stages: initial, intermediate and final stage.<sup>6</sup> As depicted in Figure 6-11, very limited shrinkage of about 3% occurs in the initial stage when the necks between particles are formed. Intermediate stage contributes the most densification, up to 93% of the relative density. Interconnected pores are produced at this stage. The final stage involves densification from the isolated pore state to the final densification, which is about 7%. This schematic clearly illustrated that time is a key factor in controlling the extent of sintering for the ceramics. Herein, based on the observation of the incomplete sintering, the firing time is extended to 10h in the following experiment.

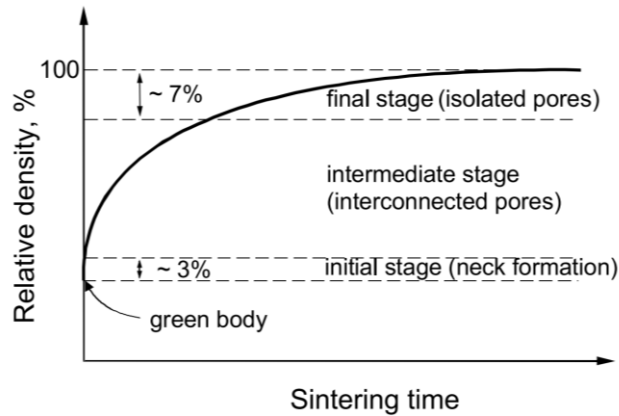


Figure 6-11. Schematic of densification curve of a compact powder through three stages over sintering time. (Figure adapted from Ref. 6)

A sandwich-structure tape (two layers of porous tape for electrodes + one layer of electrolyte + three layers of porous tape for electrodes) was laminated and co-fired at 1300 °C for 10 h. Figure 6-12 shows that the laminated layers detach from each other and a crack is observed on the surface, which is probably due to the removal of the gas between the laminated layers and differential shrinkages. Additionally, cell bending is also observed after the co-sintering.



Figure 6-12 Typical sintered laminated tape at 1300 °C for 10 h.

The microstructure of the co-sintered tape is seen in Figure 6-13. Obviously, the electrolyte layer exhibits much denser microstructure than that sintered for only 3 h but still has some isolated pores. At this time, grains grow larger to  $\sim 2 \mu\text{m}$ , showing the insufficient grain growth after sintering for 3 h. Unfortunately, the porosity of the

electrode decreases as a result of the longer sintering time.

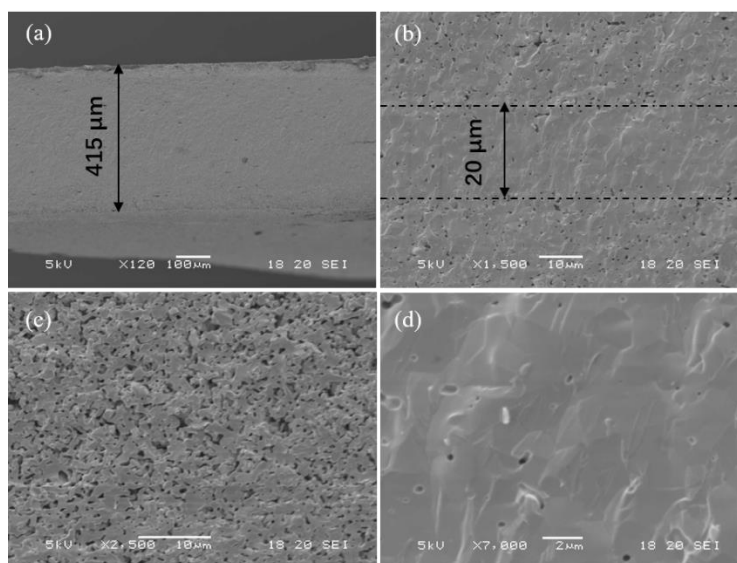


Figure 6-13. Microstructures of (a, b) the laminated tape sintered at 1300 °C for 10 h, (c) the electrode layer and (d) the electrolyte layer.

Cell flatness is one of the essential factors for its electrochemical performance for mechanical integrity and possibility of sealing prior testing, to ensure good separation between gaseous atmospheres at the electrodes. To help with the flatness of the tape during sintering, an alumina plate was placed directly on the green tape to avoid bending during sintering process. As a result, the sintered tape is much flatter than before, as shown in Figure 6-14. Meanwhile, in order to adjust the distribution of pores in the electrode, both 350 nm and 1.5 μm diameter PMMA were added as pore formers in the electrode tape. Sintering temperature was increased by 25 °C to further eliminate the pores in the electrolyte. Figure 6-15 shows that the thickness of the two electrodes is 130 and 230 μm (2 and 3 layers), respectively, and the dense electrolyte is 15 μm thick. Laminated layers are bonded tightly without detaching, exhibiting a good interface. The porosity of the electrode is enhanced and there are mixed sized of pores which are created from the different sized pore former. The mixed pores are believed to be beneficial for gas transport. However, even under the higher sintering temperature, the electrolyte seems to consist more pores than before, probably from the difficulty of

removing the organic components of the tape during sintering. It indicates that the sintering behaviour of the individual component (electrolyte or electrode) in the cell has a dramatic influence on the other component when a co-firing process is applied. Therefore, it is of great importance to find a suitable recipe of tape and sintering parameters to reach a balance between the porous electrode and dense electrolyte.

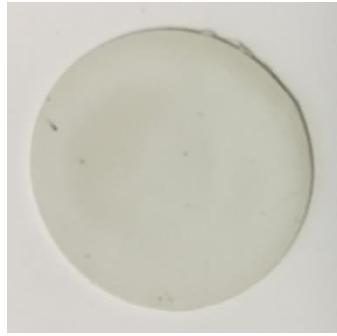


Figure 6-14 Typical sintered laminated tape at 1325 °C for 10 h with an alumina plate covering it.

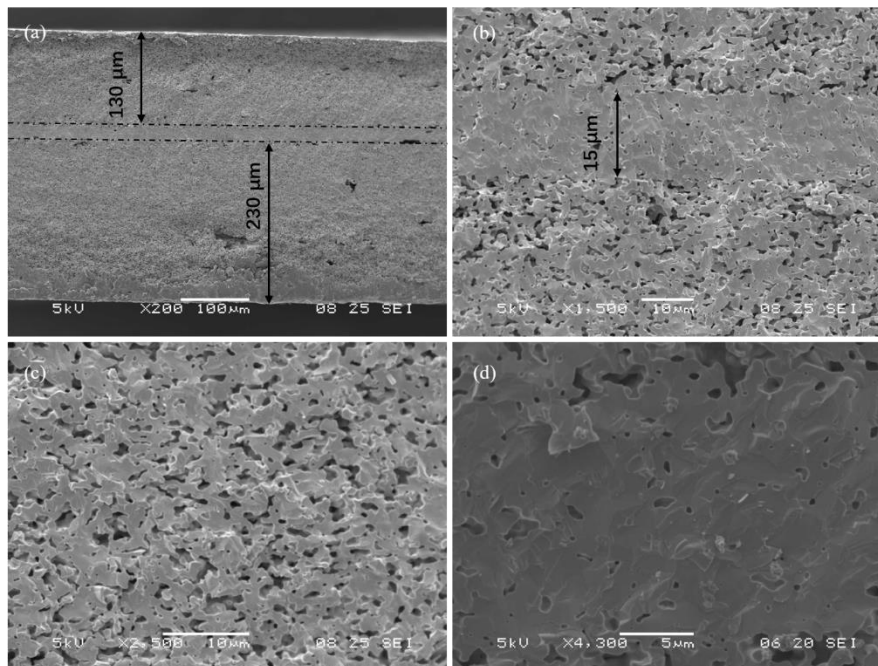


Figure 6-15. Microstructures of (a, b) the laminated tape sintered at 1325 °C for 10 h, (c) the electrode layer and (d) the electrolyte layer.

However, after many experiments of modifying the tape recipe, sintering time and

sintering temperature, we still did not obtain a cell with a good microstructure using this route. This is probably because the water system also cannot work well in the barium containing slurry as barium species can react with water in heating to form  $\text{Ba(OH)}_2$ , which is hard to eliminate and detrimental for the sintering of the ceramics. Therefore, the organic solvent system was tried in the following work.

### **6.3.3 Preparation of BCZYZ tape use an organic solvent**

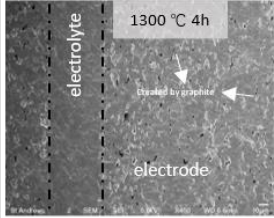
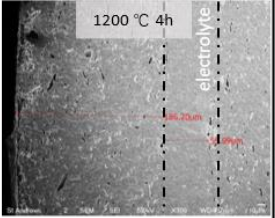
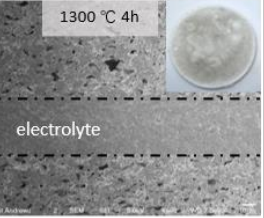
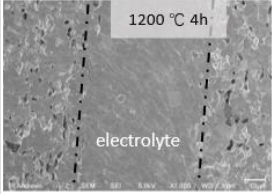
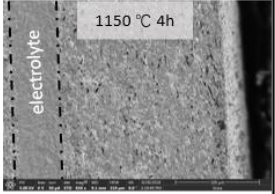
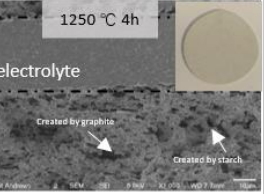
In the organic based formulations, a binary system of methyl ethyl ketone (MEK) and ethanol is used as the solvent. Typically, a binary solvent may aid the solubility of various kinds of additives in the slurry as well as modify the evaporation rate during tape drying by adjusting the physical property of the solvent.<sup>8-9</sup> For example, the low evaporation heat of MEK gives rise to rapid drying of the casted tape, which would make the green tape to be inhomogeneous. Moreover, the fast drying out produces a dried surface on the tape in a short time and thus prevents the evaporation of the solvent underneath, creating a solvent gradient. When another solvent with higher evaporation heat is added, e.g., ethanol, the drying out rate is decreased, allowing the evaporation process to be slower and producing a homogeneous green tape.

The preparation of the electrolyte tape slurry is made according to the amounts from Table 6-1 and the electrode slurry is adjusted by the amount or types of pore former (starch and graphite) and organics, as listed in Table 6-2. Meanwhile, the sintering temperature is also a controlled parameter to obtain an electrode with reasonable porosity. Electrolyte tape is laminated with symmetrical pore former-containing tapes for electrode, followed by co-sintering at high temperature with a very low heating rate to slowly burn out the organics. After sintered, the microstructure and thickness of the electrode and electrolyte are estimated by SEM, shown in Table 6-2.

Table 6-1. The formulation of the BCZYZ electrolyte slurry.

Component		Formulations (g)
Powder	BCZY+ZnO	30.6
Solvent	MEK/ethanol	14.5
Dispersant	Triton	0.195
Plasticizer	PEG	2.43
	DBP	2.19
Binder	BUTVAR	3.37

Table 6-2. Tape formulation for BCZYZ electrode slurries and the micrographs after co-sintering with electrolyte.

Component		Formulations (g)		
		Electrode 1	Electrode 2	Electrode 3
Powder	BCZY+ZnO	8.5	8.5	8.5
Pore former	Graphite	5.355 (67.3%)	6.9615 (72.8%)	3.477
	starch	-	-	2.745
Solvent	MEK/ethanol	10.15	15.225	15.225
Plasticizer	PEG	1.701	2.552	2.552
	DBP	1.531	2.296	2.296
Binder	BUTVAR	2.355	3.533	3.533
Microstructure of the cross section				
				

In the case of using the electrode 1 with a formulation 67.3 vol% graphite pore former, after co-sintering with electrolyte at 1300 °C for 4 h, the electrolyte exhibits a very dense fracture without pores. Nonetheless, only limited number of pores are found in the electrode side, and the larger pores of about 10 μm are created from the burnout of the graphite and the small ones produced from the loss of organics. The porosity in

the electrode is not supposed to be enough to provide interconnected and open diffusion path for the gas migration to the TPB sites. Therefore, the sintering temperature is further lowered to 1200 °C to decrease the shrinkage of the cell. However, the resulted electrode did not show much difference in microstructure from the one sintered at 1300 °C and the electrolyte is still dense. After that, in the formulation the volume percentage of the pore former is increased to 72.8 vol% and the amount of organic additives are increased correspondingly (Electrode 2). Unfortunately, after co-sintering at 1200 °C for 4h, similar electrolyte and electrode microstructure are present as in the previous sample, with thickness of the electrolyte approximately 56 μm and electrode 186 μm. Further decreasing the sintering temperature to 1150 °C, the porosity of the electrode seems to be increased but is still not high enough. For the electrolyte, even if the sintering temperature is very low, it still surprisingly shows a high density. Additionally, it is also noticed that the graphite created elongated, horizontal pores in the electrode, due to its original flake particle shape. This type of arrangement of pores is not effective for structure's mechanical stability and gas diffusion capability. Therefore, a mixture of flaky graphite and spherical starch was used as pore former in the following refinement of the recipe (Electrode 3) to reach an optimum distribution of porosity. After co-sintering at 1300 °C, the electrolyte demonstrates a dense microstructure, and the electrode seems to possess an improved porosity and diversity of pores but there is still room for improvement. The inserted image is the surface of the electrode after co-sintering, which seems to be inhomogeneous and the dark colour is believed to be the densified area. In order to achieve higher porosity, the sintering temperature was lowered by 50 °C. The resulted tape presents a dense electrolyte and greatly enhanced porosity of the electrode layer. Good adhesion at the interface between the dense and porous layer is also indicated from the micrograph, which is important for transporting proton ions from the electrolyte to the TPB sites in the electrode matrix. Following this optimization, it is obvious the last recipe and sintering parameters are suitable for preparing the laminated tape. However, here another severe problem appears, that is, the strength of the electrode compartment cannot be compromised with tailoring its porosity. When the electrode component is well sintered with reasonable mechanical



strength, its porosity is very low, while when the porosity is suitable, the sintered electrode tapes result in being fragile, sometimes with a powder-like layer (seen from the white sintered tape in Electrode 3) that can even be scratched off. After considerable evaluation and several adjustments, it is found that the mechanical strength of the cell and the flatness mainly comes from the dense electrolyte. Consequently, the thickness of the electrolyte has to be increased.

#### **6.3.4 Preparation of Ni, Cu-doped BCZY electrode tape**

In a solid-state proton conducting electrolysis cell, oxidation reaction occurs at the anode side and reduction processes take place at the cathode. The different reactions determine the different active catalysts on each side. For example, in the co-electrolysis of CO<sub>2</sub> and steam on a proton conducting system, steam is electrochemically split into proton and oxygen at the anode, then the resulted protons diffuse across the proton conducting electrolyte to the cathode to react with CO<sub>2</sub>. The reduction products at the cathode highly depend on the selectivity of the supported catalysts. Therefore, the anode and cathode should exhibit different catalytic activity towards their corresponding reactions. In our work, the cathode is designed to catalyse the CO<sub>2</sub> reduction process and Ni or Ni-Cu alloy nanocatalysts will be very suitable for this if produced on the porous electrode scaffold. In the previous investigation of nanoparticle exsolution, we have observed a large number of nanoparticles distributing homogeneously on the parent substrate by in-situ exsolution. Here, BaCe<sub>0.5</sub>Zr<sub>0.3</sub>Y<sub>0.16</sub>Ni<sub>0.02</sub>Cu<sub>0.02</sub>O<sub>3-δ</sub> porous electrode component is prepared by tape casting method as cathode material and the fabrication of the Ni, Cu-BCZY tape follows the same procedure as with the BCZY electrode. Note that the powder for the slurry is also the mixture of pre-calcined BCZY together with NiO and CuO. Afterwards, the green cathode tape is laminated with BCZY electrolyte tape. A porous BCZY scaffold is used as SOEC anode which will be impregnated with LSCF in the late experiment.

A different sintering behaviour from the previous materials is observed from the introducing of Ni, Cu-BCZY electrode one. Unlike the presence of white colour after

sintering, now the sintered tape exhibits a dark grey colour on both sides of the electrode structure, indicating that there may be nickel or copper migration at the cathode, diffusing throughout the electrolyte and the anode. In addition, the porosity of both electrodes is also decreased (Figure 6-16 a) in comparison with the last recipe in Table 6-2 probably due to sintering activity of the dopant metals. In order to find out whether Ni-Cu alloy nanoparticles can be exsolved from the perovskite fabricated from tape, the co-sintered tape was reduced at 700 °C for 12 h in 5% H<sub>2</sub>/Ar. However, a very limited number of nanoparticles are observed on the cathode surface (Figure 6-16 d). Moreover, some particles are also found on the electrolyte surface (Figure 6-16 b) and the BCZYZ anode side (Figure 6-16 c), confirming that during the co-sintering of the laminated tapes, there is significant migration of nickel and copper ions through the electrolyte and anode. Thus, less nickel and copper are left in the cathode to exsolve on the surface. The lower porosity of the BCZYZ electrode is also believed to result from the ion diffusion.

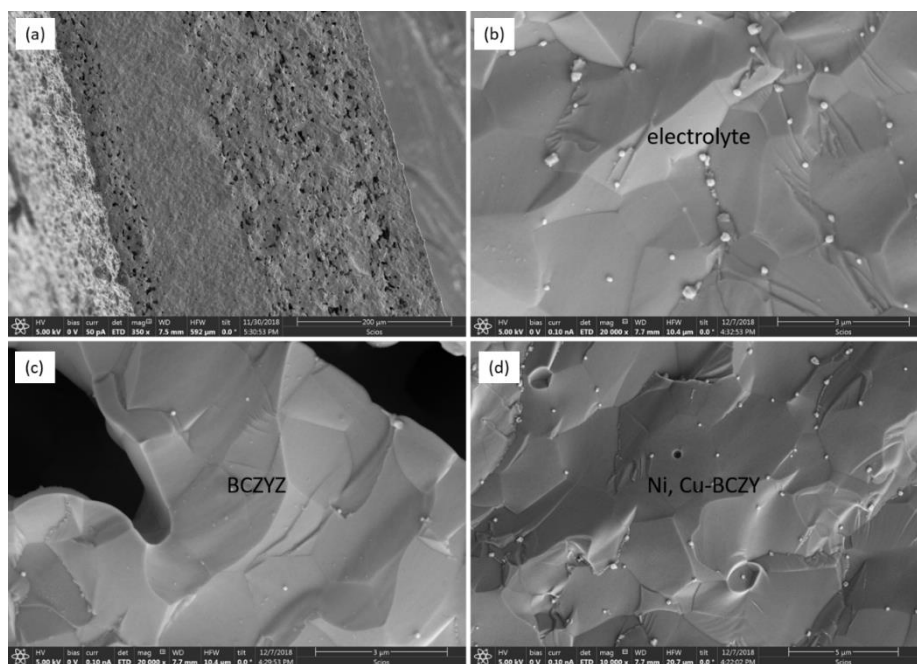


Figure 6-16. (a) SEM micrographs of the co-sintered Ni, Cu-BCZY/BCZYZ/BCZYZ tape, (b) the microstructure of BCZYZ electrolyte after reduction at 700 °C for 12 h, (c) microstructure of BCZYZ electrode and (d) Ni,Cu-BCZY electrode after reduction.

Apart from the less doping level in the Ni, Cu-BCZY oxide after co-firing, another possible factor that influences the particle exsolution is the synthesis method of the perovskite oxide. For example, even if the Cu-BCZY tape is sintered without lamination with BCZY electrolyte, a significantly decreased number of particles are observed on the surface of tape after reduction at 800 °C for 12 h (Figure 6-17) compared with the copper exsolves on the pellet prepared from solid state synthesis in Chapter 3. In addition, the particles on the sintered tape are much smaller than those obtained on the pellet. Considering the surface morphology of the sintered tape, grains are very densely packed with the grain size in the range of 0.5 - 2.5  $\mu\text{m}$ , smaller than the grains of the pellet, due to milling process involved in slurry preparation for tape casting. It is known that the sinterability and microstructure of the ceramics can be affected by several factors, including the variables related to raw materials (material variables) and sintering conditions (process variables). For the material variables, it includes powder property (shape, size, size distribution, agglomeration, mixedness, etc) and chemistry parameter (composition, impurity, non-stoichiometry); for the process variables, it consists of temperature, time, pressure, atmosphere, heating and cooling rate, etc.<sup>6</sup> Any change of these factors may give rise to a different microstructure of the final product by influencing the sintering kinetics or thermodynamics. Thus, the better packed grains of the perovskite prepared as a tape is also attributed to the highly mixedness of the reactant oxides under the existence of organics in the slurry. On the other hand, the very low heating rate in the sintering procedure also allows the homogeneous diffusion of the oxide species, consequently producing a stable structure. Exsolution is supposed to become difficult from a stable structure. Furthermore, the low heating rate would also result in smaller grain size in the sintered tape, which possesses higher surface energy than the larger one in the pellet, and this is assumed to be another reason for the smaller and fewer exsolved particles on the sintered tape.

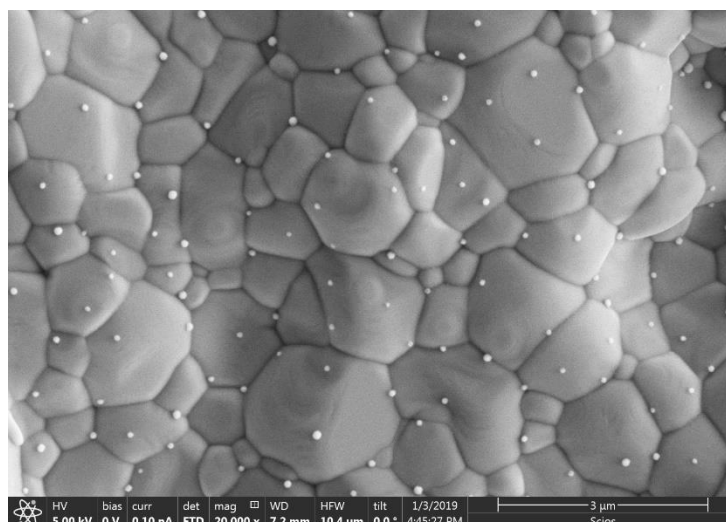


Figure 6-17. Microstructure of sintered  $\text{Ba}_{0.95}\text{Ce}_{0.5}\text{Zr}_{0.3}\text{Y}_{0.14}\text{Cu}_{0.06}\text{O}_{3-\delta}$  tape after reduction at 800 °C for 12 h in 5%  $\text{H}_2/\text{Ar}$ .

## 6.4 Slurry coating of the electrodes

### 6.4.1 Sintered powder for coating slurry preparation

As it can be seen when using the tape casting method, the co-sintering of the tapes caused problems that are difficult to control, such as the reduced porosity and ion diffusion of the electrodes, along with the difficult exsolution at the cathode. Thus, a coating method was used now for the fabrication of the two electrodes while the electrolyte was still prepared from the tape.

Screen printing is simple and cost-effective technique for the preparation of thin films and it has been extensively used for the fabrication of electrolytes or electrodes with thickness varying from a few tens of micrometres to about 200  $\mu\text{m}$ .<sup>10-14</sup> A similar technique has been used here taking into consideration the fragility of the electrolyte. In order to prevent the nickel and copper ion from diffusing into the electrolyte, the ink for screen printing was made with the ball milled powders of the single phase  $\text{BaCe}_{0.5}\text{Zr}_{0.3}\text{Y}_{0.16}\text{Ni}_{0.02}\text{Cu}_{0.02}\text{O}_{3-\delta}$  (cathode) and BCZYZ perovskite phase (anode backbone). After both electrodes were printed on the sides of the sintered electrolyte tape, the cell was calcined at 1200 °C for 2 h to remove the organics in the ink and make the electrode to bond tightly on the electrolyte. It is found that a thin electrolyte after

sintering has a strong curling edge and is lack of mechanical strength. A thicker electrolyte was prepared by laminating two layers of tape. In addition, in order to prevent the reaction with the supported alumina plate at high temperature, which is also detrimental to the flatness of the tape, a thick bed of sacrificial powders is placed underneath the tape. After sintering, the electrolyte tape presents good flatness and reasonable mechanical strength, as shown in Figure 6-18.



Figure 6-18. Sintered thick BCZY electrolyte tape.

SEM micrographs in Figure 6-19 show that the sintered electrolyte is 160  $\mu\text{m}$  thick and the BCZY and Ni,Cu-BCZY electrodes have a thickness of 15 and 35  $\mu\text{m}$ , respectively. The electrolyte is very dense with several isolated pores in it (Figure 6-19 b). Both electrodes in Figure 6-19 (c, d) reveal a porous structure which is suitable for the gas diffusion in the electrochemical test. However, the packing of grains in Ni, Cu-BCZY electrode looks inhomogeneous, as a mixture of some large particles of 2  $\mu\text{m}$  and many smaller particles, which indicates poor sintering of the electrode material. Moreover, nanoparticles are not observed on the Ni, Cu-BCZY electrode side after reduction at 700  $^{\circ}\text{C}$ , further indicating that the electrode prepared by coating with ink made from the single perovskite phase is not effective for the utilization of cell.

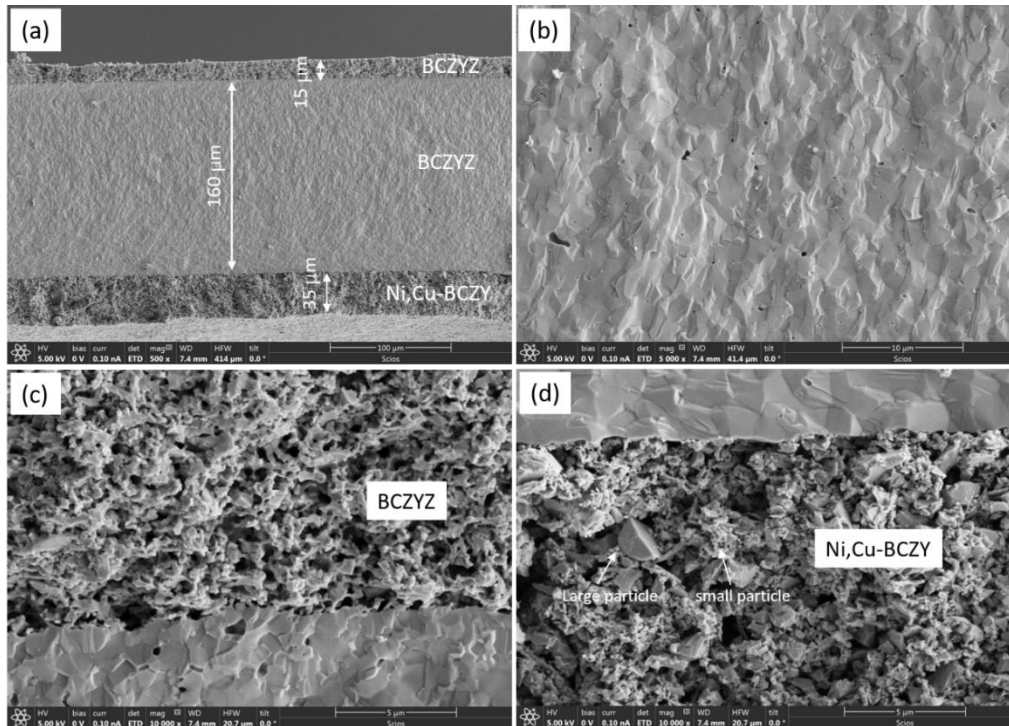


Figure 6-19. Microstructures of the cross section of the cell calcined at 1200 °C for 2 h (a), BCZYZ electrolyte (b), BCZYZ porous electrode (c), and Ni, Cu-BCZY electrode (d).

#### 6.4.2 Pre-calcined powder for coating slurry preparation

The nonuniform distribution of particles in the calcined electrode is probably due to the low calcination temperature on one hand, and on the other hand may be attributed to the presence of large particle that are difficult to sinter. This could come from unsatisfactory milling and suspension of particles during initial ink preparation. The inability to exsolve nanoparticles is supposed to result from the change of surface energy. To solve this, a mixture of pre-calcined BCZY powder with nickel and copper oxides was used to making the ink for printing. After printing the electrode material to the dense electrolyte tape, the cell was fired at 1350 °C for 8 h. The microstructure of the sintered Ni, Cu-BCZY electrode is evaluated in Figure 6-20. Obviously, the electrode still remains a porous structure and the grains are quite uniform than before without distinct large particles. This would be a much more suitable structure for testing. The grain size is in the range of 0.2 - 0.8 μm, which is much smaller than the grains

present in the solid-state synthesized pellet.

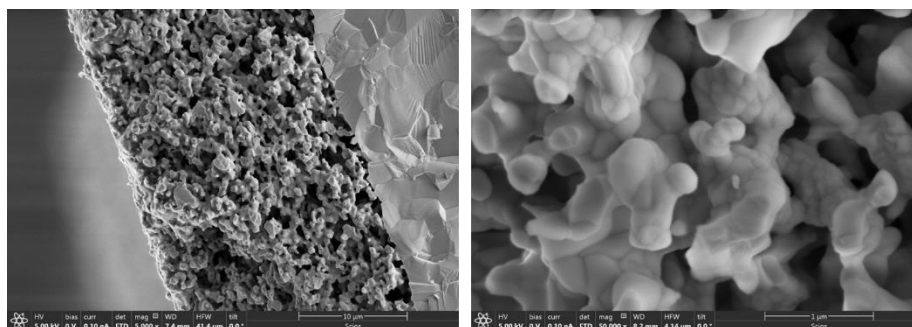


Figure 6-20. Microstructures of Ni, Cu-BCZY prepared from coating, calcined at 1350 °C for 8 h. The ink was made from the mixture powder of pre-calcined BCZY and nickel and copper oxide.

In order to obtain the electrode scaffold supported nanoparticles, the above calcined Ni, Cu-BCZY electrode was firstly reduced at 700 °C for 12 h in 5% H<sub>2</sub>/Ar in a tube furnace to check its exsolution performance before applying it in the fuel cell test. Unfortunately, as shown in Figure 6-21, a very clean surface was observed, without evident exsolved nanoparticles even comparing with the Ni, Cu-BCZY perovskite prepared in a single sintering procedure. This is consistent with the observation for the previously reduced Cu-BCZY fabricated from the tape, where only several small particles are distributed on the surface, which further suggests the significant influence of perovskite synthesis method on its property.

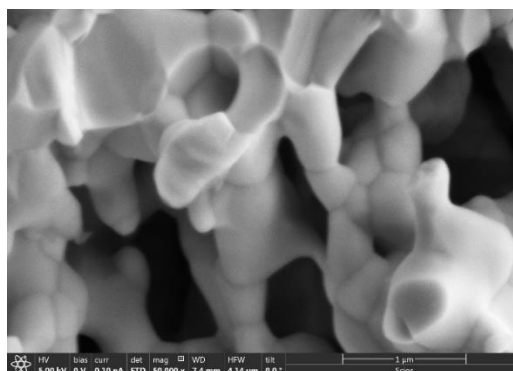


Figure 6-21. Microstructure of Ni, Cu-BCZY electrode prepared by coating after being reduced at 700 °C for 12 in 5% H<sub>2</sub>/Ar.

## 6.5 Electrochemical switching to drive exsolution

Although exsolved particles has been used to improve electrode performance, they were only achieved by the chemical reduction prior to the electrochemical test.<sup>15-18</sup> Myung et al<sup>19</sup> found that exsolution could occur electrochemically by applying voltage. Compared with several hours in the conventional chemical reduction by hydrogen, the electrochemical switching only requires hundreds of seconds to get a high extent of exsolutions. Electrochemical switching has the same driving force for exsolution with chemical reduction, that is, the  $pO_2$  gradient between the oxide lattice and external environment that gives rises to lattice reduction and subsequent exsolution. Kinetically, the much higher differential  $pO_2$  produced by voltage application (estimated  $10^{-35}$  atm) in comparison with the typical  $10^{-19}$  atm in reducing atmosphere is supposed to be the reasons for this rapid exsolution. Moreover, when the voltage is applied, the sudden flooding of the perovskite lattice with electrons significantly facilitates particle nucleation, producing small yet numerous nanoparticles. Based on the feasibility of exsolution on switching, we carried out tests of electrochemical switching on the Ni, Cu-BCZY electrode fabricated by printing, using the Ag/BCZY/Ni,Cu-BCZY configuration. The electrochemical reduction was performed by applying a voltage of 2 V under humidified hydrogen atmosphere for 2 min. The resulted microstructure of the cell and Ni, Cu-BCZY electrode are presented in Figure 6-22. Unfortunately, the cells seem to be seriously damaged by the applying of voltage and no exsolution is observed on the substrate perovskite following this first attempt. Delamination of the components could also be observed. Parameters like electrochemical reduction atmosphere, gas humidity, voltage, switching time, etc, can affect the performance of the electrochemical switching. Therefore, in the future work, these factors need to be adjusted to investigate the exsolution ability from BCZY based perovskite by electrochemical switching method. AC impedance spectra under open circuit voltage (OCV) was collected before and after the switching, plotted in Figure 6-22 (c). The ohmic resistance ( $R_s$ ) can be estimated from the high frequency intercept with the abscissa, which includes the resistances from electrolyte and electrode materials and



the contact resistance between the two components. Among these factors, electrolyte is the main contributor to the  $R_s$  value. The polarisation resistance ( $R_p$ ) of the electrode takes place at the lower frequencies and can be estimated from the intercepts between high and low frequency contributions at the real axis. Figure 6-22 (c) reveals that ohmic resistance and polarisation resistance are greatly increased after switching. The enlarged  $R_s$  and  $R_p$  value is associated with the seriously damaged microstructure of the cell.

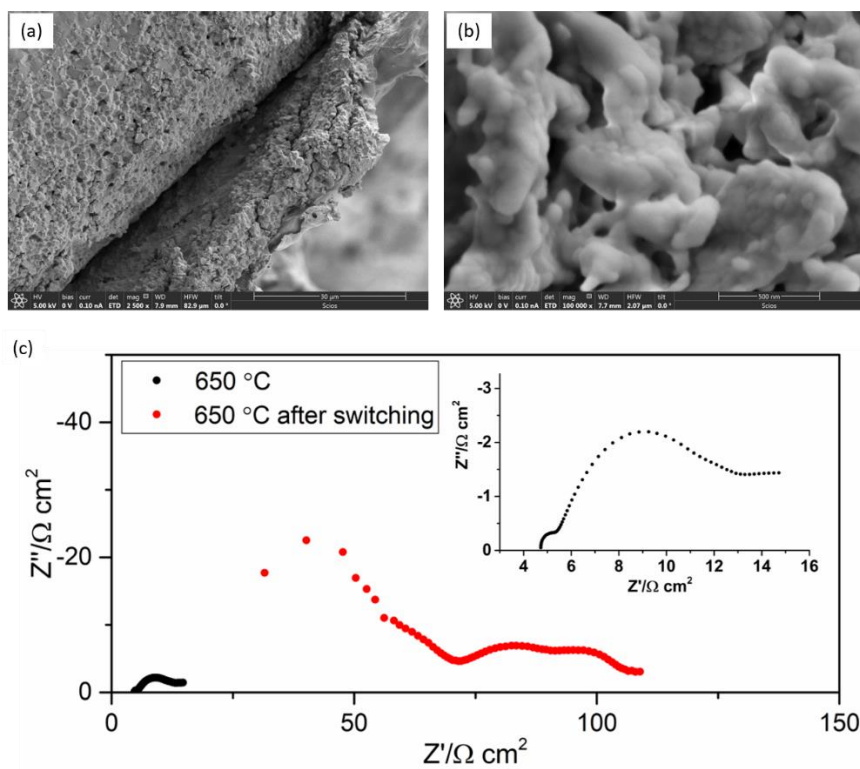


Figure 6-22. (a) Cross section of the cell after electrochemical switching, (b) microstructure of the Ni, Cu-BCZY electrode after switching, (c) AC impedance spectra of Ag/BCZYZ/Ni,Cu-BCZY in humidified  $H_2$  at 650 °C before or after switching.

## 6.6 Electrode impregnation and impedance testing

### 6.6.1 Impregnation of LSCF and Ni electrode

Impregnation, or infiltration, is a widely applied technique in the field of

heterogeneous catalysis.<sup>20-21</sup> Catalytically active particles can be introduced into the ceramic support materials by impregnation. For the loading of the particles, precursor solutions of the catalytically active materials are used to wet the surface of the porous support backbone, which is often the same composition as the electrolyte component for high compatibility, but can be an electronic or mixed conducting ceramic too. The final expected material is obtained by drying and decomposing the precursor, and sometimes a reduction process is required to achieve a metal phase. Generally, the decomposing temperature is not very high, thus the interaction between the infiltrated material and the host can be negligible. Impregnation provides a convenient way to adjust the functionalities of the electrodes, such as ionic conductivity, electronic conductivity and electrocatalytic property.

Since exsolutions did not occur as expected on the electrode fabricated by tape casting and printing, additional nickel nano-catalyst is now introduced by impregnation method into the Ni, Cu-BCZY scaffold from  $\text{Ni}(\text{NO}_3)_2 \cdot 6\text{H}_2\text{O}$  precursor. For the other electrode structure, a solution containing a  $\text{La}_{0.6}\text{Sr}_{0.4}\text{Co}_{0.2}\text{Fe}_{0.8}\text{O}_3$  (LSCF) precursor mixture ( $\text{La}(\text{NO}_3)_3 \cdot 6\text{H}_2\text{O}$ ,  $\text{Sr}(\text{NO}_3)_2$ ,  $\text{Co}(\text{NO}_3)_2 \cdot 6\text{H}_2\text{O}$  and  $\text{Fe}(\text{NO}_3)_3 \cdot 9\text{H}_2\text{O}$ ) was infiltrated into the BCZY backbone to obtain the LSCF perovskite phase which has been widely accepted as the cathode material for low temperatures SOFCs due to its high electronic and ionic conductivities. According to literature<sup>22-23</sup>,  $\text{Ni}(\text{NO}_3)_2 \cdot 6\text{H}_2\text{O}$  begins to decompose at 300 °C. However, it was reported by Klinsrisuk<sup>24</sup> that even calcinating the impregnated structure at 350 °C with a dwell time of 30 min, serious disintegration and delamination of the BCZY scaffold occurs. Moreover, an intergranular fracture which usually happens in weak grain boundaries was observed not only on the impregnated porous scaffold but extending to tens of micrometres-electrolyte area. This was assumed to be resulted from the still favourable reaction between the BCZY oxide and water that produced from crystallisation of hydrated nickel nitrate at 350 °C.<sup>25</sup> Therefore, in order to remove the water completely, Klinsrisuk<sup>24</sup> increased the firing temperature to 650 °C and no sign of degradation was found after the repeated impregnation, successfully avoiding the undesired reaction between BCZY and water. For the LSCF, the phase formation temperature is reported

to be 800 °C for 1h.<sup>26-28</sup> The morphologies of the impregnated species after decomposition in air are shown in Figure 6-23 (a) and (b). Both backbones are covered with the impregnated species, LSCF and NiO, and no obvious degradation of the skeleton ceramics is observed.

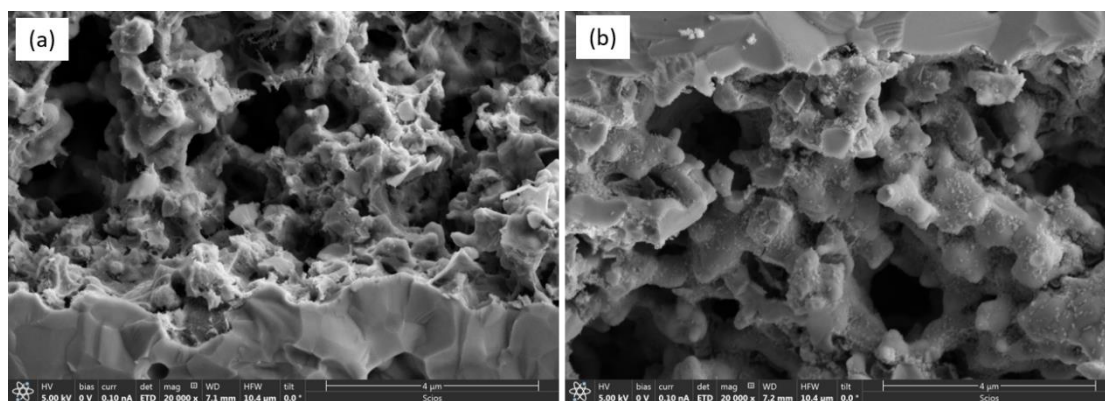


Figure 6-23. Microstructures of impregnated LSCF (a) and NiO (b).

### 6.6.2 AC impedance and I-V curve

Silver was used as a current collector to provide efficient electric contact between electrode and electrical connections. The cell was sealed in the testing jig, with the Ni side exposing to humidified hydrogen atmosphere and the LSCF electrode to air. Afterwards, the cell was heated to 600 °C in reducing atmosphere to obtain Ni metal particles on the scaffold. The AC impedance spectra under OCV mode at 600, 650 and 700 °C are plotted in Figure 6-24 (a). Both the ohmic resistance and the polarisation resistance are decreased with increasing the temperature, and polarisation resistance is influenced more by temperature. The I-V and power density curves of the single cell were measured at the temperature range of 450 °C – 700 °C, shown in Figure 6-24 (b). The OCV value of 1.14 V indicates a good sealing of the cell and satisfying separation between the anode and cathode. However, the maximum power density of the cell is very low, with a value of 5.5 mW cm<sup>-2</sup> at 700 °C and decreasing with lower temperature.

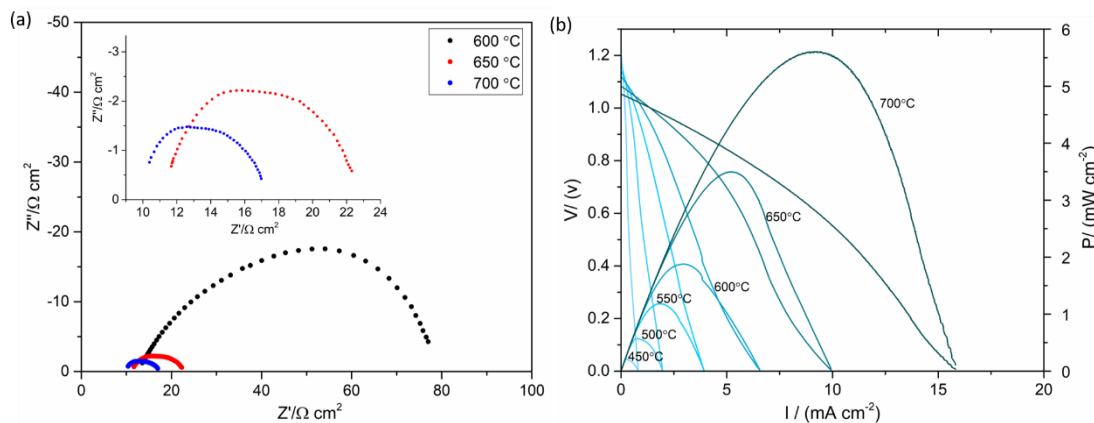


Figure 6-24. (a) AC impedance spectra of BCZYZ-LSCF/BCZYZ/Ni,Cu-BCZYZ-Ni cells with impregnated electrodes in humidified H<sub>2</sub> as a function of temperature, (b) I-V curve and power density of the cell under fuel cell mode.

The microstructure of the impregnated electrodes after testing are displayed in Figure 6-25. For the LSCF impregnated electrode, the surface of BCZYZ backbone seems to be covered with a layer of another phase, which is supposed to be LSCF material. The interface between the electrode and electrolyte component looks completely covered with LSCF phase. This morphology of LSCF is not displayed as the expected spherical nanoparticle structure that reported in literature, although a more detailed analysis at higher magnifications is required<sup>27-28</sup>. EDS mappings in Figure 6-26 (a) reveal that La, Co and Fe are distributed uniformly while Sr agglomerates in some areas. The secondary phase containing Sr is supposed to appear after the calcination of the impregnated cell but not a result of the test. Shown in Figure 6-26 (b), XRD result of the evaporated LSCF precursor solution after calcination at 800 °C for 1h indicates that the LSCF is not a pure phase, consisting of LSCF phase and SrCO<sub>3</sub> impurity. The appearance of SrCO<sub>3</sub> phase is supposed to result from the inhomogeneous solution since in the preparation of precursor solution, Sr(NO<sub>3</sub>)<sub>2</sub> was first dissolved in ethanediol due to the limited solubility in ethanol followed by mixing with the ethanol solution dissolving with the other three compounds. The cell was weighed before and after impregnation and the loaded LSCF content was calculated to be about 16%. The insufficient amount of impregnated LSCF and the existence of impurity may contribute

to low electrical conductivity of the electrode and thus produce a large  $R_p$  value. Therefore, in the future work, the impregnation of LSCF need to be further optimized and the impregnation process should be repeated for more times to achieve enough amount of deposited LSCF. On the nickel impregnated Ni, Cu-BCZY electrode, numerous spherical Ni metal particles are dispersed on the scaffold, which can not only form a percolation path for the electrical conductivity but also catalyse the dissociation of steam in steam electrolysis. The Ni concentration is about 30% and satisfied with expected loading amount.

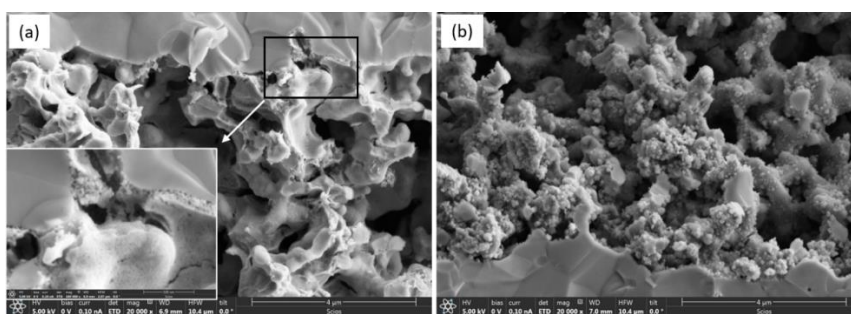


Figure 6-25. Microstructures of impregnated electrodes after testing. (a) LSCF, (b) Ni.

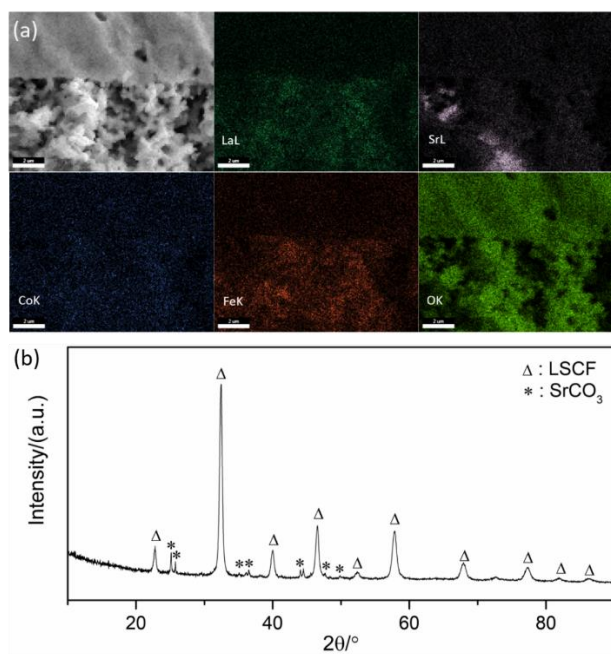


Figure 6-26. (a) EDS mappings of impregnated LSCF after testing, (b) XRD pattern of calcined LSCF precursor solution after evaporation at 800 for 1h.

Overall, a skeleton of the cell is obtained with dense electrolyte prepared from tape casting method and porous electrode from screen printing technique. Impregnation seems to be an effective way to prepare the electrode components of the electronic conduction provider and catalytic sites. But more efforts need to focus on the technique of the impregnation procedure. For the preferential in-situ exsolution method to achieve nanocatalysts on the electrode, some parameters should be refined, such as the microstructure of the substrate perovskite, the electrochemical switching atmosphere, gas humidity, switching voltage and time, etc.

## 6.7 Conclusions

1. ZnO is an effective sintering aid for BCZY oxide and a pure phase can be obtained at 1350 °C.

2. Aqueous slurry is not suitable for preparing the BCZY dense electrolyte.

3. Dense BCZY electrolyte is successfully fabricated by an organic-system tape casting method.

4. Porous BCZY and Ni,Cu-BCZY skeletons with suitable good microstructure are obtained by printing method, and the ink for printing is preferably made from the mixture of pre-calcined BCZY powder and sintering aids.

5. No exsolution occurs on the coated Ni, Cu-BCZY electrode either by chemical reducing or electrochemical switching. It may be because of the effect of perovskite synthesis method on the structure stability and surface energy of the material. For the electrochemical switching, parameters including atmosphere, humidity, switching voltage and time can also affect the exsolution result.

6. Well dispersed Ni nanoparticles are achieved by impregnation method. However, the impregnated LSCF exhibits an impure phase and its impregnation amount is not enough.

7. Ohmic resistance and polarisation resistances are decreasing with the testing temperature with polarisation resistance showing a higher dependence on the temperature than the ohmic resistance.

## References

1. Tong, J.; Clark, D.; Bernau, L.; Sanders, M.; O'Hayre, R., Solid-state reactive sintering mechanism for large-grained yttrium-doped barium zirconate proton conducting ceramics. *Journal of Materials Chemistry* **2010**, *20* (30), 6333-6341.
2. Babilo, P.; Haile, S. M., Enhanced sintering of yttrium-doped barium Zirconate by addition of ZnO. *Journal of the American Ceramic Society* **2005**, *88* (9), 2362-2368.
3. Choi, S. M.; Lee, J.-H.; Ji, H. I.; Yoon, K. J.; Son, J.-W.; Kim, B.-K.; Je, H. J.; Lee, H.-W.; Lee, J.-H., Determination of proton transference number of  $\text{Ba}(\text{Zr}_{0.84}\text{Y}_{0.15}\text{Cu}_{0.01})\text{O}_{3-\delta}$  via electrochemical concentration cell test. *Journal of Solid State Electrochemistry* **2013**, *17* (11), 2833-2838.
4. Costa, R.; Grünbaum, N.; Berger, M. H.; Dessemond, L.; Thorel, A., On the use of NiO as sintering additive for  $\text{BaCe}_{0.9}\text{Y}_{0.1}\text{O}_{3-\alpha}$ . *Solid State Ionics* **2009**, *180* (11-13), 891-895.
5. Kosasang, O.; Jareun, R.; Phongsathit, S.; Mach-mumas, S., Influence of CuO and ZnO additions on grain growth and proton conductivity of Y-doped  $\text{BaZrO}_3$ . *Journal of the Australian Ceramic Society* **2019**, *56* (2), 441-446.
6. Kang, S.-J. L., *Sintering: densification, grain growth and microstructure*. Elsevier: 2004.
7. Savaniu, C. D.; Canales-Vazquez, J.; Irvine, J. T., Investigation of proton conducting  $\text{BaZr}_{0.9}\text{Y}_{0.1}\text{O}_{2.95}$ :  $\text{BaCe}_{0.9}\text{Y}_{0.1}\text{O}_{2.95}$  core-shell structures. *Journal of Materials Chemistry* **2005**, *15* (5), 598-604.
8. Mistler, R.; Twina, E., *Tape casting: theory and practice* (Westerville, OH: American Ceramic Society). **2000**.
9. Rahaman, M. N., *Ceramic processing and sintering*. CRC press: 2003.
10. Will, J.; Mitterdorfer, A.; Kleinlogel, C.; Perednis, D.; Gauckler, L., Fabrication of thin electrolytes for second-generation solid oxide fuel cells. *Solid State Ionics* **2000**, *131* (1-2), 79-96.
11. Liao, W.-Y.; Chou, T.-C., Fabrication of a planar-form screen-printed solid electrolyte modified Ag/AgCl reference electrode for application in a potentiometric

biosensor. *Analytical Chemistry* **2006**, 78 (12), 4219-4223.

12. Ohta, S.; Komagata, S.; Seki, J.; Saeki, T.; Morishita, S.; Asaoka, T., All-solid-state lithium ion battery using garnet-type oxide and  $\text{Li}_3\text{BO}_3$  solid electrolytes fabricated by screen-printing. *Journal of Power Sources* **2013**, 238, 53-56.

13. Peng, R.; Xia, C.; Liu, X.; Peng, D.; Meng, G., Intermediate-temperature SOFCs with thin  $\text{Ce}_{0.8}\text{Y}_{0.2}\text{O}_{1.9}$  films prepared by screen-printing. *Solid State Ionics* **2002**, 152, 561-565.

14. Ge, X.; Huang, X.; Zhang, Y.; Lu, Z.; Xu, J.; Chen, K.; Dong, D.; Liu, Z.; Miao, J.; Su, W., Screen-printed thin YSZ films used as electrolytes for solid oxide fuel cells. *Journal of Power Sources* **2006**, 159 (2), 1048-1050.

15. Wang, Y.; Madsen, B.; Kobsiriphat, W.; Barnett, S.; Marks, L., Electron microscopy study of novel Ru doped  $\text{La}_{0.8}\text{Sr}_{0.2}\text{CrO}_3$  as anode materials for Solid Oxide Fuel Cells (SOFCs). *Microscopy and Microanalysis* **2007**, 13 (S02), 100.

16. Madsen, B.; Kobsiriphat, W.; Wang, Y.; Marks, L.; Barnett, S. A., Nucleation of nanometer-scale electrocatalyst particles in solid oxide fuel cell anodes. *Journal of Power Sources* **2007**, 166 (1), 64-67.

17. Kobsiriphat, W.; Madsen, B.; Wang, Y.; Shah, M.; Marks, L.; Barnett, S., Nickel-and ruthenium-doped lanthanum chromite anodes: effects of nanoscale metal precipitation on solid oxide fuel cell performance. *Journal of The Electrochemical Society* **2009**, 157 (2), B279.

18. Adijanto, L.; Padmanabhan, V. B.; Gorte, R. J.; Vohs, J. M., Polarization-induced hysteresis in CuCo-doped rare earth vanadates SOFC anodes. *Journal of The Electrochemical Society* **2012**, 159 (11), F751.

19. Myung, J. H.; Neagu, D.; Miller, D. N.; Irvine, J. T., Switching on electrocatalytic activity in solid oxide cells. *Nature* **2016**, 537 (7621), 528-531.

20. Irvine, J. T. S.; Neagu, D.; Verbraeken, M. C.; Chatzichristodoulou, C.; Graves, C.; Mogensen, M. B., Evolution of the electrochemical interface in high-temperature fuel cells and electrolyzers. *Nature Energy* **2016**, 1 (1), 1-13.

21. Lee, S.-Y.; Aris, R., The distribution of active ingredients in supported catalysts prepared by impregnation. *Catalysis Reviews Science and Engineering* **1985**,



27 (2), 207-340.

22. Yuvaraj, S.; Fan-Yuan, L.; Tsong-Huei, C.; Chuin-Tih, Y., Thermal decomposition of metal nitrates in air and hydrogen environments. *The Journal of Physical Chemistry B* **2003**, *107* (4), 1044-1047.

23. Brockner, W.; Ehrhardt, C.; Gjikaj, M., Thermal decomposition of nickel nitrate hexahydrate,  $\text{Ni}(\text{NO}_3)_2 \cdot 6\text{H}_2\text{O}$ , in comparison to  $\text{Co}(\text{NO}_3)_2 \cdot 6\text{H}_2\text{O}$  and  $\text{Ca}(\text{NO}_3)_2 \cdot 4\text{H}_2\text{O}$ . *Thermochimica Acta* **2007**, *456* (1), 64-68.

24. Klinsrisuk, S. Novel electrocatalytic membrane for ammonia synthesis. University of St Andrews, 2010.

25. Bhide, S. V.; Virkar, A. V., Stability of  $\text{BaCeO}_3$ -based proton conductors in water-containing atmospheres. *Journal of The Electrochemical Society* **1999**, *146* (6), 2038.

26. Chen, J.; Liang, F.; Yan, D.; Pu, J.; Chi, B.; Jiang, S. P.; Jian, L., Performance of large-scale anode-supported solid oxide fuel cells with impregnated  $\text{La}_{0.6}\text{Sr}_{0.4}\text{Co}_{0.2}\text{Fe}_{0.8}\text{O}_{3-\delta} + \text{Y}_2\text{O}_3$  stabilized  $\text{ZrO}_2$  composite cathodes. *Journal of Power Sources* **2010**, *195* (16), 5201-5205.

27. Liu, Y.; Chi, B.; Pu, J.; Li, J., Performance degradation of impregnated  $\text{La}_{0.6}\text{Sr}_{0.4}\text{Co}_{0.2}\text{Fe}_{0.8}\text{O}_3 + \text{Y}_2\text{O}_3$  stabilized  $\text{ZrO}_2$  composite cathodes of intermediate temperature solid oxide fuel cells. *International Journal of Hydrogen Energy* **2012**, *37* (5), 4388-4393.

28. Liu, Y.; Wang, F.; Chi, B.; Pu, J.; Jian, L.; Jiang, S. P., A stability study of impregnated LSCF–GDC composite cathodes of solid oxide fuel cells. *Journal of Alloys and Compounds* **2013**, *578*, 37-43.

## Conclusions

This study revealed the nanoparticle exsolution phenomenon from barium cerate zirconate perovskite substrate and illustrated the mechanism. In addition to the exsolution from the bulk perovskite, a competing exsolution from an intermediate phase is observed here, which includes the exsolution of Ba-M-O from the perovskite and the exsolution of M from the Ba-M-O phase.

In the Cu particle growth from the doped BCZY oxide,  $\text{Ba}^{2+}$  is suggested to firstly diffuse to the perovskite surface, forming  $\text{BaO}_x$ . The diffusion usually occurs from about 100 nm below the substrate surface. The vacancies created from barium segregation reduces the migration barrier for copper ions greatly, which leads to the copper ions transferring to the surface afterwards, forming Ba-Cu-O intermediate phases with the  $\text{BaO}_x$ . With a longer reduction time or higher reduction temperature, the copper ions exsolve from the Ba-Cu-O phase, reduced into Cu metal particles. Determined by the phase equilibrium in the BaO-CuO system, the exsolving of Cu particle from the Ba-Cu-O phase is accompanied with the segregation of  $\text{BaO}_x$ , resulting in mixing different interfaces: metal particle and perovskite substrate, metal particle and  $\text{BaO}_x$ ,  $\text{BaO}_x$  and perovskite substrate. Meanwhile, this exsolution process results in some Cu particles consisting of traces of  $\text{Ba}^0$ , existing on the surface layer of the particle, which may change the catalytic activity in catalysis or electrochemical catalysis. The morphology of Cu particles are re-constructed after oxygen plasma treatment, showing a much higher catalytic activity towards CO oxidation.

Ni doping in the barium cerate zirconate is accompanied with impurity phases of  $\text{Y}_2\text{BaNiO}_5$ , NiO and  $\text{BaNi}_{0.83}\text{O}_{2.5}$ , varied depending on the doping concentration. 5% A-site deficiency decreases the sinterability of the material, leading to a smaller grain and porous structure due to the less amount of active barium participating in forming the liquid phase to facilitate sintering. When doping 6% Ni in the stoichiometric composition, exsolution occurs in three ways. The first one is conventionally suggested exsolution from the destabilized perovskite lattice due to oxygen loss. The second one occurs at the near grain boundary area, exsolving after the volatilization of  $\text{Ba}(\text{OH})_2$

that comes from decomposition of  $\text{BaNi}_{0.83}\text{O}_{2.5}$  impurities. The third process is similar as the copper exsolution mechanism, that Ni particles decomposed from the segregated barium nickelate flakes. A-site deficiency can only weaken the segregation of barium nickelate but not eliminate.

While 4% single dopant of Cu or Ni gives rise to impure phases in the perovskite sintering, the co-doping of Cu and Ni eliminates the formation of impurities. Much nicer exsolutions were obtained in the bimetal doping perovskite, with a smaller particle size and higher population. Barium migration promotes the alloy exsolution due to the formation of Ba-Ni-Cu-O as an intermediate phase, as verified by the larger population and smaller particle size on the A-site cation rich smooth native surface. This exsolution process overcomes the drawbacks of limited B-site exsolution due to A-site enrichment on the surface. In addition, when the perovskite is doped with 2% nickel and copper for each, the resulted alloy particle has a Ni/Cu ratio of  $\sim 4/1$ , suggesting that the reducibility of the cation is strongly affected by another species. For the influence of A-site deficiency on proton conductivity, it enhances the conductivity by improving the pre-exponential factor at the grain boundary.

Unfortunately, when the doped barium cerate zirconate material is applied as solid oxide cell electrode by tape casting or screen-printing method, nanoparticles exsolution is difficult to occur, either shows a small particle size with less population or no exsolutions. This is probably inhibited by the high surface energy of the perovskite fabricating by these techniques.

#### **Future work:**

In this work, the electrode with finely distributed nanoparticles from exsolution was not successfully prepared. In future work, the cell will be fabricated by solid-state reactive sintering and tested for  $\text{CO}_2$  and  $\text{H}_2\text{O}$  co-electrolysis.

Recent work on the BCZY supported Cu particles catalyse CO oxidation shows a very high activity, especially the plasma modified pellet, with the  $r_{\text{CO}_2}$  value reaching  $0.29 \mu\text{mol}/(\text{s cm}^2)$ . The exsolved particles on BCZY is quite promising in the catalytic field. More catalytic tests on the materials with Cu or Ni-Cu alloy exsolutions will be

conducted, such as NO oxidation and WGS reaction.

The bimetallic doping behaviour in the BCZY is also worth to be investigated.